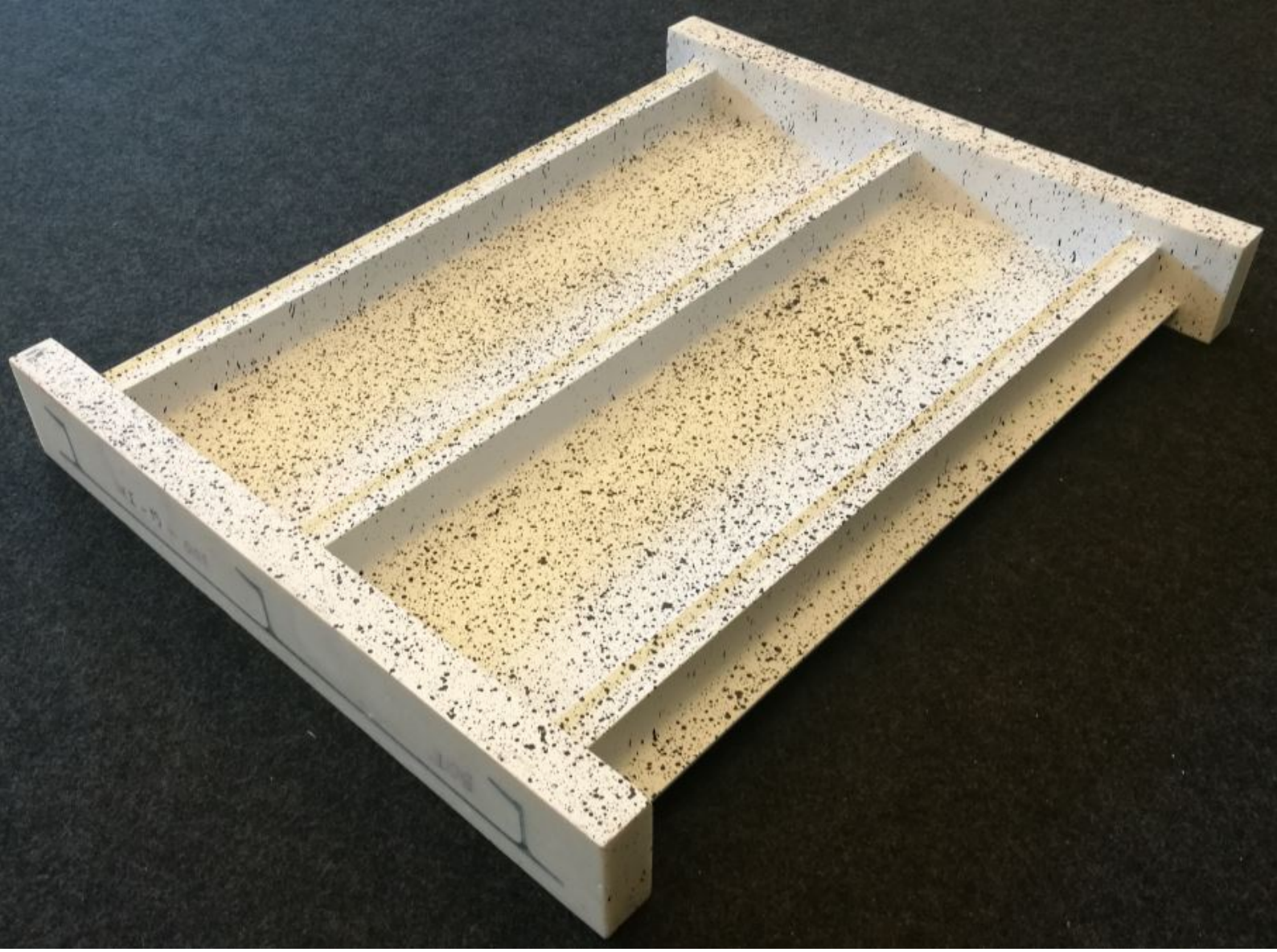

Numerical and experimental study on post-buckling skin-stringer separation in butt-joined stiffened thermoplastic panels

Master of Science Thesis

Baciu Theodor Dan

Delft University of Technology

TU Delft Delft University of Technology

Challenge the future

Numerical and experimental study on post-buckling skin-stringer separation in butt-joined stiffened thermoplastic panels

Master of Science Thesis

Baciu Theodor Dan

February 21, 2020

For obtaining the degree of Master of Science at the Delft University of Technology,
to be defended publicly from 9:00, 17th of March 2020 at TU Delft Faculty of Aerospace Eng., lecture room C.

Thesis committee:	Prof.dr. Chiara Bisagni	Chair & Supervisor TU Delft
	Dr. Sergio R. Turteltaub	TU Delft
	Dr.ir. Daniël M.J. Peeters	TU Delft
	Sen. Stress Eng. Jan Waleson	Supervisor Fokker Technologies

Delft University of Technology

ABSTRACT

So far thermoset based composites have been used in primary aircraft structures, owing to their good performance and vast research on the subject. Recently thermoplastic based composites also gained an increased attention and there is a push towards adopting these for primary aircraft structures as well. This interest for thermoplastic composites in aeronautical structures is driven by the material's advantages over thermoset parts in joining methods, damage tolerance, sustaining, shelf live, recyclability, or chemical stability. The butt-joint feature is one of the novel joining techniques made possible by using thermoplastic composites, joining technique which can used to assemble stiffened panels by co-consolidating different, typically flat, laminates. With the potential use of thermoplastic structures in primary aircraft structures being relatively recently considered, the available literature on the damage behaviour of thermoplastic stiffened panels under compression is still scarce, to say the least, especially when using this novel butt-joint feature.

In this project, the building-block approach is used to develop a robust modeling technique able to model skin-stringer separation in butt-joined thermoplastic panels under compression. Here the modeling strategy is developed in a step-by-step fashion, going from a material characterisation coupon scale, up to a sub-component scale. The separation was first modeled in a DCB coupon used to describe the $Mode\ 1$ material fracture toughness, then in a single-stringer specimen with skin-stringer de-bond and finally in a multi-stringer panel with skin-stringer de-bond.

The base of the damage modeling strategy was defined by studying the load-displacement response of a DCB specimen using multiple models. First, an experimental load-displacement response of a DCB specimen was captured by an analytical approach, with which the accuracy of the numerical models was compared. The numerical approaches tried were based on cohesive zone models (contact and element based) and on the Virtual Crack Closure Technique, with the latter proving to be better suited for this particular task. The $VCCT$ separation damage model was preferred here since it allowed the use of coarser meshes than the cohesive zone models, with a superior overall accuracy as well. As the material of the studied DCB specimen was identical with the one identical of the single-stringer specimen and multi-stringer panel aforementioned, the $VCCT$ model used to model separation was also kept identical when these larger structures were studied.

The accuracy of the FE model developed for the single-stringer specimen was also assessed by comparing its load-displacement curve and failure load with the existent experimental data, improving the modeling technique for its use in the multi-stringer panel. As an FE model which correlated well with the experimental data already existed within Fokker, using a cohesive surface based damage model, the shortcomings of this damage model was shown by applying it to the lower scale DCB specimen. Implementing this damage model for the DCB specimen led to a very poor load-displacement correlation, owing to the altered fracture toughnesses values with respect to the measured one. With the shortcomings of the old separation damage model shown, the $VCCT$ one was implemented in this already existent model, which gave a poor correlation with the experimental data. Since the $VCCT$ damage model used needed to be kept unmodified, the butt-joints of the single stringer were refined and the elements used for these areas were updated in a new FE model, these changes leading to a near excellent experiment-simulation correlation in terms of load-displacement curves and failure loads.

The modeling technique developed was then used further to study skin-stringer separation in the multi-stringer panel. A sensitivity study on the panel's compressive response with and without the de-bond damage modeled revealed the high sensitivity of its skin buckling pattern. The occurring skin buckling pattern appeared to be highly influenced by the skin's imperfect non-flat shape, asymmetric load introduction, ends boundary conditions, as well as by the de-bond damage itself. This very sensitive skin buckling pattern was attributed to the specific combination of panel's skin bays boundary conditions and skin bays aspect ratio, which likely gave a buckling coefficient governed either by a 3 or 4 longitudinal buckling half-waves. The sensitivity study on the different possibly occurring buckling patterns revealed that the ones promoting de-bond growth from a certain side of the stringer have a strong influence on the panel's failure load, decreasing the strength of the panel by as much as 25% for a 4 half-waves skin buckling pattern, the most likely to occur however having a 3 half-waves one. Similarly, the most significant strength increase was also due to a 4 half-waves skin buckling pattern, the difference between this and the aforementioned one being the stringer side

from which the de-bond grew.

Furthermore, this sensitivity study was also used to select a best blind prediction based on which the experimental test plan was defined. The test measurement set-up to correlate and validate the developed FE model was also defined based on this selected best blind prediction and it was successfully used during the experimental test to accurately capture the panel's compressive response.

The test-model correlation showed that the FE model was able to predict the compressive response of the panel with great accuracy in what concerns its load-compression response, failure load, buckling behaviour, skin out-of-plane deflections and the qualitative aspect of the de-bond growth. These qualitative aspects of the de-bond growth were its skin buckling pattern influenced location, de-bond growth front shape and its growth soon after skin buckling occurred. A initially very good correlation in terms of load-strain response was also achieved, this correlation being highly influenced by two aspects. First source of test-model strain correlation mis-match was considered to be the significant difference in the panel's skin buckling load, while the second one was the model's poor prediction of the panel's stiffness drop associated with de-bond growth. The de-bond growth was overestimated by the FE model prediction, while the panel stiffness loss as a result of the de-bond growth was underestimated.

Overall, the presented modeling strategy to model and study skin-stringer separation in thermoplastic butt-joint stiffened panel under compression proved to be robust. The robustness of this method comes mainly from the same modeling strategy used at all the addressed scales and with the same $VCCT$ damage model using the measured material fracture toughnesses. This implies that the presented method could be successfully transferred to similar panels with similar skin-stringer damage, provided that skin-stringer separation is the main failure mode.

FOREWORD

Studying at TU Deflt gave me fantastic opportunity do grow on so many levels besides the purely academical one, since it put me face to face with so many different work and cultural contexts. While I put a lot of effort during this period and especially in this final project, I also had a lot of fantastic support along the way.

First and foremost I would like to thank my family and to my parents in particular, without whom I would not have had this amazing opportunity and whom I might not be ever able to thank enough.

Furthermore I would like to thank to Sebastiaan van Hese, who made me realize that studying at TU Delft was not as unfeasible as I initially thought, which several years later brought me to the point where I obtained my MSc degree in Aerospace Engineering from this university.

Special thanks goes also to my academic supervisor Chiara Bisagni, whose valuable feedback helped shaping both the technical and result presentation side of this report. She always made time to give me valuable feedback and to find areas in which I can improve and advised me on how to do it, for which I am very grateful.

I would also like to thank Fokker Aerostructures for this great thesis opportunity and all the provided experimental data, expertise and panel to be tested. Special thanks go to Bas Tijs, Jan Waleson who supervised my thesis project on behalf of Fokker. I would also like to show my gratitude to Jaap Willem, and Ivo Lippers who provided valuable support regarding the panel's experimental testing, as well as to Sebastiaan van den Berg and Brendan Romano and for their support on the finite element modeling side of this thesis project.

Many thanks goes also to Edgar Labans, who also provided valuable support for experimental side of this thesis project, as well as to Kevin van Dooren, with whom I often consulted on numerous aspects regarding this thesis.

I would also like to thank to all of my friends who were close to me during this period and especially to those who I might also have 'polluted' emotionally. Many thanks to Emilia, Sophie, Thomas, João, Vlad, Sanjeev, Victor, Maria, as well as to the people from Schiedam's tower 6th and 9th floor with whom I spent and enjoyed my free time. I hope I will see at least some of you after my graduation and show you a less stressed, more enjoyable '2.0' version of myself.

To the people who will read this project, I can only hope that you will find the 'story' of my project and successful end test-simulation correlation interesting and valuable, I wish you an enjoyable read.

NOMENCLATURE

$ALLCCDW$	Abaqus contact constraint discontinuity work	
$ALLCD$	Abaqus energy dissipated by creep, swelling and viscoelasticity	
$ALLIE$	Abaqus total strain energy	
$ALLVD$	Abaqus energy dissipated by viscous effects	
$ALLWK$	Abaqus external work	
BC	Boundary Conditions	
$BVID$	Barely Visible Impact Damage	
$CFRP$	Carbon Fiber Reinforced Plastics	
CTD	Cold Temperature Dry	
CTE	Coefficient of Thermal Expansion	K^{-1}
CZE	Cohesive Zone Element	
CZM	Cohesive Zone Model	
CZS	Cohesive Zone Surface	
DCB	Double Cantilever Beam	
DIC	Digital Image Correlation	
E_1	Longitudinal elastic modulus	Pa
E_2	Transverse in-plane elastic modulus	Pa
E_3	Transverse out-of-plane elastic modulus	Pa
ENF	End Notch Flexure	
$ETOTAL$	Abaqus energy balance	
FE	Finite Element	
FEA	Finite Element Analysis	
FEM	Finite Element Method	
G_{12}	In-plane shear modulus	Pa
G_{13}	Transverse in-plane shear modulus	Pa
G_{23}	Out-of-plane shear modulus	Pa
$GLARE$	Glass Laminate Aluminum Reinforced Epoxy	
HW	Hot Wet	
IML	Inner Mould Line	
$LEFM$	Linear Elastic Fracture Mechanics	
$LVDT$	Linear Variable Differential Transformer	

NLR	Netherlands Aerospace Centre	
OML	Outer Mould Line	
$PEKK$	Poly-Ether-Ketone-Ketone	
RH	Relative Humidity	
RTD	Room Temperature Dry	
$SERR(G)$	Strain Energy Release Rate	$\frac{\mathrm{J}}{\mathrm{m}^2}$
$SFRP$	Short Fiber Reinforced Plastics	
$TAPAS$	Thermoplastic Affordable Primary Aircraft Structures	
UD	Uni-Directional	
$VCCT$	Virtual Crack Closure Technique	
$XFEM$	eXtendedFEM	

List of Figures

List of Tables

Contents

1 | INTRODUCTION

Nowadays the benefit of composite structures use in the aerospace sector has been widely seen and accepted. These structures have found their way into secondary, and quite for a while now also in primary, aerospace structures like spars, ribs, skins, or stiffened wing or fuselage panels to name a few. While the bulk of the composite structures used so far in secondary and primary aerospace structural applications are thermoset based, there is a recent interest in developing and adopting thermoplastic based composites for these applications as well [1]. The push for thermoplastic composites for aerospace structural applications was somewhat delayed until recently, among the likely causes being possible higher processing costs, as well as the lower level of testing and understanding these structures when compared with their thermoset counterparts [1–5]. However, the structural efficiency, damage tolerance, chemical and flame resistance, cost efficiency, or joining techniques (which can be similar to the ones used in metallic structures) are just a few of the many advantages that thermoplastic based composites can offer compared with thermoset based ones. Out of this class of thermoplastic materials, $PEKK$ (Poly-Ether-Ketone-Ketone) based ones are one of the most promising high-performance thermoplastic matrix composites that could be successfully used in aerospace structural applications, particularly when carbon fiber reinforced.

One example of the joining possibilities enabled by thermoplastic composites is the so called butt-joint feature, which is a $Carbon/PEKK$, injection moulded $SFRP$ (Short-Fiber Reinforced Plastic) used to join different $C/PEKK$ laminates together via a co-consolidation process. This novel joining technique aims at simplifying the stiffened panels assembly, while also reducing the costs associated with it and it was developed by Fokker Technologies [6], which also provided supervision for this thesis project, as well as all the data and materials necessary. With this novel joining technique, the need to study skin-stiffener separation damage of butt-joined stiffened panels under compression also arises. This damage especially needs a deep understanding, since it represents one of the common failure modes in stiffened panels loaded in compression. This failure mode becomes even more relevant when a larger design space, including post-buckling, is considered, as it could result in further increasing the structure's efficiency by accounting for its damage tolerance. In this case the current $70mm$ de-bond is considered to fall under the Barely Visible Impact Damage (BIVD) criteria, therefore the ultimate residual strength must be determined. This type of damage is particularly critical for this structures with continuously stringer joints, as existent growing de-bond could no longer be arrested at discrete joining points like fasteners. This implies that for future studies of de-bonds significantly larger than $70mm$ also the limit load capabilities need to be shown, for which the work shown in this report could be further used. As an important and interesting observations, these types of damages are likely to occur under impact only when the impacts are on the inner mould line (IML) of the skin (or inner side), as the impacts on the outer mould line (OML) of the skin (or below the stringer) hardly caused any damage. In this thesis, skin-stringer separation is numerically and experimentally studied in a butt-joined stiffened $C/PEKK$ panel in post-buckling regime, showing the ultimate load carrying capabilities of a butt-joined stiffened panel with a $BIVD$ skin-stringer de-bond.

For this study, the building-block approach [7] is used to build a robust FE modeling strategy able to accurately predict the compressive behaviour of butt-joined stiffened panels with skin-stringer de-bonds under compression. The building-block approach is a method used in structural applications to build robust designs in an logical, ordered manner, starting from a small level of detail, like material screening and characterization, to a high level of detail, like complete structures[7]. For this methodology to be robust, typically multiple aspects in what regards designing a structure, like numerical analysis, experimental testing, or manufacturing aspects (including tooling) are taken into account. The building-block approach is used in this project to evaluate separation at multiple scale levels, starting from simple material characterisation for mode I separation 2.7 using a DCB specimen, to skin-stringer de-bond in a 1-stringer specimen, to skin-stringer de-bond in a 3-stringer panel.

In the first block, separation under mode I is studied analytically and numerically, assessing the robustness of multiple numerical methods in capturing the experimental and analytical behaviour of the DCB load-displacement curve. In this first block the base of the modeling strategy is defined, which serves as an input for the second block. The modeling approach is defined from the initial stage with its final purpose in mind,

it being modeling skin-stiffener separation at panel level. In the second block, the modeling strategy used in the previous stage is applied to a simple 1-stringer specimen and the modeling approach is further improved to suit the larger model scale. This evolution is also done by assessing the accuracy of the 1-stringer specimen FE model, by comparing its load-displacement response with the test data. In this block the modeling strategy for the 3-stringer panel is defined, as the stringer geometry of this 1-stringer specimen is similar with the one of the 3-stringer panel. In the last block the developed modeling strategy is first verified to see if the geometrical simplifications previously made for the 1-stringer specimen can accurately capture the panel's nominal geometry FE model behaviour. After this response check, the panel's compressive behaviour in both its damaged and undamaged state is studied under various plausible experimental scenarios. Emphasis on this study is put on the panel's buckling behaviour and its relation with the de-bond growth in particular, as this aspect is critical for the panel's failure load. From the sensitivity study on the panel's behaviour including damage, the best blind prediction is selected to be correlated with the experimental results.

Besides the modeling side of the project, emphasis is also put on the experimental means to validate the FE model of the 3-stringer panel. This is due to the possible difficulties that can arise during the experimental test, as often the real test environment tends to differ from the simulation one. With that being said, a clever test set-up is needed to both capture the panel's compressive behaviour, as well as to capture any differences between the test and simulation environments. However, the correlation is not done considering the test observations, since a secondary goal of this thesis is to asses the accuracy of the best blind prediction, the test also being used to validate the FE model built. Correlating the test results with the best FE model prediction also serves in assessing the capabilities of the developed modeling strategy in virtual testing at panel level [8]. Virtual testing has the aim to reduce the number of traditional experimental tests, by using robust modeling techniques (often based on the building-block approach) to simulate various design configurations with sufficient accuracy, such that only the desired designs will reach the phase of experimental testing. As this project also has an experimental part, an assessment on the robustness of the FE modeling strategy with its feasibility for virtual testing use for future panel designs can also be given.

In this report, the work context regarding the skin-stringer butt-joint and the failure of $C/PEKK$ butt-joined stiffened panels is given in chapter 2. Also in this chapter the damage models used to asses and capture separation under mode I are shown, this chapter containing a part from this project's literature survey. Chapter 4.1 introduces the input used to model 3-stringer panel, with its dimensions, material data and test configuration being presented here. Details about the panel's manufacturing and test preparation are also given in this chapter. The modeling strategy development part of the project is shown in chapter 3. In this chapter first the damage model considered best suited to capture skin-stiffener separation at panel level is chosen based on its robustness and accuracy of capturing the experimental and the analytical load-displacement response of a DCB test specimen. Second, this damage model and the modeling strategy is further improved, such that the failure of a simple 1-stringer specimen with skin-stiffener de-bond is accurately captured and the modeling strategy used is validated at this scale as well using the available experimental data. Chapter 4 treats exclusively the 3-stringer panel, the modeling simplifications used in the previous chapter being again verified for the 3-stringer panel, after which a sensitivity study is done to study the un-damaged and damaged 3-stringer's panel damaged behaviour. The experimental test set-up and test results are shown and discussed in chapter 5, together with the correlation of the test results with the best blind prediction from chapter 4. Last chapter 6 presents the project's concluding remarks and the recommendations for future work.

2 | LITERATURE SURVEY

In this first section of this chapter, the butt-joint feature is explained in more details and its failure modes under different loading conditions are described. Next, the butt-joined stiffened thermoplastic panels developed and tested during the TAPAS 2 project (Thermoplastic Affordable Primary Aerospace Structures) [9] are briefly described, together with their assembly and some material characteristics. A failure analysis of these TAPAS panels is also done, for both the compression and shear load cases, due to the scarcity of the available literature on butt-joined stiffened panel's failure. The second section of this chapter treats the skin-stiffener separation damage models, briefly describing the numerical models behind. In this section three skin-separation damage models are described, these being cohesive zone models using either elements, or surface-based contact and $VCCT$ (Virtual Crack Closure Technique).

2.1 TAPAS BUTT-JOINT FEATURE

The butt-joint feature (filler) is an injection moulded joining part, here made out of short fiber $AS4/PEKK$ [10]. The fiber volume ratio is usually around 20% and the fibers are aligned on a longitudinal direction. Its main function is to join and to ensure the load transfer between different parts in an assembly, as shown in figure 2.1, with other geometries also possible, as shown in figure 2.2.

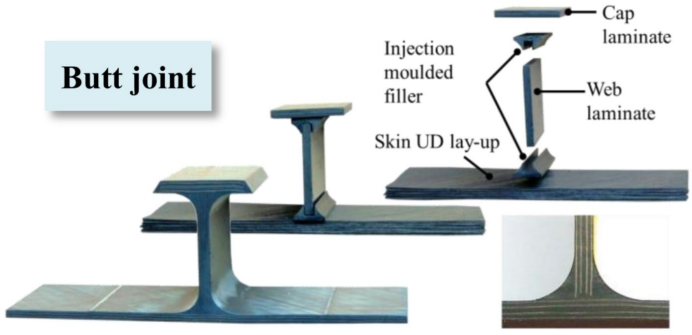

Figure 2.1: Butt-joint design [11]

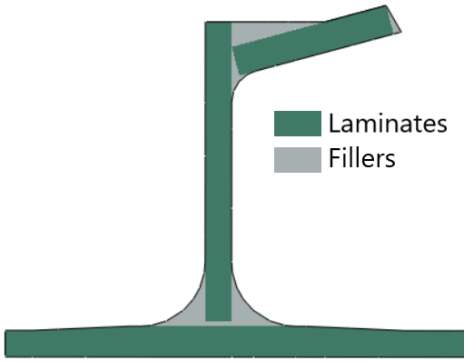

Figure 2.2: 3-stringer panel skin-stringer assembly schematic

The available data on butt-joints and their behaviour is relatively scarce, with Akkerman et al. [12] studying the failure and the cohesive zone length (or the fracture process zone length) in co-consolidated hybrid $C/PEKK$ butt-joints, Akkeram and Rietman [10] studying the pull of strength of $AS4/PEEK$ (Poly-Ether-Ether-Ketone) $T-joints$ and Kirill et al. [13] modeling the failure of butt-joints under quasi-static loading. A comprehensive review on the state of art in filler materials in composite out-of-plane joints is given by Sápi et al. [14], where the manufacturing methods, performance and failure mechanisms of multiple joint types are reviewed.

The butt-joint feature takes advantage of the intrinsic property of thermoplastic materials to be shaped and re-shaped through melting and consolidation, without major looses in their mechanical properties per re-shape. This comes with a great advantage in what concerns assemblies, enabling metal-like welding processes, which have several advantages over thermoset assemblies. For example, as it can be seen in figures 2.1 and 2.2, all the laminates are flat, which makes the assembly components easy to produce. Also, these components can be co-consolidated together, the work required to make skin-stringer assemblies reducing to co-consolidating the skin, webs and caps laminates with the joining fillers all at once. By comparison, a similar thermoset assembly generally requires either having continuous plies, or secondary bonding (adhesive bonding) of the parts together, raising both the complexity and the time needed to manufacture the stiffened panel. Another great aspect of using butt-joints in thermoplastic composite assemblies is that the

consolidated joint has continuity, with no clear interfaces. This continuity also helps avoiding stress concentrations in grid-type reinforcement, as the stingers and frames would also have continuity, therefore the stress concentrations at their intersection would be highly reduced. Regarding the transition between the laminates and the filler material, the term inter-phase would be more suited, as the matrix material is continuous throughout the whole panel, including its stringer joints. As the different reinforcements used in the laminates and in the butt-joints are embedded within the same continuous matrix, these can be considered as material phases, therefore the inter-phase term is better suited than the term of interface.

This continuous matrix in the thermoplastic welded, or co-consolidated, parts is similar with the continuous matrix achieved in the co-curing method used for thermosets parts, where also no clear interfaces can be defined. However, co-curing thermoset parts together can be significantly more difficult than co-consolidating, or welding thermoplastic parts, which could also lead to higher costs for the thermoset assemblies when compared to the thermoplastic ones. With respect to the other methods of joining thermoset structures with continuous load transfer, co-bonding and secondary bonding, as the butt-joint does not have a distinct interface, using the butt-joint represents a great advantage in structural certification for primary structures. This is due to the very strict requirements needed to certify aerospace primary structures, especially when clear interfaces can be distinguished, owing to the uncertainties related to the load transfer at these locations and the failure mode of these types of joints at these interfaces.

There are also some dis-advantages related to this type of joining technique, some of which are related to the assembly advantages. For example, not having continuous plies in the joint may improve the manufacturing and assembly aspects, but at the same time the load carrying capabilities may also be reduced. In their study, Rietman and Akkerman [12] compared the pull-off strength of an $AS4/PEEK$ butt-joint design, with an equivalent $T-joint$ design of the same material, for an I (blade) stiffener in room temperature dry (RTD: 23°C), cold temperature dry (CTD: -40°C) and hot and warm (HW: 80°C / 85% relative humidity (RH) until saturation) conditions, their results being shown in figure 2.3.

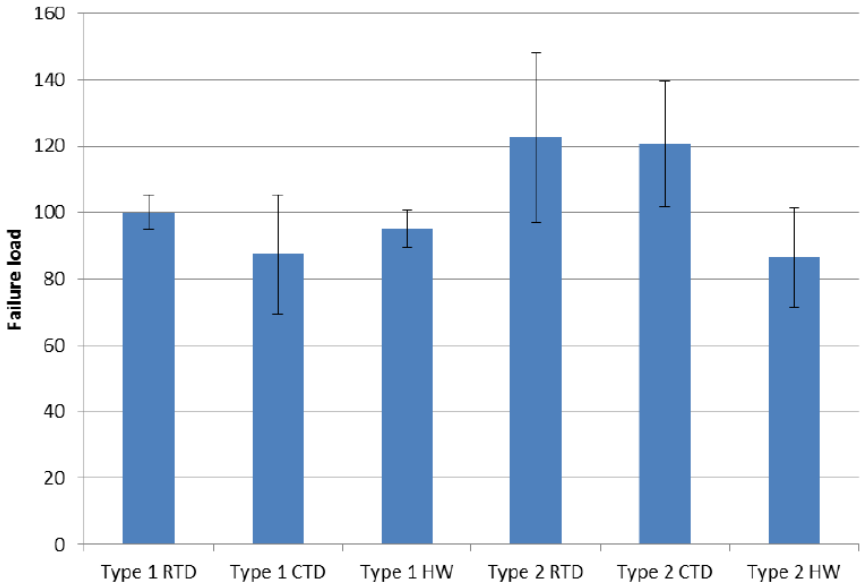

Figure 2.3: Pull-off load for butt-joints and T-joints at different testing conditions [12]

In this figure, $Type\ 1$ represents the butt-joint, while $Type\ 2$ represents the $T-joint$. Furthermore, the blue bars represent the averaged results, while the vertical black I represents the standard deviation of their experiments. As it can be seen from the above figure, one of their findings was that the butt-joint design typically provides more consistency in results, except in CTD conditions. The relatively large inconsistency of the $T-joint$ was attributed to the high scatter given by the manufacturing process, while no argument for the high scatter in the butt-joint in CTD conditions was given.

As expected, the $T-joint$ performed better in terms of stiffness and strength, being at least twice as stiff and having a higher strength of roughly 20% over their butt-joint counterparts. However, besides the higher

strength and stiffness given by the continuous plies in this type of joint, it has to be mentioned that the $T-joint$ contained approximately 30% more material as well, therefore these differences might be lower than 20% for the same joint net weight.

While for the $T-joints$ the pull-off strengths in RTD and CTD conditions were relatively the same, a decrease in pull-off strength around 15% was observed for the butt-joint design. On the other hand, on HW conditions, the butt-joint pull-off strength decrease is relatively small when compared to the RTD case, around 5%, while for the $T-joints$ the decrease is significant, being around 25%.

The authors also reported ply waviness occurring predominantly in the skin below the stiffener, which is also consistent with observations within GKN-Fokker. This waviness can act as stress raisers and have a detrimental impact on the both the static strength of the structure [15–17] and on its fatigue behaviour [18] under compressive loading. This waviness was attributed by the authors to the high pressures in the autoclave during the co-consolidation process, as well as to the different $CTEs$ (Coefficient of Thermal Expansion) of the joint components.

The authors also observed a deviation of the web with respect to the skin of approximately 1° and skin bending of an angular deflection around 0.81°. The latter was attributed to the different $CTEs$ (Coefficient of Thermal Expansion) of the filler and laminates and it is also consistent with GKN-Fokker findings. These non-conformities can be traced back to the manufacturing process and different the $CTEs$ between the joined parts, which could also lead to significant residual thermal stresses and deformations upon cooling. The thermal residual stresses were shown to be able to initiate a crack in the deltoid area of $T-joint$, having a significant effect in the load carrying capabilities of the joint. In their study [19], J. Chen and D. Fox showed that residual thermal stresses could initiate a matrix crack in order of a few millimeters ($1.3mm$), which decreased the failure load under mix-mode loading (pulling and bending) and bending alone by roughly 22% and 10% respectively.

The butt-joint's main failure modes are matrix cracking and inter-phase de-bonding, with transverse cracks and delaminations within laminate occasionally occurring as well. Figure 2.4 shows the aforementioned failure modes, with $a-b$ representing the first crack initiating in the filler and progressing towards the skin-filler inter-phase, c representing skin-filler de-bond, while d and e represent transverse cracks and delamination within the laminate respectively. These failure modes were consistently encountered in the works of Akkerman et al. [10, 12, 13] for thermoplastic butt-joints. The main failure modes are also consistent with the findings reported by Sápi et al. in [14].

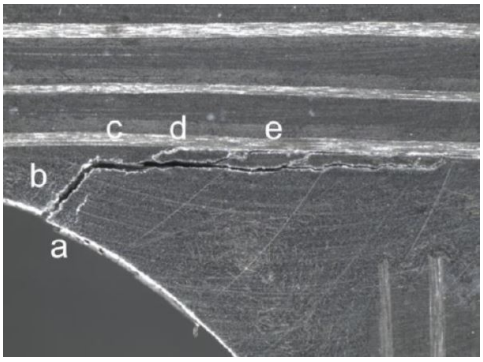

Figure 2.4: Butt-joint damage types [13]

Under 3 point-bending loading, stress concentrations in the filler radius initiate a crack, which generally propagates quickly to the filler-skin inter-phase, point from where it further propagates as a de-bond at this inter-phase. This aspect was accurately captured by Akkerman et al. [10], using a high-speed camera to capture the $C/PEEK$ butt-joint's failure mode under 3 point-bending. Two representative images capturing the damage propagation of two different layups are shown in figure 2.5

In this figure it can be seen how first the crack initiates in the filler radius, being visible in both pictures at $t = 33\mu s$. Next, once the initial crack reaches the skin-filler inter-phase, it starts to propagate along this inter-phase, as it can be seen in the above figure at a time higher than $t = 100\mu s$. The crack appears to propagate through the filler in less than $33\mu s$, while at the skin-filler inter-phase the de-bond grows in approximately 1-2ms. This means that the crack propagation through the filler takes less than 5% from the total failure time of the butt-joint. Also, it means that in terms of quantity, the extent of skin-filler de-bond seems to be far greater than the cracks through the filler. This suggests that the de-bonds could play the major role in the joint loss of the load carrying capabilities, with filler cracking mostly initiating the failure process.

Regarding their numerical model, a coupled $XFEM-CZM$ (eXtended Finite Element Method-Cohezive Zone Model) approach was used to capture the initial filler crack and the de-bond at the skin-filler inter-phase. Their 3-point bending simulation was conducted in Abaqus FEA (Finite Element Analysis) software package [20], employing a 2D quasi-static analysis. The web was connected to the filler by means of tie constrains, while an un-coupled, surface based cohesive contact was used to model the de-bond at the skin-filler

inter-phase. The 4 node bi-linear quadrilateral plane strain CPE4 elements mesh size for the cohesive contact was set to $0.1mm$, as a result of a mesh convergence analysis. The cohesive traction-separation law used was linear, with a penalty stiffness of $10^6[N/mm^3]$, in which a quadratic stress 2.11 criterion was used to initiate damage and the BK (Benzeggagh-Kenane) energy-based fracture criterion 2.5 was used to model mixed-mode de-bond propagation. The crack initiation in the filler was modeled using a maximum principal stress criterion, while propagation was modeled using a $VCCT$ criterion.

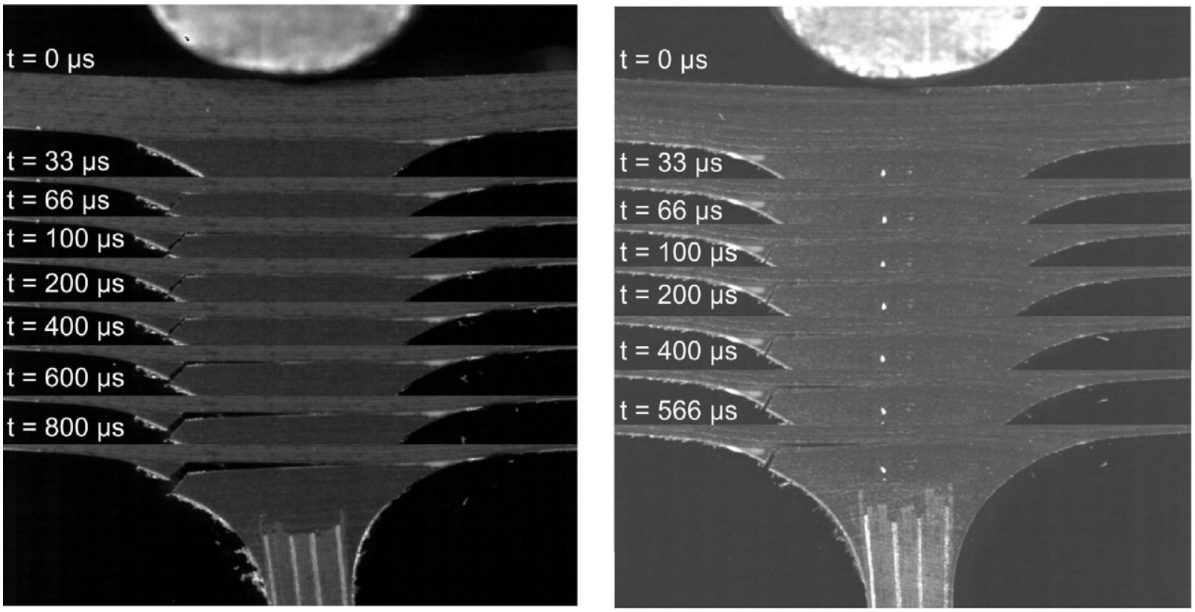

Figure 2.5: Crack propagation in $C/PEEK$ butt-joints with different laminate layups [10]

Using this procedure, and accounting for residual thermal stresses, their numerical model was able to accurately capture the stiffness, the location of crack initiation, its propagation and the load drop during damage propagation. Furthermore, it was found that initially the de-bond grows under a dominant mode I opening, while mode II and III became more significant near the end of the de-bond growth process[10].

Out of the modes in which the butt-joint could sustain damage in service, one of the most common mode is through impact. Damage could occur during impact in butt-joints due to the locally increased stiffness given by the stringer. As the local stiffness increases, the structures's ability to deflect and to absorb energy locally decreases as well, leading to filler cracks and laminate-filler de-bonds [14]. As previously mentioned, an important observation is that impacts from below the stringer (OML side) hardly produce any damage, the impacts from the stringer side being the ones prone to cause butt-joint cracks, or skin-stringer de-bonds. This failure mode could be ameliorated in several ways, with the influence of the filler material, filler geometry, laminates, inserts, through the thickness reinforcements, interweaving, vascular networks, or curing parameters is shown in Sápi et al. work on the state of art in out-of-plane joints filler materials [14].

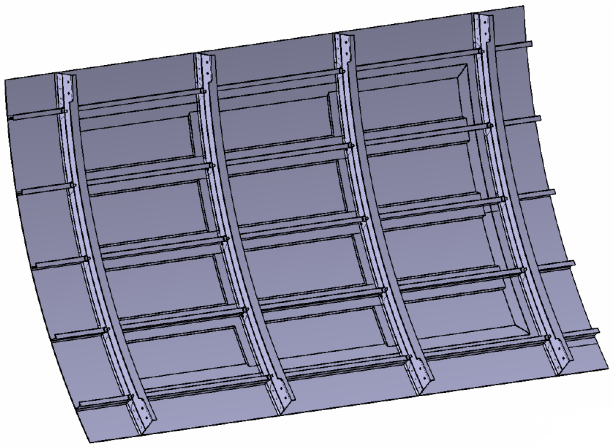

Figure 2.6: TAPAS $C/PEKK$ grid panel [21]

Furthermore, in the literature review also the failure of the TAPAS $C/PEKK$ butt-joined grid panels was studied, one example of such a grid panel being shown in figure 2.6. TAPAS [9] is a consortium between Dutch aerospace-related companies and research institutes, some of the most important being Fokker Aerostruc-

tures, NLR (Netherlands Aerosplace Center), TenCate, or Delft's University of Technology and the aircraft manufacturer Airbus.

The TAPAS ortho-grid panels were developed to asses the capabilities of thermoplastic composites to be used in aircraft primary structures. The highlights of this chapter was that $C/PEKK\ UD$ (Uni-Direcional) lamina behaviour does exhibit some non-linearities, especially in in-plane shear and inter-laminar shear behaviour and that these aspects could only be considered relevant locally and mostly regarding the de-bond growth. This is due to the compression loading scenario treated in this project for which the expectations based on previous tests indicate that the global strains would not exceed the linear-elastic behaviour threshold. The second relevant aspect of this chapter is that skin-stringer separation can indeed be the major failure mode, depending on its design, panel configuration, or existent damage. However, the butt-joint in itself is not considered an inherent weakness of any stiffened panel making use of this novel joining technique. The actual details of this section were removed due to company privacy reasons. An overview of these panels can be found in [11], where the advantages of using butt-joint to build stiffened panels and the new panel concept are discussed.

2.2 SKIN-STRINGER SEPARATION DAMAGE MODELS

As a result of a literature survey on previous works regarding skin-stringer separation, it resulted that Abaqus seems to be the preferred numerical tool to model this type of damage at panel level [22–28]. Therefore, modeling skin-stiffener separation during this thesis is also chosen to be done using Abaqus FEA package and familiarizing with the $VCCT$ and CZM procedures implemented in it are of paramount importance. In this section, the $VCCT$ and CZM procedures implemented in Abaqus Standard are described in more detail.

2.2.1 ABAQUS VCCT IMPLEMENTATION

The Virtual Crack Closure Technique ($VCCT$) is based on the $LEFM$ (Linear Elastic Fracture Mechanics) assumption that the energy needed to create a crack is equal to the energy needed to close that same crack. The aforementioned assumption also implies that $VCCT$ needs the crack path to be known apriori and it is best suited in capturing brittle crack growth behaviour. In order to model the crack propagation phenomena, $VCCT$ makes use of the strain energy released under the three different crack opening modes, shown below in figure 2.7

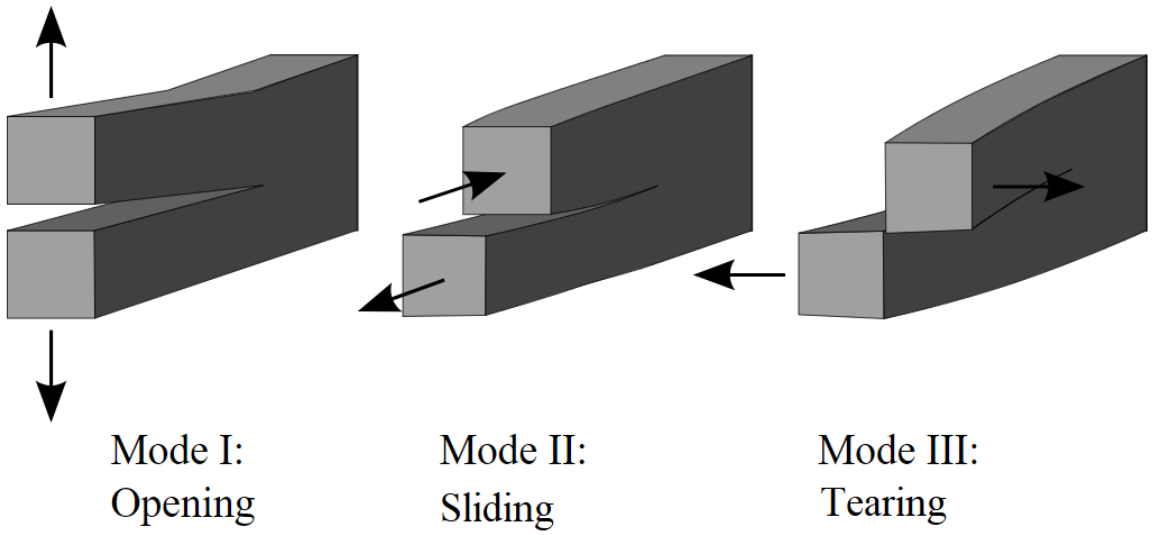

Figure 2.7: Fracture modes [29]

The $VCCT$ separation analysis in Abaqus is carried in a nodal based fashion, with the nodes de-bonding when the fracture criterion index reaches a value of 1 within a certain tolerance:

$$f_{LL} \leq 1 \leq f_{UL} \tag{2.1}$$

where $f_{LL} = 1$ and $f_{UL} = 1 + f_{tol}$. The fracture criterion tolerance default value for $VCCT$ is 0.2 and its purpose is to cut-back the increment size, such that only one node per increment is released at the crack front. This option can be neglected if the unstable crack growth option is chosen, case in which multiple nodes can be released without cutting back the increment, regardless if they are at, or ahead the crack tip. If unstable crack growth is specified, the fracture criterion 2.1 becomes:

$$1 + f_{tol} \leq f \leq 1 + f^u_{tol}, with\ f_{tol} \leq f^u_{tol} \tag{2.2}$$

where f^u_{tol} is the unstable crack growth tolerance. This tolerance can be specified as well, the default value being infinity. When unstable crack growth option is enabled, node pairs that satisfy the criterion are released until the nodes pairs at, or ahead of the crack front, no longer satisfy the criterion. One example of the $VCCT$ implementation in Abaqus for mode I is given in figure 2.8 below:

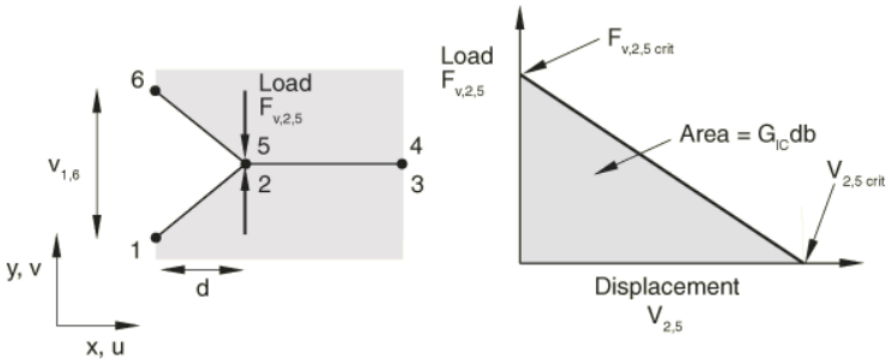

Figure 2.8: Abaqus VCCT nodal release under Mode I [30]

where:

- b - width of the elements at the crack front
- d - length of the elements at the crack front
- $F_{v,2,5}$ - vertical force between nodes 2 and 5
- $v_{1,6}$ - vertical relative displacement between nodes 1 and 6
- G_I - mode I strain energy release rate
- G_{Ic} - critical mode I strain energy release rate allowable

In the above figure, nodes 2 and 5 will be released under mode I when the following criterion is met:

$$f = \frac{G_I}{G_{Ic}} = \frac{1}{2G_{Ic}} \frac{v_{1,6} F_{v,2,5}}{bd} \geq 1 \tag{2.3}$$

with similar formulations existing for mode II and mode III openings. To account for all modes, a node will be released when a criterion based on equivalent strain energy release rates:

$$f = \frac{G_{equiv}}{G_{equivC}} \geq 1 \tag{2.4}$$

where:

- G_{equiv} - equivalent strain energy release rate calculated at a node
- G_{equivC} - equivalent strain energy release rate allowable determined via a mix-mode criterion

Abaqus offers 3 different mode mixity criteria, suggesting that the criterion selection is best done empirically. The 3 mode mixity criteria are:

$$BK\ law\ [31]:\ G_{equivC} = G_{Ic} + (G_{IIc} - G_{Ic}) \left(\frac{G_{IIc} + G_{IIIc}}{G_{Ic} + G_{IIc} + G_{IIIc}} \right)^{\eta} \tag{2.5}$$

$$Power\ law\ [32]: \quad \frac{G_{equiv}}{G_{equivC}} = \left(\frac{G_I}{G_{Ic}}\right)^{a_m} + \left(\frac{G_{II}}{G_{IIc}}\right)^{a_n} + \left(\frac{G_{III}}{G_{IIIc}}\right)^{a_o} \tag{2.6}$$

$$\begin{aligned} Reeder\ law\ [33]: \ G_{equivC} = G_{Ic} + (G_{IIc} - G_{Ic})\left(\frac{G_{IIc}+G_{IIIc}}{G_{Ic}+G_{IIc}+G_{IIIc}}\right)^{\eta} + \\ +(G_{IIIc} - G_{IIc})\left(\frac{G_{IIIc}}{G_{IIc}+G_{IIIc}}\right)\left(\frac{G_{IIc}+G_{IIIc}}{G_{Ic}+G_{IIc}+G_{IIIc}}\right)^{\eta} \end{aligned} \tag{2.7}$$

where the Reeder law is best applied when $G_{IIc} \neq G_{IIIc}$ (otherwise reducing to the BK law) and only for 3D problems.

Variable critical strain energy rates can also be specified, case in which any specified constant strain energy rates are ignored, the critical strain energy release rates being interpolated from the nodes. In order to use this option, the critical strain energy release rates have to be specified for all slave surface nodes in the input file, as this option is not yet supported in the software's graphic user interface. Abaqus also provides an Enhanced $VCCT$ option, which basically allows two sets of strain energy release rate constants: one for initiation, one for propagation. The former set of fracture toughnesses are used to initiate the crack propagation (using the same criterion as the one shown in equation 2.4), or to initiate nodal release, while the latter are used in the actual crack propagation stage, or to separate them until the release is completed. Provided are also several numerical tools to help with convergence and to ease the computational effort, like viscous dampening, linear scaling, or the possibility to specify different incrementation settings after the $VCCT$ criterion has been satisfied. Another important option available is the de-bonding force ramp-down mode, which can be $RAMP$, or $STEP$. As the name suggests, $STEP$ option releases the traction between the two nodes in the following increment, while the $RAMP$ option gradually releases the traction between the nodes over several succeeding increments. Enhanced $VCCT$ is only relevant when used with the latter, using it with the former yielding the same results as using normal $VCCT$. Temperature, or other user-defined field can also be specified when using $VCCT$. Furthermore, the $SERR$ (Strain Energy Release Rates) can also be requested, which can help understanding which separation mode 2.7 is the dominant one and how the crack/de-bond propagates during the analysis.

Recommendations are also given when using $VCCT$ with Abaqus Standard, these being:

- use small increments due to the node-by-node crack tracking algorithm
- carefully use dampening to achieve convergence and verify the expected accuracy by checking the amount of artificial energy introduced
- use matched meshed where possible, otherwise use $small-sliding, surface-to-surface$ formulation for increased accuracy
- specify small clearance to the contact pair to be used at the start of the analysis, this helps eliminating possible unnecessary severe discontinuity iterations
- geometric non-linearity might help the analysis convergence
- avoid using tie multi-point constraints for the slave surface, as Abaqus is not able to resolve the over-constraint
- master surface has to be continuous
- for the $surface-to-surface$ contact formulation at least two rows of elements should be used behind the crack front
- regular, rectangular, first order elements tend to work best for crack propagation analysis

2.2.2 ABAQUS CZM IMPLEMENTATION

There are two different CZM approaches implemented in Abaqus, element and surface based. While the implementation might differ from the element to the surface based behaviour, the damage model remains very similar. Since cohesive elements are best suited when an adhesive layer is modeled, the surface based behaviour is more representative to the butt-joint damage behaviour reviewed in 2.1, therefore the cohesive surface based damage model [34] is described in the following section in more detail.

The behaviour of the contact property is modeled as a linear elastic response, written in terms of tractions and separations:

$$t = \begin{pmatrix} t_n \\ t_s \\ t_t \end{pmatrix} = \begin{bmatrix} K_{nn} & K_{ns} & K_{nt} \\ K_{ns} & K_{ss} & K_{st} \\ K_{nt} & K_{st} & K_{tt} \end{bmatrix} \begin{pmatrix} \delta_n \\ \delta_s \\ \delta_t \end{pmatrix} = K\delta \tag{2.8}$$

where:

- t_n, t_s and t_t are the normal and shear tractions
- δ_n, δ_s and δ_t are the corresponding separations
- K_{ij} (i,j = n,s,t) are the penalty stiffness matrix

The components of the stiffness matrix can be specified, with coupled, uncoupled and single mode behaviour formulations being possible within the model.

The cohesive damage model itself can be split in two main parts, namely the damage initiation part and the damage propagation one. The initial response is linear elastic until the damage initiation criterion is satisfied, after which degradation occurs following a specified damage evolution law. Figure 2.9 shows one example of a bi-linear damage evolution law, here in terms of tractions and separations. There can be multiple traction-separation law shapes, out of which Abaqus provides bi-linear, exponential and tabular. Damage initiation occurs when a traction, or separation, failure criterion is met. Checking for initiation only is also possible, case in which damage evolution must not be specified and specific output request has to be required. The available initiation criteria are:

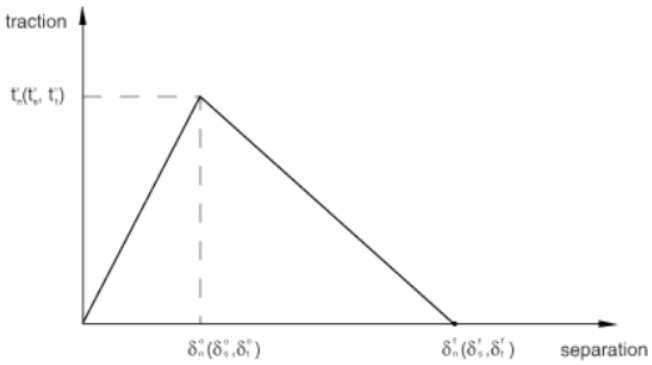

Figure 2.9: Abaqus bi-linear cohesive damage law [34]

$$max\left\{\frac{\langle t_n\rangle}{t_n^o}, \frac{t_s}{t_s^o}\frac{t_t}{t_t^o}\right\} = 1, \quad Maximum\ stress\ criterion \tag{2.9}$$

$$max\left\{\frac{\langle \delta_n\rangle}{\delta_n^o}, \frac{\delta_s}{\delta_s^o}\frac{\delta_t}{\delta_t^o}\right\} = 1, \quad Maximum\ separation\ criterion \tag{2.10}$$

$$\left\{\frac{\langle t_n\rangle}{t_n^o}\right\}^2 + \left\{\frac{t_s}{t_s^o}\right\}^2 + \left\{\frac{t_t}{t_t^o}\right\}^2 = 1, \quad Quadratic\ stress\ criterion \tag{2.11}$$

$$\left\{\frac{\langle \delta_n\rangle}{\delta_n^o}\right\}^2 + \left\{\frac{\delta_s}{\delta_s^o}\right\}^2 + \left\{\frac{\delta_t}{\delta_t^o}\right\}^2 = 1, \quad Quadratic\ separation\ criterion \tag{2.12}$$

where n, t and s subscripts are used to represent pure normal, or pure first and second shear directions with respect to the interface, while the Macaulay brackets $\langle\rangle$ are used to signify that damage progression cannot occur under compression loading or displacement. Damage evolution is accounted using a scalar damage variable D, which monotonically grows from 0, representing undamaged state, to 1, representing complete failure. This scalar damage variable is applied to the traction vector according to the following formulation:

$$t = (1 - D)\,\bar{t} \tag{2.13}$$

where $\bar{t}$ is the elastic prediction of the undamaged traction vector and with an extra condition for the normal direction for tensile damage only.

The traction-separation law can specified in terms of displacements/separations or energy, for which both a linear and exponential softening law can be chosen. When the damage evolution criterion is specified in terms of displacements, the tabular option becomes available to define the softening law.

The mode mixity is defined as ratios of normal and shear contributions at the contact point. By defining the total work done by the tractions and their correspondent separations as $G_T = G_n + G_s + G_t$, the mode mix definitions are:

$$\begin{aligned} m_1 &= \frac{G_n}{G_T} \\ m_2 &= \frac{G_s}{G_T} \\ m_3 &= \frac{G_t}{G_T} \end{aligned} \tag{2.14}$$

The energies above can be either computed on the current state of the deformation, or based on the deformation history at an integration point. The use of the former is recommended where the dominant energy dissipation is associated with crack growth, while the other is recommended when other significant dissipation mechanisms govern the global structural response.

Besides this energy based measure of the mode mix, there is also a separation based measure. The separation mode mixity is defined as follows:

$$\begin{matrix}\phi_1 = \left(\frac{2}{\pi}\right) tan^{-1}\left(\frac{\tau}{\langle t_n \rangle}\right) \\ \\ \phi_2 = \left(\frac{2}{\pi}\right) tan^{-1}\left(\frac{t_t}{t_s}\right)\end{matrix} \quad , \; where \; \tau = \sqrt{t_s^2 + t_t^2} \; is \; the \; effective \; shear \; traction \tag{2.15}$$

where the $2/\pi$ factor is used to normalize angles. A descriptive picture of the mode mixity based on the normal and two shear shear tractions being shown in figure 2.10.

One important mention is that there are differences between the energy and traction based mode-mix behaviours. While a pure mode I separation is possible when the energy formulation is used, in a coupled traction-separation behaviour the shear components of the tractions might be different than 0. Also, depending on the method used to compute the energies, different results might be found, as for the energies computed based on the deformation history, the previously mode-mix ratio will have a weight in the current mode-mix ratio as well.

When the damage evolution is separation based (instead of energy based), the effective separation at failure has to be specified. This separation is defined as the difference between the complete separation at failure and the separation at damage initiation $\delta_m^f - \delta_m^o$. The effective separation comes as the difference between those two quantities, as before $\delta_m = \delta_m^o$ the effective separation has not occurred yet, the deformation until this point being linear-elastic. The scalar damage variable for a constant mode-mix softening, excluding the tabular definition, has the following forms:

$$\begin{matrix} D = \frac{\delta_m^f(\delta_m^{max} - \delta_m^o)}{\delta_m^{max}(\delta_m^f - \delta_m^o)}, for \; linear \; softening \\ \\ D = 1 - \left\{\frac{\delta_m^o}{\delta_m^{max}}\right\}\left\{1 - \frac{1 - exp\left(-\alpha\left(\frac{\delta_m^{max} - \delta_m^o}{\delta_m^f - \delta_m^o}\right)\right)}{1 - exp(-\alpha)}\right\}, for \; exponential \; softening \end{matrix} \tag{2.16}$$

where δ_m^{max} is the maximum value of the effective separation during the loading history and α is a non-dimensional parameter that describes the damage evolution.

When a energy based damage evolution is specified, and neglecting the tabular formulation, the damage scalar variable has the following form:

$$\begin{matrix} D = \frac{\delta_m^f(\delta_m^{max} - \delta_m^o)}{\delta_m^{max}(\delta_m^f - \delta_m^o)}, \; with \; \delta_m^f = 2G^C / T_{eff}^o, \; for \; linear \; softening \\ \\ D = \int_{\delta_m^o}^{\delta_m^f} \frac{T_{eff}}{G^C - G_o} d\delta, \; for \; exponential \; softening \end{matrix} \tag{2.17}$$

where

- T_{eff}^o - the effective traction at damage initiation
- T_{eff} - the effective traction
- G_o - the elastic energy at damage initiation
- G^C=G_{equivC}

The mode mixity for an energy based damage evolution are tabular, the *Power* law 2.6 and the *BK* law 2.5 previously shown for the $VCCT$. Upon total node release, two different behaviours can be used for the slave node. In one case, a normal contact behaviour is established by default, in which friction can also be specified. In this case the possible tendency of the surfaces to inter-penetrate will cause compressive and friction stresses, while separation occurs freely. In the other case, slave nodes coming back in contact with the master surface can develop cohesive behaviour again, this case being best suited when modeling sticky surfaces that can repeatedly come into contact.

Viscous regularization is also possible for avoiding convergence issues, with the recommendations previously mentioned for $VCCT$.

The cohesive contact damage model presented above shares many aspects of its formulation with the formulation of the cohesive element. By comparision, when cohesive elements are used, the cohesive contact linear-elastic relation 2.8 is rewritten in terms of element stiffnesses and strains:

$$t = \begin{pmatrix} t_n \\ t_s \\ t_t \end{pmatrix} = \begin{bmatrix} E_{nn} & E_{ns} & E_{nt} \\ E_{ns} & E_{ss} & E_{st} \\ E_{nt} & E_{st} & E_{tt} \end{bmatrix} \begin{pmatrix} \epsilon_n \\ \epsilon_s \\ \epsilon_t \end{pmatrix} = E\epsilon \tag{2.18}$$

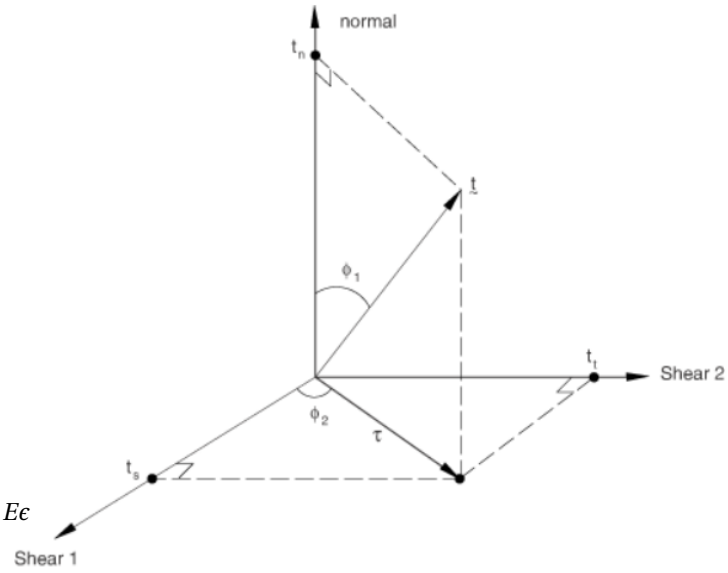

Figure 2.10: Traction based mode-mix [34]

where, the ϵ_n, ϵ_s and ϵ_t strains are calculated by dividing the δ_n, δ_s and δ_t to the original thickness of the cohesive element. Also, as now the cohesive behaviour is formulated as a material property for an element, the separation based initiation criteria from relations 2.10 and 2.12 being re-written using the element strains from above, while the traction based ones from relations 2.9 and 2.11 remain the same. Similar to these differences, all the other ones between these two approaches stem from their different implementation, without any differences regarding the actual damage model used.

3 | DAMAGE MODEL SELECTION AND VALIDATION

In order to build confidence and to develop a solid *FE* modeling strategy, the building-block approach is used in this thesis project. This approach was developed by *NASA* in collaboration with industry in their attempt to develop technologies that would significantly increase the overall performance of the aerospace sector [7]. In this approach, developing new technologies is done in a step-by-step manner, each step requiring complete understanding of all the involved factors before going a level higher. This presumed that the behaviour of the researched structure/process was well understood, making it predictable through *FE* analysis and repeatable through manufacturing and experimental testing. This approach is preferred here in order to verify that the damage model is able to capture separation starting from one of the simplest configurations, namely the *DCB* material characterization specimen for mode I fracture, to the increased complexity of the 1-stringer specimen and 3-stringer panel.

One descriptive schematic of such a building-block approach is shown in figure 3.1, under a testing pyramid form. The views on the building-block approach pyramid might differ in literature, depending of the level of detail used to differentiate between certain steps, figure 3.1 depicting a relatively broad segmentation. Regardless, the general relative position of the pyramid segments with respect to each-other remains the same.

The width of the pyramid segment is related to the number of tests conducted at that level, while the height of the pyramid segment is related to the cost and complexity of these tests per specimen. For example, the *coupon* tests for material characterization located at the base of the pyramid are conducted in large numbers, the costs implied per specimen being insignificant when compared to the tests performed at *component* level. At the last level, the costs involved in testing are highly restrictive for the number of specimens tested and in extreme cases only one test article per component is tested.

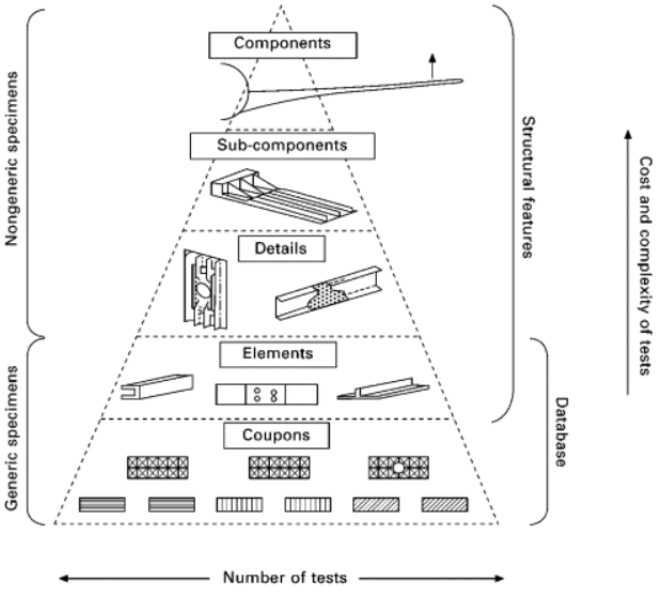

Figure 3.1: Testing building-block-approach [35]

Usually at the first level the coupons for material characterization are found. These can include coupons to determine several properties from the material's load-displacement behaviour under different types of loading scenarios, including environmental effects, or damage. At this level also material models can be defined or refined to represent the experimentally observed material behaviour. Typically at this level there's a good level of understanding in what concerns the material's behaviour and how to measure it, most of the coupons for material characterization being standardized. The second block addresses simple joints and structural elements, in which, for example, their buckling behaviour, strength, various failure mechanisms, of influence of different damages on their structural behaviour can be studied. At this level the test standardization is already very limited, as typically there is an exponential decrease in standardization starting from the *coupon* level up. In these first two pyramid sections, one can find generic specimens, as the geometry and the structural features are fairly simple. These specimens can also be included in a database, using different stringer geometries, layups, or simple joining methods config-

urations. The next block addresses the structural details of larger components. Under this category one can find small reinforced panels, reinforced areas, or joints of increased complexity. Here the structural response of the parts can be studied taking into account various loading scenarios, boundary conditions, or existent damage. The $sub-components$ level can address structures that are fairly complex, for which typically an analysis capturing the material's behaviour globally in high detail might be unfeasible. Under this category one can find fairly large assemblies, or sub-assemblies, few examples being stiffened structures, like wing and fuselage panels, engine mountings, or the structures of various control surfaces. The last level depicts full components, under which one can find structures such as wings, fuselages, or empennages. At this level, besides the costly experimental tests, also the FE models and analyses tend to be highly complex and time consuming, often with limited damage modeling.

With respect to the pyramid sections from figure 3.1, the starting point of the thesis FE modeling strategy is at $coupon$ level, the damage model used in the 3-stringer panel being first chosen and validated using a DCB test. Then, the step inside the $element$ level is done using a 1-stringer specimen, in which the damage model selected in the previous level is implemented. As for this 1-stringer specimen an already correlated FE model exists and its behaviour is well understood within the company, the approached used in the DCB specimen is only verified for this 1-stringer specimen. This means that for the damage model validation at this level only a check in terms of load-displacement response and failure load is done. As the stringer geometry in this 1-stringer specimen is similar with the one of the 3-stringer panel, the modeling approach of the butt-joints from this model is also carried to the next level for the 3-stringer panel. The 3-stringer panel, addressed separately in chapter 4, sits somewhere at the border between the $detail$ and $sub-component$ levels shown in figure 3.1, as it can be considered a sub-component being a stiffened panel, at the same time being a structure relatively small in size.

In what follows, the chapter is split in two large sections, one treating the 'Damage model selection' 3.1, the other treating the 'The damage model validation' 3.2.

In the first section the load-displacement response of a DCB specimen from the material characterization report [36] is chosen to asses the capabilities of the analytical and numerical models tried. Using the geometry and the material properties from this report, the load-displacement response of the analytical models was first compared against the experimental one and the best suited analytical model was further kept to asses the accuracy of the numerical models as well. At the end of this section the most promising numerical damage model for the intents and purposes of this thesis project was determined and validated in a 1-stringer specimen, discussed in the second section of this chapter

The 1-stringer specimen used in the second section already had a FE model that correlated well with the experimental data. This models however made use of some engineering artifacts concerning the material parameters, restricting its use in further de-bond analyses at different scale levels. In this section the damage model selected in the previous section is implemented in the already existent FE model and it shortcomings when used to the selected damage model are shown. The influence of the altered material parameters in modeling de-bond at different scales using the DCB model from section one is also shown here. Furthermore, a new FE model of the 1-stringer specimen with a refined skin-web butt-joint is build and gradually improved, this FE model accurately capturing the experimental load-displacement curve and failure load. In both sections the FE models built are shown, motivating the choices made and stating any assumptions taken.

3.1 DAMAGE MODEL SELECTION

The DCB test was chosen as the staring point to investigate skin-stringer separation, as the damage model must be able to capture the expected dominant opening mode, which is mode I in this case. This assumption is based on the tendency of the buckling shape to open the already existent de-bond. Capturing this mode is of paramount importance, as failing to capture this mode in one of the simplest configurations means that mode I opening would not be accurately described at higher scales and complexity levels. The DCB test describing mode I opening is also one of the most reliable and generally accepted test in literature to characterize fracture, as various difficulties are encountered when trying to characterize mode II and mode III openings. Some of these issues are related to having a pure mode II, or especially III, as well as having a stable crack growth. The mode I separation of the DCB specimen can also be described analytically, two solutions based on $LEFM$ being used here. Besides these analytical solutions to model the DCB test, the accuracy of the damage model used in the DCB test is also verified against the experimental curve, the accuracy of all

three being assessed in terms of load-displacement curves.

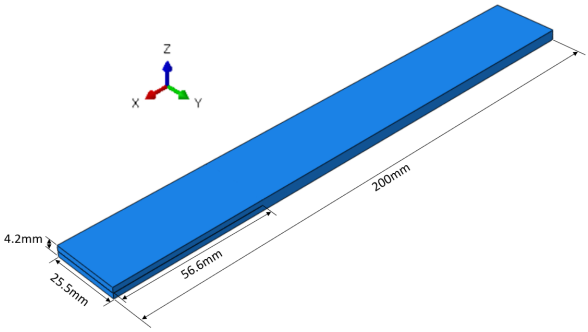

Figure 3.2: DCB specimen's geometry

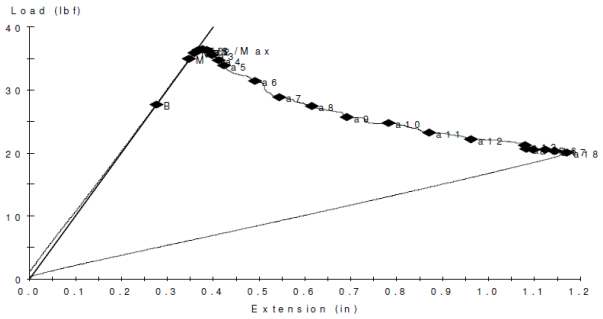

Figure 3.3: DCB specimen's experimental load-displacement curve

The geometry of the DCB specimen was taken from the material characterization report [36], except its length, which had to be assumed. The specimen in question had a $56.6mm$ initial crack, which can be seen together with its global geometry in figure 3.2. The experimental loading mode of this DCB specimens is usually displacement based, by keeping the lower end of the de-bonded side fixed, while the upper end of the same side is displaced vertically. The loading fixture also typically allows free rotations around the specimen's width axis, or Y axis, from figure 3.2, in order to allow a pure mode I opening. As the vertical displacement between the de-bonded beams increases, so does the de-bond length, the fracture toughness being obtained as a function of the specimen's geometry, the vertical displacement of the ends and the reaction force recorded by the machine.

The experimental load-displacement curve of the selected DCB specimen can be seen in figure 3.3 and it was taken also from the material characterization report [37]. In this figure, the horizontal axis represents the vertical displacement of the beams, or $Extension$, in units of length ($1in = 25.4mm$), while the machine's reaction force, or $Load$ is shown on the vertical scale, in units of force ($1lbf \approx 4.45N$).

The DCB test experimental load-displacement curve has two main areas of interest, the initial linear-elastic part and the non-linear propagation part. The first area represents the loading of the specimen without damage growth and it is characterized by a linear, or quasi-linear, relation between the vertical displacement of the DCB beams and the its corresponding reaction force. The second area represents the loading of the specimen as damage propagates (de-bond grows) and it is characterized by a non-linear, exponential decrease in the specimens reaction load as the vertical displacement between the DCB beams increases. These two curve areas, especially the propagation part, should be accurately captured by the damage model used, in order for it to be able to accurately model separation in structures of increased complexity.

The initiation point for this DCB specimen, taken as the intersection of the initial linear-elastic part and the non-linear propagation part is at roughly $0.375in$ ($9.5225mm$) in displacement, which corresponds to a load of roughly 36.5 lbf ($162.4N$).

Based on the literature study, in which the CZM and $VCCT$ were deemed to be best suited in modeling skin-stringer separation at panel level, three different numerical approaches using these damage models are investigated using the DCB specimen geometry and load-displacement curve shown above in figures 3.2 and 3.3. These three different approaches are:

- Cohesive Zone Elements (CZE) tied between the separating parts
- Cohesive Zone Surface (CZS) based contact behaviour between the separating parts
- VCCT surface based contact behaviour between the separating parts

These three numerical approaches are compared in terms of accuracy (comparing load-displacement curves), physical base (damage model and properties used) and in terms of running times. The approach with the best overall performance at this $coupon$ level is then selected to be implemented in the already correlated FE model of a 1-stringer specimen with a skin-stringer de-bond damage, addressed in the second section of this chapter 3.2. This intermediate step has the purpose to verify that the damage model is able to capture skin-stringer separation at element level as well 3.1, in a specimen with significantly more complex global behaviour. In doing so, sufficient confidence in the damage model is built to implement it at a larger scale, namely in the 3-stringer panel treated in chapter 4.

3.1.1 LEFM DCB ANALYTICAL MODEL

The analytical models for the DCB used are selected from the $ASTM$ standards for DCB test $ASTM5528$ [38] and Mixed Mode Bending test $ASTMD6671/D6671M$ [39], both using the same type of specimen. The MMB test combines the loading mode of the DCB test for determining the mode I fracture toughness, with the one of the End-Notch-Flexure test for determining mode II fracture toughness. Figure 3.4 shows the test schematics of the DCB, MMB and ENF specimens. As it can be seen in this figure, the test specimens are identical, the only difference between these tests being in the way the test specimen is loaded. These specimens have a pre-crack of length a_0, while l, b and h, represent the specimen's length, width and half-thickness of the specimen.

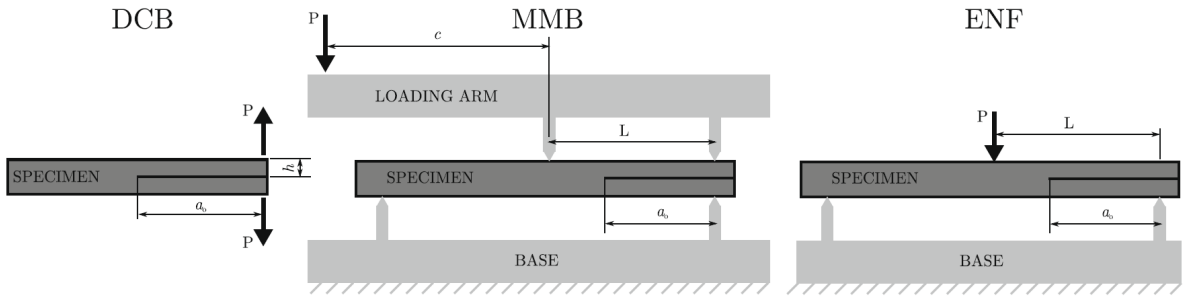

Figure 3.4: DCB, MMB and ENF test specimens configuration [40]

For the DCB test, the loading mode is already described in the beginning of the current chapter 3, while the ENF and MMB are briefly described below. As shown in the above figure for the ENF, the loading mode is 3-point-bending. The specimen edges are simply supported, with a load applied in the middle of the specimen, L representing the half-span of the specimen. In this test, both the boundary conditions and the load are applied with rollers, as they allow free rotation of the specimen along its length. The mode II fracture is induced by the tendency of upper and lower beams to have different radii due to bending, which loads the crack in shear as shown in figure 2.7 for mode II fracture. The MMB test as mentioned earlier combines the loading modes of the DCB and ENF tests, the mode-mixity being varied with the help of the loading arm length c. The loading arm represents the distance between the half-span of the specimen and it is measured starting from the half-span towards the pristine side of the specimen (the one without a pre-crack). When this loading arm is 0, a pure mode II is achieved, since the loading mode in this case is identical to the one of the ENF test. Pure mode I can be achieved by removing the middle hinge, by simply puling the upper edge of the pre-cracked end upwards, while the lower edge of the pre-cracked end is only allowed to rotate along the specimen's length. Due to its capabilities to model both mode I and mode II fracture, the $LEFM$ model for MMB was also considered here, in the pure mode I configuration.

The load-displacement behaviour of the DCB test according to the $ASTM5528$ [38] can be obtained using:

$$F_{DCB} = \sqrt{\frac{G_{Ic} \cdot b \cdot EI}{a^2}}$$
$$U_{DCB} = F_{DCB} \cdot \frac{2 \cdot a^3}{3 \cdot EI} \tag{3.1}$$

where a is the crack length and $EI = E_1 bh^3/12$ is the beam's flexural stiffness. The above equation can be used with the known material properties from tables 3.1 and 3.2, together with the DCB specimen's geometry from figure 3.2, by incrementally increasing the crack length from the initial one of $a_0 = 56.6mm$. Important to mention here is that the h in the above equation represents the half thickness of the DCB specimen, while in figure 3.2 the whole specimen thickness is shown. Furthermore, the above equation is only for the propagation part, with two easy options being available to obtain the initial linear-elastic part as well. The easiest one would be to use the test's initial point, 0 load and displacement and the propagation's initial point, using the same relations shown in the above equations 3.1, for the initial crack of $a_0 = 56.6mm$. The other option is also very similar and it can be done in increments as for the propagation part. For this second option, the DCB load F_{DCB} from the U_{DCB} displacement equation shown in 3.1 can be increased in increments, with the value of the crack length kept constant to the initial one $a = a_0 = constant$.

The load displacement relation for the MMB test according to the $ASTMD6671/D6671M$ can be obtained using:

$$F_{MMB} = \sqrt{\frac{G_c \cdot 64 \cdot b \cdot L^2 \cdot EI}{4 \cdot (3c-L)^2 \cdot (a+\chi \cdot h)^2 + 3 \cdot (c+L)^2 \cdot (a+0.42 \cdot \chi \cdot h)^2)}}$$
$$U_{MMB} = F_{MMB} \cdot \frac{4 \cdot (3c-L)^2 \cdot (a+\chi \cdot h)^3 + (c+L)^2 \cdot \left[3 \cdot (a+0.42 \cdot \chi \cdot h)^3 + 2 \cdot L^2\right]}{96 \cdot L^2 \cdot EI} \tag{3.2}$$

where a is the crack length, c is the lever length, G_c is the equivalent fracture toughness according to the BK criterion 2.5 and χ is the crack length correction factor.

In the equation for the equivalent fracture toughness G_c, the quantity in the last parenthesis represents the mode mixity. This quantity is served as a very low input value (1E-10 being used here) to represent a pure mode I fracture specific to the DCB test. From equation 3.3, it can be seen that replacing the quantity in the last parenthesis with an infinitesimal small value will yield $G_c \approx G_{Ic}$. This indeed corresponds with the simulation of a DCB test, in which pure mode I fracture governs the load-displacement response.

$$BK\ law\ [31]:\ G_{equivC} = G_{Ic} + (G_{IIc} - G_{Ic}) \left(\frac{G_{IIc} + G_{IIIc}}{G_{Ic} + G_{IIc} + G_{IIIc}}\right)^{\eta} \tag{3.3}$$

The crack length correction factor χ has the following form:

$$\chi = \sqrt{\frac{E_1 \left[3 - 2 \cdot \left(\frac{\Gamma}{1+\Gamma}\right)^2\right]}{11 \cdot G_{13}}},\ with\ \Gamma = 1.18 \frac{\sqrt{E_1 \cdot E_2}}{G_{13}} \tag{3.4}$$

The lever length c is computed using:

$$c = \frac{12 \cdot k^2 + 3 \cdot MMR + 8 \cdot k \cdot \sqrt{3 \cdot MMR}}{36 \cdot k^2 - 3 \cdot MMR} \cdot L,\ with\ k = \frac{a_0 + \chi \cdot h}{a_0 + 0.42 \cdot \chi \cdot h} \tag{3.5}$$

where MMR parameter is $MMR = (1 - mode\ mixity)/mode\ mixity$.

The load-displacement relations for the damage propagation regions of the DCB and MMB from the $ASTM$ standards used here can also be seen in [40].

With the $ASTM\ DCB$ and $MMB\ LEFM$ based analytical models described below, the only missing ingredient to apply them are the $APC\ C/PEKK$ laminate material properties used in the test specimen. These material properties were taken also from the material characterization report [36], the elastic properties being shown in table 3.1, while the fracture toughnesses are shown in table 3.2. More general information about the material type used can be found on the manufacturer's data-sheet [37], with the important mention that this data-sheet is for a slightly different material, with slightly different allowables.

Another important mention here is that the reported stiffnesses E_1 and E_2 are for compression. This is seems counter-intuitive when considering the global tensile loading of the specimen under mode 1. However, the compressive set of elastic properties were also chosen for the DCB specimen as aim is to build a robust FE modeling strategy to be used in the 3-stringer panel. As the end goal is to study skin-stringer separation under compression in the 3-stringer panel, the compressive elastic properties are also used for the DCB specimen.

		Density $[g/cm^3]$	Poisson ratio	Stiffnesses [GPa]				
Material	Type	ρ	μ_{12}	E_1	E_2	G_{12}	G_{13}	G_{23}
APC (PEKK FC UD)	Lamina	1.56	0.319	126.1	11.2	5.46	5.46	3.32

Table 3.1: DCB APC C/PEKK lamina material properties [36]

APC fracture toughness			APC Strength allowables [MPa]					
G_{Ic} $[kJ/m^2]$	G_{IIc} $[kJ/m^2]$	G_{IIIc} $[kJ/m^2]$	X_T	X_C	Y_T	Y_C	S_L	S_T
1.41	2.2	2.2	2259	-1575	83.1	-284	198	138

Table 3.2: APC fracture toughnessess and strength allowables [36]

Using the DCB and MMB load-displacement relations from equations 3.1 and 3.2 and the material properties from tables 3.1 and 3.2, the load-displacement response of the DCB test with the specimen geometry showed in figure 3.2 is computed. The separate elastic and propagation parts of these $LEFM$ models are shown in figure 3.5, together with the experimental load-displacement curve previously shown in figure 3.3.

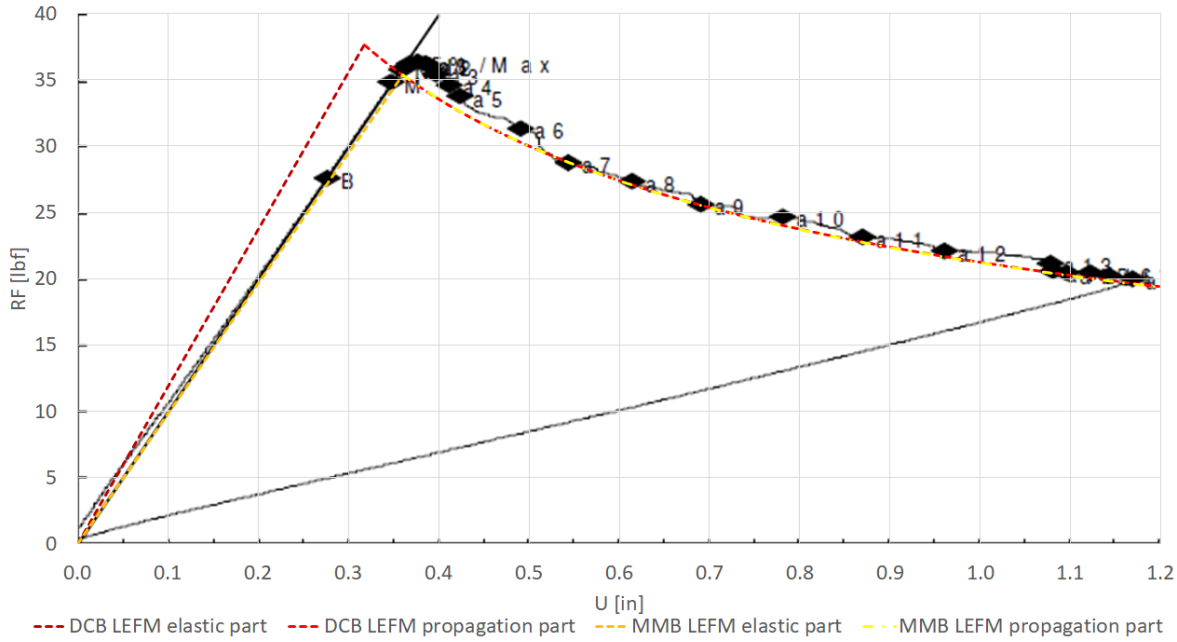

Figure 3.5: Load-displacement correlation of the LEFM ASTM DCB and MMB models with the experimental DCB curve

In the above figure, the dark red line represents the elastic part of the $ASTM\ DCB$ model, while the vivid red represents the propagation part of the same model. Similarly, the orange line represents the elastic part of the MMB model, while the yellow line represents the propagation part of the same MMB model.

As it can be noticed from figure 3.5, for the initial linear-elastic part representing the undamaged response of the experimental DCB load-displacement, the two $LEFM$ models do no show an identical response. For this initial part, the linear-elastic response of the $MMB\ ASTM$ model has an excellent correlation, while the $DCB\ ASTM$ model behaves significantly stiffer. In terms of damage initiation point (the intersection of the two linear-elastic and non-linear curves), the MMB model also correlates better. This model's initiation point in terms of load is slightly lower than the one of the experimental specimen, by roughly -1.24lbf (-5.5N), or -3.4%. The mis-match in terms of displacement for this model due to the lower initiation load is around -4%, or -0.015in (-0.381mm). For the DCB model, the mis-match in the initiation point is significant, owing to its significant stiffer initial linear-elastic response. The mis-match in terms of load is 1.03lbf (4.56N), or 2.8%, while the mis-match in displacement is -14.67%, or -0.055in (-1.397mm). The DCB model correlates slightly better with the experimental initiation point than the MMB one in terms of the initiation load, but significantly poorer in terms of the initiation displacement, due to its significantly stiffer behaviour.

For the damage propagation part of the load-displacement curve, both the DCB and MMB correlate well with the experimental curve, with the analytical curves perfectly overlapping each-other. However, when comparing the damage propagation part of the analytical curves with the experimental one, one can notice that the experimental one is slightly higher. This aspect was expected here, since experimental propagation value for mode I fracture toughness of the selected experimental DCB test is slightly higher than the allowable value used in the model, at 1.53kJ/m^2, compared with the allowable of 1.41kJ/m^2. This DCB experimental curve was chosen such that the experimentally determined value for mode I opening of this specimen does not differ much from the allowable used and shown in table 3.2 and such that the propagation part of the load-displacement was relatively smooth. These selection criteria were adopted to increase the relevancy of a visual comparison in terms of load-displacement curves between the experimental and analytical modes. As the $MMB\ ASTM$ model gives a better overall correlation with the experimental data than the $DCB\ ASTM$

model, the former is used in the next sections to compare the accuracy of the three numerical approaches studied. The analytical model is chosen here for further comparison with the numerical ones since as clearer comparison can be made, as the accuracy of numerical models can be assessed by how close they follow load-displacement response of the analytical one.

3.1.2 CZE DCB

The idea of using CZE tied to the separating parts comes from a modeling perspective and it is aimed at using different element sizes to capture the de-bond growth and the panel's global behaviour. In this manner, the necessity to use a refined mesh is only restricted to the damage propagation zone, the rest of the panel possibly having a slightly greater mesh size. The approach using cohesive elements with shared nodes with the rest of the DCB beams was not initially tried, as the main purpose of using cohesive elements was to investigate if different mesh sizes between cohesive elements and the other structural elements can be used. The final intended location of the tied cohesive elements is shown in figure 3.6. This location is chosen since it covers all the filler's width and more importantly only the filler material's properties would be redefined in terms of cohesive elements stiffnesses. This means that the structural impact on the global behaviour of the panel is kept to minimum, as the $SFRP\ C/PEKK$ filler material is weaker than the APC laminates.

The mesh size restriction in the damage propagation zone comes together with the use of CZM, which usually requires meshes smaller than $0.5mm$, as at least 2-3 elements are needed in the fracture process zone for CZM to be accurate [41]. This limitation is especially important here, as the cohesive zone length is directly proportional with the fracture toughness. This means that the cohesive zone length for the DCB specimen is proportional with the mode I fracture toughness, this fracture value being the one restricting the mesh size for this model. The starting point for the DCB models mesh size was using $0.5mm$ value for the mesh seed, as the mesh size resulted should provide accurate results for all the approaches studied.

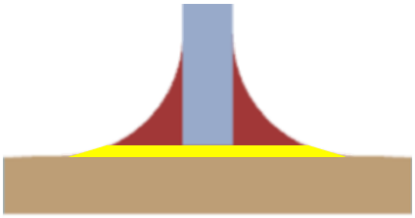

Figure 3.6: Tied cohesive elements location in the butt-joint

Starting from this mesh size, the plan is to gradually increase the mesh, with the aim of using a mesh with one element per thickness in the 3-stringer panel to model both the panel's global behaviour and the skin-stringer damage. This would imply proving that the DCB numerical models work with mesh seeds between $2mm$ and $3mm$, as the DCB beam thickness and the panel's laminates fall within this margin. Here the mesh seed instead of mesh size is used, since the DCB specimen's geometry is fixed and giving a specific mesh seed would result in having elements with dimensions close (but not exactly) to this mesh seed size.

DCB CZE MODEL

In order to apply the aforementioned approach to the DCB specimen, a layer of cohesive elements of thickness 2E-$6mm$ are tied to the DCB beams. This small thickness is chosen, to keep the beam thickness as close as possible to the experimental beam thickness. The tie type is $surface-to-surface$, with default settings. In the default settings, adjusting the slave initial position is on, this being more of a redundant measure, as for an ideal contact between the tied surfaces the same sketch for the beams and filler was used. Using the same sketch allowed using the same edges to define the interfaces between the filler and the beams, thus establishing a perfect contact between them. Also, the other default setting in the tie formulation is to tie rotational DOFs, if applicable, but as in this case the SC8R continuum shell and the COH8D3 cohesive elements do not have rotational degrees of freedom, this setting is not applicable here. Concluding, the only tie option that can influence the results is the discretization method, here the $surface-to-surface$ being chosen, based on the recommendation in the Abaqus documentation [42]. Regardless, the differences between the discretization methods should not be large in this case particularly, as the surfaces in contact are simple and so is the global response of the coupon. The $surface-to-surface$ tie discretization is chosen since it is not very sensitive to the master-slave definition, while the $node-to-surface$ tie discretization is generally preferred when complex surfaces need to be tied.

The DCB beams material behaviour is linear-elastic, lamina type, with the material properties shown in table 3.1. The element type used is SC8R continuum shell element, with reduced integration and default settings, for which a $[0]_{30}$ specimen layup is attributed using the composite layup section of Abaqus. The number of integration points was 3, with Simpson thickness integration rule, as output at the shell edges is required

for the 3-stringer panel and as the approach to be used in the 3-stringer panel must be valid also for the DCB specimen. The section integration was done before the analysis, as the material behaviour is linear-elastic and with no thickness modulus defined, as the out-of-plane loads are considered negligible in this case. The analysis type is $Dynamic$, $Implicit$, with non-linear geometry ON and default settings. The incrementation settings are 1E-5 for the initial increment, 0.001 for the maximum increment, 3E-16 for the minimum increment, with the time period being 1. The maximum number of iterations allowed is changed from 5 to 20, measure taken to avoid analysis abortion due to excessive need to cut-back the increment size, which is not uncommon when modeling damage propagation.

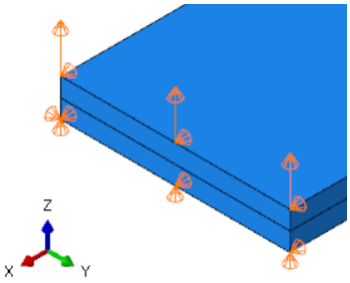

Figure 3.7: DCB boundary conditions and loading

The boundary conditions and the applied load can be seen in figure 3.7. As in can be seen from this figure, the BC applied are restricted $U1$ and $U3$ translations of the lower edge, restricted $U1$ translation of the upper edge, restricted $U2$ translation applied at the lower beam right corner. The load is introduced is displacement based, by applying a displacement of $20mm$ on the upper edge. The aforementioned BC are specified in the initial step of the analysis, while the displacement based loading is specified in a subsequent loading step. Regarding the damage model's propagation values, the ones shown in table 3.2 are used. The mix-mode criterion used is the BK criterion 2.5, with an exponent of 2.2, recommendation given from Fokker based on the previous knowledge gathered with this material. The damage evolution law used is linear, with propagation and mix-mode definitions in terms of energy. The tolerance for the fracture criterion is left at the default value of 0.2. In order to decrease the computational burden with minor possible loss in accuracy, a small viscosity of 1E-6 is used. This viscosity must not be mistaken with the viscosity that can be applied to the cohesive element itself, as in this case the viscosity is applied to stabilize the cohesive damage, in the material section of Abaqus.

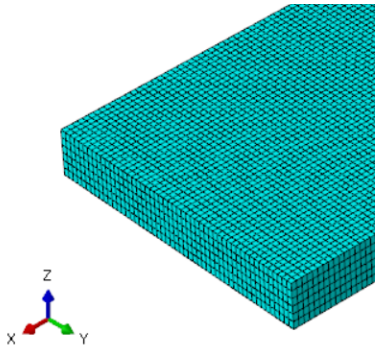

Figure 3.8: 3 element/ thickness, 0.5mm mesh seed

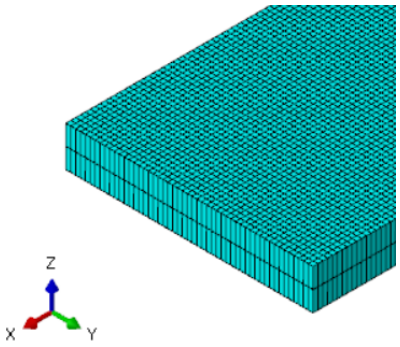

Figure 3.9: 1 element/thickness, 0.5mm mesh seed

The influence of this small viscosity was checked in the model by making sure that the ratio of the approximated energy due to viscous regularization to the total internal energy is small, a value below 1% being considered negligible. This is done by requesting the $ALLIE$ (all internal energy) and $ALLCD$ (energy associated with viscous regularization for cohesive elements and cohesive contact) Abaqus energy outputs for the whole model [43] [44]. Two mesh configurations are applied, one with 3 elements per thickness, the other with one element per thickness, both having a mesh seed of $0.5mm$ in lengthwise and width-wise directions. The two different meshing approaches considering the number of elements per beam thickness can be seen in figures 3.8 and 3.9. These two mesh configuration with respect to the number of elements per thickness are chosen for several reasons. First reason is to study the influence of the beam elements number per thickness and to verify if one element per beam thickness is sufficient to accurately describe the beam's bending behaviour for this experiment. The number of 3 elements per thickness is chosen since it is the smallest natural non-trivial divisor of 15, which is the number of plies assigned to the separating beams. When assigning the composite layups to the DCB beams, care was taken to assign the correct layup, as the layups are assigned per element and not per part thickness. This meant that, for example, in the 3 elements per thickness case, the upper and lower beams a $[0]_5$ layup assigned, which multiplied with the number of elements per thickness and the

number of beams gives the nominal DCB layup of $[0]_{30}$.

Important to mention here is that these settings are valid for all damage modeling approaches run for the DCB simulations from this section.

Regarding the DCB model with tied cohesive elements, the cohesive element's undamaged behaviour is linear-elastic as well, traction type, with a initial uncoupled penalty stiffness of 5E5 N/mm^2]. The penalty stiffness has the unit in terms of N/mm^2], as it is defined in this case as a ratio between the cohesive traction (MPa, or N/mm^2) and its corresponding strain (mm/mm) in the cohesive initial linear-elastic response 2.18. The penalty stiffness is chosen based on the values reported in [41], this value being in the range of recommended values for the used element size. The rest of the damage model setting were left to default ones, while for the COH3D8 the only adjusted parameter was the maximum degradation parameter reduced from 1 to 0.999. This adjustment was also made to reduce the computational load, with a minimum impact on the accuracy of the DCB model with tied CZE. The Abaqus damage model initiation criteria used is defined in terms of nominal tractions, with the formulation shown in equation 2.11, with all the initiation values set to $\tau = 90MPa$. The initiation values are chosen based on recommendations coming from within the company, as these set of values were found to yield satisfactory results. The value of $83.1MPa$ shown in table 3.2 for the transverse tensile strength is not chosen as a first approximation since the failure does not occur as a delamination within the skin laminate, but at the skin-filler inter-phase. As a result, blended initiation values between the butt-joint filler and laminate properties are chosen for damage initiation. The rest of the damage model settings are left default and the damage model is applied to the tied elements via section assignment tab from Abaqus. A summary of the mesh and damage model details initially used for the CZE DCB model are shown in table 3.3.

Mesh and material details				Damage model details		
Part	Element	Mesh size [mm]	Material properties		Onset	Mixed mode
Beams	SC8R	0.5x0.5x0.69/2.2	Shown in 3.1 and 3.2	Criterion	Quadratic stress 2.11	BK 2.5
Filler	COH3D8	0.5x0.5x2E-6	Traction: K_i=5E5 MPa	Parameters	τ_i=90MPa	$\eta = 2.2$

Table 3.3: CZE DCB model parts mesh and damage model details

COHESIVE ZONE LENGTH CRITERION MESH SEED DENSITY CHECK

The mesh seed of $0.5mm$ mentioned above can be verified with the formulas for estimating the cohesive zone length l_{cz} [41], using the aforementioned initiation value of $90MPa$ and the beam thickness. The general formula for estimating the cohesive zone length is shown below:

$$l_{cz} = M \cdot E \cdot \frac{G_C}{\tau^2} \tag{3.6}$$

where the parameter M can range from 0.21 to 1 (depending on the model) and E represents the material's transverse stiffness. In two of the most used models in literature, this M parameters has values of 0.88 and 1 respectively. Using aforementioned initiation value of $90MPa$, with the APC laminate transverse stiffness from 3.1, mode I fracture toughness from 3.2 and with $M = 1$ gives the following cohesive zone length:

$$l_{czG_{Ic}}^{\tau=90} = M \cdot E_2 \cdot \frac{G_{1C}}{\tau^2} = 1 \cdot 11200N/mm^2 \cdot \frac{1.41N/mm}{(90N/mm^2)^2} = 1.95mm \tag{3.7}$$

With a cohesive zone length of $1.95mm$, the mesh seed of $0.5mm$ proves more than enough to have at least 3 elements in the fracture process zone. Using a parameter value $M = 0.88$ also gives a cohesive zone length covering at least 3 elements, the cohesive zone length in this case being $1.716mm$. On the other hand, same is not the case when the most conservative value for M is used ($M = 0.21$). Using this value gives a cohesive zone length of $0.4095mm$, which is even smaller then the mesh seed used. However, as mentioned earlier, the most common used values for the M parameter are 0.88 and 1, in this case both giving at least 3 elements, of $\approx 0.5mm$ in length, inside the cohesive zone length. Furthermore, for delamination in slender bodies the cohesive zone length is both a material and structural property [41]. For delaminations in slender bodies, the cohesive zone length has the following formula:

$$l_{czSB} = \left(E \cdot \frac{G_C}{\tau^2}\right)^{1/4} \cdot t^{3/4} \tag{3.8}$$

Using the same material parameters as previously used in 3.7 and the DCB specimen thickness value of t=4.2mm, the cohesive length using the above formula gives a value of:

$$l_{czSB}^{\tau=90} = \left(E_2 \cdot \frac{G_{1C}}{\tau^2}\right)^{1/4} \cdot t^{3/4} = 11200N/mm^2 \cdot \frac{1.41N/mm}{(90N/mm^2)^2}\Big)^{1/4} \cdot (4.2mm)^{3/4} = 3.37mm \tag{3.9}$$

which for the ≈0.5mm mesh length gives 6 elements in the fracture process zone. However, while for the DCB specimen this might be valid, same is not the case for the 1-stringer specimen and for the 3-stringer panel, as the skin-stringer de-bond in those cases does not fall under de-bonds in slender bodies.

DCB CZE MODEL RESULTS

The load-displacement responses of the previously described model with the two mesh configurations shown in figures 3.8 and 3.9 are shown in figure 3.10.

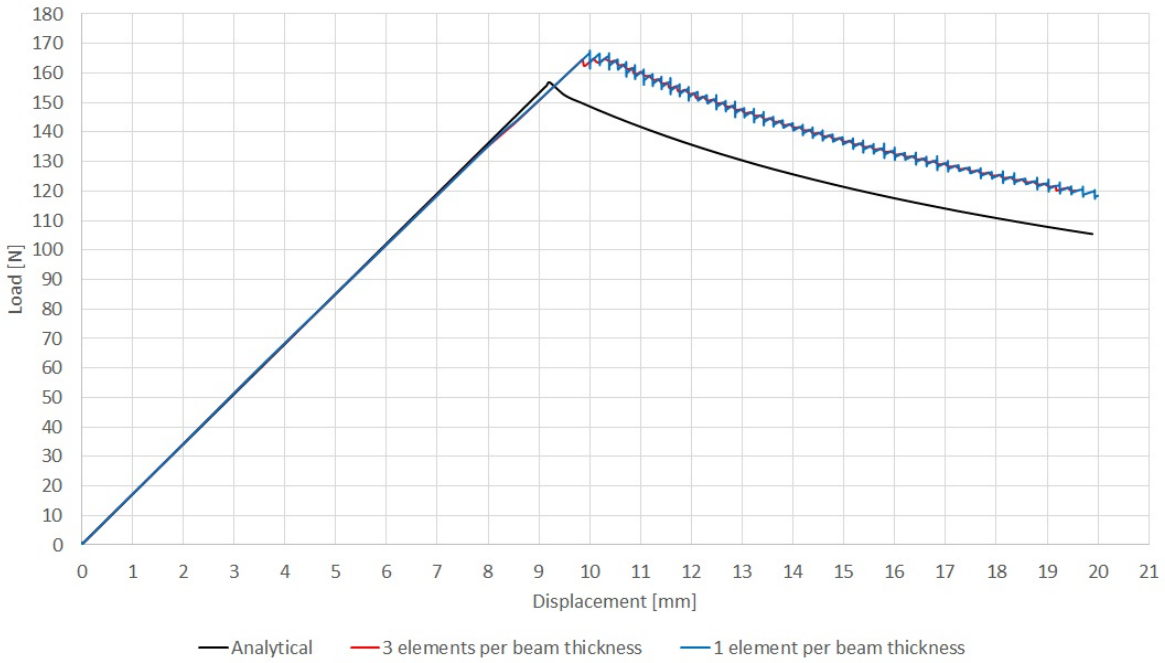

Figure 3.10: CZE DCB number of elements per beam thickness comparison

As it can be seen from the above figure, there is an excellent match in the initial stiffness of both mesh configurations until near the initiation point. The small mis-match near the initiation point suggests that in the FE model the initiation occurred earlier than it should. This behaviour is also reported in literature [40, 41, 45, 46], as a result of using lower damage initiation values. This would suggest that the initiation value of 90MPa should be increased to capture the analytical load-displacement behaviour with higher accuracy. However, this aspect has little impact in this case, as the initiation values mis-match is not large enough to significantly alter the accuracy of the simulation and as the mesh size is small enough to avoid an overshoot in the propagation region. This is due to the fact that, once the damage is initiated, the DCB behaviour is governed by the propagation value. Therefore, once damage is initiated, although the initial undamaged stiffness is no longer kept, the curve should tend towards the propagation curve for the DCB specimen, provided that the mesh size is small enough. Another aspect that suggests that this effect is not excessively large is the post-initiation stiffness, which does not differ much from the initial one.

Next, both mesh configurations overshoot significantly the propagation curve, while their load-displacement curves are overlapping each-other. One can also observe that using 3 elements per thickness gives slightly better results than using 1 element per beam thickness, the load-displacement curve in the former being smoother. This aspect is likely caused by the high aspect ratio of the continuum shell elements in the 1 element thickness mesh configuration. The convergence rate in terms of the total number of iterations is also better for the 3 elements per thickness, this model needing 2186 iterations to complete the analysis, while

the other needed 5344. In other words, decreasing the number of elements per beam thickness from 3 to 1 increased the number of iterations by a factor of ≈ 2.44. Although being related to the running time as well, a straight relation cannot be established in this case based only on the number of iterations, as a difference by a factor of 3 between the number of elements of the two models also exists. This significant difference in the number of elements also implies that the time taken for a single iteration significantly differs between the two models. To have however an estimation in terms of running time as well, the simulation for the 3 elements per beam thickness mesh configuration took ≈ 6.6h on the faculty's cluster on 10 CPUs, while for the 1 element per beam thickness mesh configuration ≈ 7.8h. Important to mention here is that these CPU times are only to provide a rough estimate, as the running times on the cluster can vary depending on the load on it.

As for both mesh configurations the same mis-match in the propagation curve was observed, a sensitivity study was done using the 3 elements per thickness mesh configuration, since it was both faster and more accurate. The first study is on the influence of the penalty stiffness, as this parameter is one of the few parameters that must be chosen empirically, or as a result of a sensitivity study. Therefore, the penalty stiffness is varied by an order of magnitude, to the values of 5E4 N/mm^2 and 5E6 N/mm^2. The results using these element penalty stiffnesses, together with the initial one of 5E5 N/mm^2 can be seen in figure 3.11 for the 3 elements per beam thickness mesh configuration.

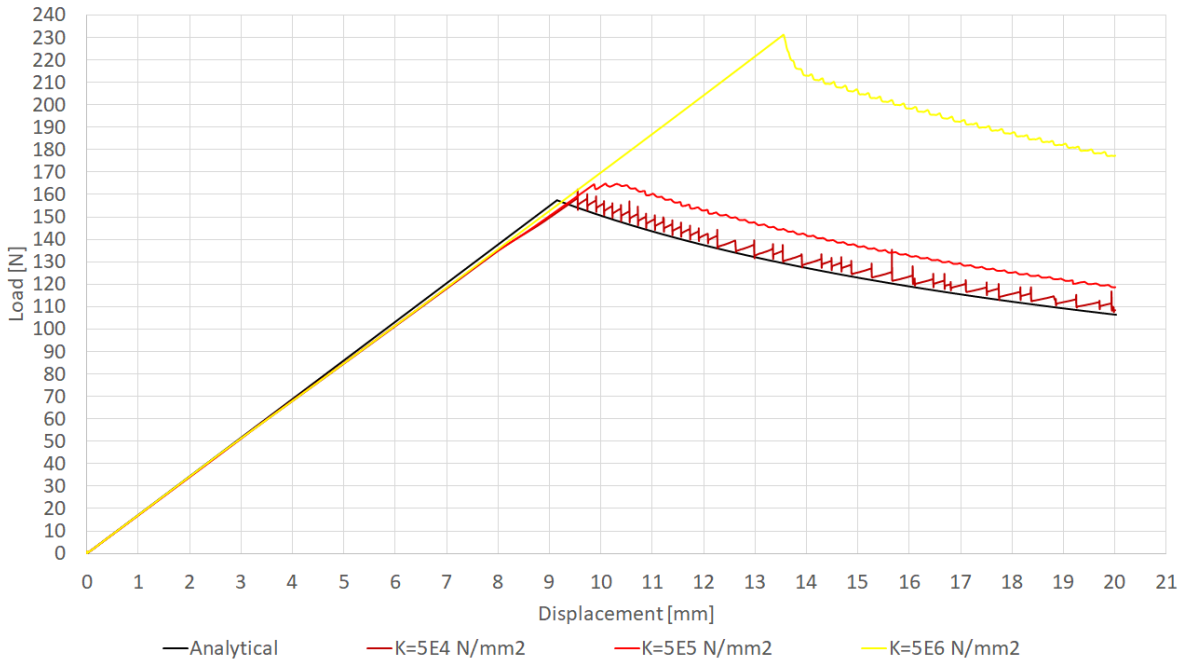

Figure 3.11: CZE DCB number of elements per beam thickness energies comparison

From this figure one can see the influence of the penalty stiffness on the propagation value, which increases as the penalty stiffness is increased. This behaviour was not expected, as the element penalty stiffness should have no, to very limited influence on the propagation curve. Changing the penalty stiffness also had an influence on the running time. Lowering the element penalty stiffness by an order of magnitude caused a high increase in the total number of iterations, from 2186 to 6396 (increase by a factor of ≈ 2.92), while increasing the element penalty stiffness by an order of magnitude decreased the number of iterations to 1778 (decrease by a factor of ≈ 0.81). Here the comparison in terms of iterations also gives a more reliable relative time comparison between the models, as the only difference is the penalty stiffness and not the number of elements.

DCB CZE SENSITIVITY STUDY AND MODEL ERRONEOUS BEHAVIOUR DISCUSSION

As regularly using cohesive elements to model DCB tests is known to work properly, some possible sources of this error were investigated in a sensitivity study.

First, the tie discretization method was changed from $surface-to-surface$, to $node-to-surface$, as the other tie formulation settings should have no influence over the simulation. Using the $node-to-surface$

tie discretization gave identical load-displacement behaviour, meaning that the tie discretization was not the source of the error.

Next, the effect of the tie itself was investigated. To verify if indeed the issue was with the tie constraints used to link the cohesive elements with the two DCB beams, a model with the same specification was built, except now the cohesive elements no longer had a matching mesh with the DCB beams mesh, but matching nodes. With the tie constraint removed, the model with 3 elements per beam thickness also showed identical load-displacement behaviour as the one from figure 3.10. This suggested that the tie constraints used worked properly and the source of the issue lied somewhere else.

Last, as investigating the tie influence has not revealed the source of the issue, the energy associated with the viscous dissipation was verified, even though the small viscosity parameter applied should not have caused such a significant difference. In order to do this, energy outputs of the models shown in figure 3.10 were requested. First the internal energy ($ALLIE$) and the energy associated with the viscous damping for cohesive elements ($ALLCD$) were verified, revealing that the models behaved identically in terms of energies and that the energy associated with viscous damping for cohesive elements was 0. Furthermore, the influence of the added viscosity was not found in any of the models non-zero energy components. Running another model without any viscosity applied for the 3 elements per beam thickness mesh configuration revealed identical behaviour. This might suggest that the viscosity must be applied at the element level, instead of applying it to stabilize the cohesive damage, for it to be introduced in the model.

The models also showed another un-expected behaviour in terms of energies, as the $ALLWK$ quantities representing total work done by the models differed than the models total internal energy $ALLIE$ from the point when the damage started to propagate. Also from this point the energy balance quantity $ETOTAL$ ceased to be constant and close to 0, owing to the aforementioned difference between the $ALLWK$ and $ALLIE$ quantities. As the energy balance $ETOTAL$ were negative, the models appeared to be 'leaking' energy, since the total work done was higher than the total internal energy.

This investigation on the erroneous behaviour of the $CZE\ DCB\ FE$ models suggests that the issue must have been from the cohesive elements implementation in the model. This affirmation is based on the fact that in literature cohesive elements are known to be able to accurately model the behaviour of DCB specimens. Furthermore, the study using this approach to model separation was somewhat done in parallel with the ones described in sections 3.1.3 and 3.1.4, where good results were obtained straight away, with the same DCB beams modeling technique and a very similar approach when cohesive surface based behaviour was used. Therefore, the sensitivity study using this approach ends here, due to the issues encountered with its corresponding FE model and as the cohesive surface based behaviour and the $VCCT$ approaches investigated somewhat in parallel, and described in sections 3.1.3 and 3.1.4, readily gave the expected behaviour.

3.1.3 CZS DCB

Similar to the approach using cohesive zone elements from the previous section 3.1.2, the cohesive zone surface (CZS) based damage model is also aimed to be implemented at the skin-filler inter-phase. The location of the contact definition for the CZS shown in figure 3.12 is identical with the one of the $VCCT$ approach described in section 3.1.4 that follows. Although using this approach can be more computationally expensive than using cohesive elements, having the damage model implemented at a surface level, rather than at the element level has several benefits. One advantage is the better representation of the skin-filler butt-joint debonding phenomenon depicted in section 2.1. This is due to the fact that in this case the inter-phase has 0 thickness, while cohesive elements typically represent better adhesives of finite thicknesses.

This approach also has another side-benefit, as the contact formulation prevents the inter-penetration of the two surfaces between which the cohesive property is defined [34]. This is helpful when considering the 1-stringer specimen and the 3-stringer panel, as the buckling pockets deflecting towards the stringer could make these surfaces to come into contact after they de-bonded.

CZS DCB MODEL

The FE model of the cohesive surface based behaviour shares most of its features with the cohesive element based behaviour $DCB\ FE$ model, the biggest differences being with respect to how the damage model is implemented. The shared features are the material paremeters, analysis type and incrementation settings, loading and BC applied, as well as the aspects related to modeling the beams, excepting the model's assembly. In this model, the upper and lower beams of the DCB specimens are modeled individually, since the damage

model is specified as an interaction between their surfaces. Therefore, a separate surface tie constraint is no longer needed, the connection between the upper and lower beam being defined in the initial step through this cohesive interaction. The damage model is specified in a $surface-tosurface, smallsliding$ contact interaction between the upper surface of the bottom beam (master surface) and the lower surface of the upper beam (slave surface). The de-bonded surface regions were left out of the this contact interaction, the cohesive surface behaviour being only specified for the intact part of the DCB specimen. A set with the slave surface nodes of the upper beam was defined in order to specifically limit bonding to the desired nodes, as well as to adjust the slave nodes to be in perfect contact with their corresponding master nodes. The contact property was defined as cohesive behaviour, with the same, uncoupled penalty stiffnesses magnitudes used in the cohesive elements approach and same properties of the damage model. In order to make sure that the correct slave nodes are used in the analysis, the option of specifying the slave nodes in the contact interaction was used.

The $smallsliding$ tracking method is chosen here since for the DCB specimen no, or very limited sliding is expected, falling therefore under the applicability of this tracking algorithm. Moreover, this tracking algorithm is also deemed to be more robust and could also ease the computational load. The $surface-to-surface$ discretization is chosen for two reasons, first being that it generally provides better accuracy for minimal additional computational load with respect to the $node-to-surface$ discretization [47]. The second reason is to keep the initial settings of the 3 different damage models as similar as possible. However, as for the 1-stringer specimen and for the 3-stringer panel mode II and III separation can also be significant, the $finite\ sliding$ tracking algorithm is also investigated later in the thesis.

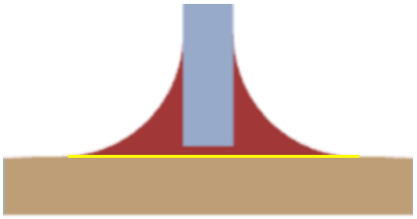

Figure 3.12: Cohesive and VCCT surface location in the butt-joint

CZS DCB MODEL RESULTS

For the adjusted damage model to cohesive surface based behaviour, the $CZS\ DCB\ FE$ model was run with the two mesh configuration shown in figures 3.8 and 3.9, the load-displacement curves of these models being shown in figure 3.13.

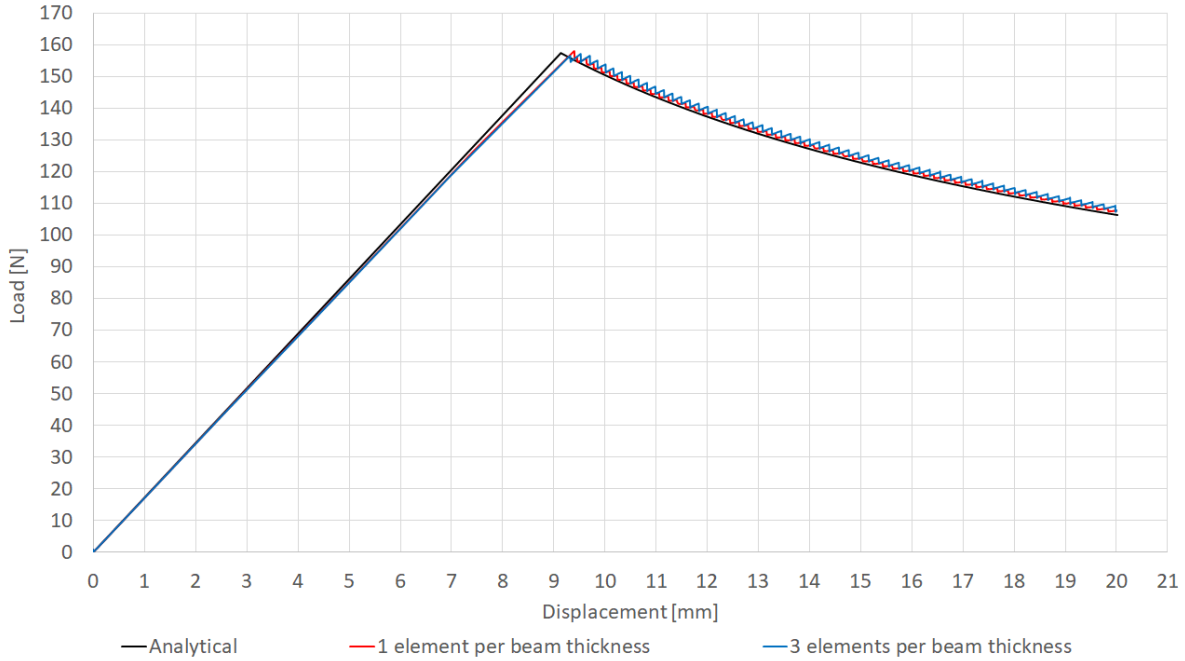

Figure 3.13: CZS DCB number of elements per beam thickness load-displacement curve comparison

Unlike for the $CZE\ DCB\ FE$ model, one can see from the above figure that the CZS model's load-displacement

curves closely follow the analytical curve for both mesh configurations. An excellent agreement in the initial part of the linear-elastic load-displacement curve is achieved, with a small mis-match observed towards the end of this region, feature which also observed in figure 3.10 for the CZE approach. There are also some further minor differences between the two mesh configurations, having 3 elements per beam thickness yielding a slightly coarser curve this time, unlike for the previous cohesive zone element approach. Having 3 elements per beam thickness also gave a slightly lower initiation value and a slightly higher propagation curve.

In terms of convergence, using 3 elements per beam thickness only gave a small improvement, as in this case 5300 iterations were needed, with respect to 5500 iterations needed when 1 element per beam thickness was used. Moreover, in this case using 1 element per beam thickness proved to be significantly faster, as it ran in $6h$, compared with the $14.8h$ needed to complete the simulation when 3 elements per beam thickness was used for this model. Again these CPU times were obtained using 10 cores and these are only estimates to be used for a relative comparison between the two models.

DCB CZS MODELS ENERGY BALANCE

Unlike for the previous CZE DCB model, for the CZS one the $ALLCD$ energy output to check the influence of the viscosity was different than zero. Therefore the ratio of $ALLCD/ALLIE$, representing the ratio between the energy associated with cohesive damage stabilization and the total internal energy, could be plotted. The $ALLCD/ALLIE$ ratios for both mesh configurations regarding the number of elements per beam thickness can be seen in figure 3.14.

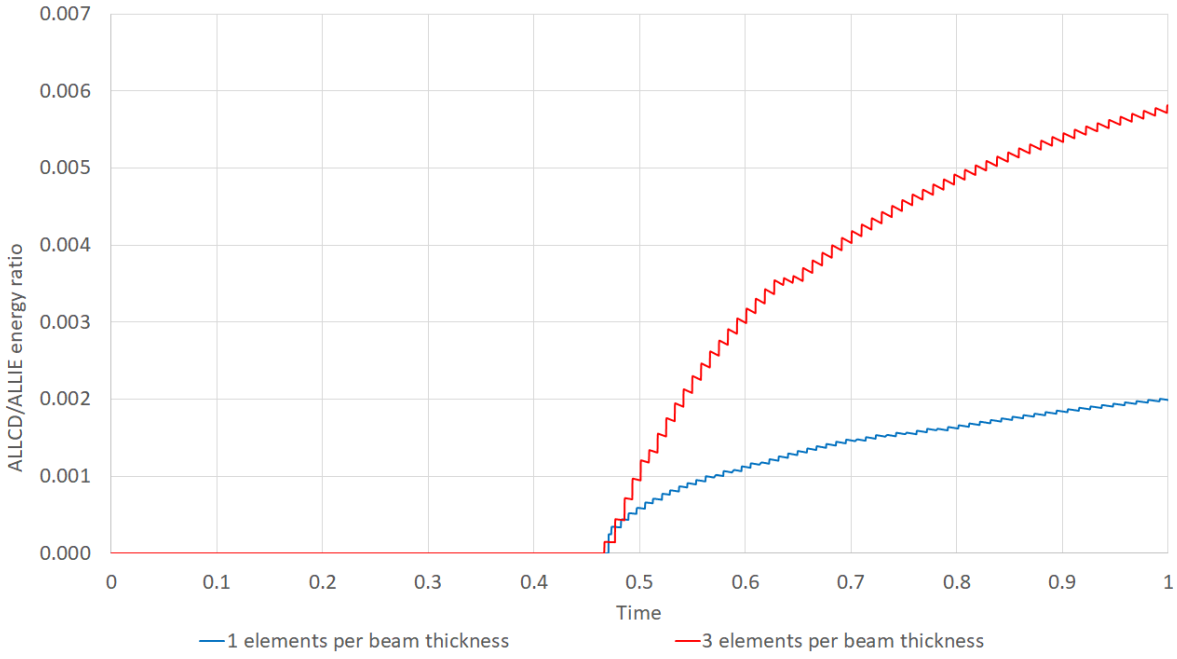

Figure 3.14: CZS DCB number of elements per beam thickness energies comparison

In this figure one can see that both curves are overlapping until somewhere in between a displacement of $9mm$ and $10mm$. This represents the linear elastic region of the curves shown in figure 3.13. Also, from this figure it can be noticed that damage initiates for both models roughly at the same time, with a slightly earlier initiation in the 3 elements per beam thickness model. The artificial energy dissipated for damage stabilization for the 3 elements per beam thickness configuration is roughly 3 times higher than the one of the 1 element per thickness model. Moreover, both are in the 1E-3 order of magnitude, which confirms that the viscosity added is not large enough to adversely influence the accuracy of the simulation.

Similarly as in the previous section, to verify that these models using the cohesive surface based behaviour work properly, the energy output of the 1 element per beam thickness model were requested in a history output. The 1 element per beam thickness model alone was chosen for this study since it was shown in the section describing the previous approach that both mesh configuration had the same behaviour in terms

of energies. Furthermore, this model showed less viscous energy dissipated than the 3 elements per beam thickness model, better CPU time and also slightly better accuracy.

Unlike in the previous approach, for this model the total internal energy $ALLIE$ equaled the total work done in the model $ALLWK$ throughout the whole analysis, including the damage propagation part. However, the energy balance $ETOTAL$ component still ceased to have a constant, near 0, value after damage started to propagate. This happened as, due to the surface based cohesive contact behaviour damage model, another non-zero energy output was introduced. This $ALLCCDW$ component represents the energy associated with contact constraint discontinuity work and it comes from the damage model definition, which is now specified as a contact interaction. This component is non-physical and should tend towards 0 with decreasing the increment size. It is also common for this energy output to have large values without influencing the accuracy of the solution [48, 49]. Important to mention here is that the sign of this component was negative and that typically a negative value of this energy output is found when closing forces are involved, while the global contact behaviour of the DCB model implies opening forces. The negative sign of this $ALLCDW$ component after damage starts to propagate made the $ETOTAL$ energy balance component model to be positive, the model appearing to 'gain' energy. However, considering that this problem is not a true contact one, that the model yields satisfactory accuracy and the aforementioned description, significance and influence of the $ALLCCDW$ in the model from the Abaqus 2017 documentation [48, 49], the model is considered to work properly. With this in mind, a sensitivity study is done for the DCB model with this cohesive contact damage model as well, here using the 1 element per beam thickness mesh configuration.

DCB CZS MODEL SENSITIVITY STUDY

First, the penalty stiffness was varied in the same way as in the previous approach. Here the same values were used to investigate the influence of the penalty stiffness, with the mention that here, as the damage model is specified at a surface level, the units are in terms of N/mm^3, instead of the N/mm^2 from the previous CZE approach. The load-displacement curves for the 3 different penalty stiffness values (5E4 N/mm^3, 5E5 N/mm^3 and 5E6 N/mm^3) can be seen in figure 3.15.

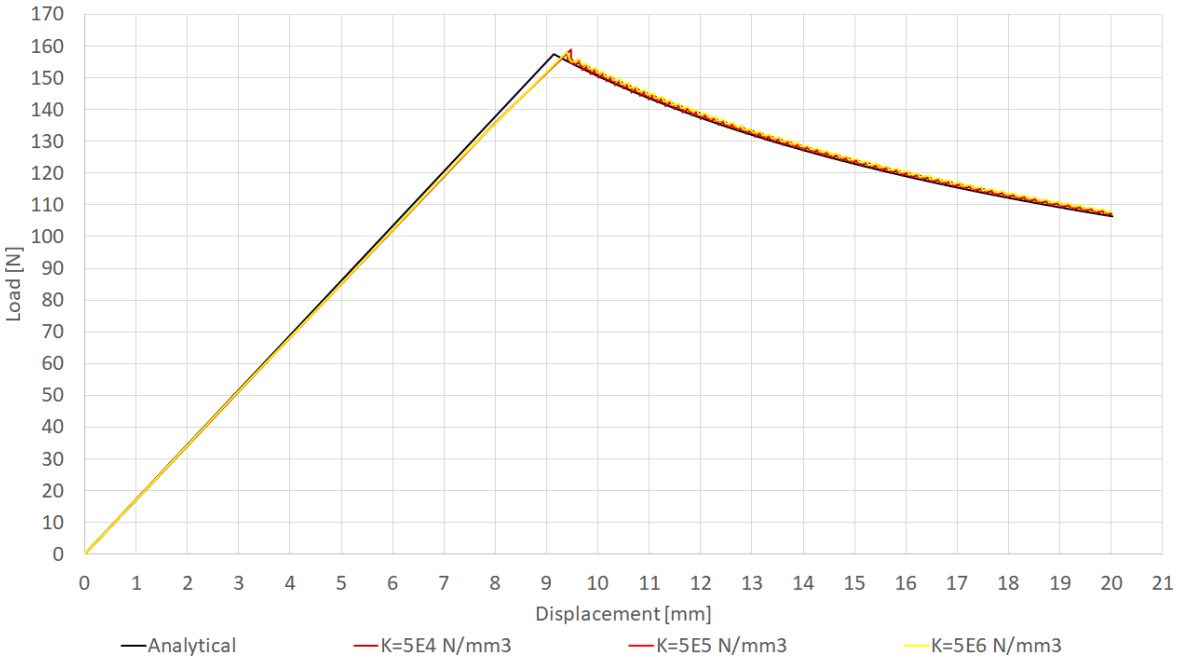

Figure 3.15: CZS DCB number of elements per beam thickness energies comparison

As it can be seen from this figure, when using the CZS damage model for the DCB specimen, the penalty stiffness no longer has the high influence over the propagation curve seen in figure 3.11 for the CZE approach. This behaviour is expected, as for a robust DCB FE model, increasing the penalty stiffness should improve its accuracy and definitely not alter the propagation curve. Some small differences in the initiation point can be seen between these models shown in figure 3.15, but a clear trend as a function of the penalty

stiffness cannot be observed, as the highest value used, 5E6N/mm^3-shown in the yellow curve, has the initiation point between the other two. Same is not the case with the propagation curve, as lowering the penalty stiffness seems to have the same effect on the propagation curve as in the previous CZE approach, shown in figure 3.11, but here the difference is negligible.

In terms of running times and convergence rate, a clear trend could not be seen, as using a penalty stiffness of 5E6 N/mm^3 gave the best convergence and CPU time, while using a penalty stiffness of 5E5 N/mm^3 gave the worst one. Since increasing the penalty stiffness also improves the accuracy and the CPU time, this 5E6 N/mm^3 penalty stiffness was adopted in all the subsequent sensitivity studies in this section.

Next, same as for the previous approach, the influence of the contact discretization was studied, using the two $surface-to-surface$ and $node-to-surface$ contact discretizations types. As suggested in the Abaqus 2017 documentation [47], the $surface-to-surface$ contact discretization yielded slightly better results, as for the model using it the propagation curve is slightly closer to the analytical one. The higher accuracy of the $surface-to-surface$ contact discretization was also seen in the non-physical quantities of the energy outputs, which were smaller than when the $node-to-surface$ contact discretization was used, these differences being in orders of magnitudes. The only advantage of the $node-to-surface$ contact discretization over the $surface-to-surface$ one in the studied DCB models was the better convergence of the former, which also led to a better CPU time.

INCREASING THE MESH SEED IN THE CZS DCB MODEL

With the model yielding good accuracy, regardless of the penalty stiffness, number of elements per beam thickness, or contact discretization type, the mesh size was gradually increased in 0.5mm steps to 2.5mm. This was done with the aim of using this damage model in the 1-stringer and 3-stringer panel with a mess seed that would allow having one element per thickness and an aspect ratio close to 1.

When increasing the mesh seed to 1mm, the criterion to have at least 2-3 elements in the fracture process zone is no longer satisfied. Remembering that the cohesive zone length from relation 3.7 was 1.95mm, having a mesh seed of 1mm means that only one element is in the fracture process zone. This mesh restriction can be avoided using a engineering solution, in which the damage initiation value is artificially decreased to increase the cohesive zone length[41]. For this mesh size multiple initiation values were used, these being 90MPa, 75MPa, 60MPa, 50MPa and 40MPa. The cohesive zone lengths of these initiation values can be seen in the relations the below, where $M = 0.88$ was used in relation 3.6.

$$l_{czG_{Ic}}^{\tau=75} = 2.417mm, \quad l_{czSB}^{\tau=75} = 3.798mm \tag{3.10}$$

$$l_{czG_{Ic}}^{\tau=60} = 3.86mm, \quad l_{czSB}^{\tau=60} = 4.246mm \tag{3.11}$$

$$l_{czG_{Ic}}^{\tau=50} = 5.559mm, \quad l_{czSB}^{\tau=50} = 4.651mm \tag{3.12}$$

$$l_{czG_{Ic}}^{\tau=40} = 8.686mm, \quad l_{czSB}^{\tau=40} = 5.2mm \tag{3.13}$$

As it can be seen from these relations, the cohesive zone lengths significantly vary depending on the relation used. While the relation 3.6 gives initially lower cohesive zone lengths than the relation for slender bodies 3.8, the former cohesive zone length rapidly increased with decreasing initiation values. The first initiation value used that gives 3 elements in the fracture process zone is the one of 60MPa when relation 3.6 is used, while for slender bodies the cohesive zone length for all the initiation values used here satisfy the criterion.

The load displacement curves of the DCB model using these initiation values can be seen in figure 3.16, together with the mesh size of ≈1mm used.

As it can be seen from the above figure, the traction initiation values of $T = 90MPa$ and $T = 75MPa$ significantly overshoot the analytical curve, with the $T = 75MPa$ initiation value giving an even higher overshoot than using $T = 90MPa$ for damage initiation. This behaviour is not generally expected, the general trend being the opposite. This opposite trend can be seen when the initiation values of $T = 60$, $T = 50$ and $T = 40MPa$ respectively are used, trend also seen in [40, 45, 46]. Compared with the other curves for the finer mesh size, it can be seen there that for the 1mm mesh seed, besides the softening at the end of the linear-elastic part, also the propagation curve is coarser than when a mesh seed of 0.5mm was used. This behaviour is expected, as

now there are less nodes along the length and the width of the specimen that have to release the same energy required for fracture propagation. This would mean that also the horizontal step between the propagation's curve peaks increases with increasing the mesh size and so does the amplitude of the local maximums and minimums of the propagation curve along the vertical direction. In other words, the propagation part of the DCB load-displacement curves tends to become coarser with increasing mesh size.

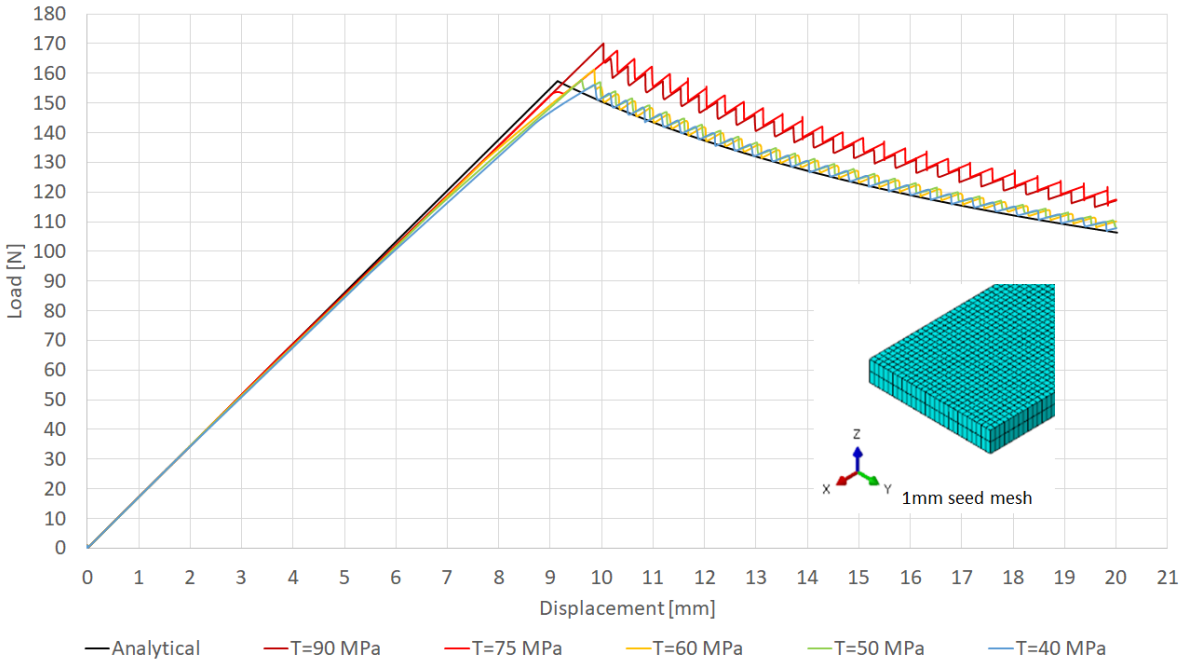

Figure 3.16: CZS DCB 1 element per beam thickness, 1mm mesh seed, initiation value comparison

Regarding the accuracy of the tried initiation values, the tractions starting from $T = 60MPa$ and below gave satisfactory results, with the $T = 50MPa$ one giving the best accuracy, as the initiation point is the closest to the analytical one. Regardless, the propagation curves are relatively similar for the $T = 60MPa$, $T = 50MPa$ and $T = 40MPa$ initiation values. The fact that only the models with initiation values below $T = 75MPa$ gave satisfactory results comes as no surprise when considering the cohesive zone lengths given by relation 3.6. When using this relation, only for the initiation values from $T = 60MPa$ and below the 2-3 elements in the fracture process zone criterion was satisfied. However, when considering relation 3.8 for slender bodies, the results for the initiation values of $90MPa$ and $75MPa$ are surprising. For these initiation values the relation for slender bodies also gave 2-3 elements in the fracture process zone, therefore satisfactory accuracy for these simulations were also expected. This difference however suggests that the relation for the cohesive zone length for slender bodies3.8 might not be as reliable as the other one3.6.

The CPU time decreased significantly from $6h$ on 10 cores on the university's cluster, to around $1h$ for all these models, on an Intel i7-7700HQ processor with 16 GB RAM (2400 MHz). These times are only relevant in showing the high decrease in computational time related to decreasing the mesh seed from $0.5mm$ to $1mm$, as these running times can vary slightly depending on the machine's load. Also, in the following paragraphs of this section the same machine was used to run the other DCB models. In terms of convergence rate, lowering the traction values for damage initiation improved the convergence rate, with 2520 iterations being needed to complete the analysis with $T = 90MPa$, compared with the 1875 needed to complete the analysis with $T = 40MPa$.

As the models yielded satisfactory results for this mesh $1mm$ mesh seed with lowered damage initiation values, the process of increasing the mesh seed in $0.5mm$ steps was continued until the $2.5mm$ mesh seed was reached. Similar as in the previous case when the mesh seed was increased, the starting initiation values were also decreased. The CZS DCB model damage initiation values tried were from $T = 30MPa$ to $T = 10MPa$, decreasing it with the same step of $10MPa$. The damage initiation value of $T = 30MPa$ was chosen as the starting point since this was the first one that gave satisfactory accuracy for the $2mm$ mesh seed. The cohesive zone length estimations for the initiation values of $T = 30MPa$, $T = 20MPa$ and $10MPa$ can be seen in

the relations below:

$$l_{czG_{Ic}}^{\tau=30} = 15.441mm, \quad l_{czSB}^{\tau=30} = 6.005mm \tag{3.14}$$

$$l_{czG_{Ic}}^{\tau=20} = 34.742mm, \quad l_{czSB}^{\tau=20} = 7.354mm \tag{3.15}$$

$$l_{czG_{Ic}}^{\tau=10} = 138.97mm, \quad l_{czSB}^{\tau=10} = 10.4mm \tag{3.16}$$

While all the initiation values tried here are likely to be accurate based on relation 3.6, the one for slender bodies 3.8 give $T = 10MPa$ as the first initiation value likely to give satisfactory accuracy. For these very low initiation values, also the cohesive zone length estimations using relations 3.6 and 3.8 tend to highly differ, the one for slender bodies being significantly more conservative, as it can be best seen from relation 3.16 for an initiation value of $10MPa$

The load-displacement curves for these initiation values and the DCB mesh with the $2.5mm$ mesh seed can be seen in figure 3.17 below.

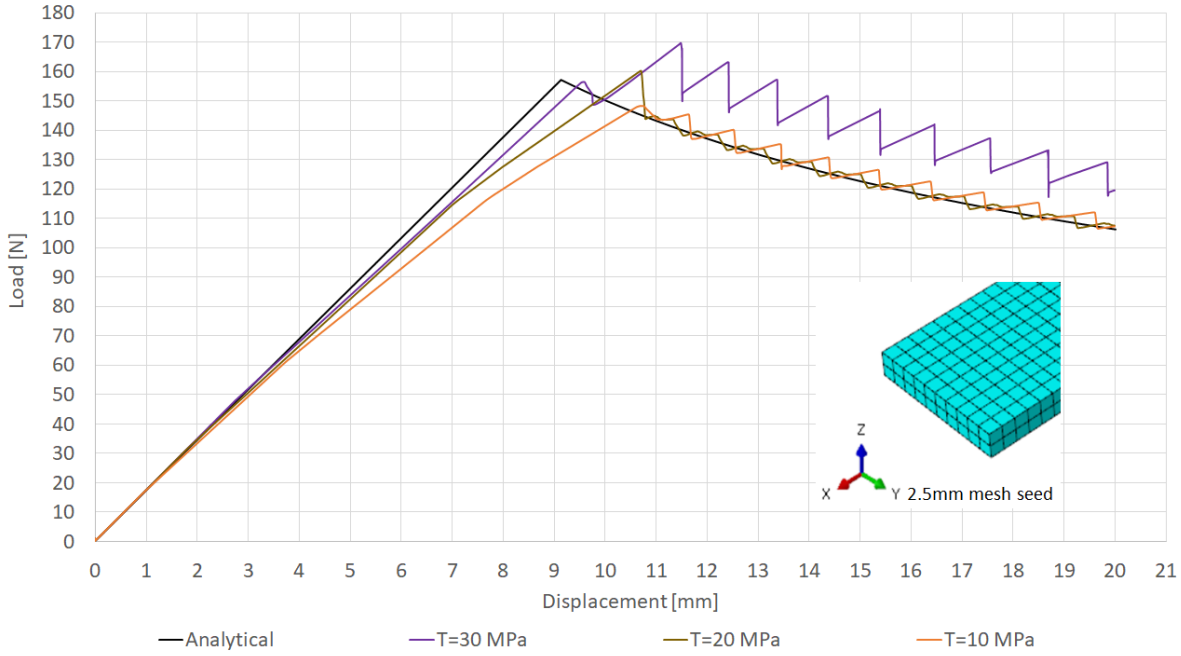

Figure 3.17: CZS DCB 1 element per beam thickness, 2.5mm mesh seed, initiation value comparison

With this mesh seed of $2.5mm$ a fair correlation is obtained using $T = 20MPa$ and $T = 10MPa$ initiation values, while for $T = 30MPa$ the correlation with the analytical load-displacement curve is poor. Regardless, using $T = 20MPa$ still slightly overshoots the analytical propagation curve, while having a good match in the initiation load. On the other hand, using $T = 10MPa$ gives a significant mis-match in both the initiation load and displacement, but matches well the analytical propagation curve after the two curves intersect.

The CPU time decreased exponentially with increasing the mesh size, these $2.5mm$ mesh seed models with lowered damage initiation values running in approximately $7min$. In terms of convergence the same trend is seen, namely improved convergence with increasing the mesh size and decreasing the initiation values. The model with $T = 30MPa$ needed 1496 iterations to complete the analysis, while the model with $T = 10MPa$ needed 1327 iterations to complete the analysis. Again, this is just a general trend, as for example in this case the model with $T = 20MPa$ needed slightly fewer iterations then the one for $T = 10MPa$, the difference however being negligible (17 iterations).

These models with the severely altered initiation values still behaved similarly with the initial ones with initiation values of $T = 90MPa$ and a $0.5mm$ mesh seed in terms of energies, as negligible differences are found

in this aspect between these models. Furthermore, the magnitude of the other energy components was sill roughly the same, the only significant difference being the higher magnitude of the step changes given by a coarser mesh size. This is due to the higher amount of energy released when a node line along the specimen is released, which is proportional with the de-bonded area within the DCB specimen. This shows that increasing the mesh size does not adversely influence the general behavior of the model, as the changes in terms of total internal energy, total work done by the model and the ratio between the two was not influenced in terms of magnitudes.

Another trend noticed when increasing the mesh seed and lowering the damage initiation values was the accuracy of the results based on the 2-3 elements inside the fracture process zone criterion and the estimation given by the two relations used to predict the cohesive zone length 3.6 (for thick bodies) and 3.8 (for slender bodies). While at the beginning for the $0.5mm$ mesh seed the cohesive zone length relation for de-bonds thick bodies proved to predict better the combination of mesh size and lowered initiation values which would give accurate results, as the mesh seed increased to $2.5mm$ the latter proved to give a better prediction. For the $30MPa$ initiation value, the cohesive zone length relation for de-bonds in thick bodies gave 6 elements in the fracture process zone, yet using this value still gave a poor accuracy. On the other hand, using the relation for de-bond in slender bodies only gave 2 elements in the fracture process zone for this mesh seed and damage initiation values, suggesting that the accuracy given by the mesh seed and initiation values used is questionable. Therefore, for lower initiation values the relation to estimate the cohesive zone lengths for slender bodies 3.8 seems better suited than the other one 3.6 for the DCB specimen. However, this is merely a trend, the relations investigated here giving inconsistent predictions on which mesh sizes and damage initiation values combinations gave satisfactory correlation with the analytical load-displacement response of the DCB model studied.

3.1.4 VCCT DCB

The $VCCT$ approach is very similar with the cohesive surface based behaviour described in the previous section 3.1.4, having the same desired way of implementation in the 3-stringer panel as the one shown in figure 3.12.

VCCT DCB MODEL

As mentioned above, the $VCCT\ DCB$ model is almost identical with the CZS one described in the previous section. The only differences between the $VCCT\ DCB$ model from this section and the previous $CZS\ DCB$ one from section 3.1.3 is interaction defined between the de-bonding surfaces and the need to define a crack for the contact pair interaction. The $VCCT$ damage model can be used here since there is an existent damage in the DCB specimen, namely the $56.6mm$ de-bond/pre-crack. Similarly, an existent damage also exists in the 1-stringer specimen and 3-stringer panel, namely the skin-stringer de-bond. In order for Abaqus to recognize the crack front, the interaction needs to be defined between the whole beam's surfaces, including the already separated region as well. This is due to the fact that Abaqus defines the crack front using this contact interaction, together with a node set containing only the bonded nodes of the slave surface. This node set has to be mentioned in the bonding tab of the $surface-to-surface$ contact interaction, otherwise Abaqus would not recognize the crack/de-bond tip. For this contact interaction, the same $smallsliding$ with $surface-to-surface$ discretization was used as for the CZS model, with adjusted slave nodes and limiting bonding to the predefined slave set of nodes. One important difference in defining this interaction for the $VCCT$ damage model, is that the contact interaction has to be defined in the loading step, unlike in the previous $CZS\ DCB$ case where this interaction had to be defined in the initial step.

For the contact property a fracture criterion was specified, $VCCT$ type, with a 0.2 tolerance, 1E-6 viscosity, propagation values and BK as previously used for the DCB models studied. The direction of the crack propagation relative to the local 1-direction option was left default, as this feature is applicable only to enriched regions in Abaqus Standard. Unstable crack growth tolerance was not specified, meaning that the de-bond grows in a node-by-node manner in individual increments. The crack defined for the contact pair was $VCCT$ de-bond type and it was also specified in the loading step. Furthermore, as previously discussed in section 2.2.1, there two options to choose the way in which the nodes will be released are available, namely a $Step$ and $Ramp$ manner. Here the $Ramp$ option was chosen, as this would represent better the physical phenomena using a relatively coarse mesh. This is due to the fact that in reality the separation occurs in a more continuous manner, while here the discrete nodes at relatively large distance between themselves are released. Therefore, releasing gradually the nodal forces would give a smoother reaction force in the model,

while completely releasing them in distinct steps would give a staggered reaction force evolution. Although using $Step$ as a node releasing approach is more appropriate to model the physical phenomenon, a highly refined mesh would be needed to obtain a smoother load-displacement curve that accurately captures the experimental data. Therefore, the $Ramp$ option is preferred here as a modeling artifact to obtain similar results with a coarser mesh, saving important CPU time. This concludes the differences between the CZS DCB model described in the previous section and the one treated here.

VCCT DCB MODEL RESULTS

Same as for the previous approaches, the load-displacement curves for the $0.5mm$ mesh seed for 3 and 1 elements per thickness are shown for the $VCCT$ approach in figure 3.18.

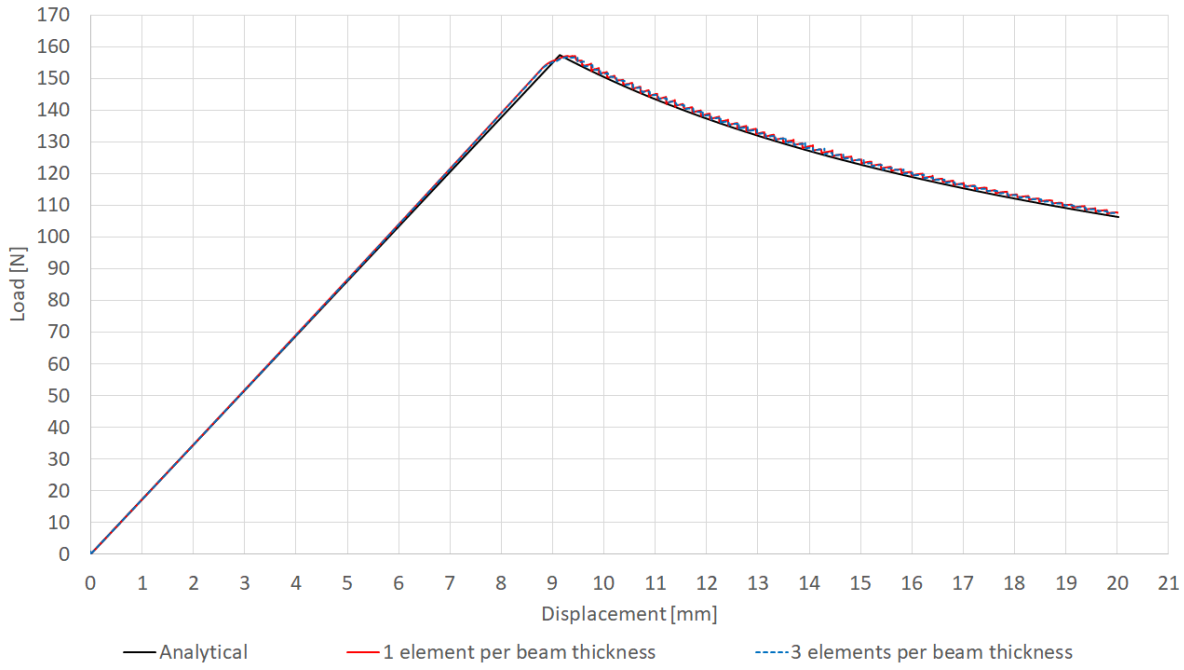

Figure 3.18: VCCT DCB number of elements per beam thickness comparison

In this figure one can notice that the two load-displacement curves for the two different mesh configurations are in excellent agreement between themselves. Due to this reason, the line style of the load-displacement curve of the 3 elements per beam thickness mesh configuration model (blue line) was changed to a discontinuous type. Furthermore, these numerical curves are in excellent agreement with the $ASTM$ MMB $LEFM$ model.

For both curves a small stiffening behaviour can be noticed in the linear-elastic part. While in the initial stage both curves perfectly overlap with the analytical one, in the later stage of the linear-elastic part one can notice that the numerical $VCCT$ load-displacement curves show a slightly stiffer behaviour than the analytical model, while the numerical curves still overlap each-other. The agreement in terms of initiation and propagation is also very good, with a smoother transition from the linear-elastic part to the propagation part than seen in the $VCCT$ load-displacement curves. This behaviour was first observed while using this approach, as in the previous approaches for the DCB model described in sections 3.1.2 and 3.1.3 this transition was relatively sharp, similar to the analytical one. Similar as in the previous cohesive surface based approach from section 3.1.3, also in this case a small, negligible, overshoot in the numerical propagation curves is observed, while the degree of smoothness of the curves is very similar for the same mesh configuration.

In terms of convergence, the two mesh configurations showed similar behaviour, as 3833 iterations were needed for the 3 elements per beam thickness, while 3862 iterations were needed for the 1 element per thickness configuration. When compared to the CZS DCB models that yielded good accuracy, for the same mesh size and incrementation settings, the $VCCT$ approach showed far superior convergence rate. For the 3 elements per beam thickness the $VCCT$ approach needed 1467 iterations less, while for the 1 element per beam

thickness approach $VCCT$ needed 1638 iterations less. However, in terms of actual CPU time, the using 3 elements per beam thickness took roughly $20.8h$ for the same number of cores, compared to the roughly $14.8h$ needed for the CZS approach, while the one element per thickness $VCCT$ took roughly $9.3h$, compared to the roughly $6h$ needed for the CZS equivalent approach. Therefore, it can be concluded that for the DCB models studied, for the same mesh configuration, using $VCCT$ tends to be slower than cohesive surfaced based behaviour to model mode I separation.

Next, the influence of the viscosity parameter added is also shown in figure 3.19, for the 3 and 1 elements per beam thickness, with a $0.5mm$ mesh seed $VCCT$ DCB models. For these models, the ratio that has to be verified is now $ALLVD/ALLIE$, $ALLVD$ representing the viscous dissipated energy [44].

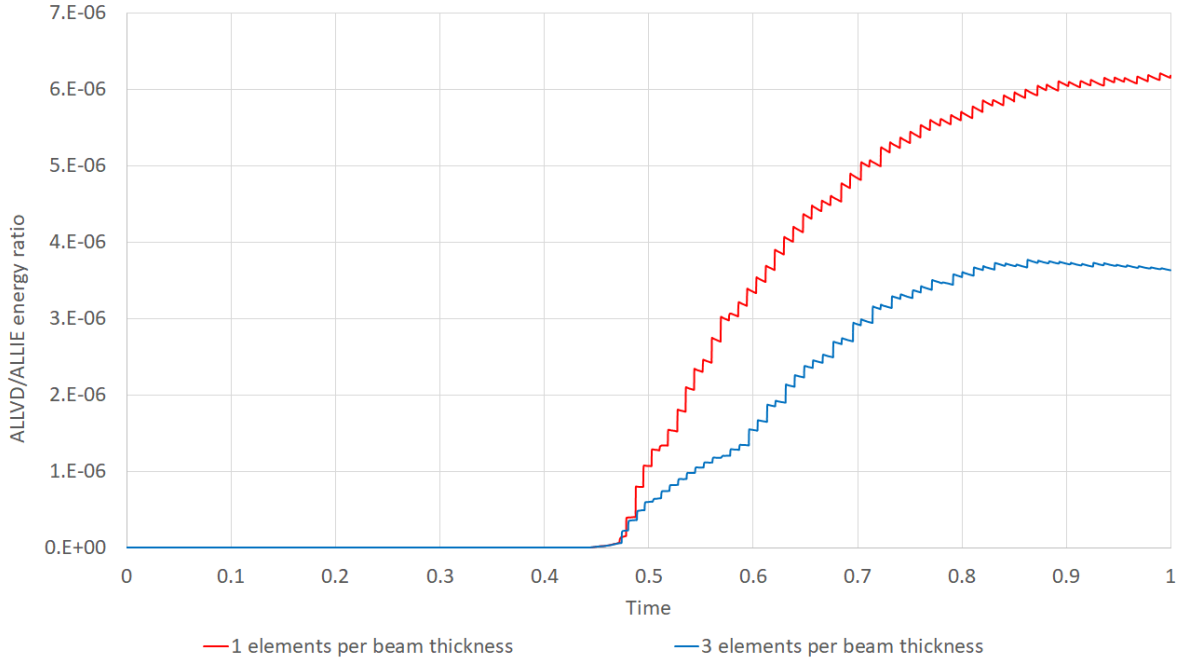

Figure 3.19: VCCT DCB number of elements per beam thickness energies comparison

When comparing the ratio of energy dissipated due to damage stabilization to total internal energy of previous working CZS approach, the order of magnitude is roughly 3 times lower when the $VCCT$ damage model is used. Another difference with respect to th previous approach was that in this case using 3 elements per beam thickness dissipated less energy than using 1 element per beam thickness. These significantly lower ratios suggest that the $VCCT$ models are more efficient, which is also supported by their superior convergence rate.

Since the differences in terms of accuracy between using 3 elements per beam thickness and 1 element per thickness is negligible for significant differences in CPU times and more importantly since one element per laminate thickness is also desired for the 3-stringer panel, the 1 element per thickness $VCCT$ DCB model is used for further analysis.

When using the $VCCT$ damage model the mode independent $SERR$s (Strain Energy Release Rates) can be requested for the whole model. These can be used to verify that indeed the separation in the DCB model occurs under a dominant mode I. This was done here by comparing the ratios of each independent $SERR$ to total $SERR$, total achieved by simple summation the three independent components. The ratios of the individual $SERR$s over the total $SERR$ are shown in figure 3.20.

In figure 3.20, the horizontal axis shows the vertical displacement of the DCB beams, while on the vertical axis the ratios of the different modes with respect to the total $SERR$ is shown on a logarithmic scale. The logarithmic scale is chosen here to show that the ratios of mode II (yellow line) and III (blue line) are indeed negligible when compared to the one of mode I (red line), which confirms the dominant mode I separation in the DCB model.

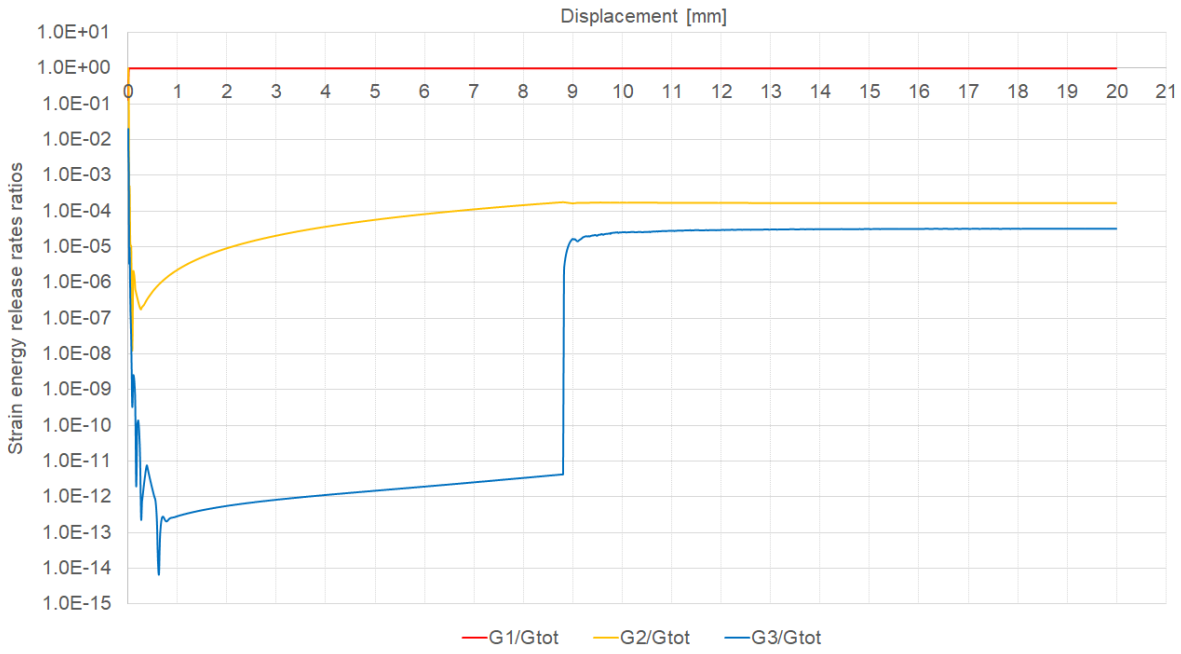

Figure 3.20: VCCT DCB 1 element per beam thickness energies

Some oscillations in the separation modes at the beginning of the analysis can also be seen in this figure, these tending to stabilize after a vertical displacement of $1mm$ is reached. While these are mostly visible in the *Mode II* and *Mode III* components, these are also occurring for the *Mode I* component, but it is not visible in the above graph due to the extreme difference in the order of magnitude of these components. Another aspect that can be seen from this figure is the small exchange between the *Mode II* and *Mode III* components once damage starts to propagate, the latter increasing by several order of magnitude, while still being negligible at ratios around $1E^{-5}$.

Similarly as for the previous approaches studied, the energy balance of the *VCCT DCB FE* model also ceased to be constant after damage started to propagate. In this case the model behaviour in terms of energies was more similar to the first numerical approach tried, the cohesive tied elements approach, shown in section 3.1.2. Here also the total work done *ALLWK* by the model was higher than the total internal energy *ALLIE* in the model after damage started to propagate. Furthermore, the energy balance *ETOTAL* appeared to have opposite expected sign as in its formulation the total work done is subtracted from the total internal energy, the former having a higher magnitude. Another awkward behaviour of the Abaqus *FEA* software used for this project was the missing *ALLCCDW* energy component when the *SERR* was requested, as well as the fact that requesting the *SERR* or not can have an influence on the outcome of the analysis.

Considering the excellent correlation between the numerical curves and the analytical one from figure 3.18, the erroneous behaviour of the *ETOTAL* energy component and the similarities seen between the energy outputs of this model with the previous *CZE* and *CZS* ones, no further comparisons in terms of energies for the *VCCT* approach are made in this section.

INCREASING THE MESH SEED IN THE VCCT DCB MODEL

Since the correlation with the experimental curve of the the numerical was excellent and as the previous *CSZ DCB* model using the cohesive surface based behaviour yielded satisfactory results for the desired mesh seed range of $2.5mm$, the mesh seed for the *VCCT DCB* model was increased straight to $2mm$ and then to $2.5mm$.

Unlike for the previous model, where the damage initiation value had to be changed for accurate results, here all the parameters were left identical as the ones initially used for the *VCCT DCB* model with a $0.5mm$ mesh seed. The load-displacement curves for the *VCCT DCB* model using a mesh seed of $2mm$ and $2.5mm$ are shown in figure 3.21.

As it can be seen from this figure, the correlation between the *VCCT DCB* models with the increased mesh seed and the analytical model regrading the propagation part of the load-displacement response is still very

good. These numerical propagation curves show increased coarseness with respect to the propagation curves shown in figure 3.18, where a $0.5mm$ mesh seed was used. However, this coarseness and the overall correlation of the propagation curve for this mesh seeds are significantly better than the ones of the previous cohesive surface based approach, shown in figure 3.17 for the $2.5mm$ mesh seed.

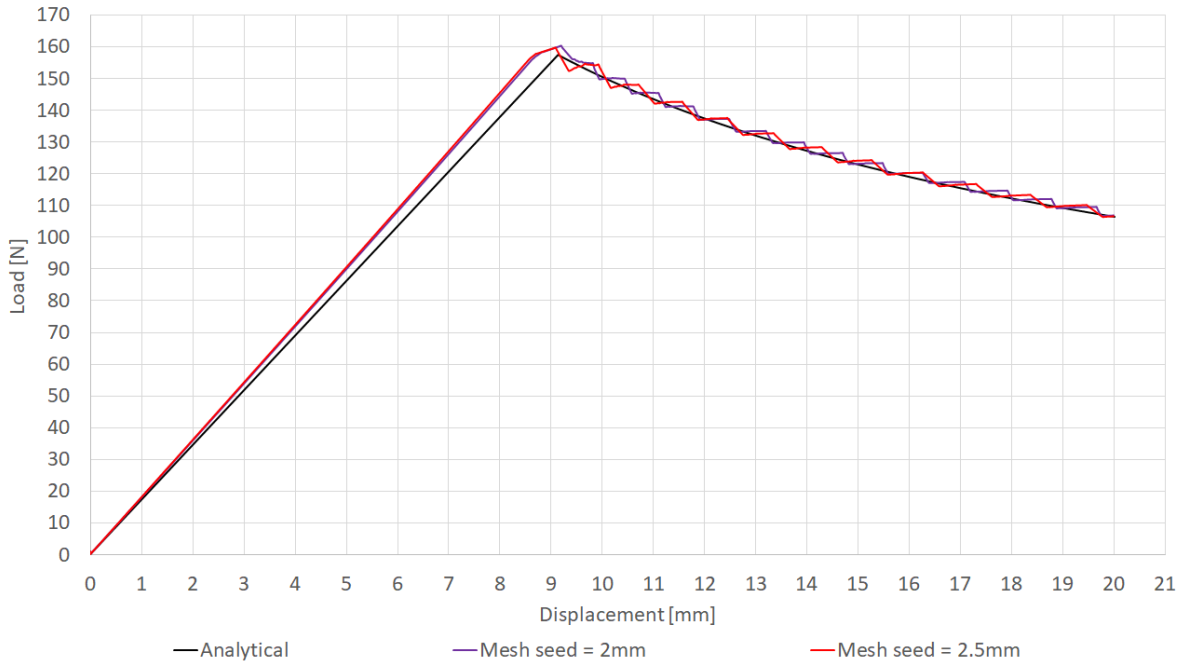

Figure 3.21: VCCT DCB 1 element per beam thickness 2mm and 2.5mm mesh seed load-displacement curves

Unlike the behaviour showed in the linear-elastic part of the previous approach, where a softening with respect to the analytical curve was observed, the opposite is observed for the $VCCT$ approach, namely a stiffening behaviour. Similar to the $CZS\ DCB$ models, here this stiffening behaviour is also likely to be the cause of the mis-match in the initiation point of these $VCCT\ DCB$ load-displacement curves.

In terms of convergence, the $DCB\ VCCT$ performs better than their DCB equivalent model using the previous CZS approach, as 1208 (1324 needed for the $CZS\ DCB$ with $T = 10MPa$) iterations were needed to complete the analysis for the $2mm$ mesh seed, with a running time of $17min$ ($13min$ needed for the $CZS\ DCB$ models). The same trend was noticed also for the models with a $2.5mm$ mesh, as the $VCCT$ model needed 1139 iterations (1327 needed for the $CZS\ DCB$ with $T = 10MPa$) to complete the analysis, with a running time of $10min$ ($7min$ needed for the $CZS\ DCB$ model). This difference in running times adds further support to the affirmation previously made, namely that the cohesive surface based behaviour tends to be faster than $VCCT$ for the studied DCB models. However, the $VCCT\ DCB$ models showed better convergence and more importantly, they showed a better correlation with the analytical model, without altering any of the material properties to unrealistic values.

VCCT DCB MODEL SENSITIVITY STUDY

In what comes next, same as for the previous approaches, a sensitivity study as also performed on the $VCCT\ DCB$ model, but here straight on the $2.5mm$ mesh seed mesh configuration. Similarly as in the previous models, the discretization method for the $VCCT\ DCB$ model was also varied from $surface-to-surface$ to $node-to-surface$ method. The load-displacement curves correlation between the analytical model and the $2.5mm$ mesh seed $VCCT\ DCB$ model using the $node-to-surface$ discretization can be seen in figure 3.22.

Comparing the red continuous curve from figure 3.22, representing the $2.5mm$ mesh seed $VCCT\ DCB$ load-displacement curve using the $node-to-surface$ discretization, with the red continuous curve from figure 3.21, representing the same model, but with $surface-to-surface$ discretization, one can see that the former no longer shows the significant stiffening behaviour in the linear-elastic part. The response in this

linear-elastic part is still stiffer than the one of the analytical model, but in this case this stiffening can be considered negligible. Furthermore, for this specific 2.5mm mesh seed, a small drop right after the initiation point was observed, the overall correlation with the analytical propagation curve being still very good. Since this significant load-drop was observed soon after the initiation point, the mesh seed was varied with $\pm 0.5mm$ to see if this is influenced by the particular mesh seed chosen.

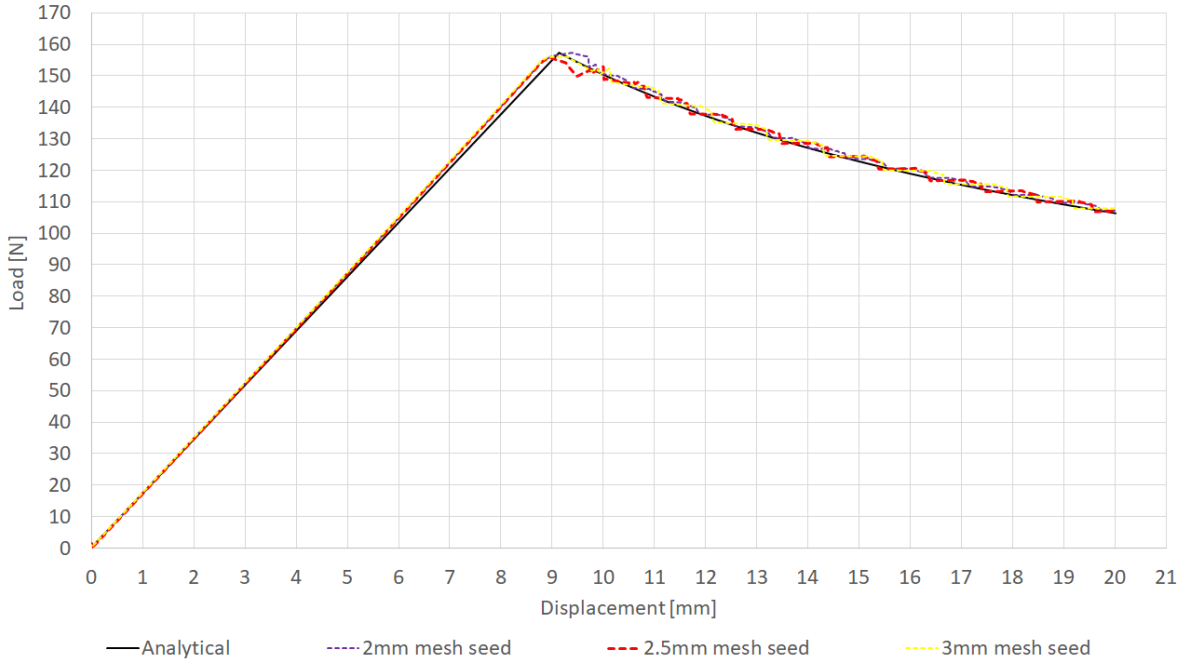

Figure 3.22: VCCT DCB 1 element per beam thickness 2mm, 2.5mm and 3mm mesh seed load-displacement curves with node-to-surface contact discretization

The load-displacement curves of the $2mm$ and $3mm$ mesh seed can be seen on the same figure 3.22 as the one of the initial 2.5mm mesh seed one. When comparing these curves it seems that indeed the load-displacement response in the propagation region soon after damage initiates seems to be significantly influenced by the mesh size. Using a $2mm$ mesh seed (purple dis-continuous line) led to a small overshoot of the propagation curve, a 2.5mm mesh seed led to a small undershoot of the propagation curve, while a mesh seed of $3mm$ (yellow dis-continuous line) described very well the analytical curve in all its regions.

In terms of convergence, the $node-to-surface$ discretization appeared to converge a bit harder, with 1180 iteration needed to complete the analysis, compared with the 1139 iterations needed to complete the analysis when the $surface-to-surface$ discretization was used for the same $2mm$ mesh seed configuration. However, the CPU time was better for the $node-to-surface$ discretization, as this model ran in approximately $8min$, compared to the $10min$ needed for the $surface-to-surface$ discretization. This contact discretization method also reduced the difference in CPU times between the $VCCT$ and CZS approach, as for the same mesh seed the latter needed roughly $8min$ to complete the analysis. For reference only, the trends seen with increasing mesh seed for the $VCCT\ DCB$ model was also confirmed when using a mesh seed of $3mm$, as the number of increments needed to complete the analysis further decreased to 1119, with a running time of approximately $7min$.

As the overall correlation between the $VCCT\ DCB$ model and the analytical model improved when using the $node-to-surface$ discretization, this discretization method is kept in the remaining parts of this section.

With the $node-to-surface$ discretization yielding better results for the $VCCT\ DCB$ model, contradicting somewhat the recommendation given in the Abaqus 2017 documentation [47], where the $surface-to-surface$ discretization was suggested as the more accurate approach, the sliding formulation of the contact interaction is also investigated. As a reminder, all the results presented so far were obtained using the $Small\ sliding$ formulation, with the $Finite\ sliding$ formulation also being available. Also, particularly for the $VCCT$ approach, the node release manner could be chosen between the $Step$ and $Ramp$, the latter being used so far in this report. In order to investigate these options as well, two $VCCT\ DCB$ model simulations

were run varying only the aforementioned options sliding and nodal release formulations with respect to the previously used settings. As a reminder, the previously used settings are $Small\ sliding$, $node-to-surface$ discretization and $Ramp$ nodal release manner for the $VCCT$ crack. The influence of the $Finite\ sliding$ formulation and of the $Step$ node release with respect to the $Small\ sliding$ formulation with $Ramp$ node release can be seen in figure 3.23 for the mesh seed of $2.5mm$ model.

Figure 3.23: VCCT DCB 1 element per beam thickness 'Finite' sliding and 'Step' node release influence

As expected, the difference between the sliding formulations is negligible, as at least in the DCB specimen no, or very limited sliding is expected. This is due to the loading applied, meant to give a dominant mode I opening. However, when mode II and III components are present, the contact formulation might give different results. The load-displacement curves of the two sliding formulation perfectly overlap, reason why the blue curve for $Finitesliding$ formulation was made dis-continuous. Also the differences in running times and CPU times between these two sliding formulations is negligible.

On the other hand, the difference between the $Ramp$ (red continuous line) and $Step$ (green continuous line) node release is insignificant prior damage propagation, while the difference after damage starts to propagate is high. As one can see from figure 3.23 above, in the linear-elastic region the two load-displacement curves perfectly overlap, showing a significant mis-match after the damage starts to propagate. Releasing the nodes in a $Step$ manner gives both a very coarse propagation curve with high and sharp oscillations and a underestimation of the analytical curve for damage propagation. This type of behaviour was expected based on the coarse mesh used, with each load drop and oscillation occurring exactly when a line of nodes along the specimen's width is released. The $Step$ node release manner also has a more pronounced mis-match in the initiation load, as in this case the nodes are released as soon as they fail, making it look as if damage occurred earlier than when the $Ramp$ nodal release manner was used. However, upon a closer look one can notice that, also for the $Ramp$ nodal release manner, the place of the first slope change is identical with the first load drop of the $Step$ nodal release manner. This suggests that the initiation points of these two nodal release types are very close, if not identical, the higher peak in the $Ramp$ case being given by the gradual node release.

In terms of convergence, using the $Ramp$ option seemed better, while in terms of CPU times both needed approximately $16min$ to run with the mention that the actual times can vary depending on other additional loads on the machine. Concluding, using the $Ramp$ nodal release manner could give more representative results when compared with the analytical response, with a better convergence, therefore also likely for a better CPU time than using the $Step$ nodal release manner.

The effect of the $VCCT$ fracture criterion tolerance was also studied by decreasing it gradually to 0.1, 0.01 and

0.001. For these different fracture criterion tolerances all the numerical load-displacement curves perfectly overlap, with the only differences being in their convergence, hence their CPU time as well. As expected, the trend with decreasing this tolerance value is to increase the number of iterations needed to complete the analysis, which also correlates with an increase in the CPU time. The number of iterations needed to complete the analysis went from 1180, for a tolerance of 0.2, to 1186, to 1268, to 1854 for the tolerance values of 0.1, 0.01 and 0.001 respectively. This also correlated with increased running times, with approximately $8min$ needed for a tolerance of 0.1 (roughly the same as for a tolerance of 0.2), while approximately $9min$ and $13min$ respectively was needed to complete the analyses with 0.01 and 0.001 tolerances respectively.

DAMAGE MODEL SELECTION SUMMARY

In the the first part of this section 3.1.1, two analytical models (the $ASTM\ DCB\ LEFM$ [38, 40] and the $ASTM\ MMB\ LEFM$ solutions [39, 40]) were compared with an experimental load-displacement curve of a DCB specimen. Out of these two analytical models, the MMB one was found to follow better the experimental curve, owing to its excellent match in terms of stiffness, which also led to a good correlation in terms of initiation point, as it can be seen in figure 3.5. At the end of this section 3.1.1 the $MMB\ ASTM\ LEFM$ solution was chosen as the reference for the studied numerical approaches, their accuracy being assessed by comparing the numerical load-displacement curves with the $ASTM\ MMB\ LEFM$ analytic load-displacement curve.

In the second part of this section 3.1.2, the possibility of using tied cohesive elements to the DCB beams was studied. This approach was chosen with the aim of using a finer mesh for the cohesive elements and a coarser mesh of the DCB beams, approach that would have also translated in the 1-stringer specimen and the 3-stringer panel. This approach was found to be unsuccessful, most likely due to an implementation error for the $DCB\ FE$ models studied. A high dependency of the propagation curve was found as a function of the penalty stiffness, which can be seen in figure 3.11. Owing to the erroneous behaviour of the propagation curve as a function of the penalty stiffness, the aforementioned CZE approach was abandoned, especially since the other two approaches immediately showed the expected load-displacement behaviour.

The first successful approach tried was using cohesive surface based behaviour, described in the third part of this section 3.1.3, which for an equivalent formulation to the tied cohesive elements one tried in section 3.1.2 immediately yielded a good correlation with the analytical load-displacement curve. For this approach, the previous erroneous influence of the penalty stiffness on the propagation part of the load-displacement seen in section 3.1.2 was no longer observed, as it can be seen in figure 3.15.

As this approach seemed to yield the expected results for the $0.5mm$ mesh seed, the mesh size was increased gradually to a $2.5mm$ mesh seed, which roughly corresponds to a mesh seed that would give an aspect ratio close to 1 for the 3-stinger panel, when 1 element per thickness is used. The effect described in literature with increased mesh size for cohesive elements for the same initiation values and the effect of lowering the initiation values for coarser meshes were also observed here [40, 45, 46] and was shown in figure 3.16 for the $1mm$ mesh seed and figure 3.17 for the $2.5mm$ mesh seed. These effects were the increased coarseness of the propagation curve, overshoot in the propagation curve, as well as increased softening in the linear-elastic part. For the $2.5mm$ mesh seed, a good correlation was obtained in the propagation part for the $T = 20MPa$ and $T = 10MPa$, with a significant mis-match in the linear-elastic part, owing to these very low initiation values.

The viscous energy dissipated $ALLCD$ for this $2.5mm$ mesh seed were also very low when compared with the internal energy $ALLIE$ and the energy outputs were also very similar with the ones for the $0.5mm$ mesh seed with $T = 90MPa$, proving that increasing the mesh seed and decreasing the initiation values did not adversely influence the model's overall behaviour in terms of energies.

The last approach tried, the $VCCT$ one described in section 3.1.4, was also successful. The $VCCT$ approach also allowed requesting $SERR$s outputs for each mode independently. These outputs were used to verify the ratio of each mode with respect to the total $SERR$, computed as the summation of the 3 independent modes. For the DCB specimen, the expected mode I dominant component was also found in the numerical model, as it can be seen in figure 3.20.

Despite the erroneous energy balance $ETOTAL$ computation, the $VCCT$ models were considered to work properly, owing to the excellent correlation of the $VCCT$ models with a $0.5mm$ mesh seed with the analytical MMB load-displacement curve.

As the previous CZS approach gave satisfactory results for mesh seeds up to $2.5mm$, the $VCCT\ DCB$ model was run directly $2mm$ and $2.5mm$ mesh seeds as well. These also gave a good correlation with respect to the analytical load-displacement curve, as it is shown in figure 3.21. In this figure it can be seen that the

linear-elastic part of the $VCCT\ DCB$ is significantly stiffer with respect to the analytical one, unlike for the previous CZS approach for the same mesh seed, where a softer response in this region was observed. In the propagation part of the curve, the $VCCT\ DCB$ model showed a better correlation with the analytical curve than the $CZS\ DCB$ model, as the coarseness of former was lower. This can be seen comparing figure 3.17 for the $CZS\ DCB$, with figure 3.21 for the $VCCT\ DCB$ model. Also in this section it was found that the $CZS\ DCB$ model tends to run faster than the $VCCT\ DCB$ model for the same mesh seed, provided that the initiation values of the former are decreased, such that a good correlation with the analytical model for the propagation curve is achieved.

With the $2.5mm$ mesh seed $VCCT\ DCB$ model also giving satisfactory results, a sensitivity study was carried also for the $VCCT\ DCB$ model using this mesh seed of $2.5mm$.

Changing the contact discretization from $surface-to-surface$ to $node-to-surface$ was found to significantly alleviate the stiffer response of the $VCCT\ DCB$ models in the linear-elastic part the load-displacement curve. This aspect can be seen by comparing figure 3.21, where the $surface-to-surface$ contact discretization was used with mesh seeds of $2mm$ and $2.5mm$, with figure 3.22, where the $node-to-sturface$ contact discretization was used for the mesh seeds of $2mm$, $2.5mm$ and $3mm$. The additional models with $2mm$ and $3mm$ mesh seeds were ran since a small undershoot on the propagation curve was observed soon after damage started to propagate for the $2.5mm$ mesh seed, this behaviour being associated with the mesh size used. Since the $node-to-surface$ contact discretization alleviated the stiffer behaviour of the $VCCT\ DCB$ model with respect to the analytical solution in the linear-elastic part, this contact discretization was kept in the rest of sensitivity study.

Next, changing the contact sliding formulation from $Small\ sliding$ to $Finite\ sliding$ had no effect for the DCB specimen studied, these two contact sliding formulation giving identical results. Same was not the case when the nodal release mode was changed from $Ramp$ to $Step$. As it can be seen from figure 3.23, the propagation curve of the $VCCT\ DCB$ model with $Step$ nodal release manner was well below the analytical propagation curve and also far coarser than when a $Ramp$ nodal release manner was used. Abrupt oscillations in the reaction load were also found when the $Step$ nodal release manner was used, which corresponded to the release of an entire line of nodes along the specimen's width. This model also appeared to initiate slightly sooner than the model with $Ramp$ nodal release manner, but this aspect is only caused by this node release option. While the first change in the slope of the load-displacement curve occurs in both $Ramp$ and $Step$ cases at the same point, the gradual nodal force release of the former gives a smoother transition from the initial linear-elastic part to the propagation part of the DCB's load-displacement curve.

Last, for this $VCCT\ DCB$ model the tolerance of the $VCCT$ fracture criterion was decreased from 0.2, to 0.1, to 0.01 and last to 0.001. Decreasing this tolerance in the studied model appeared to have a significant impact in CPU time for tolerances lower than 0.1, with a minimal impact, if any, on the model's accuracy.

Concluding this damage model selection, it appears that the best suited damage model for describing mode I separation, based on the DCB specimen studied, is the $VCCT$ model. The $VCCT$ model with $node-to-surface$ discretization correlated very well with the MMB analytical load-displacement curve, therefore also with the experimental load displacement curve. This means that it also correlate well with the experimental curve, as the the MMB analytical curve correlated well with the experimental one, correlation shown in figure 3.5.

While the $CZS\ DCB$ models also gave an excellent correlation with the analytical model for a $0.5mm$ mesh seed, the damage model gave poorer results then the $VCCT\ DCB$ models for the desired mesh seed in the $2.5mm$ range. The initial excellent correlation was due to the fact that for that case the model fell under its applicability range when the mesh seed of $0.5mm$ was used together with the measured fracture toughness and the assumed damage initiation value. However, the combination of fracture toughness, damage initiation values and more importantly desired mesh size around $2.5mm$ meant that the cohesive damage model was no longer in its applicability range. Lowering the damage initiation values as an engineering artifact proved to alleviate this issue, but the accuracy of these models was still poorer than when the $VCCT$ damage model was used. Furthermore, significantly lowering the damage initiation values, from $90MPa$ to $20MPa$ and $10MPa$, needed to achieve satisfactory results for the $CZS\ DCB$ model with a $2.5mm$ seed meant that the damage model is not as robust as the $VCCT$ one, the latter working for all the tried mesh seeds with the experimentally measured material parameters. This means the $VCCT$ damage model is more robust and is also less likely to need tuning when used at different scale levels, as the model gave good accuracy for all the tried mesh seeds tried for the DCB model.

While implementation errors hindered the study using the CZE approach, as this damage model is based on

the same principles as the CZS one, this model would have been likely affected by the same mesh restriction. Even as different mesh seeds could have been used between the beams and the filler, the difference between the working $0.5mm$ mesh seed for the CZS model to the desired one of $2.5mm$ would have gave similar mesh size restriction for the CZE approach.

Since for the $VCCT$ model performed well for all the mesh seeds tried without any artificial adjustments of the material parameters, the $VCCT$ damage model with $node-to-surface$ discretization, 1E-6 viscosity parameter to stabilize the damage, $Small\ sliding$ formulation and $Ramp$ nodal release manner was further used for the 1-stringer specimen and the 3-stringer panel. As the tolerance seemed to influence more the CPU time than the accuracy of the results, this tolerance value for the $VCCT$ fracture criterion is decreased to 0.1 for the following models. This was done as the same, or slightly better, accuracy is expected of this small decrease in tolerance, for a minor (if any) increase in CPU time.

3.2 DAMAGE MODEL VALIDATION

With the $VCCT$ damage model considered to be best suited from the numerical approaches previously investigated in this chapter, this damage model was applied to an already correlated FE model of the 1-stringer specimen.

Here by 'already correlated' it is meant that an FE model for the 1-stringer specimen already existed and it was adjusted such that it correlated well with the experimental data. With that being said, here the aim is to check the performance of the damage model selected, against the old damage model used in this 1-stringer specimen FE model. The old damage model used for the correlated FE model was the cohesive contact based one studied in section 3.1.3 using the DCB specimen. Similarly as for the DCB models studied, also in the FE model of the 1-stringer specimen using this damage model the initiation values were altered. Furthermore, the fracture toughness was also altered in this model to reach a good correlation with the experimental data.

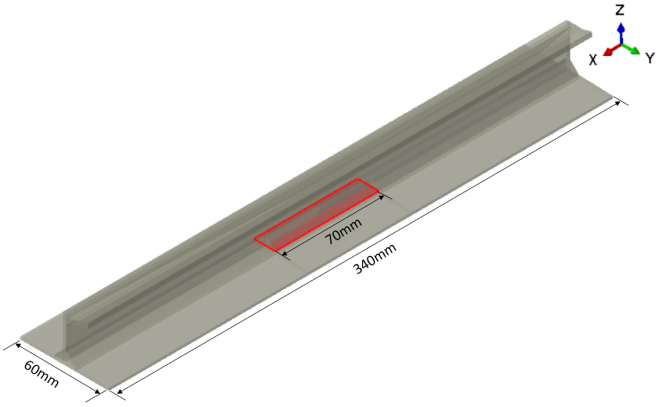

Figure 3.24: 1-stringer specimen's length, width and damage size

3.2.1 1-STRINGER SPECIMEN'S FE MODEL GEOMETRY AND MATERIAL DATA

The geometry and the assigned sections of this 1-stringer specimen's FE model can be seen in figures 3.24 and 3.25. The nature of the damage in this 1-stringer specimen is identical with the one from section 4.1 for the 3-stringer panel, being a de-bond between at the skin-filler inter-phase, with a length of $70mm$.

The layups associated with the sections shown in figure 3.25 can be found in table 3.4, for which the material parameters from table 3.5 were used. Here the $APC\ C/PEKK$ lamina properties are identical with the ones used for the DCB specimen 3.1, except the Poisson ratio which is now 0.3, instead of 0.319. The staking sequences of the skin and cap laminates are in the positive sense of the Z axis, while the staking sequence of the web laminate on the negative sens of

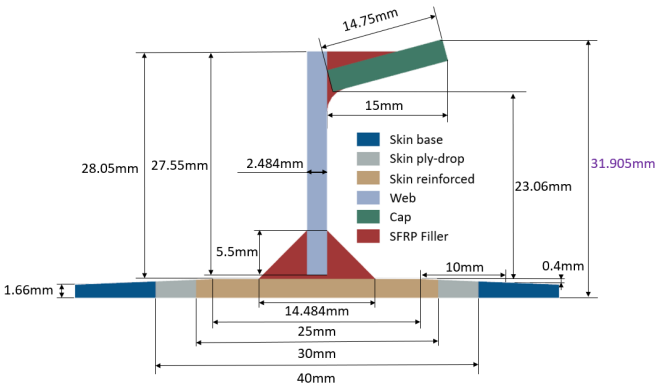

Figure 3.25: 1-stringer specimen stringer geometry and sections (1-stringer specimen's height shown in purple)

the Y axis.

The 0 plies shown in red in table 3.4 are due to the different material used. The main purpose of these plies placed below the stringers was not necessarily structural, as these glass plies main purpose was to alleviate the tendency of the skin to wrap around the stringer during the manufacturing process. This wrapping tendency comes from the higher CTE of the butt-joint filler with respect to the APC laminate, which upon cooling compresses the upper part of the skin, inducing a local curvature of the skin around the stringer. These roughly $0.1mm$ thick glass plies were cut in $10mm$ width strips, placed below the stringer and co-consolidated at the same time with the skin.

Another mention that has to be made about the 1-stringer specimen's FE model geometry is its modified skin-web butt-joint geometry with respect to the nominal one. As it can be seen from figure 3.25, the skin-web filler is triangularly shaped and has a 2x5.5mm and a $14.484mm$ overlap length with the web and skin respectively. While the overlap lengths are the nominal one, same is not the case of the triangular shape of the butt-joint. In reality the butt-joint has a $6mm$ radius, its shape being similar with the previous ones shown (e.g. 2.2). A more detailed description of the 1-stringer specimen can be found in [50].

Part	Layup	Material
Cap	$[45/90\text{-}45/0/45/0/\text{-}45/0/0/90]_S$	APC
Web	[45/90/-45/0/45/0/-45/0/45/-45/0/-45/0/45/0/-45/90/45]	APC
Skin base	$[45/\text{-}45/0/90/45/\text{-}45]_S$	APC
Skin ply-drop	$0/0/[45/\text{-}45/0/90/45/\text{-}45]_S$	HexForce 108 [51]/KEPSTAN 7002[52] and APC
Skin reinforced	$0/0/0/0/[45/\text{-}45/0/90/45/\text{-}45]_S$	HexForce 108 /KEPSTAN 7002 and APC
Fillers	-	C/PEKK SFRP

Table 3.4: Materials used and laminate layups of the 1-stringer specimen [50]

		Density	Poisson ratios			Stiffnesses [GPa]					
Material	Type	$\rho\ [g/cm^3]$	μ_{12}	μ_{13}	μ_{23}	E_1	E_2	E_3	G_{12}	G_{13}	G_{23}
APC (PEKK FC UD)	Lamina	1.56	0.3	-	-	126.1	11.2	-	5.46	5.46	3.32
HexForce 108/KEPSTAN 7002	Lamina	2.2	0.3	-	-	25	25	-	3	3	2.7
C/PEKK SFRP filler	Anisotropic	1.56	0.42	0.42	0.51	13.252	6.579	6.579	2.389	2.389	2.145

Table 3.5: Material properties used in the 1-stringer specimen FE model [36]

3.2.2 FOKKER 1-STRINGER SPECIMEN FE MODEL

This FE model was built by extruding the skin, web and laminates in one part, while the fillers were built in other parts and positioned together in the Assembly module of Abaqus. The elements used for the laminates are SC8R continuum shell elements with $Enhanced$ hourglass control, while for the filler C3D8R 8-node brick elements with reduced integration were used. The cap-web filler was tied to the cap and web laminates using default tie constrains and discretization. THE slave initial position was adjusted, the slave in both cases being the filler surfaces. The same type of tie was also used to join the web with the skin-web filler, while for the connection between the skin and the skin-web filler a contact interaction was defined, together with a damage model. This interaction was defined between the bonded skin and filler surfaces, with $Small\ sliding$ contact formulation and with a $node-to-surface$ discretization method. Same as for the aforementioned tie constrains, the filler slave surface was adjusted to remove the potential over-closure of the two contact surfaces. The contact property used default contact enforcement method for the traction separation behaviour, the node sets being into contact being specified as any slave nodes experiencing initial contact. For the damage model assigned to this contact interaction, the quadratic traction criterion was used, with highly decreased initiation values of $T = 7.2MPa$. The damage evolution was energy based, linear softening, independent mode behaviour, with a decreased fracture toughness of $G = 0.681kJ/m^2$ (for all there modes) and without any damage stabilization.

For this 1-stringer model, a $0.5mm$ mesh seed was used for the skin and skin-web filler along the length, such that issues would not be encountered with the cohesive damage model due to an insufficient number of elements in the fracture process zone. The mesh configuration of the 1-stringer specimen along its length and of its stringer can be seen in figures 3.26 and 3.27.

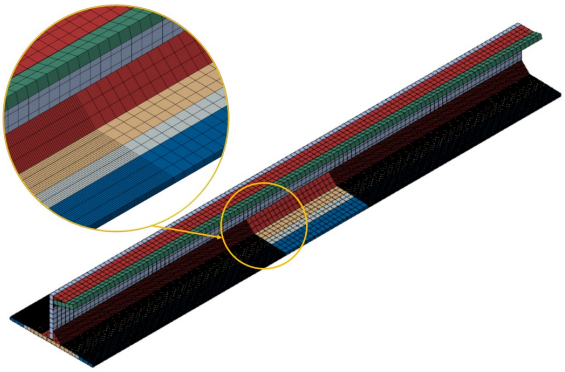

Figure 3.26: 1-stringer specimen mesh configuration along its length

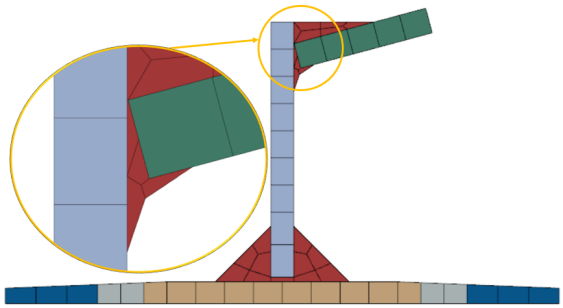

Figure 3.27: 1-stringer specimen cross-section mesh

Figure 3.26 shows the mesh of the 1-stringer specimen, with a detail on the transition between the mesh associated with the damage model, having fine mesh seed of $0.5mm$ along the specimen's length and the one associated with the de-bond, with a coarse mesh seed of $3mm$ along the length. One important mention is that the coarse mesh is not over a length of $70mm$ corresponding to the de-bond length, but over a length of $60mm$. This is most likely due to a sensitivity of the model to different de-bond lengths being also studied using this mesh configuration. In figure 3.27, the mesh configuration of the 1-stringer specimen cross section can be seen, with a detail on the web-cap filler. Similarly with the 3-stringer panel case, see figure 4.4, there is a small resin gap between the cap and the web, in the 1-stringer specimen's case this gap being slightly larger.

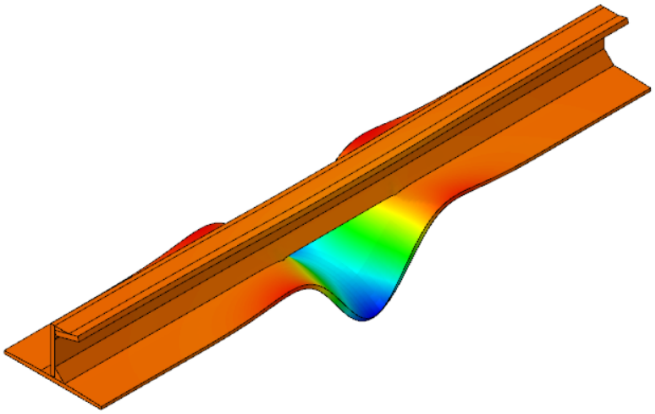

Figure 3.28: 1-stringer specimen imperfection

The loading and BC were applied to reference points at the ends of the specimen that had coupled translations with the specimen's end surfaces. The analysis type was $Static\ general$, with non-linear geometry On, without any stabilization and over a time period of 1. The incrementation settings were 0.01 for the initial and maximum increment, with 100 increments allowed and with a minimum increment of 1E-10. The total number of attempts was also increased to 35, in order to prevent the analysis to crash before attempting the smallest increment allowed. To load the specimen, clamped BC were applied in the initial step for one edge of the specimen, while the other end was only allowed to translate along its length. The load was applied in the loading step as a $3.3mm$ displacement BC at the end with allowed translation BC applied in the initial step.

To achieve a good correlation, an imperfection to resemble the measured 1-stringer's skin shape was introduced in this model. This imperfection was based on an eigenvalue analysis and its main feature is the skin below the de-bond deflecting away from the stringer. This imperfection shape is shown in figure 3.28. Important to mention here is that the eigenvalue used was the first one, with a minus sign and an amplitude of 0.175. The minus sign was used since contact cannot be defined for an eigenvalue in Abaqus, the resulted 'positive' shape being with the skin deflecting towards the stringer and overlapping with it. Therefore, the minus sign was applied for the aforementioned 0.175 amplitude, resulting in an imperfection shape as the one shown in figure 3.28.

FOKKER 1-STRINGER SPECIMEN FE MODEL RESULTS

As the aforementioned model was built and run within Fokker in Abaqus 6.13 (2013 version) and since this thesis the Abaqus 2017 is used, the load-displacement using both the 6.13 and the Abaqus 2017 versions are

shown in figure 3.29, together with one of the experimental curves of the 1-stringer specimen. Also in this figure, the de-bond lengths before unstable de-bond growth occurred and at the last increment are shown for the models ran.

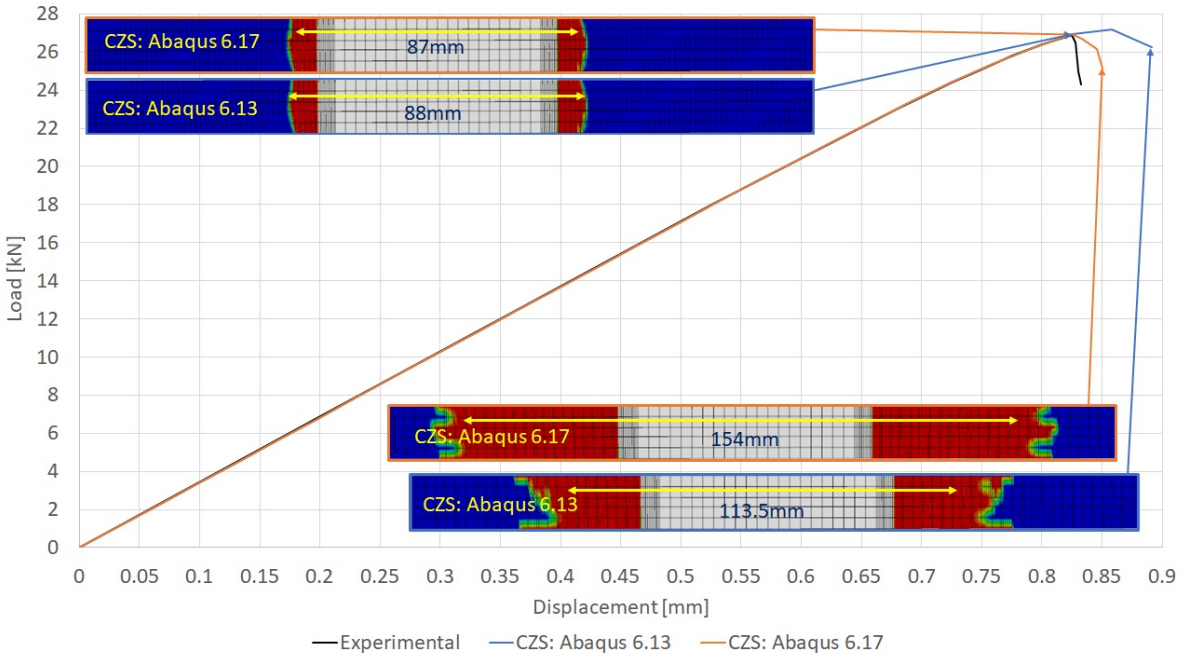

Figure 3.29: 1-stringer specimen Abaqus 6.13 and 2017 version FE models correlation with the experimental load-displacement curve

In the above figure, the experimental failure load is 26.8kN, while in the other specimen (only two specimens tested in quasi-static compression) the failure load was 27.7kN. Both the 6.13 and the 2017 Abaqus versions give an excellent correlation regarding the stiffness of the 1-stringer specimen and a very good correlation in what concerns its failure load, especially the 2017 version. Moreover, both the 6.13 and the 2017 Abaqus versions show softer collapse than the experimental curve, reason why the mis-match between the experimental collapse displacement and the numerical ones is more significant than the one in failure load. In what concerns the collapse, the newer Abaqus 2017 version captures better the experimental one, as the load drop at collapse is more pronounced. In terms of de-bond growth, the CZS model showed unstable de-bond growth after a de-bond length of 88mm, at a load of approximately 27kN, which ultimately led to collapse in the FE models. In the experimental tests however, the unstable de-bond growth occurred in a spur, after which the test was stopped and the specimen was considered failed. This unstable de-bond growth led to a total visible de-bond length over 135mm, the stringer still being attached to the skin [53].

For these analyses unstable de-bond growth occurs at the same location on the load-displacement curve, having roughly the same maximum de-bond length as well. The difference here between the 6.13 and 2017 Abaqus versions load-displacement responses appears to be given by the way the de-bond grows in the unstable region, with the 2017 version showing a sooner collapse, with a larger maximum de-bond length as well.

Concerning the de-bond lengths at the last increment shown in figure 3.29, these values were measured taking into consideration only the regions in which all the nodes along the specimen's width were failed. Otherwise, if the maximum de-bond length would have been considered, these distances would have been 139mm and 174mm for the 6.13 and 6.17 Abaqus versions respectively. The 2017 Abaqus version gives a greater de-bond length at failure than the 6.13 one regardless of the slightly lower collapse load and also a significantly lower failure displacement.

In terms of energies, these models showed the expected behaviour, the energy balance $ETOTAL$ being constant before the de-bond started to propagate in an unstable-manner. Here the total internal energy component $ALLIE$ and the energy associated with the total work done by the model $ALLWK$ diverged after the load drop, which marks the beginning point of the unstable de-bond growth. After unstable de-bond growth

occurred, the energy associated with the contact constraint discontinuity work $ALLCCDW$ also increased rapidly, which gave the inconstant energy balance $ETOTAL$ after this point.

Important to mention here is that this model appears to behave correctly when looking at the energy balance, as the $ETOTAL$ has a constant value, close to 0, right until the unstable de-bond growth occurs. Interestingly enough, this energy balance was not constant for the previous, simpler, $DCB\ CSZ$ models from section 3.1.3, the energy balance ceasing to be constant as soon as damage started to propagate. As for the 1-stringer specimen this only occurred when unstable de-bond growth occurred, while for the DCB models studied it occurred during the stable de-bond growth.

THE INFLUENCE OF ALTERING THE FRACTURE TOUGHNESS AT DIFFERENT SCALES-DCB CASE

When comparing the fracture toughness value of $G = 0.681 kJ/m^2$ used in the 1 stringer specimen's FE model with the measured ones from table 3.2, one can notice that this is roughly 2 times lower than the one for mode I and more than 3 times lower than the ones for mode II and III. While lowering the initiation values for cohesive damage models is a common engineering artifact, same is not be the case for the fracture toughness, as this governs the de-bond propagation. Altering this value is more risky, as it directly influences the de-bond propagation and it can have different effects depending on the FE model studied. However, this correlation was made after the experimental test was conducted and it was chosen with the main aim to have a model that correlates well for this mesh size with the experimental test. As an example on how this propagation value can influence a FE model behaviour, the $CZS\ DCB$ model with a mesh seed of $2.5mm$ and initiation values of $T = 10MPa$ and the $VCCT\ DCB$ model were run with the aforementioned lower fracture toughness. The results of these DCB models were compared with their results using the measured fracture toughness and with the analytical load-displacement response and shown in figure 3.30 below.

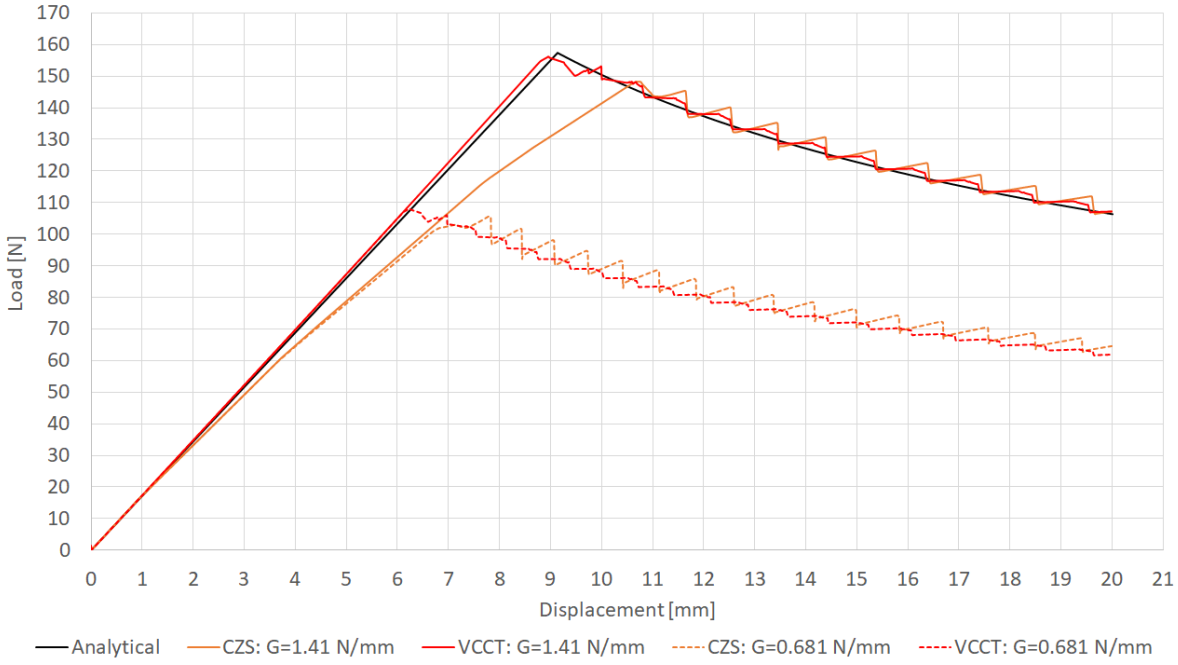

Figure 3.30: 2.5mm mesh seed CZS and VCCT DCB models fracture toughness influence

In the above figure, the red continuous line is the same one as the red dis-continuous line from figure 3.22, while the orange continuous line is the same as the one shown in figure 3.17 for the $T = 10MPa$ initiation values. These continuous lines have the fracture toughness equal to the allowables shown in table 3.2, while the dashed lines represent the same models, but now with the decreased fracture toughness to the 0.681 kJ/m^2 value used previously for the 1-stringer model. As it can be seen from the above figure, the load-displacement response of the DCB models with the adjusted fracture toughness behave significantly different than their corresponding models with the measured fracture toughness. As expected, there is a negligible difference in the initial linear-elastic response, the major difference being in the propagation part of these curves, which for the adjusted fracture toughness is significantly lower. This shows that the used fracture

toughness was chosen such that the 1-stringer FE model would correlate well with the experimental test, this value being far to low to yield a good correlation with the experimental DCB test. As for thesis thesis project the building block approach is used, this adjusted $0.681 kJ/m^2$ fracture toughness was changed to the measured fracture toughness allowables for the $VCCT$ skin-stiffener separation damage model.

FOKKER 1-STRINGER VCCT DAMAGE MODEL IMPLEMENTATION RESULTS

With the same VCCT damage model as described in section 3.1.4 applied to the existent 1-stringer FE model, the model was ran again, with the initial allowed increment and maximum allowed increment changed from 0.1 to 0.01. Also, two further simulation were run with changed analysis type from $Static\ General$ to $Quasi-static\ Dynamic\ implicit$, one with unstable de-bond growth not allowed, one with unstable de-bond growth allowed. The unstable crack growth option was left default, which means that the $f^u_{tol} = \infty$ in the fracture criterion shown in equation 2.2 was 'infinite', meaning that multiple nodes can be released for the same increment until the fracture criterion is no longer satisfied. The load-displacement behaviour of these simulations are shown in figure 3.31.

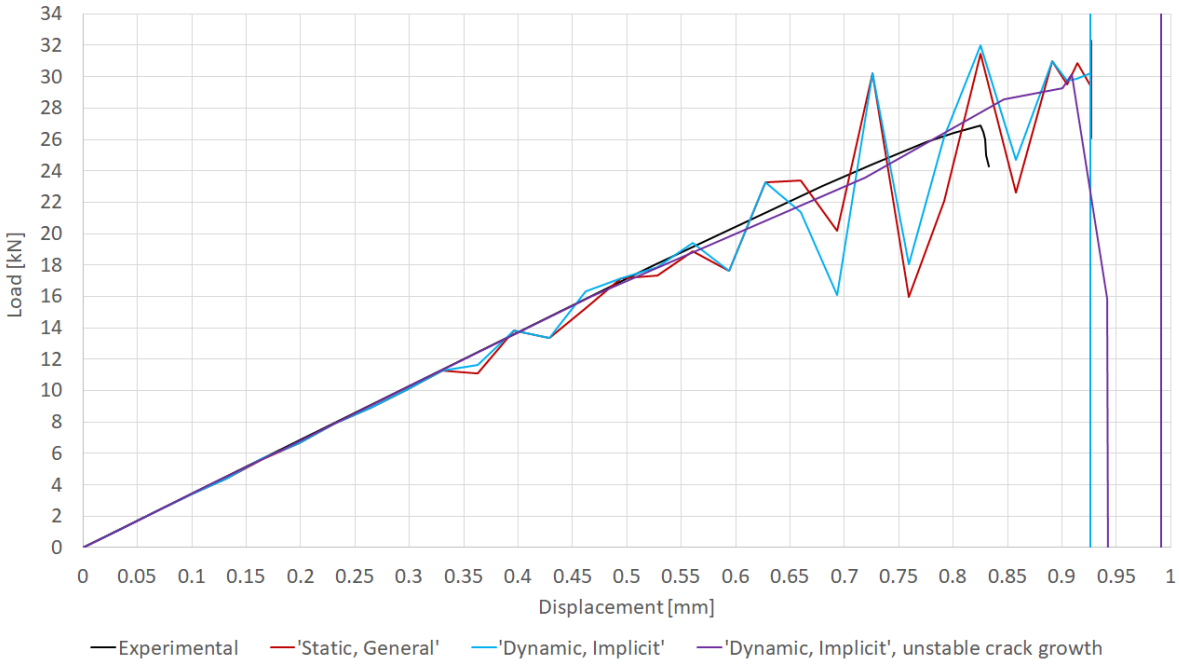

Figure 3.31: 1-stringer model with VCCT damage model load-displacement response

In this figure it can be seen that initially the stiffness is correctly captured, after which severe oscillations occur for the analyses without unstable crack growth. Also, for these analyses small oscillations can also be seen in this region where the initial stiffness is accurately captured by the model. Specifying unstable crack growth seemed to delay the oscillations, as well as to allow a greater displacement for which the analysis aborts. Regardless, the models ran definitely did not work as expected.

It was later found out that these oscillations originated from a few heavily distorted elements near the reference point $RP1$. This reference point was coupled with the 1-stringer specimen's end on which the displacement-based load is applied, reference point from which the reaction force was requested. The heavily distorted elements can be seen in figure 3.32. On the other end of the model, where no distortion was observed in the elements, the reaction load was smooth. The load-displacement response using the reaction force output from the other end, using the $RP2$ reference point of the model, are shown in figure 3.33, together with the de-bond lengths at collapse. In this figure the reaction load was used with its absolute

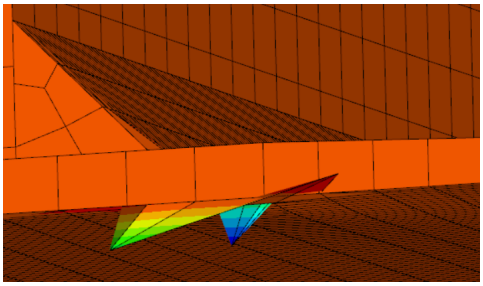

Figure 3.32: Mesh distortion near RP1

value, its sign in the model being negative.

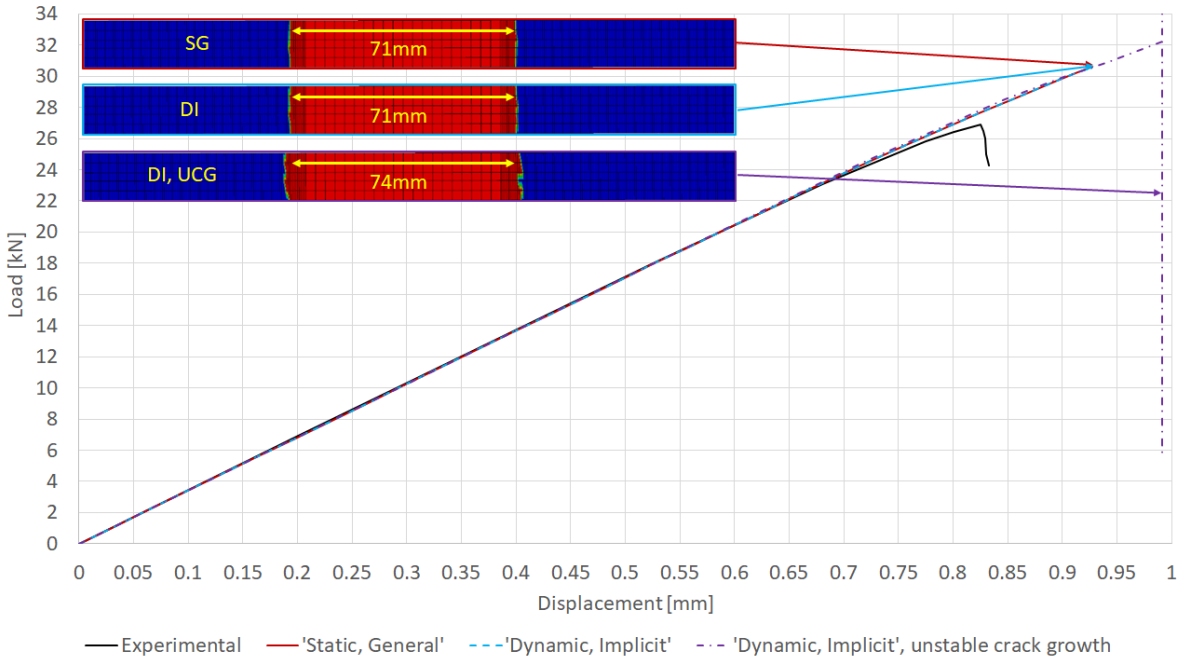

Figure 3.33: 1-stringer model with VCCT damage model load-displacement response, using the 'RP2' reaction force and de-bond length at collapse

As it can be seen from this figure, now the correlation in stiffness is excellent up to a load around $25kN$, after which the softening of the experimental curve becomes significant. The load-displacement response of the static and dynamic analyses perfectly overlap for the same incrementation settings and without unstable crack growth specified. All three numerical analyses overshoot the experimental final failure load of roughly $27kN$. The dynamic one using unstable de-bond growth has the higher overshoot, with a failure load of roughly $32.3kN$, while the failure load of the other two is at roughly $30.9kN$. Regarding the de-bond length at the end of these analyses, one can notice that when unstable de-bond growth is not allowed, the analysis aborts as soon as de-bond growth occurs, with a maximum de-bond length of $71mm$, compared to the initial one of $70mm$. When unstable de-bond growth is allowed, a higher final de-bond length is reached, with a maximum de-bond length of $74mm$. However, the model still seems to behave unrealistically, as the analysis still crashes and as the de-bond profile shows an unexpected feature. This unexpected feature is clearly visible on the right de-bond growth front, where a nonuniform de-bond growth front can be seen.

To alleviate this issue, the mesh structure of the skin cross-section was adjusted such it had matching nodes with the skin-web filler. This adjusted skin cross-section mesh can be seen in figure 3.34. Using this mesh, another buckling analysis was conducted to obtain the desired imperfection for this mesh configuration. This buckling analysis yielded the same first buckling shape, also for a similar eigenvalue: 0.24009, compared to the initial 0.24097 one obtained with 6.13 version of Abaqus. Furthermore, to ensure that the shapes imposed on the two analyses are comparable in magnitude, for the same 0.175 amplitude the maximum out-of-plane skin displacement below the stringer was checked for these two mesh configurations, the differences being negligible.

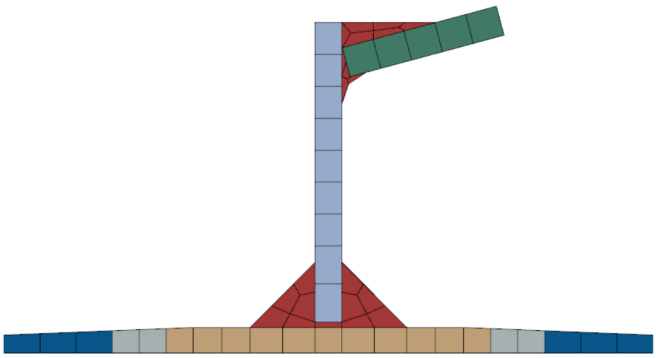

Figure 3.34: 1-stringer specimen adjusted skin cross-section mesh

With this adjusted mesh, the model with a $Quasi-static\ Dynamic\ Implicit$ procedure and unstable de-bond growth was ran again. Its load-displacement response and de-bond lengths at collapse are shown in figure 3.35. Since adjusting the mesh led to a complete analysis, the shown de-bond lengths are before and after the point where a major stiffness drop and a change in the de-bond profile was observed. In this figure, it can be seen that the change in the skin mesh had a negligible effect in the initial stiffness of the 1-stringer specimen, as the two numerical load-displacement curves perfectly overlap prior to the failure of the model with the old mesh.

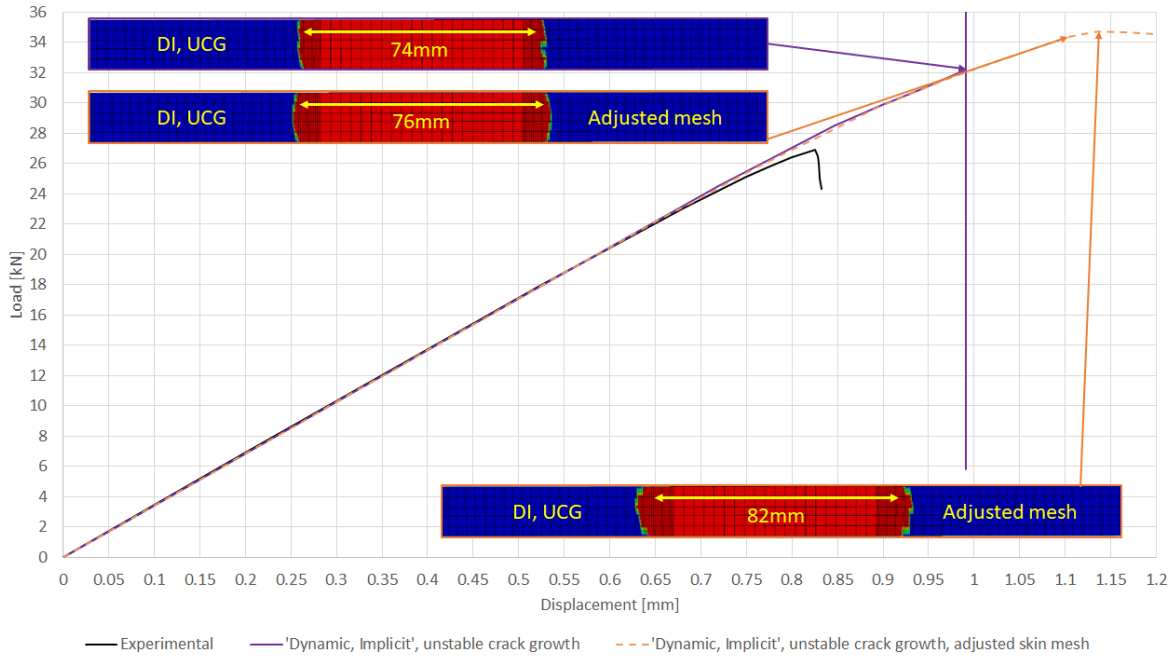

Figure 3.35: 1-stringer model old mesh vs adjusted mesh load-displacement and de-bond length at collapse comparison

For the adjusted mesh configuration, as the analysis does not crash before completion and also the de-bond continues to grow until the end of it. This behaviour might not be realistic, as failure could occur as soon as a drop in load due to unstable de-bond growth occurs. This is due to the fact that the growth of the de-bond could induce other failure modes like material failure, induced by the skin buckling away from the stringer. Other failure modes that could occur as the de-bond grows are stringer related, as this would also buckle locally (the cap flange), or globally, which could lead to crippling in the cap, or web-cap filler failure. Therefore, the load-displacement curve of this model was only plotted up to a displacement of $1.2mm$, at which it can already be seen that the slope of this curve is negative. Regardless of the model now seemingly behaving better, there is still a significant overshoot in the failure load, this model showing failure at a load around $34.3kN$, compared with the roughly $27kN$ experimental one.

3.2.3 1-STRINGER SPECIMEN FE MODEL EVOLUTION

With the $VCCT$ model now running well for a mesh size far smaller than the maximum mesh size along the length tried for the DCB specimen described in section 3.1.4 ($0.5mm$ for the 1-stringer specimen compared with $3mm$ for the $VCCT\ DCB$ specimen), it was deemed that the approximation of the skin-web filler could be the mainly one causing the correlation mis-match. Aside from this skin-web filler approximation, the high aspect ratio of the SC8R continuum shell might also be a source of the mis-match, together with the reduced integration formulation of the C3D8R brick elements [54].

Starting from the skin-web filler approximation, the cross section area of the approximated filler is significantly larger than the real one. Also, in the way in which the filler was approximated, it provides a far stronger connection of the skin-web butt-joint. This is due to the fact that in a real-case scenario, a failure similar to the ones shown in figures 2.4 and 2.5 would be expected, as material failure would occur under a dominant mode I de-bond opening prior any de-bond in the thin filler edges. With this in mind, a new skin filler approx-

imation is proposed, such that the cross-section area of the skin-web filler is comparable with the nominal one. Also, in this new approximation the overlap distances of the skin-web filler with the skin and web laminates were kept relatively equal. This new approximation has a $3.5mm$ overlap with the skin on both sides of the web, for which the corresponding overlap length with the web for the desired cross-section area gave a length of $3.42mm$. The computation of the nominal skin-web filler cross-section area is shown in equations 3.17, together with the computation of the areas of the previous and novel skin-web filler approximations.

$$\begin{aligned} A_{skin-web\ filler\ nominal} &= 2[6mm \cdot 6mm - \tfrac{\pi}{4}(6mm)^2] + 2.484mm \cdot 0.5mm = 16.693mm^2 \\ A_{approximated\ skin-web\ filler\ old} &= 6mm \cdot 6mm + 2.484mm \cdot 0.5mm = 37.242mm^2 \\ A_{approximated\ skin-web\ filler\ new} &= (2 \cdot 3.5mm + 2.484mm)0.5mm + 2\tfrac{3.5mm \cdot 3.42mm}{2} = 16.712mm^2 \end{aligned} \tag{3.17}$$

As it can be seen from this cross-section areas, the previous one was more than 2 times larger than the nominal one, while the new skin-web filler approximation gave a comparable cross-section area as the nominal one. With this novel skin-web filler, a new FE model for the 1-stringer specimen was also built. In this new model, the tie constraints between the different parts were eliminated, the whole model being build in one part. This approach was chosen here in order to remove all the previous tie constraints, resulting in a more robust FE model. In order to assign the different layups and material section to this one part model, partitions were used to create cell sets for every distinct regions.

As eliminating the ties between the individual parts also eliminated the surfaces used to apply the $VCCT$ damage model, new surfaces had to be created. To create these surfaces a lateral, trapezoidal shaped, cut at the skin-filler inter-phase was done in the model. The trapezoidal shape was chosen for the cut since a rectangular lateral cut would have altered the mesh at the edges cut, as elements with the same size as the cut height would have been needed. With a trapezoidal shaped cut, the only change to the mesh at these edges would be that the first row of elements along the width are no longer perfectly rectangular. The cut length is $200mm$ (the 1-stringer specimen is $340mm$) and it was chosen to release some of the computational burden, since the specimen is expected to fail before a total de-bond length of $200mm$ is reached. Another benefit of this approach is that a mesh refinement can be done exclusively in this area designated to damage propagation. The cut height is negligible, at 5E-5mm, compared with the smallest filler thickness of $0.5mm$. This cut was done taking material from the skin-web filler and not from the skin, since the filler material is significantly weaker than the skin laminate. This further minimizes the influence of the already small thickness cut in the model. A figure with the highlighted cut and its length is shown in figure 3.36.

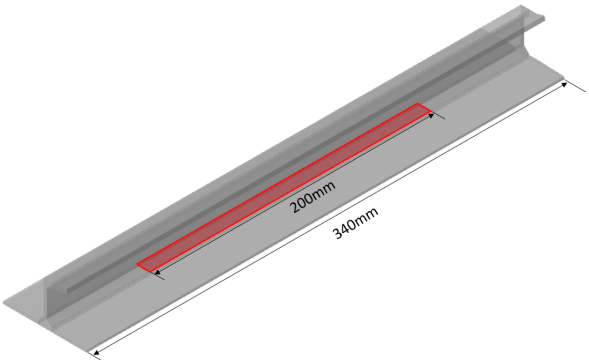

Figure 3.36: 1-stringer specimen one part model lateral cut

The other simplifications done to the model are the removed upper small filler gap between the cap and the web, highlighted in figure 3.27. Also, since that small $R3$ radius of the cap-web filler would have complicated the mesh regularity on that area, or limiting the mesh size, this radius was removed. This is considered to have a negligible impact in the model, since its area is roughly $1mm^2$, compared with the roughly $12mm^2$ one of the entire cap-web filler. Other changes made to the 1-stringer model consisted in changing mesh seed, which is now $2mm$ for the whole model. The hourglass control for the SC8R continuum shell elements is left to $Enhanced$ and to ensure a structured mesh, some filler elements were changed from C3D8R hexahedral elements to C3D6 wedge elements. The general mesh size and structure can be seen in figure 3.37, where an isometric view of the 1-stringer specimen is shown, together with the assigned material sections and layups according to table 4.1.

Figure 3.38 shows the 1-stringer specimen's cross-section mesh, with individual colors according to the element used. As mentioned earlier, the laminates, shown here in dark red colour, have SC8R continuum shell elements, while the fillers have solid brick elements of hexahedral (C3D8R, shown in grey), or wedge (C3D6 shown in green) shapes.

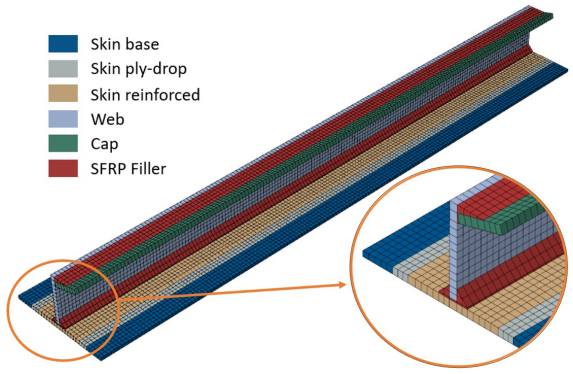

Figure 3.37: 1-stringer specimen mesh

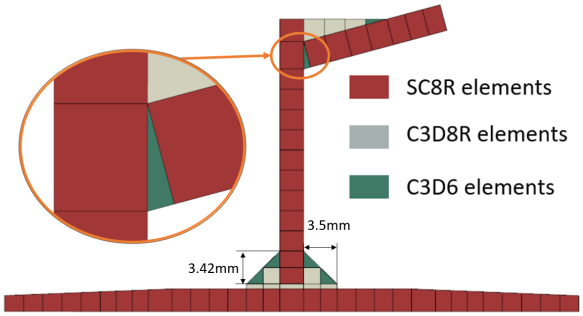

Figure 3.38: 1-stringer specimen stringer new geometry and element types

Comparing this figure 3.38 with the corresponding one for the previous cross-section mesh 3.27, it can be seen that the mesh in the fillers is better structured, especially when the cap-web filler is considered. This was possible due to the wedge elements used at the filler edges, which for this model with shared nodes allowed a uniform structured mesh in the adjacent laminates. In the above figure the skin-web and cap-web fillers simplifications can also be seen, now the cap upper left edge being in contact with the web and the skin-web filler having a slightly different configuration.

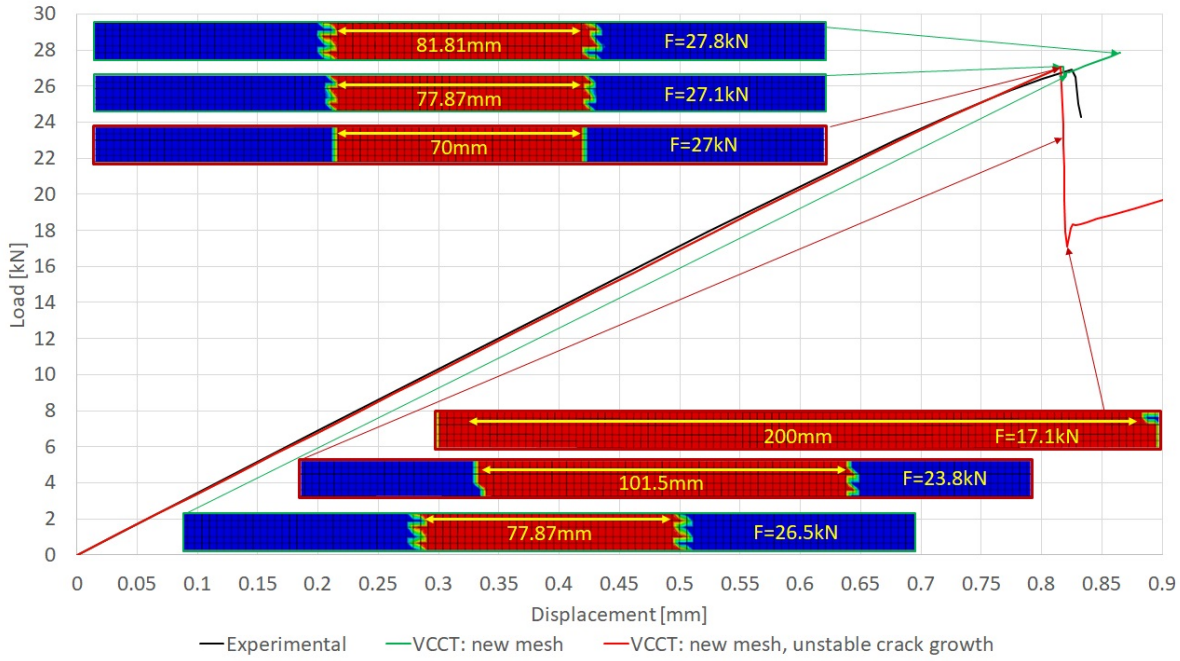

Figure 3.39: 1-stringer model new mesh load-displacement response and de-bond growth behaviour

1-STRINGER SPECIMEN FE MODEL EVOLUTION RESULTS

Similarly with the previous mesh adjustment, another buckling analysis was done to obtain the imperfection shape for this new mesh. Same as for the previous case, the same first buckling shape was obtained, but now with a small difference in the eigenvalue, now having a value of 0.23565, compared with the 0.24009 and the 0.24097 obtained for the old mesh and adjusted old mesh respectively. Due to this different eigenvalue, a small adjustment was also needed for the amplitude of the implemented imperfection, which was now 0.18, compared with the previous one of 0.175 (also with a minus sign). With this mesh configuration and with a comparable imperfection implemented, the model was ran again with both unstable crack growth allowed

and not allowed.

The load-displacement response using this mesh configuration for the aforementioned unstable crack growth options is shown in figure 3.39, together with their de-bond growth behaviour. In this figure the load-displacement response with unstable crack-growth not allowed is shown in green, while its correspondent de-bond pictures have light green edges and their locations on the load displacement curve are pointed with light green arrows. Similarly, the load-displacement response of the model with unstable crack-growth allowed is shown in red, with the de-bond pictures having dark red edges and their location on the curve being shown with dark red as well.

When comparing this figure with figures 3.33 and 3.35 for the previous mesh configurations, one can observe a small, decrease in initial stiffness. It can be seen from the above figure that the numerical curves are slightly under the experimental one, while for the previous models they overlap slightly better. This decrease in stiffness comes as a result of adjusting the fillers, especially the skin-web one, as the cross section area of this particular one was decreased by more than 50% with respect to the previous mesh configurations. However, as now the cross-section area of this filler is closer to the nominal one and as this difference in stiffness can be considered negligible, the model is still considered accurate in capturing the 1-stringer's global behaviour.

Looking at the curve where unstable de-bond growth was not allowed, one can see that there is a small mis-match in stiffness, the experimental 1-stringer specimen being slightly stiffer. For this numerical model the load drop occurs at a load of $27.1kN$ and the maximum de-bond length at this point is $77.87mm$. This load-drop point is comparable with the experimental failure point, having a roughly $+0.3kN$ mis-match in load ($\approx$+1.12 %) and a roughly $-0.01mm$ mis-match in displacement ($\approx$-1.21%). This mis-match is given by the model not capturing some initial stable de-bond growth, which led to some softening in the experimental load-displacement curve near the failure point. Immediately after the load drops to $26.5kN$, this model shows no de-bond growth associated with this load drop. After this load drop the de-bond grows only up a maximum length of $81.81mm$, after which the analysis crashes at a load of $27.8kN$.

When looking at the load-displacement curve where unstable crack-growth was allowed, the same mis-match in stiffness with respect to the experimental one can be observed. The load drop also occurs roughly at the same point, but in this case no de-bond growth was shown prior to this point and the de-bond continued to grow until the maximum allowed de-bond length of $200mm$ was reached.

Comparing the two unstable crack growth options, allowing the de-bond to grow unstable led to a more realistic behaviour and also gave a better correlation with the experimental load-displacement curve, its failure load also being in good agreement with the experimental one. However, when looking at the de-bonds patterns shown in figure 3.39, one can see that the de-bond edges show an unrealistic behaviour. The de-bond profile at the edges is highly rugged, the expected behaviour being closer to the parabolic one shown in figure 3.35 for the adjusted mesh.

Until now the filler elements used were C3D8R, these elements being known to have issues when accurately capturing the bending behaviour of a structure. With that in mind, the filler elements were changed to C3D8I, solid brick elements with incompatible modes, which are better suited to capture bending [54] than the C3D8R elements. Since the expected de-bond pattern was achieved with a $0.5mm$ longitudinal mesh seed, a simulation was also ran with this mesh configuration. The load-displacement curves of these two simulations, with unstable crack-growth allowed, are shown in figure 3.40.

In this figure the de-bond patterns at the maximum load and the load at which the de-bond reached its allowed limit are shown. As it can be seen comparing figure 3.40 with figure 3.39, for the same mesh configuration the load-displacement response is roughly the same, for the model with C3D8I elements the maximum load being slightly larger. However, now the de-bond pattern is no longer staggered like the one shown in figure 3.39, but straight. The expected parabolic shape was achieved in the simulation with $0.5mm$ longitudinal seed mesh refinement, which also led to a slightly better correlation. This slightly better correlation with the experiment came from the refined mesh, this model showing some stable de-bond growth before the maximum load was reached. This small de-bond growth also translated into a small softening of the load-displacement curve near collapse. These de-bond pattern changes showed that indeed the C3D8R filler elements were not displaying a realistic behaviour, with the C3D8I elements improving this aspect.

Regarding the global compressive behaviour, the difference in the load-displacement response of the 1-stringer specimen is negligible. Since the difference between the two mesh configurations with the C3D8I filler elements can also be considered negligible and as for the 3-stringer panel the $0.5mm$ longitudinal mesh seed would highly increase the computational load, in what follows the energy balance and the dominant separation mode of the $2mm$ mesh seed model are shown. Important to mention here is that there are no

significant differences neither in the energy balance, nor in the dominant separation mode between these two mesh configurations with C3D8I filler elements.

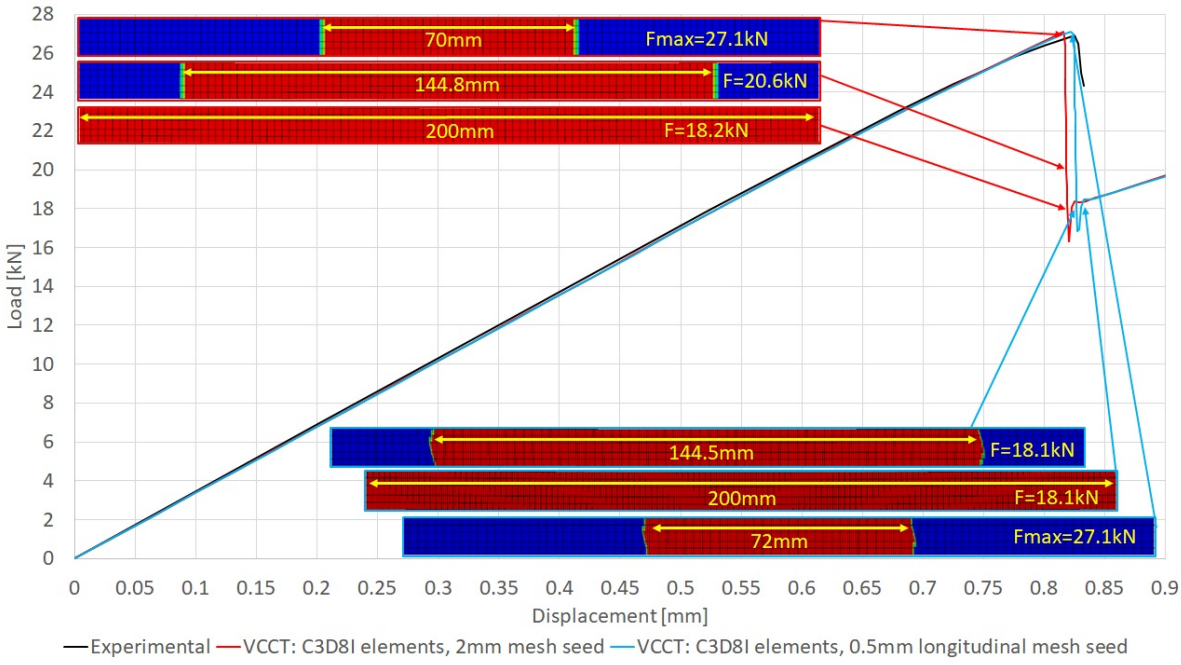

Figure 3.40: 1-stringer model C3D8I filler elements with 0.5 longitudinal mesh seed

In terms of energies, the 1-stringer model shows similar behaviour with the previous $DCB\ VCCT$ models. Also in the case of the 1-stringer specimen, the energy balance $ETOTAL$ ceases to be constant after damage started to propagate, as also the total internal energy component $ALLIE$ diverged from the total work component $ALLWK$ at this point. These two main components diverge as soon as damage initiates due to the total contact discontinuity work component $ALLCCDW$ ceasing to be 0, which is also similar with the CZS and $VCCT\ DCB$ models. Unlike for the DCB models two energy components, the $ALLDMD$ related to damage accumulation and the $ALLVD$ related to the damage viscous dissipation were missing, although the damage model used was identical. One significant difference between the 1-stringer model and the $VCCT\ DCB$ model is that the damage model is now specified between two different element types. Looking into the software's documentation there were no indications found that this caused the missing of the two energy components. Regardless, since studying the particularities of the the FEA tool used does not make the topic of the project, the model was left as is.

Similar as for the $DCB\ VCCT$ model, also for the 1-stringer model the $SERR$s were requested and the dominant separation mode was computed based on these. The separation modes ratios of the 1-stringer specimen are shown in figure 3.41 against the specimen's compressive displacement.

As it can be seen from this figure, the main loading mode is mode I, with the second component in magnitude being mode II. At the beginning of the analysis, mode I reaches its peak, at a displacement of $\approx 0.03mm$, at this point the loading being almost completely under mode I. Prior to this point, the mode I loading decreases, with the increase of both mode II and mode III loading. However, this is only the loading mode, not the actual separation, as the actual separation begun only around a displacement of $0.82mm$. As it can also be seen in the load-displacement response shown in figure 3.40, the $VCCT\ FE$ model of the 1-stringer specimen showed unstable de-bond growth. Looking now at figure 3.41, around this $0.82mm$ displacement there is a significant drop in the mode II component, which is balanced by a significant increase of the mode III component, together with a small increase in the mode I component. Then, as the de-bond continues to grow there is a significant drop in the mode I component, which is balanced by a significant increase in mode II component. After this change all components became constant, since the maximum de-bond distance allowed was reached. This significant change between modes I and II likely comes from the significant stiffness mis-match between the skin and the stringer, as the skin tends to deform more under the same applied compressive displacement. As the de-bond grows and the skin is allowed to deform more and more

independently of the stringer, there is also a change between the mode I and mode II component, the latter becoming more and more significant. A similar behaviour is also expected for the 3-stringer panel, as the mode I component is expected to decrease as the de-bond grows, favouring an increase in the mode II separation mode.

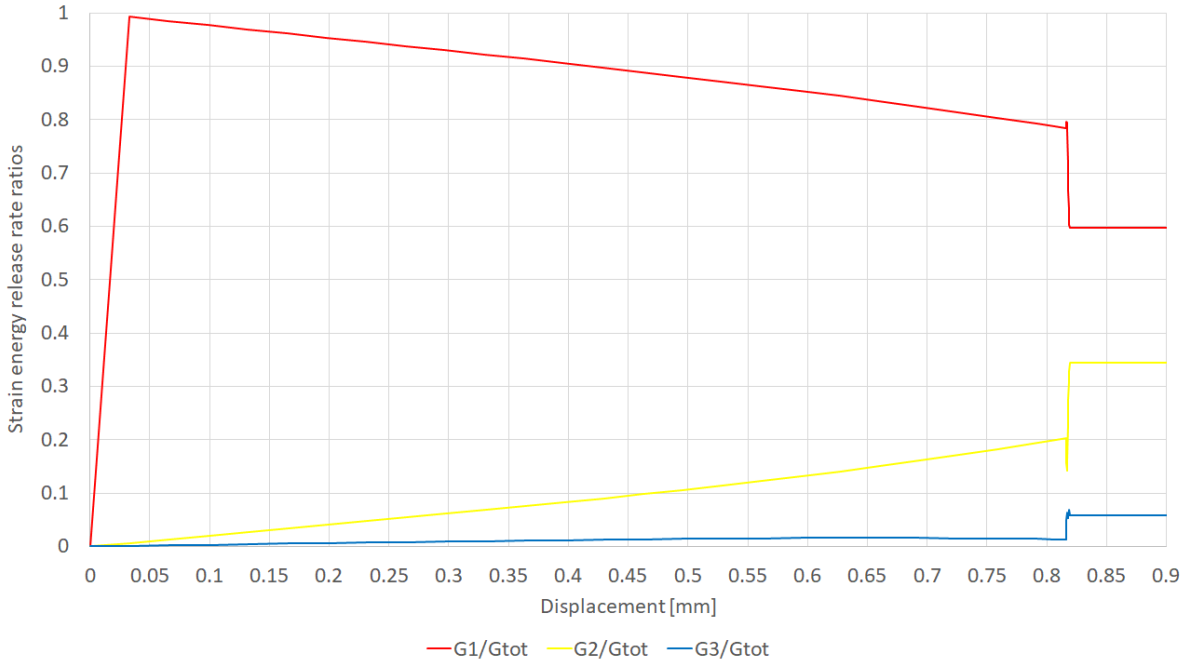

Figure 3.41: 1-stringer model separation mode ratios

3.2.4 1-STRINGER FE MODEL EVOLUTION AND RESULTS DISCUSSION

In the second section of this chapter, the $VCCT$ damage model used in the DCB specimen in the first section was used to model the compressive behaviour of a 1-stringer specimen with skin-stringer de-bond. For this 1-stringer specimen a FE model was already built within Fokker, using a cohesive surface based damage model with damage initiation values significantly lower than the real ones and with a fracture toughness roughly two times lower than the measured one. These lowered properties were found to be inconsistent with the building block approach used for this project, as the damage models which gave an initial good correlation with the experimental and analytical DCB specimen load-displacement curves, failed to do so when the damage model material properties initially used in the 1-stringer FE model were used. The influence of using these lowered damage model initiation values and fracture toughness was shown in figure 3.30, where the lowered fracture toughness altered the previously good correlation with the analytical load-displacement curve.

Simply changing the damage model specified as a contact interaction between the 1-stringer specimen's skin and skin-web butt-joint in the initial FE model did not work, owing to a high failure load estimation and inducing high element distortion near the loaded end. As the damage model and parameters used had to be kept the same regardless of the scale at which separation was modeled, the other aspects of the 1-stringer specimen model were changed to improve its correlation with the experimental results.

The first aspect changed was to refined the mesh at the inter-phase between the skin and the skin-web butt-joint. This refinement presumed overlapping the nodes of the skin with the ones skin-web butt-joint, such that any errors given by the contact definition would be minimized. While this change had a significant influence over the model's behaviour, the changes were not towards a better correlation, as the failure load predicted diverged further from the experimental one.

The second aspect tried was to eliminate the tie constraints in the FE model for the 1-stringer specimen and to use a skin-web butt-joint geometry in the model that has the same cross-section area as its nominal geometry. This new model immediately gave the expected results, its load-displacement curve and failure load correlation with the experimental ones being very good when unstable de-bond growth was allowed

in the model. For this models however the de-bond pattern appeared to be highly unrealistic, the de-bond growth front appearing to have a staggered shape, compared with a parabolic one expected.

The last improvement done for this new FE model of 1-stringer specimen was to change the C3D8R elements from the butt-joints to C3D8I type ones, which are better suited to capture bending. This last change significantly improved the de-bond pattern, while the changes in terms of load-displacement response and failure load were negligible. Using C3D8I instead of C3D8R filler elements gave a more realistic de-bond growth behaviour for a $2mm$ overall mesh seed, the de-bond growth front being now straight. Refining the mesh along the specimen's length using a $0.5mm$ mesh seed gave the parabolic expected de-bond growth front, as well as slightly improving the already good overall correlation with experimental load-displacement curve and failure load.

The highlight of this section and chapter is the fact that the $VCCT$ damage model which gave the best results, for the 2-2.5mm desired mesh size, in modeling the $Mode\ 1$ fracture characterisation test of a DCB specimen at coupon level, also proved to accurately model compressive behaviour of a 1-stringer specimen with skin-stringer de-bond at element level. Equally important is that the $VCCT$ damage model was able to so using the material's measured fracture toughness shown in table 3.2, with which gave accurate results on both the aforementioned FE models and scales. This shows the robustness of the proposed strategy and gives further confidence in using it to study skin-stringer separation at a higher scale level, in the 3-stringer panel.

4 | 3-STRINGER PANEL ANALYSIS

This chapter, the 3-stringer panel analysis is split into four sections. In the first section 4.1, the 3-stringer panel is described. In this section aspects like the panel's geometry, damage, materials used, manufacturing aspects or testing configuration are given.

The second section addresses the 3-stringer panel's FE model built and the measures taken to verify its reliability. First in this section the FE modeling simplifications are described, after which the model's convergence is shown. Furthermore the response of the FE model with the geometrical modeling simplifications made is verified against a FE model with the panel's nominal geometry. This was done to ensure that the simplifications made are not changing the model's overall behaviour and to build confidence in using the simplified FE model further in the study.

In the third section, the panel's undamaged compressive behaviour is studied in terms of buckling pattern and load-displacement curves. The influence of its tab boundary conditions, occurring skin buckling pattern, loading imperfection, or real skin imperfection on the panel's compressive behaviour is also studied. This sensitivity study is relevant to understand the panel's general compressive behaviour and its skin buckling pattern sensitivity to different factors. This study was also used to better understand the impact of the existent damage on the panel's compressive behaviour from the last section on this chapter, by comparing the panel's general compressive behaviour with and without damage under the same conditions.

In the last section, the de-bond damage is introduced in the FE model and the sensitivity study done in the previous section is re-done with the damage included. Moreover, the panel's compressive behaviour sensitivity towards the damage related aspects is also studied. This study included different damage sizes, as well as different fracture toughnesses used in the damage model. At the end of this section, the FE model thought to give the best blind prediction was selected for further correlation with the experimental data from chapter 5

4.1 PANEL DETAILS

In this section all the relevant 3-stringer panel supplied by Fokker is described. Aspects like geometry, damage, material data, manufacturing and test preparation are treated here.

4.1.1 PANEL GEOMETRY AND MATERIALS

The 3-stringer panel's nominal geometry and different material sections can be seen in figures 4.1 and 4.2 below. The panel's measured width is $1.2mm$ smaller than the nominal one, while the cap width is also $0.25mm$ smaller than the nominal one, based on the 5-stringer's panel Catia model [55]. The measured width and the panel's measured thickness are shown in appendix A.

The panel orientation throughout this report is kept as shown in figure 4.1, with the X axis along the panel's length, caps oriented with respect to the web on the Y axis positive sense, and stringers oriented with respect to the skin on the positive Z axis direction. The stringer numbering is also done in the positive Y axis direction.

As it can be seen in figure 4.1, the panel's stringer pitch is $152.4mm$, the pitch being calculated between the medial axes of the stringer webs. The skin overhang is $20mm$, this dimension being similarly taken from the medial axes of the side stringers to their corresponding skin edges.

An $\approx 42mm$ skin-stringer de-bond was artificially made by placing an upilex [56] foil between the skin and the middle stringer's butt-joint $SFRP$ filler, the de-bond's location being centered with respect to the panel's length and covering the whole width of the joint. The upilex foil was kept in place during panel co-consolidation with adhesive and the de-bond was later extended to an $\approx 70mm$ one. The de-bond extension was made in a displacement controlled machine and its purpose was to achieve a realistic fracture surface at the de-bond edges. This specific nominal final de-bond length was chosen assuming that it falls under the $BVID$ (Barely Visible Impact Damage) inspection criterion for this type of damage. The panel also had a low velocity im-

pact of 50J under the third stringer. This impact was made using a $\approx 3kg$ weight, with a spherical tub with a diameter of 12.5mm. However, during post-impact ultrasonic scan, no damage was found at the impacted location, the only pre-test damage being the de-bond between the middle stringer and the skin. The A, S and C-scans of the middle stringer area prior de-bond extension and of the de-bond after its extension can be seen in the appendix B.

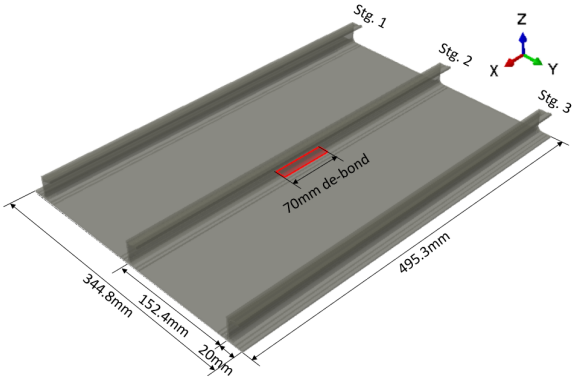

Figure 4.1: 3-stringer panel's length, width, damage and orientation

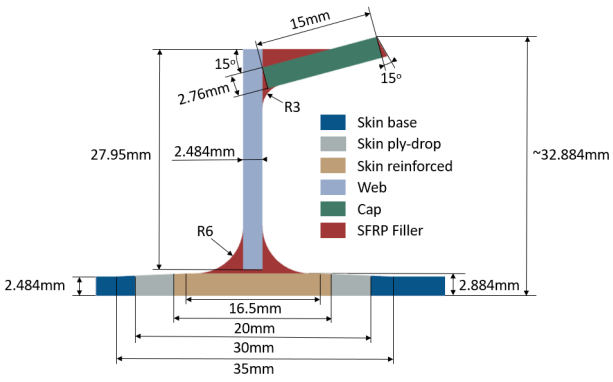

Figure 4.2: 3-stringer panel's stringer geometry and material sections

Figure 4.3 presents a detail of the ramp-down area near the stringer. As it can be seen here, the real ply-drop location does not match the geometrical ramp-down area, the 16.5mm and 35mm dimensions in figure 4.2 representing the geometrical ramp-down start and end respectively. Moreover, based on the Catia geometry of the stringer [55], when looking closer at the cap-web filler, a small gap between the cap and the web can be noticed, the distance between these being in the order of 1E-6mm. This resin gap is similar with the one of the previously studied 1-stringer specimen, a detail of this feature being shown in figure 4.4 for this panel.

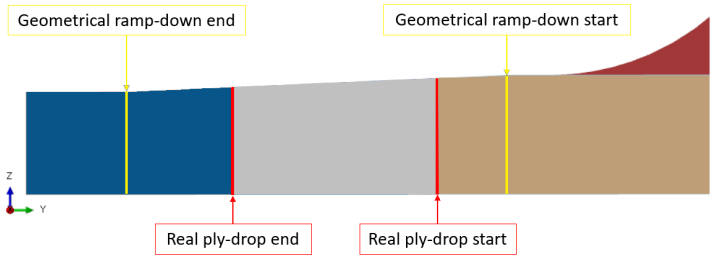

Figure 4.3: Skin ramp-down area detail

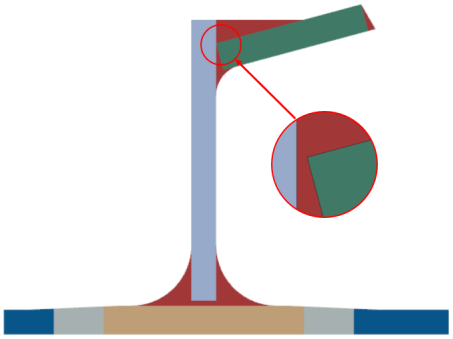

Figure 4.4: Web-Cap butt-joint detail

The materials used and the laminates staking sequence are shown in table 4.1. The laminates stacking sequences are in the positive sense of the Z axis for the skin and caps and in the negative sense of the Y axis for the webs (first web ply towards the web-filler inter-phase in the web-cap butt-joint assembly). An important mention here is that the skin layups are different form the ones from report [57], the skin layups shown in this report being based on the experimental observations. The difference in the skin's layups consist in a different skin stacking sequence normal positive sens, which resulted in changing the sign of the ± 45 plies. This difference can also be noticed when observing the surface ply orientation of the skin's top ply from figure 4.9. This figure was also used to make sure that the layup in the FE model is correct, as it shows the top skin's ply orientation with respect to the stringer caps.

Part	Layup	Material
Caps	$[45/90\text{-}45/0/45/0/\text{-}45/0/0/90]_S$	APC
Webs	[45/90/-45/0/45/0/-45/0/45/-45/0/-45/0/45/0/-45/90/45]	APC
Skin base	$[\text{-}45/45/0/\text{-}45/90/45/\text{-}45/0/45]_S$	APC
Skin ply-drop	$0/0/[\text{-}45/45/0/\text{-}45/90/45/\text{-}45/0/45]_S$	HexForce 108 /KEPSTAN 7002 and APC
Skin reinforced	$0/0/0/0/[\text{-}45/45/0/\text{-}45/90/45/\text{-}45/0/45]_S$	HexForce 108 /KEPSTAN 7002 and APC
Fillers	-	C/PEKK SFRP

Table 4.1: Materials used and laminate layups

The elastic properties of these materials were previously shown for the 1-stringer specimen FE model in table 3.5, here the $APC\ C/PEKK$ lamina properties being identical with the one used for the DCB models 3.1. This means that for this lamina a Poisson ratio of 0.319 was used. Furthermore, the same material fracture properties as used for the DCB and 1-stringer specimen models, previously shown in table 3.2.

The nominal ply thicknesses can be obtained by dividing the number of plies from table 4.1 to their corresponding thickness from figure 4.2. When doing so, one arrives at a ply thickness of $0.138mm$ for the APC plies and $0.1mm$ for the $HexForce\ 108/KEPSTAN\ 7002$ plies.

4.1.2 PANEL MANUFACTURING

The manufacturing method of this panels made use of the novel thermoplastic joining method developed during the TAPAS project, previously described in section 2.1. This technology was used here to assemble the automated tape laying manufactured straight laminates for the skin, webs and caps into a stiffened panel. Using the butt-joint here led to a stiffened panel assembly from straight laminates possible in just two steps. The first step was ultrasonic welding the cap-web butt-joint to the cap. The welding tool for this step is shown in figure 4.5.

Figure 4.5: Cap-filler welding tool

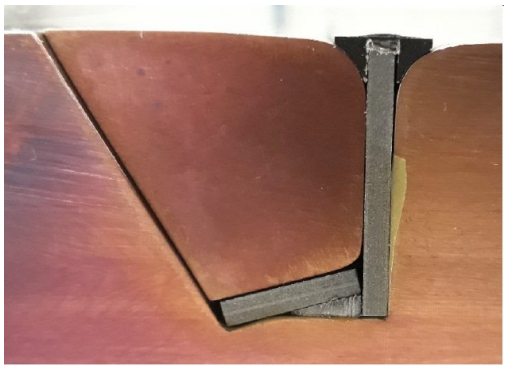

Figure 4.6: Stringer assembly components in the stiffened panel co-consolidation tool

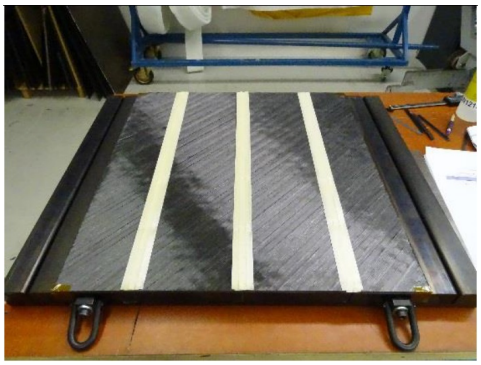

Figure 4.7: Complete parts assembly placed inside the tool

In this figure the cap-filler assembly can be seen placed inside its die to keep the parts in place, while the welding tool is covered with upliex foil to prevent the welding head to get stuck on the part. After this process, the cap with the cap-web filler welded is placed together with the web laminate and skin-web filler in the panel assembly tool 4.6, after which the skin is laid over within the co-consolidation tool 4.7. Once all the parts needed for the panel assembly are placed inside, the tool is introduced in an autoclave, where the co-consolidation process takes place. The end result, after the panel was machined to its final dimensions, can be seen in figures 4.9 and 4.10, showing a 3-stringer panel from a stringer and a skin view respectively. A white primer was applied after the machining process, after which the panel was impacted and had its de-bond extended. The white primer also helped in visually assessing the de-bond growth, with the visible crack length and its location being marked at both sides of the stringer. The visible butt-joint crack on the cap side was $68mm$, while on the other stringer side it was only $62mm$. However, these were the visible crack lengths on the butt-joint side radii, with the ultrasonic testing confirming a de-bond size of roughly $70mm$, as also shown in figure 4.8.

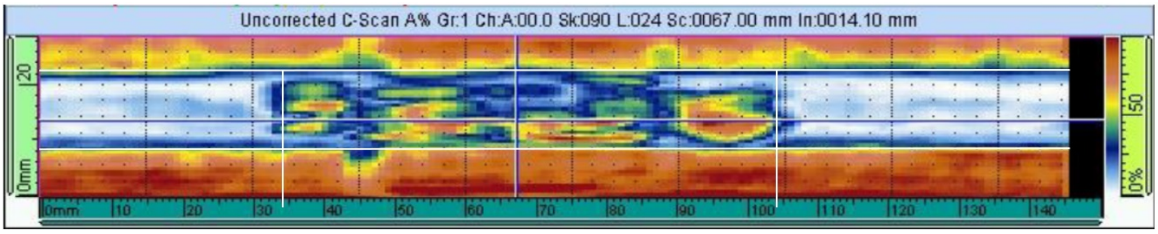

Figure 4.8: Panel's de-bond C-scan [57]

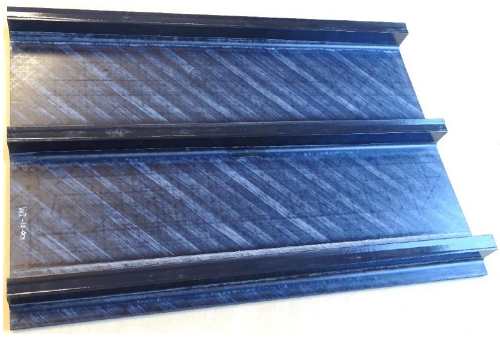

Figure 4.9: raw panel stringer view

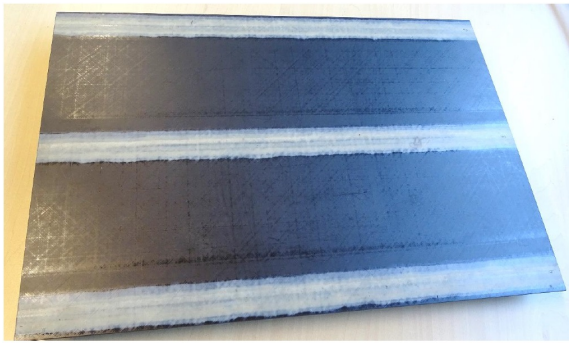

Figure 4.10: raw panel skin view

The manufacturing of this panel also gave some small non-conformances, all with the disposition to be used as is. The list of these small non-conformances is shown below:

- some small voids in the caps
- minor dents across the panel
- small skin waviness below the stringers
- glass plies waviness
- thickness steps at the ramp-down areas
- small circular resin excess from the co-consolidation tool
- small chips
- web-cap filler slightly lower than the web edge

Regardless, all these non-conformances are assumed to have a minimal impact regarding the panel's compressive behaviour, therefore in the test result as well. More details about the manufacturing of these panels can be found in [57].

The panel also showed a different skin shape compared with its intended flat one. Significant skin curvature around its stringers was observed, owing to different skin laminate and skin-web filler CTEs. To measure this imperfect shape of the panel's, a 3D DIC scan was used to measure the out-of-plane skin deformation. As the deformation amplitude was considered significant, in the testing plan the panel was to be straightened during the resin tabs casting process.

PANEL TEST RESIN TABS CAST

The necessity to cast in resin the panel's top and bottom ends is to ensure an uniform load introduction during panel testing, as well as to avoid the brooming of the edges. The resin cast tabs nominal dimensions are 386 x 59 x 25.4mm, which can also be seen in figure 4.11, depicting the panel model with the resin blocks cast at both ends. The material properties of the resin cast material are shown in table 4.2.

As the panel's ends were already machined flat and parallel with respect to each other before casting the resin blocks, Fokker came with an approach to cast the ends of the panel in resin without the need to machine the panel's ends again. This implied casting the resin blocks directly on the test-bench of the compression machine in which the panel was set to be tested. The resin cast material properties are shown in table 4.2, properties which were also used for the panel's FE model.

As also mentioned earlier, the panel had a significant skin deformation, as a result of its manufacturing process. The main feature of this deformed shape was a curvature of the panel around the stringer. As this deformation was significant, being observable also to the naked eye, it was decided by Fokker to test the panel in its intended 'flat' configuration. This meant that the panel's skin had to be straightened during the resin casting process, the resin tab having also the purpose here to keep the panel straight. The straightening process was done using two flat aluminum plates and clamps to press the panel's skin against these flat plates.

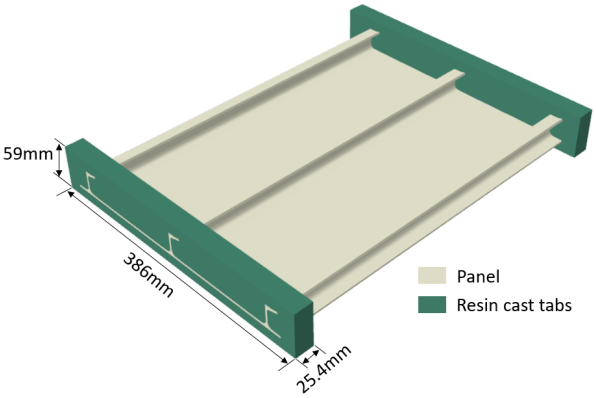

Figure 4.11: Panel model with resin blocks at the ends

While casting the resin, a load around $10kN$ was applied to keep the panel secure in its place. At this point, it was noticed that the panel ends are either not perfectly flat, or not perfectly parallel with respect to each-other. This observation was done using a source of light on one side of the panel, which in case of perfect contact between the panel's top end and the upper test-bench should not have passed through with the panel under load. As it can be seen from figure 4.12, this is not the case here, as the light did pass trough, showing a small gap between the panel and the test-bench. As mentioned in this figure, the distance over which the light could be seen passing trough was more than the panel half width, meaning that the bay with one stringer cap in it would be loaded slightly more during the test.

Part	Resin cast tabs
Material	FC 52 Isocyanate/FC 52 Polyol/Filler DT 082
Material type	Isotropic
Density ρ $[g/cm^3]$	1.6
Poisson ratio μ	0.3
Compressive stiffness E_C [GPa]	2.1
Compressive strength X_C[MPa]	38

Table 4.2: Resin cast tabs material properties [58]

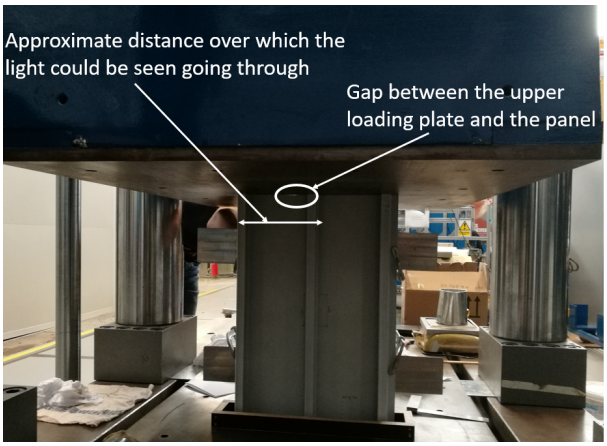

Figure 4.12: Panel visible imperfect edge machining under load and using light

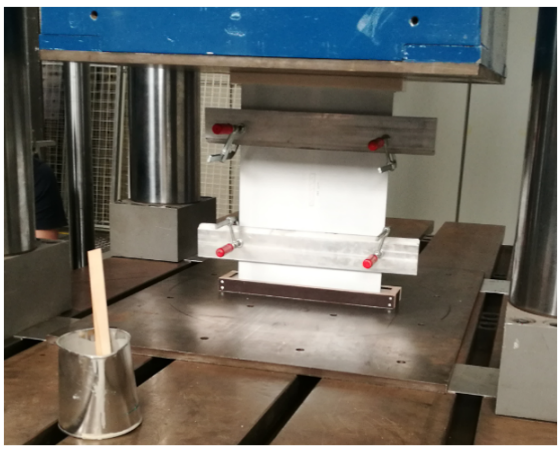

Figure 4.13: Test bench plates alignment for parallel load introduction surfaces

After the resin tab cast at one end was left to cure for about an hour, the panel was flipped and the casting process was repeated. A figure with the panel during the curing stage of the second resin cast is shown in figure 4.13, where also the aluminium plates and clamps used to straighten the panel during this process can

be seen better.

This manner of casting the resin resulted in changing the panel's shape into a 'flat' configuration, but unfortunately only for a limited time. While the panel's skin still looked flat in the first few days, in time the panel assumed roughly the same deformed shape, with minor improvements with respect to its original shape. This deformed shape is shown in figure 4.40, representing the DIC measurement of the panel's skin out-of-plane deformation. Other modifications were not done to straighten again the panel, it being tested in this deformed state.

4.2 PANEL FE MODEL BUILT

Unlike in the section 3.2, where the FE model of the 1-stringer specimen was already verified and correlated within the company, for this 3-stringer panel no FE model existed. This meant that care was taken to verify that the butt-joints simplifications made for the 1-stringer model and the ones further made here do not alter the panel's global response. In order to verify that, first a mesh convergence for the panel's FE model with simplified geometry was done. After the mesh convergence is verified, the response of this model in terms of buckling eigenvalues and load-displacement curves is compared with the one of the FE model of the panel with nominal geometry. At the end of this section the natural frequencies of the simplified and nominal geometry FE models are also compared between them and with the experimental results.

4.2.1 PANEL'S GEOMETRY SIMPLIFICATIONS

The panel's FE model with nominal geometry is done according to the dimensions shown in figures 4.1 and 4.2, using the 152.4mm stringer pitch. Also, the Catia cap width of 15mm, instead of the 14.75mm measured one, and the nominal panel width of 344.8mm, instead of the measured 343.6mm one, were used here. This was chosen as the differences given by these small deviations are thought to be negligible and in order to stick with the nominal geometry defined in the Catia model [55].

As several aspects of the panel's real geometry could induce significant computational load and as a structured, uniform mesh is desired, the panel's nominal geometry was simplified to an equivalent one. One modeling simplification of the 3-stringer panel was done to the skin ply-drop area, the difference between the nominal and the simplified skin ply-drop areas being shown in figures 4.14 and 4.15. This simplification is done since it would have introduced small elements between the real ply-drop and the geometrical ramp-downs.

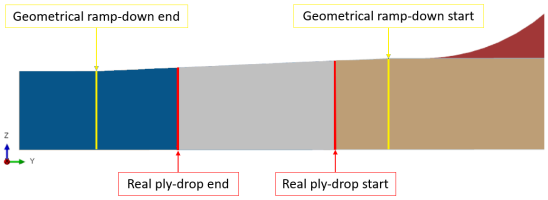

Figure 4.14: Nominal skin ramp-down area detail

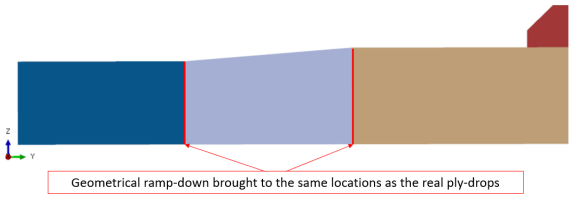

Figure 4.15: Simplified skin ramp-down area detail

Also, for the 3-stringer panel the same skin-web butt-joint geometry was kept as the one used in the last model evolution of the 1-stringer specimen, shown in figure 3.38 from section 3.2. Also, similar to the 1-stringer specimen, the web-cap butt-joint was simplified, such that the filler gap between the cap and the web was eliminated, as shown in figure 3.38 for the 1-stringer specimen. All the differences between the nominal panel geometry and the simplified one are summarized in figure 4.16. With the first 4 differences between the nominal and simplified FE model geometries being previously explained, the fifth difference (removing the cap extra resin) was done for several reasons. One of these reasons was that having such a weak material [37] at the end of the cap would have a negligible influence on the analysis. Furthermore, the elements in this region would have had a high aspect ratio, which could both yield less accurate results and add unnecessary computational load.

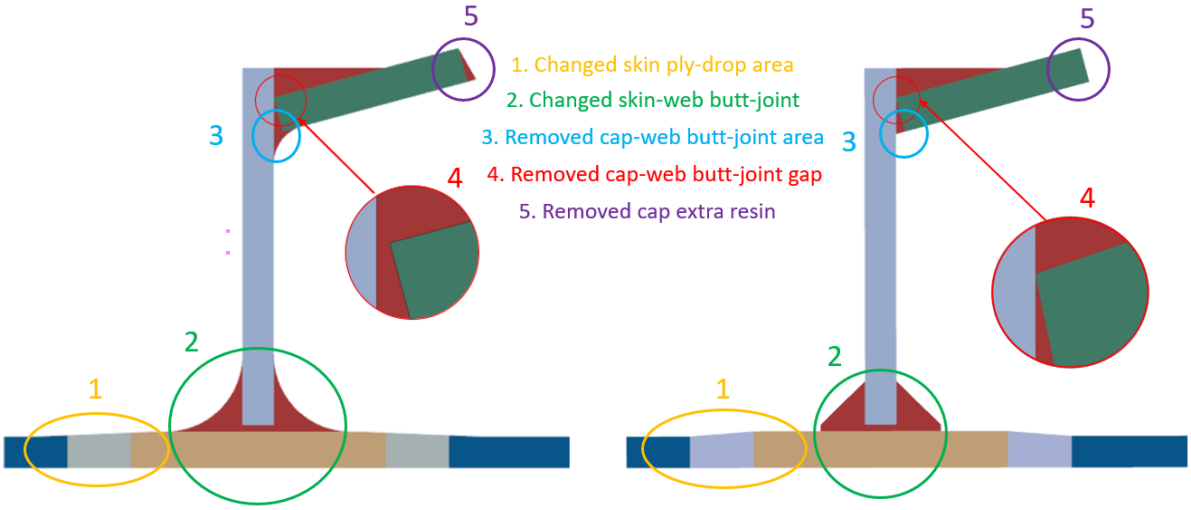

Figure 4.16: Nominal vs Simplified FE model geometrical differences

PANEL FE MODLES WEIGHT CHECK

With these simplification done, it is important to verify that the *FE* panel's weight is still close to the nominal one and also close to the measured one. Knowing the panel geometry and the material used in each region and their density, the theoretical weights of the two *FE* panel models could be computed. This was done by simply calculating the weights of the glass plies, carbon plies, butt-joints and the one of the cap extra resin, their summations giving the total panel's weight. Besides the 'hand' calculation of the two panel geometries weight, Abaqus also computes the *FE* model's weight, based on the same information. The panel's 'hand' calculated weights are compared with the panel Abaqus *FE* models weights and with the panel's measured weight in table 4.3.

Panel	Weight [g]	ΔWeight [%]
Simplified geometry, calculated	1015.96	-0.98
Nominal geometry, calculated	1020.71	-0.51
Simplified geometry, FE model	1015.96	-0.98
Nominal geometry, FE model	1022.86	-0.31
Experimental	1026	-

Table 4.3: Panel weight comparison

One important mention here is that for the cap extra resin weight estimation, the same density as for the carbon laminates and butt-joints was used, for both the calculated and in the *FE* model weight calculation. The *PEKK* resin's density was taken as such since the *APC* lamina, having a fiber volume ratio around 60%, and the butt-joint material, having a fiber volume ratio around 20% have the same density, therefore the density of the pure *PEKK* resin was assumed to be very close to this value. Furthermore, as the quantity of the extra *PEKK* resin is very small when compared to the panel weight, the influence of an erroneous pure *PEKK* density in the panel's weight estimation is assumed to be negligible.

As it can be seen table 4.3, all the calculated weights are below the measured weight of the panel. The small difference between the calculated nominal geometry panel weight and the nominal geometry *FE* model weight could be due to the skin ply-drop area, as in the former only the plies, without the extra resin in this area, were taken into account. Another possible reason for this small mis-match in weight could be the way Abaqus computes the weight in these ply-drop areas, the properties being smeared in these sections of varying thickness, including the density. On the other hand, for the simplified geometry, the difference between the calculated and *FE* model weights is negligible, as the simplifications made led to a ply-drop region of the same area as the glass plies.

When comparing the nominal geometry *FE* model's weight, which can be considered slightly more accurate than the calculated one (as it also considers the ply-drop area), with the experimental measured weight, one possible reason why the latter is slightly larger could be the weight of the primer on the real panel. The

highest relative total weight difference with respect to the experimental weight is found for the simplified panel geometry. The relative weight difference between the measured and the FE model panel weight with simplified geometry is smaller than 1%, which can be considered negligible.

4.2.2 PANEL FE MODEL MESH CONVERGENCE

Further, a mesh convergence study for the simplified FE model was done. This mesh convergence study was done using both a buckling and a free vibration frequency response analysis. In what follows, the FE model buckling analysis and free vibration frequency response analyses are described.

BUCKLING ANALYSIS FE MODEL

For the buckling eigenvalue analysis, in order to both constrain and load the panel, two reference points were fully coupled kinematically with the end surfaces. This approach is identical with the one used for the 1-stringer specimen previously described in section 3.2. In order to constrain the panel, the reference point coupled with the right end surface from figure 4.17, highlighted in red, was fully constrained (clamped boundary conditions). Constraining also the rotational degrees of freedom is somewhat redundant, as the element types used do not have rotational degrees of freedom. The other edge was also fully constrained, except the translation along the panel's length.

As for the real compressive test a resin block was cast at the panel edges, tab equivalent boundary conditions were applied for the FE model. As these resin blocks have the role to introduce uniformly the compressive load and to avoid the brooming of the edges, in this report these resin blocks are also referred as tabs, or resin tabs. In order to apply tab equivalent boundary conditions, the edges of the panel were partitioned over a length of $25.4mm$ $(1in)$, for which the boundary conditions were applied. These regions are highlighted in red in figure 4.18 and they represent only the side surfaces, without the panel's ends cross-section surfaces shown in figure 4.17. For these surfaces, all degrees of freedom were constrained, except the translation along the panel's length. In order to determine the panel's initial stiffness as well, the buckling eigenvalue analysis was done both displacement and load based. For the displacement based buckling eigenvalue analysis, a $-1mm$ displacement was applied to the loaded edge, while for the load based buckling eigenvalue analysis, a compressive load of $-1000N$ was applied to the same edge. This specific choice of displacement and load values was such that the eigenvalues from the displacement based buckling analysis are read straight into mm, while the eigenvalues from the load based buckling analysis are read straight into kN. Regarding the analysis, a buckling, linear perturbation with $Subspace$ solver analysis procedure was used, with 18 vectors used per iteration and a maximum iterations number of 30 was allowed.

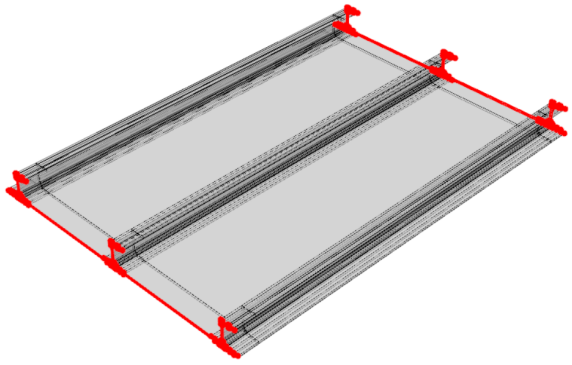

Figure 4.17: Edge surfaces coupled with reference points

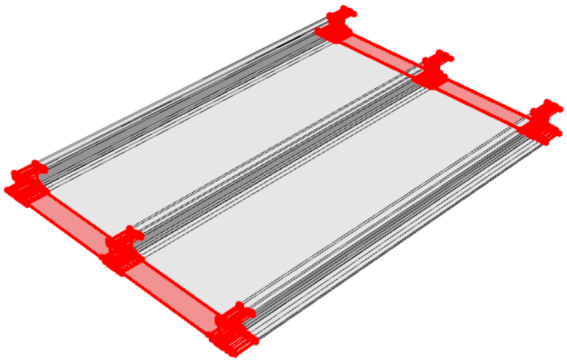

Figure 4.18: Areas over which the tab equivalent boundary conditions are applied

Another FE modeling simplification is that the glass plies are grouped two by two. This simplification meant that in the areas where the glass plies were used, one ply of $0.2mm$ thickness was defined instead of two plies of $0.1mm$ thickness. The influence of this simplification is considered negligible, as the total thickness of the glass plies was not changed with respect to the nominal one and as the grouped plies have identical orientations.

FREQUENCY RESPONSE ANALYSIS FE MODEL

For the free vibration frequency response eigenvalue analysis the panel model was used with no boundary conditions were applied. Important for this type of analysis is also to remove the reference points, as these can adversely influence the result of the analysis. Similar as for the buckling analysis, also a linear perturbation procedure was used, but now the analysis type being frequency. The eigensolver here is $Lanczos$, with default settings and a range of interest frequencies from $1Hz$ to $1kHz$.

4.2.3 PANEL FE MODEL MESH CONVERGENCE RESULTS

With the buckling and frequency FE models set, a mesh convergence study was done using mesh seeds of 2, 3 and $4mm$. For a better grasp on the panel meshes using the aforementioned mesh seeds, the stringer meshes are shown in figure 4.19 for the used mesh seeds.

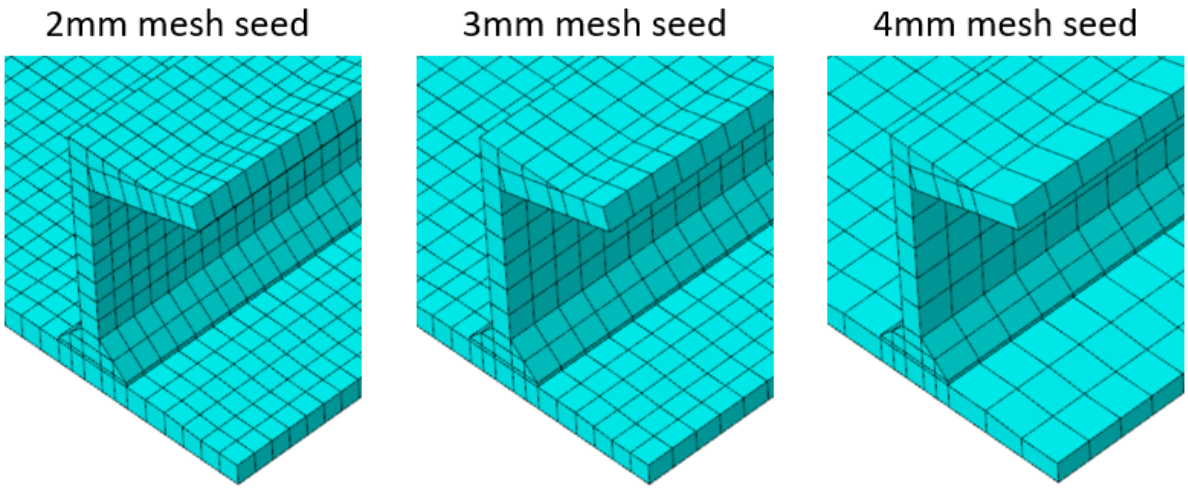

Figure 4.19: Mesh configurations

FE MODEL BUCKLING BASED MESH CONVERGENCE

For the used mesh seeds, the displacement and load based buckling eigenvalue analyses results are shown in tables 4.4 and 4.5.

Simplified FE model displacement based buckling eigenvalues/Displacement [mm]					
Mesh seed [mm]	Mode 1	Mode 2	Mode 3	Mode 4	Mode 5
2	0.75560	0.76694	0.82627	0.83182	0.87084
3	0.75565	0.76700	0.82626	0.83205	0.87095
4	0.75595	0.76734	0.82638	0.83282	0.87148
Relative error with respect to the 2 mm mesh seed [%]					
Mesh seed [mm]	Mode 1	Mode 2	Mode 3	Mode 4	Mode 5
3	-0.0066%	-0.0078%	0.0012%	-0.0277%	-0.0126%
4	-0.0463%	-0.0522%	-0.0133%	-0.1202%	-0.0735%

Table 4.4: Mesh convergence study: displacement based buckling eigenvalue analysis

Looking at table 4.4, one can see that for the first 5 buckling modes, all mesh seeds used showed the same buckling shape. This aspect is also found for the load-based buckling eigenvalue analysis results, as shown in table 4.5.

One further important aspect that can be noticed from these tables is the small differences between the first two buckling modes, in both the displacement and load based buckling eigenvalue analyses. This is relevant as this small difference between these eigenvalues suggests that the panel could buckle in either of these two modes. Furthermore, when the tab equivalent boundary conditions are omitted, the first two buckling shapes are changed between them, which shows this panel's first buckling shape high sensitivity to boundary conditions, possibly also to initial imperfections.

Simplified FE model load based buckling eigenvalues/buckling load [kN] (Applied load: -1000N)					
Mesh seed [mm]	Mode 1	Mode 2	Mode 3	Mode 4	Mode 5
2	100.38	101.88	109.76	110.50	115.68
3	100.40	101.91	109.78	110.55	115.72
4	100.47	101.98	109.83	110.68	115.82
Relative error with respect to the 2 mm mesh seed [%]					
Mesh seed [mm]	Mode 1	Mode 2	Mode 3	Mode 4	Mode 5
3	-0.0199%	-0.0294%	-0.0182%	-0.0452%	-0.0346%
4	-0.0897%	-0.0982%	-0.0638%	-0.1629%	-0.1210%

Table 4.5: Mesh convergence study: load based buckling eigenvalue analysis

Regarding the mesh convergence, for all the buckling modes, a clear mesh convergence can be seen, as a clear drop in the buckling eigenvalues is observed. The relative errors in tables 4.4 and 4.5 are computed with respect to the $2mm$ mesh seed results. As it can be seen from these relative errors, the mesh seeds tried resulted in an errors lower than 0.2%. This shows that, at least for the buckling eigenvalue analyses ran, the model shows very good convergence, the relative errors between the $2mm$ and $3mm$ mesh seed meshes being lower than 0.05%.

Using the $Mode$ 1 displacement and load based buckling analysis eigenvalues from tables 4.4 and 4.5, an estimation of the initial stiffness of the panel can also be done. This is simply done by dividing the load by the displacement, which in this case yields: $100.32kN/0.7556mm$=$132.85kN/mm$.

FE MODEL FREQUENCY RESPONSE BASED MESH CONVERGENCE

Next, in terms of free vibration frequency response, the frequency eigenvalues for the first 5 modes are shown in table 4.6.

Simplified Frequency eigenvalues [Hz]					
Mesh seed [mm]	Mode 1	Mode 2	Mode 3	Mode 4	Mode 5
2	53.417	80.433	131.96	241.30	308.09
3	53.425	80.431	131.97	241.27	308.09
4	53.458	80.445	132.04	241.19	308.09
Relative error with respect to the 2 mm mesh seed [%]					
Mesh seed [mm]	Mode 1	Mode 2	Mode 3	Mode 4	Mode 5
3	-0.0150%	0.0025%	-0.0076%	0.0124%	0.0000%
4	-0.0768%	-0.0149%	-0.0606%	0.0456%	0.0000%

Table 4.6: Mesh convergence: frequency response eigenvalue analysis

The mesh convergence seems to be less obvious when looking at this table, as only modes 1, 3 and 5 show the expected behaviour with lowering mesh size, namely decreasing frequencies eigenvalues with decreasing mesh size. However, the absolute relative error between the eigenvalues of the $2mm$ mesh seed and the others are below 0.08%, which suggests that although a clear mesh convergence is not observed in all the shown modes, the model does yield consistent results.

4.2.4 PANEL SIMPLIFIED VS NOMINAL GEOMETRY FE MODEL RESPONSE COMPARISON

In order to verify that this simplified geometry model does indeed mimic the behaviour of the nominal geometry one, a FE model was also done for the nominal geometry, for which also a $2mm$ mesh seed was used to mesh the panel. The stringer mesh of the nominal geometry panel is shown in figure 4.20. Similar with the simplified geometry model stringer mesh, also for this model some partitioning and C3D6 wedge elements were needed to ensure a relatively uniform and regular mesh size. These wedge elements are shown in green this figure, where it can also be seen that the butt-joint mesh are relatively finer in the nominal geometry model. Also for this model's butt-joints mesh, there are significantly more C3D8I elements, which could have a small influence on the results. Using this nominal panel geometry FE model the same analyses as for the simplified panel geometry FE model were done and their results were compared.

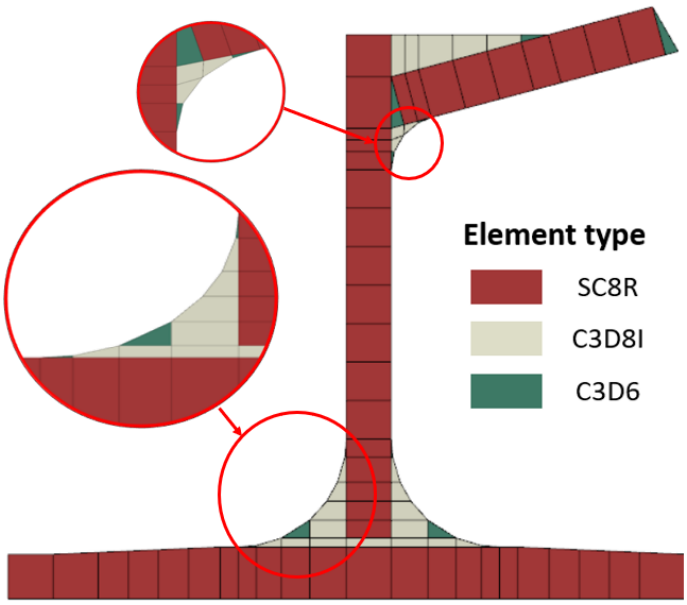

Figure 4.20: Nominal geometry stringer mesh and assigned element type

SIMPLIFIED VS NOMINAL PANEL FE MODELS BUCKLING COMPARISON

The same buckling analyses done for the previous, simplified geometry FE panel model were also done for this nominal geometry model. The comparison between the nominal and simplified geometry models buckling eigenvalues is shown in table 4.7.

Buckling displacement eigenvalues comparison [mm]					
Model's geometry	Mode 1	Mode 2	Mode 3	Mode 4	Mode 5
Nominal	0.75676	0.76907	0.83703	0.84651	0.85957
Simplified	0.75560	0.76694	0.82627	0.83182	0.87084
Relative error [%]	-0.153	-0.277	-1.285	-1.735	1.311
Buckling load eigenvalues comparison [kN]					
Model's geometry	Mode 1	Mode 2	Mode 3	Mode 4	Mode 5
Nominal	101.06	102.71	111.78	113.05	114.79
Simplified	100.38	101.88	109.76	110.50	115.68
Relative error [%]	-0.673	-0.808	-1.807	-2.256	0.775

Table 4.7: Nominal vs Simplified geometry FE model load and displacement buckling eigenvalues comparison for a $2mm$ mesh seed

As it can be seen from this table, the relative error between the nominal and simplified model geometries for the first two and the fifth eigenvalues were around 1%, while for modes 3 and 4 were around 2%. In terms of buckling pattern, the same ones were found for the first, second and fourth modes, a similar one was found for the third, while a completely different one was found for the fifth. The comparison between the buckling patterns of the first 5 modes of the nominal and simplified panel geometries is shown in figure 4.21.

As it can seen from this figure, the first two buckling patterns are identical, the first one having a 3 half-waves buckling pattern, while the second one has a 4 half-waves buckling patterns. One of these first two buckling patterns were also expected in the experimental test, with the first one obviously being more likely to appear. The other buckling modes were highly unlikely to be observed during the experimental test, as the there is a significant difference in buckling load and displacement between the first two modes and the others. The stiffness of the FE model with nominal geometry can be computed in the same manner as for the simplified

geometry one, yielding a stiffness of $101.06kN/0.75676mm$=$133.54kN/mm$. The relative error between the two geometries in terms of stiffness is -0.52%, the one of the nominal geometry model being slightly stiffer.

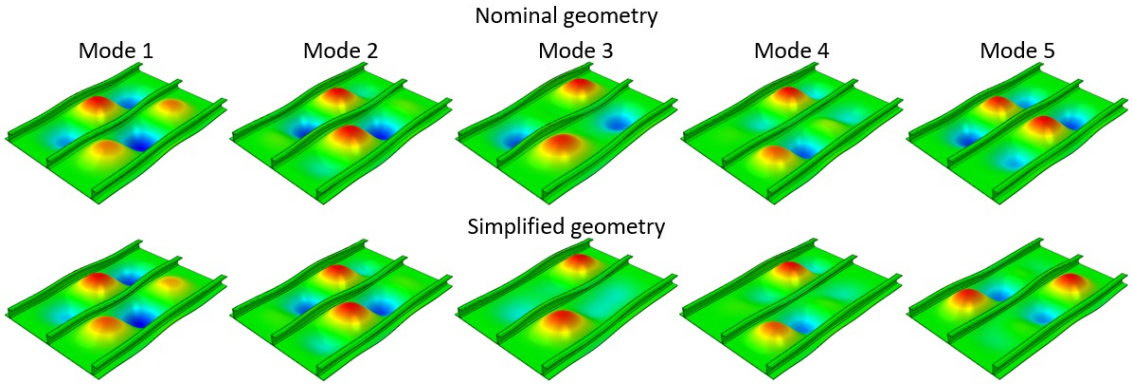

Figure 4.21: Nominal vs Simplified buckling patterns comparison

SIMPLIFIED VS NOMINAL PANEL FE MODELS FREQUENCY RESPONSE COMPARISON

For this analysis type the experimental results of the panel's free vibration frequency response was also available, some details about the measurement done being shown in appendix C. The experimental values are shown and compared in table 4.8 against the simplified and nominal geometries panel FE models.

Frequency eigenvalues comparison [Hz]				
Model's geometry	Mode 1	Mode 2	Mode 3	Mode 4
Nominal	53.024	80.412	131.33	240.66
Simplified	53.417	80.433	131.96	241.30
Experimental	53.750	79.000	132.00	236.50
Relative errors [%]				
Simplified w.r.t. Nominal	0.741	0.026	0.480	0.266
Simplified w.r.t. Experimental	-0.620	1.814	-0.030	2.030
Nominal w.r.t. Experimental	1.351	1.787	-0.508	1.759

Table 4.8: Nominal and simplified geometry FE model frequency eigenvalues comparison with respect to the experimental values for a $2mm$ mesh seed

As it can be seen from this table, the differences between the $Nominal$, $Simplified$ and $Experimental$ frequency eigenvalues are relatively small. The differences between the nominal and simplified FE model's frequency response is small and can be considered negligible, as the relative errors for the first 4 modes are below 1%.

A clear statement cannot be done on which geometry gives a frequency response closer to the experimental ones, as the errors vary depending on the frequency mode. The simplified geometry gives a closer response for the first and third mode, while the nominal geometry gives closer response for the second and forth mode. Furthermore, the FE models also do not show a clear consistency in their comparison with the experimental model, as for the first mode the simplified model showed a lower frequency response, while the nominal one showed a higher frequency. The two FE model's response are higher than the experimental one for the second and fourth mode, while for the third mode both FE models showed a lower frequency than the experimental one.

Regarding the shapes assigned to these first four modes, the same shapes were found for the two FE models. These shapes were also found for the experimental panel, with the mention that for the first 3 modes, the FE models showed the inverted modes. However, these inverted modes have the same frequency as the initial ones, therefore in figure 4.22, the first 3 frequency modes of the FE models are inverted to match the experimental ones. As it can be seen from figure 4.23, the shapes between the nominal and simplified geometry FE models match the experimental ones. When looking at the $Mode\,2$ frequency shape, one can notice that this mode is not perfectly symmetric, as the panel is not bent along the middle stringer, but along a slightly

oblique line crossing the middle stringer. This aspect is also captured by the FE models, but somewhat at a lesser extent, as the aforementioned non-symmetric shape is more obvious in the experimental scan.

Another observation that can be done is on the apparent higher deformation scale of the experimental shapes. However, a clear observation cannot be done regarding this aspect, as this can also come from the scaling differences between Abaqus and the software used to measure the panel's free vibration frequency response. One last observation can be done about $Mode\ 4$, which on the experimental panel appears highly rugged. This difference could be due to manufacturing reasons, as in the FE model a perfectly flat, constant thickness panel geometry was studied, while the real panel included significant skin deformations, small stringer deformations and small thickness variations.

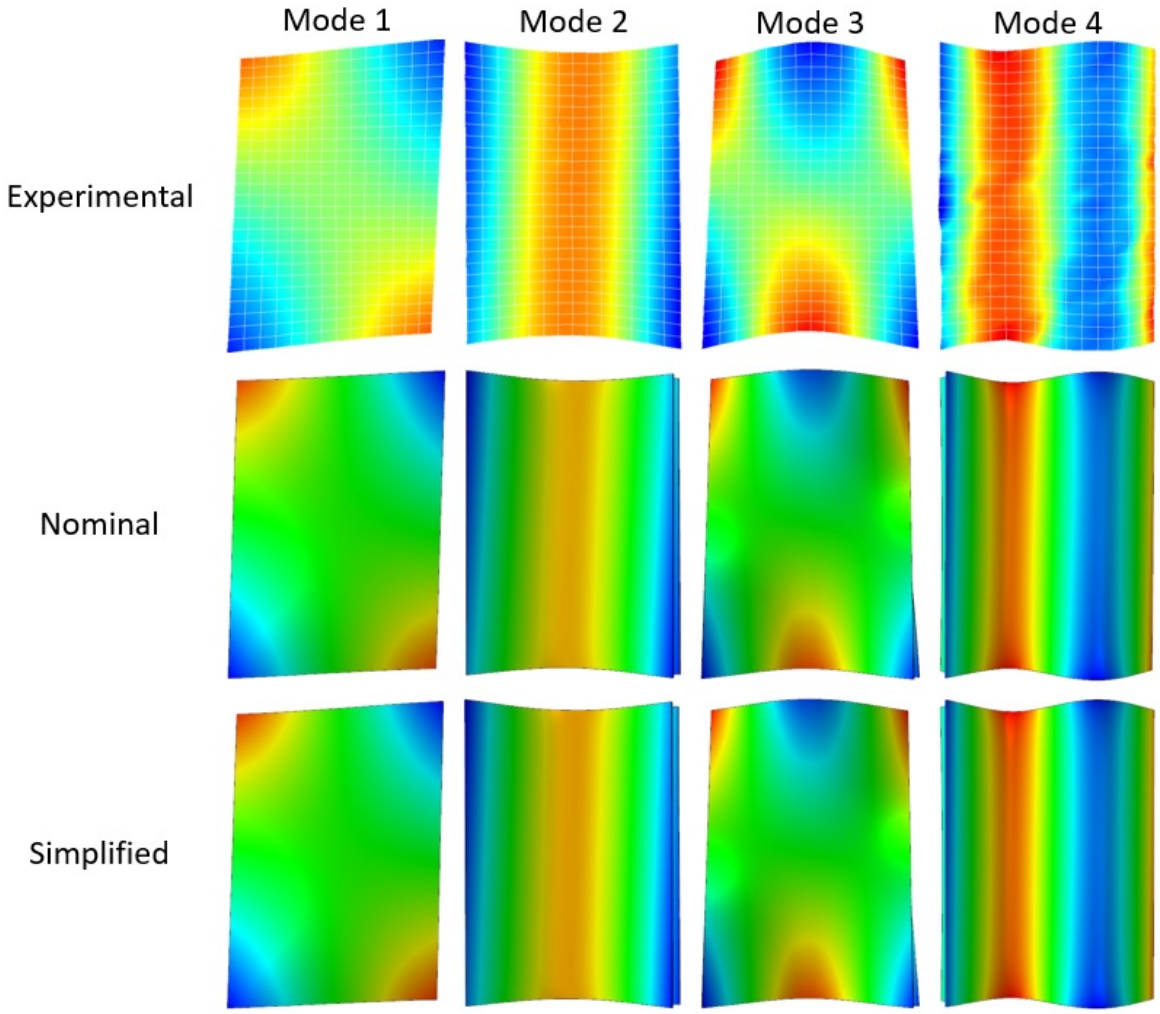

Figure 4.22: FE models vs experimental frequency mode shapes correlations, skin view

A better grasp on the actual deformation shapes of these frequency modes can be achieved by looking at figure 4.23, where these frequency mode deformation shapes are shown from an isometric view.

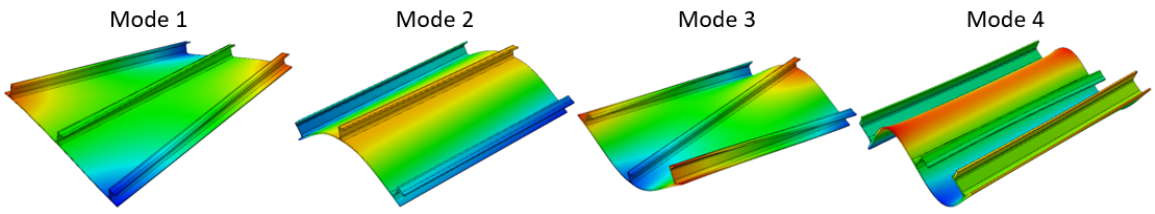

Figure 4.23: Nominal geometry FE models frequency modes, isometric view

SIMPLIFIED VS NOMINAL PANEL FE MODELS COMPRESSIVE RESPONSE COMPARISON

The compressive load-displacement behaviour of the two panel geometries FE models was also studied. The same analysis procedure as the one used in the previous DCB and 1-stringer specimen was used, namely a $Quasi-static\ Dynamic\ Implicit$ procedure, with a 0.01 time step and a number of 10 000 of increments allowed. The applied displacement was -4mm on the loading reference point, while the boundary conditions were the same as the one used for the previous buckling analyses. The load-displacement response of the two panel geometries are shown in figure 4.24. Also in this figure, the skin view of the panel's skin out-of-plane displacement during several relevant points of the load-displacement curve are shown.

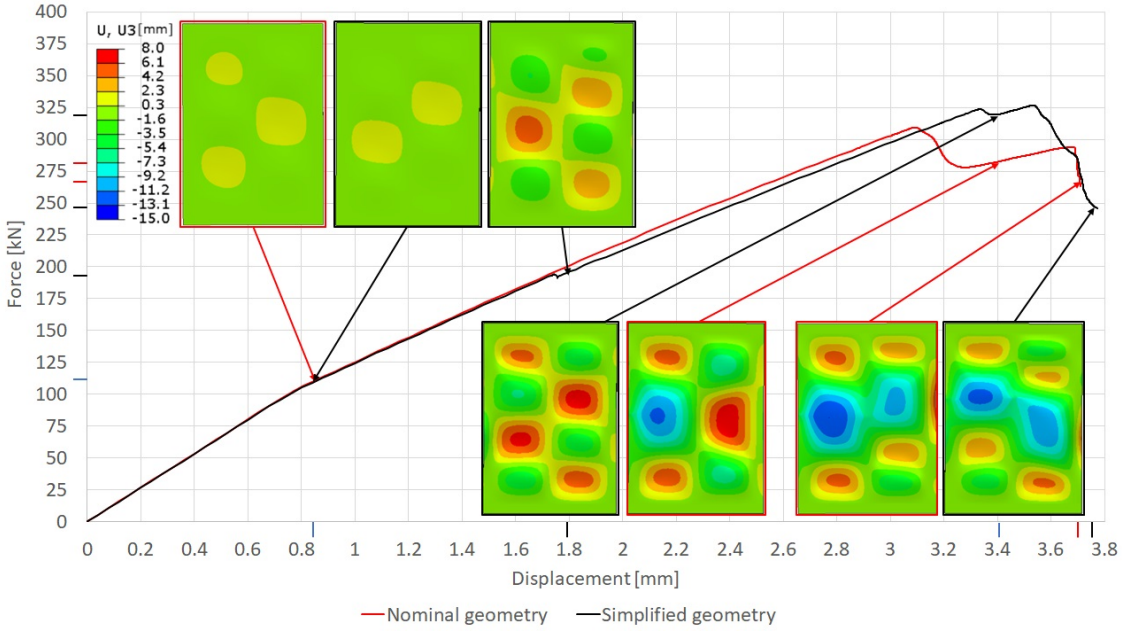

Figure 4.24: Nominal vs Simplified load-displacement curve

In this figure, the red color was used for aspects related to the nominal geometry model results, while the black color was used to show aspects related to the simplified geometry model results. The sign of the out-of-plane displacement is consistent with the orientation shown in figure 4.1, with the + sign depicting deflections towards the stringers. Here it can be seen that both load-displacement curves end before the applied displacement based loading of -4mm. This is due to the allowed limit of 10 000 increments being reached. The advantage of the simplified geometry model in terms of convergence can already be seen when looking at the displacement reached by these two models, the simplified panel geometry model advancing more than the nominal panel geometry model within the allowed 10 000 increments.

Buckling occurs roughly at the same point for both panel model geometries, around a load of 100kN. As the load increases for the nominal panel geometry, the skin pockets deflections continue to grow until the middle stringer cap fails under crippling and the stringer 1 buckles (numbering according to figure 4.1). This failure can also be noticed on the load-displacement curve with a load drop from 310kN to 275kN. The location of the middle stringer cap crippling along the panel length coincides with the locations of the peak deflections of the panel's middle skin pockets. The final load-drop for the nominal geometry occurs when all the stringers buckle and as the skin buckling pockets in the two adjacent panel bays tend to unite, as it can be seen from the last out-of-plane displacement capture of the nominal geometry.

For the simplified panel geometry a secondary buckling occurs at a load around 194kN, the 3 half-waves buckling pattern changing into a 4 half-waves one, which is also marked by a small load-drop. The load-drop due to stringer cap crippling in the model occurs at a higher load, at around 325kN, which is followed by another load-drop caused by another stringer cap crippling at around the same load. The first cap crippling occurs in the first stringer, with the second stinger cap crippling occurring in the middle stringer. Similar with the stringer cap crippling in the nominal panel geometry, also for the simplified geometry the cap crippling occurs next to a skin pocket deflection of a positive sign (towards the stinger). The final collapse occurs after all the stringer buckle, with the skin buckling pockets in the two adjacent bays tending to unite, which

ultimately leads to global panel buckling. This global failure sequence is also similar with the one seen in the nominal geometry panel model.

Comparing the compressive behaviour of these two panel geometries, one can notice that there is an excellent correlation in the initial and post-buckling stiffnesses until a load around $195kN$, after which the simplified geometry shows secondary buckling. After this secondary buckling its stiffness does not change much with respect to the nominal geometry panel stiffness, as the two load-displacement curves are roughly parallel until the first load-drop seen for the nominal geometry load-displacement curve.

The secondary buckling in the simplified geometry panel is likely to be caused by the different skin-web butt-joint geometry, with the simplified geometry possibly giving a more realistic result. The above affirmation is based on the high difference in mesh quality of the skin-web filler and also on the counter-intuitive buckling behaviour based on the width of the skin-web filler.

In terms of mesh quality, the aspect-ratio (ratio between the longest and shortest edge of an element) of the skin-web filler elements of these two panels are compared. For the quad elements, the average aspect ratio of the nominal panel geometry model is 8.81, with the worst one being 23.86, while for the simplified panel geometry model the average aspect ratio is 3.79, the worst one being 4.97. For the wedge elements, the average aspect ratio for the nominal panel geometry is 16.53, the worst one being 23.86, while for the simplified panel geometry the aspect ratio is a constant 1.43. From this skin-web filler aspect ratio comparison, it can be noticed that the nominal panel geometry model has an aspect ratio far worse than the simplified panel geometry one, the ideal aspect ratio of these elements being 1. The difference in the aspect ratio is more significant for the wedge elements, which is expected, as the sharp filler edges of the nominal panel geometry are meshed with wedge elements. These bad aspect ratio elements of the filler near the edge for the nominal geometry could give erroneous results. These elements might give unrealistic skin bay edge boundary conditions, being somewhat less constraining than the one of the simplified filler. This lesser skin edge edge constraints of the nominal panel geometry would have an equivalent effect as having a lower bay aspect ratio, which would tend to give a bay buckling pattern with less half-waves. On the other hand, based on the skin-web filler width, the nominal geometry has the tendency to give a buckling pattern with more half-waves. This is due to its larger width when compared to the nominal geometry, mimicking a skin bay with a higher aspect ratio. Therefore, from this point of view, there is a tendency for the nominal geometry to give a buckling pattern with more half-waves than the panel with simplified geometry.

The strong influence of the skin-web butt-joint with respect to the panel's buckling pattern is somewhat expected, as the difference in the buckling eigenvalues for the 3 and 4 half-waves buckling pattern modes observed during the buckling analysis were very small for both the nominal and simplified panel geometries.

Regarding the collapse of these two panels, the load levels at which stringer cap crippling and stringer buckling occurs is not necessarily relevant, as the damaged panel is expected to fail (due to skin-stiffener separation) fairly earlier than the load levels at which stinger crippling occurs for these two panel geometries.

CONCLUSIONS

The response of the simplified panel geometry model was checked against the nominal panel geometry model in terms of buckling, free vibration and compressive response. The correlation between the two FE models in terms of buckling eigenvalues was very good for the first five modes shown and with relative errors below 1% for the first two modes of interest, the maximum relative error for first 5 modes being lower than 2.5%.

In terms of free vibration analysis, for which experimental data was available, both the nominal and simplified panel geometry models showed identical modes, the largest relative error with respect to the experimental values for the first 4 modes being around 2%.

The compressive response in terms of load-displacement curves and skin out-of-plane displacement was also checked, the simplified geometry showing excellent correlation with the nominal geometry FE model in terms of pre-buckling and initial post-stiffness. The most significant difference found between the compressive response of these panel was the secondary buckling seen for the simplified panel geometry. This behaviour was deemed more realistic as the edge skin-web butt-joint mesh quality of the nominal panel geometry was significantly worse than the one of the simplified panel geometry and as also this difference was counter-intuitive based on the skin-web butt-joint width.

Overall, these 3 response checks of the simplified panel geometry against the nominal panel geometry showed a very good correlation between these two FE model geometries, with the simplified one possibly having a closer behaviour with respect to the experimental one. This means that the geometrical and modeling sim-

plifications made had a negligible impact on the panel's overall behaviour in what concerns the expected failure load. Therefore, the simplified panel geometry *FE* model is further used to study the panel's general undamaged and damaged compressive response with skin-stringer separation.

4.3 PANEL UNDAMAGED SENSITIVITY STUDY

In this section the undamaged panel compressive behaviour was studied in terms of load-displacement curves and skin out-of-plane displacement, taking into account multiple aspects that could give a different response during the test than in the *FE* simulation environment. The aspects treated in this section are the influence of modeling the panel edge resin tabs, multiple buckling patterns, loading imperfections and real skin deformed shape.

4.3.1 PANEL RESIN TAB INFLUENCE

As mentioned earlier in chapter 4.1, for the experimental test the panel ends are cast in resin, which help introducing the load uniformly and avoid the brooming of the ends. In accounting for these resin tabs there are two main approaches, to apply equivalent boundary conditions over the areas in contact with these resin tabs, or to simply model the resin tabs. Prescribing boundary conditions to the panel areas cast in resin has the advantage of relieving the computational effort of the simulation, while potentially having insignificant differences in the panel's compressive behaviour.

As for now equivalent boundary conditions were prescribed in the resin areas in contact with the panel, now the resin casts are modeled and their influence over the compressive behaviour of the panel is studied. The isometric views of the panel model with resin tabs and of the real panel are shown in figure 4.27 and 4.28, while their cross sections are shown in figures 4.25 and 4.26.

Figure 4.25: Panel FE model cross-section view

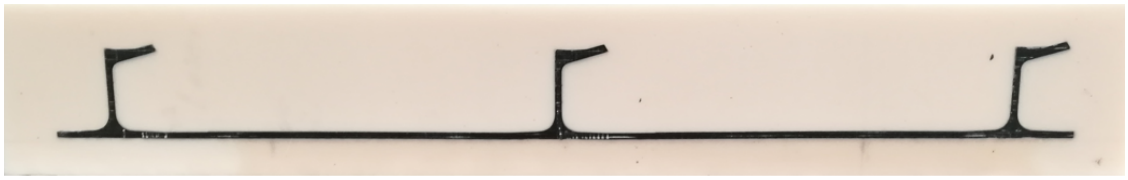

Figure 4.26: Real panel cross-section view

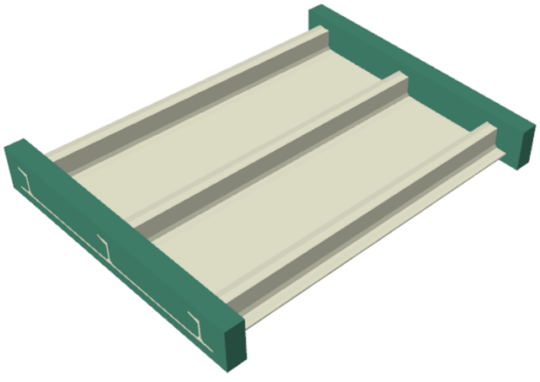

Figure 4.27: Panel FE model isometric view

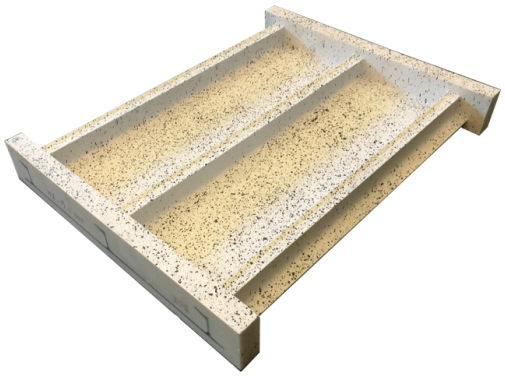

Figure 4.28: Panel isometric view

As an observation, the relative mis-alignment of the side stringers in figure 4.26 is exaggerated by the camera view, the angular deviation between the stringers and the skin at their corespondent skin-web butt-joint being less than 1°.

PANEL FE MODEL WITH RESIN TABS

Regarding the FE modeling strategy, the same approach as before was used, the panel with the tabs also being built as a one part model. In building this model, first the geometry of the resin tabs was extruded with the panel length, after which a cut was used to remove the excess resin in the middle of the panel. The rest of the panel details (skin areas, webs, caps and fillers) were created by means of partitions. Modeling the resin tabs is done in a similar manner with modeling the butt-joint fillers, the only difference being that now the material behaviour type assigned to the resin tabs was isotropic, with the material properties shown in table 4.2

The only other changes done to the model in order to run it was to remove the tab equivalent boundary conditions (since the resin tabs now are modeled as well) and to recreate the geometry sets used to link the panel ends to their corespondent reference points, such that now the tab surface is also included. As a new model was made to study the influence of the resin tabs, a check for this new model in terms of weight, buckling response and free vibration frequency response was done again.

PANEL FE MODEL WITH RESIN TABS WEIGHT CHECK

The mass of the panel with the resin tabs modeled was also compared with the weight of the panel. The real panel with the resin tabs cast had a weight of 2542.5g, while the FE model weight is 2760.3g, which gives a relative error of 8.57%. This error could be partially due to slightly different resin cast volume, or due to a different resin density.

Considering the higher weight due to a different volume, the possibility of higher volume in the FE model coming from a different overlapping area along the panel's length is limited, as the resin was cast up to a 25.4mm level marked on the panel itself, as discussed in chapter 4.1. This aspect is relevant since a different buckling pattern could be induced by changing panel area over which the resin is cast, especially for this panel with close buckling eigenvalues between the first two modes.

The higher weight due to a different resin cast density might be given by having slightly less DT 082 $Filler$ [58] in the resin cast, which decreases the resin's density. As for the resin the filler material significantly changes the mechanical properties, having less filler material could also give a decrease in the resin's elastic modulus. Having a less stiff resin behaviour might also change the buckling mode of the panel, as a more compliant resin would provide less skin bay support. With this in mind, a parametric study is also done for different resin stiffnesses, for both a increased and decreased stiffness.

Another cause of different weights between the real panel and its corespondent FE model might be due to the geometrical simplifications made at the panel's butt-joints, the FE model having slightly more resin than the real panel. Considering that the density of the casting resin is higher than the density of the filler, a higher weight of the FE model is expected. However, this difference due to the geometry simplifications made is in order of grams at most.

Based on the resin cast data sheet [58], on the panel weights with and without tabs and on the assumption that the real panel and FE model's resin casts have identical volume, the density and material properties of the real panel's resin material can be estimated. The resin weights of the panel and of its corresponding FE model can be easily obtained by subtracting the panel weights shown in table 4.3, from the aforementioned panel weights (in which the resin casts were included). This gives 2542.5g-1026g=1516.5g for the real panel resin weight and 2760.3g-1015.96g=1744.34g for the panel FE model resin weight. Taking into account that from the resin data-sheet [58] the material density and elastic modulus without the filler is $1g/cm^3$ and $1000MPa$ and the resin properties with the filler shown in table 4.2, a linear interpolation can be done with the aforementioned assumption. Assuming that the real panel's resin casts have the same volume as the FE model's one, a simple system of two equations can be defined to find the density that would give the same resin weight as the real panel. This is done by defining the resin volume based on the FE model such that:

$$\rho_{model} = \frac{W_{resinmodel}}{V_{model}} \Leftrightarrow V_{model} = \frac{W_{model}}{\rho_{model}} = \frac{1744.34g}{1.6g/cm^3} = 1090.2125cm^3 \tag{4.1}$$

With the resin volume calculated based on the FE model, the panel's resin tabs density can be determined using the panel's resin weight:

$$\rho_{panel} = \frac{W_{resinpanel}}{V_{model}} = \frac{1516.5g}{1090.2125cm^3} = 1.391g/cm^3 \tag{4.2}$$

Having now the an estimate for the real panel's resin density, a linear interpolation can be used between the resin properties with and without filler to get also an estimate for the panel's modulus. This equation can be defined for the resin's elastic modulus as a function of the resin's density:

$$E(\rho) = \frac{2100MPa - 1000MPa}{1.6g/cm^3 - 1g/cm^3} \cdot \rho + constant[MPa] \tag{4.3}$$

Plugging either of the resin densities with their corresponding elastic modulus in the above equation yields a value of -833.(3) MPa for the constant, the slope being 1833.(3)$MPa \cdot cm^3/g$. With this value for the constant the elastic modulus of the resin with a density of $1.391g/cm^3$ can be found:

$$E(\rho_{panel}) = 1833.333MPa \cdot cm^3/g \cdot 1.391g/cm^3 - 833.333MPa = 1716.833MPa \tag{4.4}$$

Using these values for the resin tabs's density ($1.391g/cm^3$) and elastic modulus (1716.833MPa), the compressive behaviour of the panel is compared with the compressive behaviour of the panel with the resin properties shown in table 4.2. As no difference could be seen between these two simulation with different resin tab material properties, no results are shown in this report. The fact that no differences in the panel's compressive behaviour were seen between the sets of resin properties show the small influence of the panel's resin stiffness on the panel's compressive behaviour. Therefore, in what follows, the nominal resin properties from table 4.2 are used in this report.

PANEL FE MODEL WITH RESIN TABS BUCKLING RESPONSE CHECK

Similar as before for the model with tab equivalent boundary conditions, also for the panel FE model with the resin tabs modeled two buckling eigenvalue analyses (displacement and load based) were performed. The comparison in terms displacement and load based eigenvalues between the two approaches to account for the resin tabs is shown in table 4.9.

As it can be seen from this table, there are some differences between the panel's buckling eigenvalues with the tab modeled and with tab equivalent boundary conditions applied. For the panel with the tab modeled, both the load and displacement eigenvalues tend to be higher than the ones of the panel with tab equivalent boundary conditions. Furthermore, there is also a small difference between the panel stiffnesses, as the panel with equivalent boundary conditions had a stiffness of 138.85 kN/mm, while the panel with the modeled tab has a slightly lower stiffness, at $132.21kN/mm$.

Buckling displacement eigenvalues comparison [mm]					
Tab	Mode 1	Mode 2	Mode 3	Mode 4	Mode 5
Modeled	0.76933	0.77986	0.85541	0.8592	0.87194
Boundary conditions	0.75560	0.82627	0.87084	0.83182	0.87084
Relative error [%]	-1.785	-1.657	-3.407	-3.187	-0.126
Buckling load eigenvalues comparison [kN]					
Tab	Mode 1	Mode 2	Mode 3	Mode 4	Mode 5
Modeled	101.71	103.11	113.1	113.6	115.28
Boundary conditions	100.38	101.88	109.76	110.50	115.68
Relative error [%]	-1.308	-1.193	-2.953	-2.729	0.347

Table 4.9: Tab equivalent boundary conditions vs modeled tab FE model buckling eigenvalues comparison

Having the resin tabs modeled also led to some different buckling shapes, with the first two modes being identical, as it can be seen in figure 4.29.

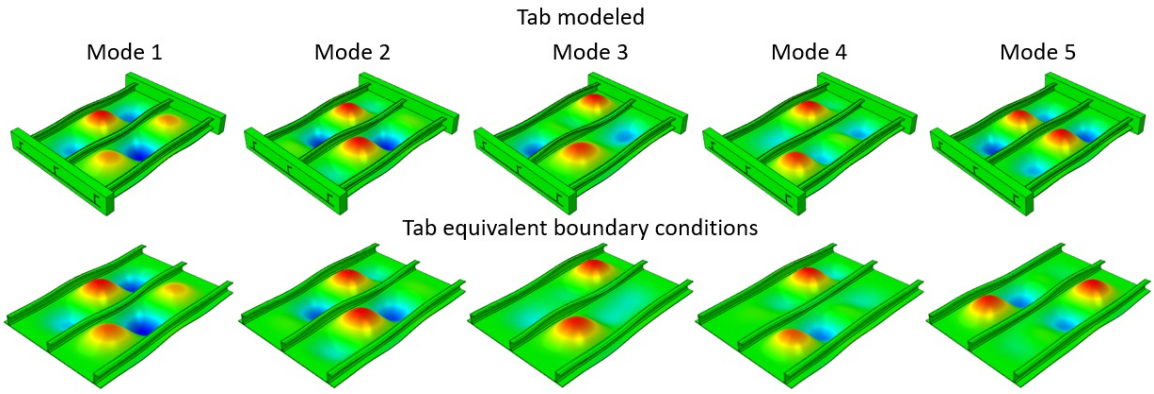

Figure 4.29: Tab boundary conditions vs modeled tab panel buckling shapes

The slightly higher buckling point with the slightly lower stiffness might be counter-intuitive, but this behaviour is closely linked to the small eigenvalues difference between the first two modes.

To better explain this behaviour, an analogy with the buckling behaviour of plates with isotropic material behaviour is done. This analogy is chosen since the buckling equations are simpler for plates with isotropic material behaviour than for composite plates with symmetric layups, while their general sensitivities to different loading scenarios, boundary conditions and aspect ratios remain the same.

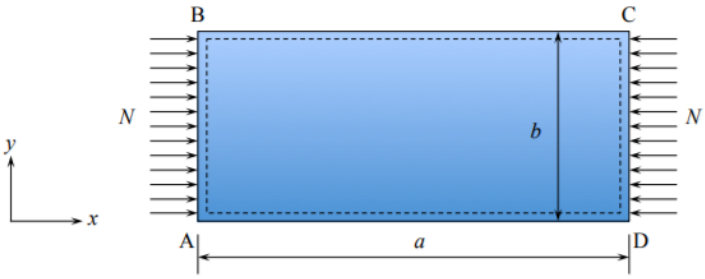

Figure 4.30: Plate schematics,loading and boundary conditions [59]

The buckling equation for an isotropic, simply-supported plate [59], as shown in figure 4.30, is:

$$N_{cr} = k_c \cdot \frac{\pi^2 D}{b^2} \tag{4.5}$$

where:

$$k_c = \left(\frac{mb}{a} + \frac{a}{mb}\right)^2 \tag{4.6}$$

$$D = \frac{E \cdot H^3}{12(1-\nu^2)} \tag{4.7}$$

and where:

- N is the distributed load along the plate's width
- a is the plate's length
- b is the plate's width
- N_{cr} is the buckling load
- k_c is the buckling coefficient
- m is the number of buckling half-waves along the plate's length
- D is the plate stiffness
- E is the elastic modulus of the plate's material
- H is the plate thickness
- ν is the Poisson ratio of the plate's material

As m must be an integer, the buckling coefficient k_c can be obtained using relation 4.6 by plotting k_c as a function of the ratio a/b (plate aspect ratio) for multiple m numbers of longitudinal buckling half-waves.

For a simply supported, isotropic plate under uni-axial compression, such a graphic is shown in figure 4.31. In this graph the minimum value of the k_c coefficient as function of the aspect ratio is shown with a dark, continuous line, the aspect ratio governing the number of longitudinal half-waves that the buckling pattern displays. As it can be seen from this figure, for each number of longitudinal half-waves, the buckling coefficient has a minimum value, after which the buckling coefficient keeps increasing until the curve for a higher number of longitudinal half-waves is intersected. This behaviour is also noticed for different plate boundary conditions, as shown in figure 4.32.

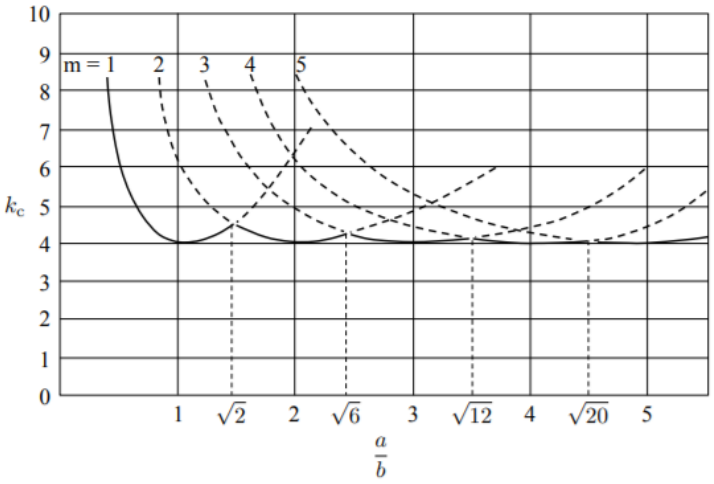

Figure 4.31: Buckling coefficient as a function of aspect ratio and number of half-waves [59]

Out of this figure, the curves of interest are the ones for the load cases with clamped and simply supported un-loaded edges (case A and C), with clamped and simply supported loaded edges. These situations are relevant here as the boundary conditions imposed at the panel's ends in both cases are purely clamped, while the areas cast in resin have different boundary conditions depending on the resin tab modeling technique. When tab equivalent boundary conditions are used, the relevant curves for the k_c buckling coefficient are the ones shown with dashed lines for cases A and C. The relevancy of both cases A and C comes from the fact that at the unloaded sides the stringers provide boundary conditions somewhere in between simply supported and clamped. As it can be seen when looking at the aforementioned cases, these also show the buckling coefficient curve inflection points described above.

On the other hand, for the panel with modeled resin tabs, besides the two aforementioned cases, now also relevant are cases A and C shown with continuous lines. These cases are now relevant since the resin allows some deformation and the loaded edges can no longer be considered purely clamped along the area cast in resin, as they offer slightly less support to the panel edges. However, the difference between the two resin tabs modeling techniques is hardly at the magnitude shown in figure 4.32 for cases A and C for clamped and simply supported loaded edges, as the support given by the modeled resin tabs should be very close to clamped.

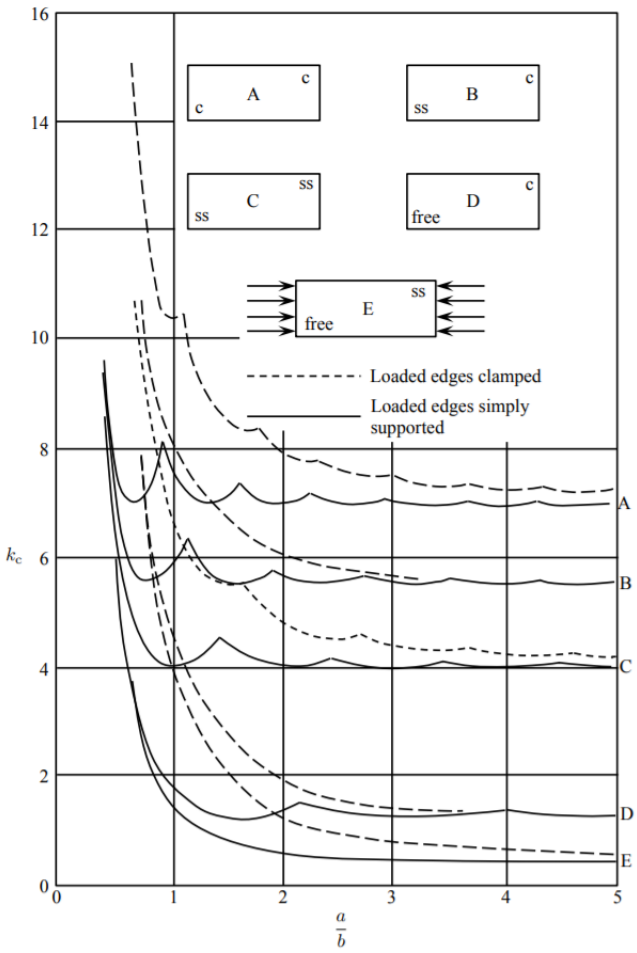

Figure 4.32: Buckling coefficient for different boundary conditions [59]

While the values shown in figures 4.31 and 4.32 are not relevant for the composite bays of the panel, the behaviour of the buckling coefficient in this case also shows the inflections points at the intersections of curves plotted for consecutive number of longitudinal half-waves.

These inflection points for the buckling coefficient k_c can also explain why the panel with modeled resin tabs has a slightly higher buckling point than the one with tab equivalent boundary conditions, despite the fact that the latter provides a stronger edge support. Such a behaviour could be explained if the aspect ratio of the panel when the resin tab is accounted is very close to the inflection point between the curves representing the buckling coefficient for a number of 3 and 4 longitudinal half-waves. In supporting this affirmation there are a number of solid arguments.

First, the difference between the first two panel buckling modes for both the load and displacement eigenvalues is small. Furthermore, when the tab is not accounted and boundary conditions are only applied to the panel's ends, the first two buckling patterns are inverted and the first buckling load remains roughly the same. This means that in that case the aspect ratio went over the inflection point, as the first buckling mode was a 4 half-wave buckling pattern. Moreover, during the simulation where the compressive behaviour of the panel is studied, a secondary buckling occurs in the panel skin bays, the buckling pattern changing from the initial one with a number of 3 longitudinal half-waves, to one with 4 longitudinal half-waves. Last, the differences between the first two buckling load and buckling displacement eigenvalues for the panel with the resin tabs modeled are smaller than the corresponding buckling eigenvalue differences for the model with tab equivalent boundary conditions. This means that the buckling points for the first two buckling modes of the panel with the resin tabs modeled are closer together than the ones of the panel with tab equivalent boundary conditions. This also suggests that the former appears to have a slightly higher aspect ratio than the latter.

PANEL FE MODEL WITH RESIN TABS FREQUENCY RESPONSE CHECK

The comparison between the free vibration frequency response eigenvalues of the panel's FE model with the tabs modeled and of the panel with the resin tabs cast is shown in table 4.10, while the comparison between their correspondent vibration modes is shown in figure 4.33.

Panel results	Frequency response comparison [Hz]			
	Mode 1	Mode 2	Mode 3	Mode 4
FE model	55	340	362	418
Experimental	69	336	365	462
Relative error [%]	-20.3	1.2	-0.8	-9.5

Table 4.10: Comparison between the free vibration frequency response eigenvalues of the FE model with modeled tabs and of the panel with resin tabs

As it can be seen from this table, the errors in frequency response between the model and the experimental values are greater than the ones for the panel without resin tabs, shown in table 4.6. This suggests that the model with the resin tabs modelled might be less representative for the panel with the resin tabs cast, than in the previous case for the panel without tabs. While the relative error in this case is significantly larger than in the previous case for the panel without the resin tabs cast, there is still a good correlation between the first four frequency modes.

Disregarding the differences between the color scale, in figure 4.33 identical deformation shapes can be observed for the modes 1, 2 and 4, while a similar shape is observed for mode 3. This suggests that the panel FE model with the resin tabs modeled is still able to capture the panel's global behaviour qualitatively, while the quantitatively aspect might be slightly altered. However, considering that the resin tabs dimensions might slightly differ between the panel and its FE model, the difference in the panel's measured weight and the theoretical weight of its FE model, the small uncertainty of the resin's material properties and the high sensitivity of the free vibration analysis towards these aspects, a clear assessment of the panel's FE model robustness cannot be done based solely on this analysis.

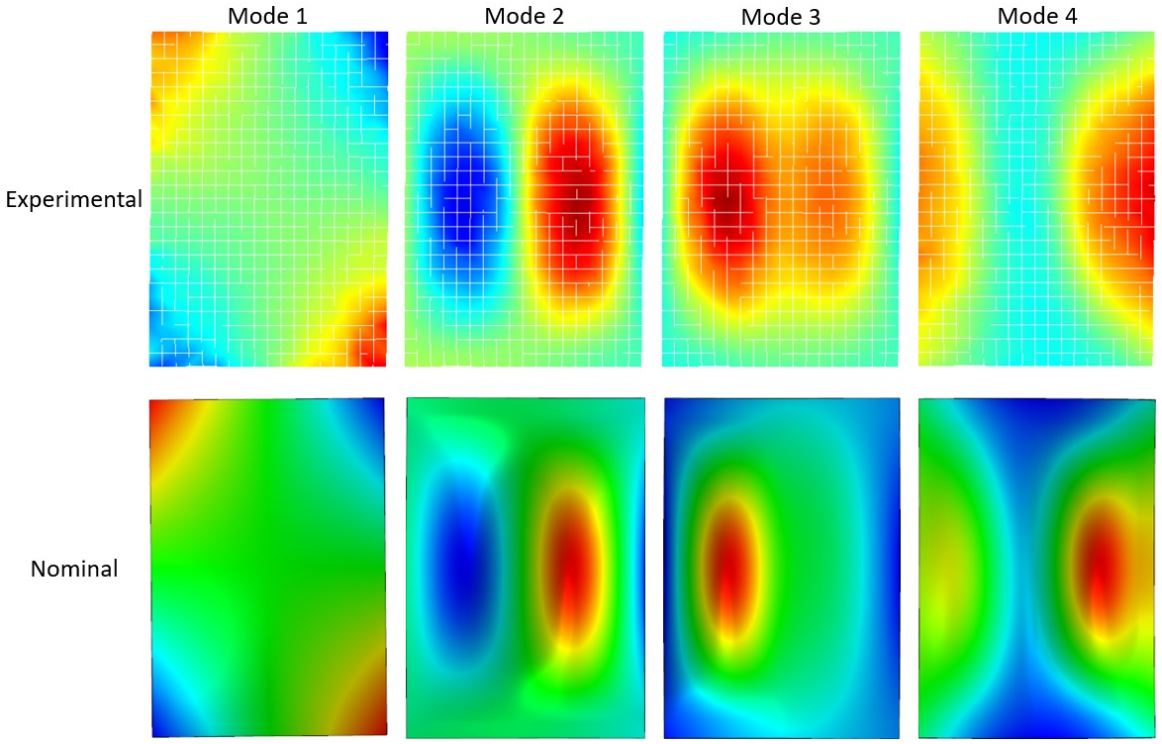

Figure 4.33: Tab boundary conditions vs modeled tab panel compressive response

PANEL FE MODEL WITH RESIN TABS COMPRESSIVE RESPONSE CHECK

The comparison in terms of load-displacement response and skin out-of-plane displacement of the two approaches to take the tab into account are shown in figure 4.34.

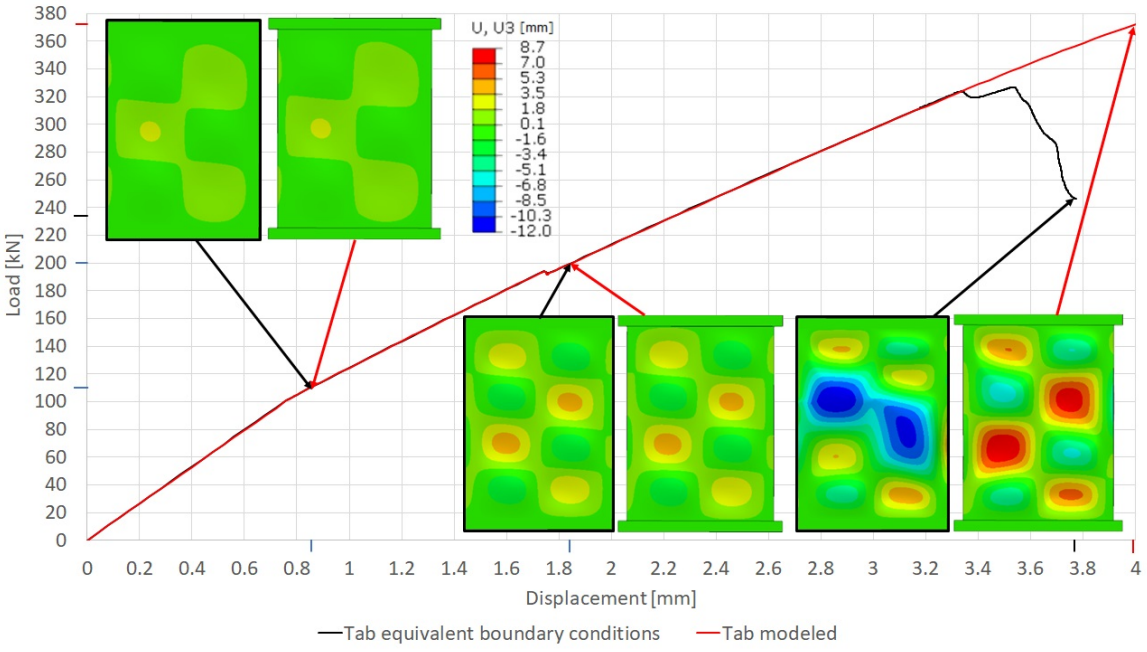

Figure 4.34: Tab boundary conditions vs modeled tab panel compressive response

As it can be seen from this figure, there is an excellent correlation up to a load around $200kN$ between the two tab modeling approaches. After this point the model with tab equivalent boundary conditions shows

stringer buckling and crippling as described in the previous section 4.2, which ultimately lead to panel global buckling.

While the panel with the tab equivalent boundary conditions begins its collapse at a load around $320kN$, the panel with the tab modeled keeps taking load until the displacement of $4mm$ applied is reached. For this panel model the buckling pockets continue to grow, with the middle pockets deflecting towards the stringers tending to unite. This tendency could mean that the panel with the resin tabs modeled tends to have a different global buckling deflection than the one with tab equivalent boundary conditions, the latter deflection in the direction opposite to the stringers. This difference in the panel's compressive behaviour implies that there is also a difference in the support offered by the modeled tab and the one offered by the tab equivalent boundary conditions.

Since this different support might be important in the stage where the damage is taken into account and since modeling tab should also give a more accurate result, in the following sensitivity studies the panel model with the resin tabs modeled will be used.

The differences in the buckling eigenvalues and shapes between the panel model with tab equivalent boundary conditions and with the tab modeled also support the decision to keep the latter model for the following sensitivity study. This is related to both the slightly different buckling eigenvalues shown by the model with the resin tabs modeled and to the different buckling patterns observed (although the buckling patters of the highest interest, the first two, are identical).

Furthermore, the free vibration frequency response also revealed that the modeling the resin tabs is indeed more representative for the actual testing configuration of the panel.

4.3.2 PANEL SKIN BUCKLING PATTERN INFLUENCE

The sensitivity of the undamaged panel towards different buckling shapes is important mostly for determining in the later stages where the behaviour of the damaged panel was studied, if the buckling shape observed in the later is due to the panel damage, or is a result of the panel's intrinsic global behaviour. Another useful aspect that can be found from this sensitivity study is the panel's sensitivity towards different buckling shapes. In other words, the ease with which the panel can buckle in different modes.

For this sensitivity study, the displacement-based buckling eigenvalue analysis done for the panel with the tabs modeled was used. For this analysis a node displacement output file was requested, the obtained shapes being included in a subsequent analysis as an imperfection before the loading step.

As the buckling points of the first two buckling modes were close between them, the sensitivity of the panel towards different buckling shapes is done using these first two buckling modes. In the sensitivity study of these two modes, the first two buckling deformation shapes are included as an imperfection before the loading step with a ±0.1 amplitude. The ±0.1 amplitude is chosen such that it was small enough to make the panel initially buckle into the desired buckling mode. The ±0.1 amplitude translated into a roughly +0.1mm maximum skin buckling pocket deflection towards the stringer and a roughly -0.1mm maximum pocket deflection away from the stringer. The minus sign is chosen to study the influence of the inverted buckling shapes of the first two modes as well, which naturally have the same eigenvalues as the first two buckling shapes shown in figure 4.29.

PANEL SENSITIVITY TOWARDS THE FIRST BUCKING MODE

The comparison between the pristine panel and the first buckling shape (both with a positive and negative amplitude) is shown in figure 4.35 in terms of load-displacement curves and skin out-of-plane displacement.

The color red depicts the results of the model in pristine shape, labeled also $Pristine$ in the graph's legend. The color blue depicts the results of the model with an imperfection shape with 0.1 amplitude based on the first buckling mode, labeled as $Buckling$ 3+ in the graph's legend. This label is from the initial imperfection shape applied, this having 3 half-waves along the panel's length and since the amplitude sign is positive. Similarly, the yellow color depicts the results of the model with an imperfection shape with a -0.1 amplitude based on the same first buckling mode, labeled $Buckling$ 3− following the same reasoning as for the previous sets of results. The red dot represents the buckling point determined from the buckling load and displacement eigenvalue analyses.

In this figure the skin out-of-plane deformations are shown without the resin tabs, while the scale is determined by the highest and lowest out-of-plane deformations out of these three analyses. With the skin out-of-plane displacement of the pristine panel described and shown in the previous section, this model is only

discussed here in comparison with the other two.

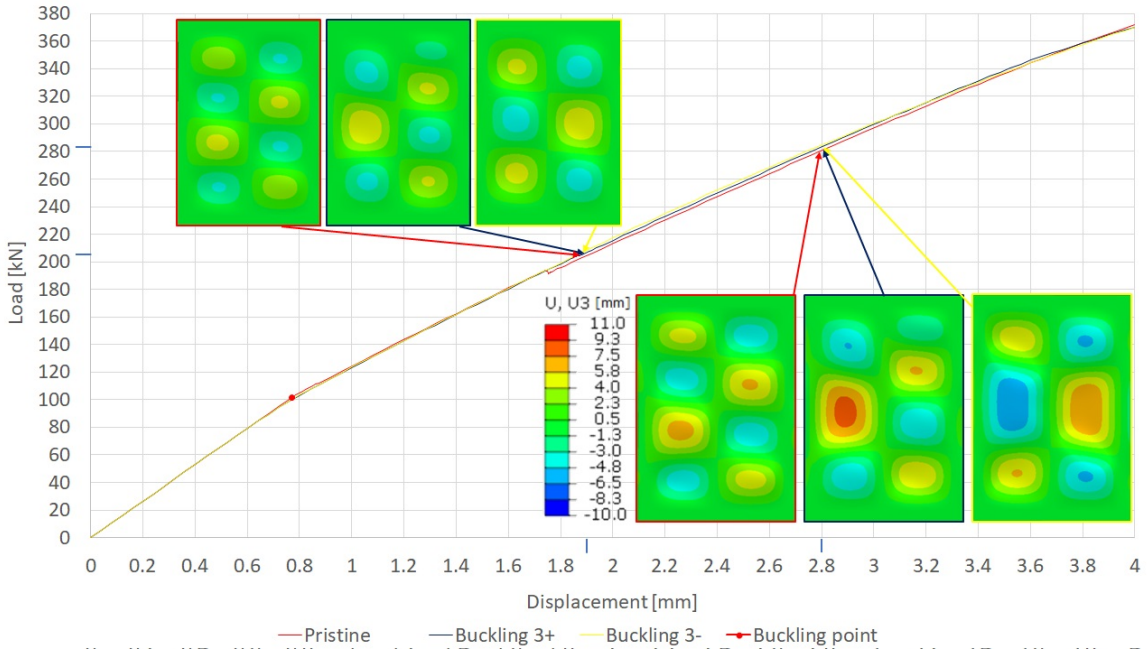

Figure 4.35: Comparison between the pristine shape and first buckling mode based imperfection shapes in terms of load-displacement response and skin out-of-plane displacement

When looking at the curves around the buckling point, it can be noticed that the ones of the models in which an initial imperfection was applied do not cross the point through its middle, unlike the red curve representing the pristine panel. For the models with the imperfection applied indeed the panel's skin buckled according to the applied deformation shape. Furthermore, the buckling imperfections introduced had a significant impact over the buckling behaviour of the models with respect to the pristine shaped one. While a positive amplitude changed the resulting buckling pattern after secondary buckling occurred in model $Buckling\ 3+$ with respect to the $Pristine$ one, the negative amplitude cancelled the secondary buckling event altogether.

This difference most likely comes form the asymmetric behavior of the panel, given by its asymmetric stringers. This difference is unlikely to come from the different deflection magnitudes of the eigenvalue analysis, as for the first mode the skin deflections had roughly the same magnitude for the positive and negative signs, with 1 for the positive and -0.99 for the negative. This different behaviour could also suggest that this panel's buckling pattern might be very sensitive to the skin's shape or other manufacturing imperfections.

The highest deflection in magnitude tends to occur in the left bay of the panel for all the three models shown, this bay being the one with 1/3 stringer caps. This can especially be seen in the last set of skin out-of-plane deflections, where even for the $Pristine$ model the pockets in the left skin bay in the middle are larger than the ones on the right skin bay, while for the $Buckling\ 3+$ and $Buckling\ 3-$ models this aspect is easier to observe. Furthermore, the pockets deflecting towards the stinger also tend to be slightly higher in magnitude.

Regardless of the panel's skin buckling pattern, the load-displacement response of the models are very similar, the differences being negligible.

PANEL SENSITIVITY TOWARDS THE SECOND BUCKING MODE

Similarly as for the first buckling shape, the sensitivity of the panel model towards the second buckling mode was studied and the models responses were compared with the pristine configuration. As the response of these models were very similar with the response of the $Pristine$ model, here the outcome of the comparison is only briefly treated.

Also in this case the applied ± 0.1 amplitudes were sufficient to made the panel's skin to buckle with the intended buckling pattern. Secondary buckling did not occurred for these models, as they both had an initial skin buckling pattern with 4 half-waves. Furthermore, their load-displacement curves were identical in between them and near identical with the one of the $Pristine$ model, the only minor mis-match being between

the buckling point and the point where secondary buckling occurred in the $Pristine$ model.

Regarding the magnitude of the skin pockets out-of-plane deflections, also for these models the highest magnitudes were observed in the middle pockets of the left skin bay. Also similarly as for the $Buckling$ 3+ and $Buckling$ 3− models, for these models the highest skin pocket deflection was towards the stringer.

4.3.3 PANEL LOADING IMPERFECTION INFLUENCE

The panel's compressive response under different loading imperfection scenarios is important to study, as these loading imperfections are likely to occur during the experimental testing. Furthermore, the panel edges themselves might not be completely parallel with respect to each-other and this behaviour can also be simulated as a loading imperfection.

Four asymmetric loading scenarios were studied individually in this section and the model's compressive behaviour with these loading imperfections applied was also compared with the one of the $Pristine$ model shown in the previous sections.

ASYMMETRICAL LOAD INTRODUCTION IN THE PANE'S FE MODEL

The individual loading asymmetries were applied as rotations around the Y and Z axes of the panel. A rotation around the Y axis translates into differences in the load seen by the skin and stringers, while a rotation around the Z axis translates into differences in load seen by the left and right sides of the panel. In other words, a rotation around the Y axis would translate into an asymmetrical loading along the panel's height, while a rotation around the Z axis would translate into an asymmetrical loading along the panel's width.

Regarding the FE modeling technique, this rotation was applied in a step created between the initial and the displacement based loading step, on the reference point coupled with the loaded panel end. Furthermore, the reference point kinematically coupled with the load introduction surface (panel's edge) was moved at the panel edges, in an attempt to introduce a pure compression load in the panel during the rotation step. The same analysis procedure as described before for the compressive step in section 4.2.4 was used for the rotation step, the only difference being that now the size of the increment is 0.1, instead of 0.01.

PANEL FE MODEL ASYMMETRIC LOADING ALONG ITS WIDTH

For the asymmetric load introduction along the panel's width, a difference in displacement of $0.2mm$ was chosen between the panel sides. This magnitude was chosen as an acceptable expected difference between the panel's sides shortening during the experimental testing, taking into consideration the panel's width. Using the panel's width of $344.8mm$, the rotation along the panel's Z axis could be computed such that at the end of the step the difference between the panel's sides along its X axis would be $0.2mm$. This rotation would be $atan(0.2mm/344.8mm) = 0.000580046rad$ $(0.033234207°)$.

In order to obtain a pure compression load during the additional rotation step, the loading reference point a was moved a the panel's sides as a function of the sense of the rotation applied. The model's boundary conditions were also re-defined using new coordinate systems defined with the same global orientation and origin identical with the moved reference points. This was done in an attempt to move the rotation axis at the panel sides, such that the aforementioned would have gave a side completely unloaded, while the other one would have had a $0.2mm$ compressive displacement at the end of the rotation step. However, unfortunately this approach did not worked as intended, as the rotation axis remained the same. This meant that the end of these rotation steps the distances along the X axis between the panel's sides were indeed the desired one of $0.2mm$, but one side was compressed, while the other one was extended.

At the end of these rotation steps, a small positive displacement for the reference point was observed. This is likely due to the point rotating around the global coordinate system, despite redefining all the loads and boundary conditions using a coordinate system with the same orientation as the global one and with its origin coincident with the loading reference point. Furthermore, a reaction load was not seen at the end of these rotation steps, therefore the exact reaction force at the end of this step was not computed.

Regardless, the real load seen by the panel at the end of this step would be small, as one panel bay is in tension, while the other is in compression. If a reaction force would have been calculate, its sign should have been different as a function of the applied sign of the rotation, as this panel is not symmetric about an XZ plane.

However, as the difference between the reaction loads after these different rotation steps are not expected to be large, the load-displacement curves of these models are plotted using the displacement at the end of

the rotation steps as an offset, such that that the load-displacement curve of the compression step is plotted starting from a $0kN$ load and $0mm$ displacement. For the positive rotation around the Z axis an offset of $0.100681mm$ is used, while for the negative rotation an offset of $0.099324mm$ is used. The small difference in these values also confirms that there's a small difference between the loads taken by the panel as a function of which panel bay is loaded more.

PANEL SENSITIVITY TO ASYMMETRIC LOADING ALONG ITS WIDTH

The load-displacement curves and the skin out-of-plane deflection of the models with an asymmetric load introduction along the panel's width are compared against the ones of the $Pristine$ in figure 4.36.

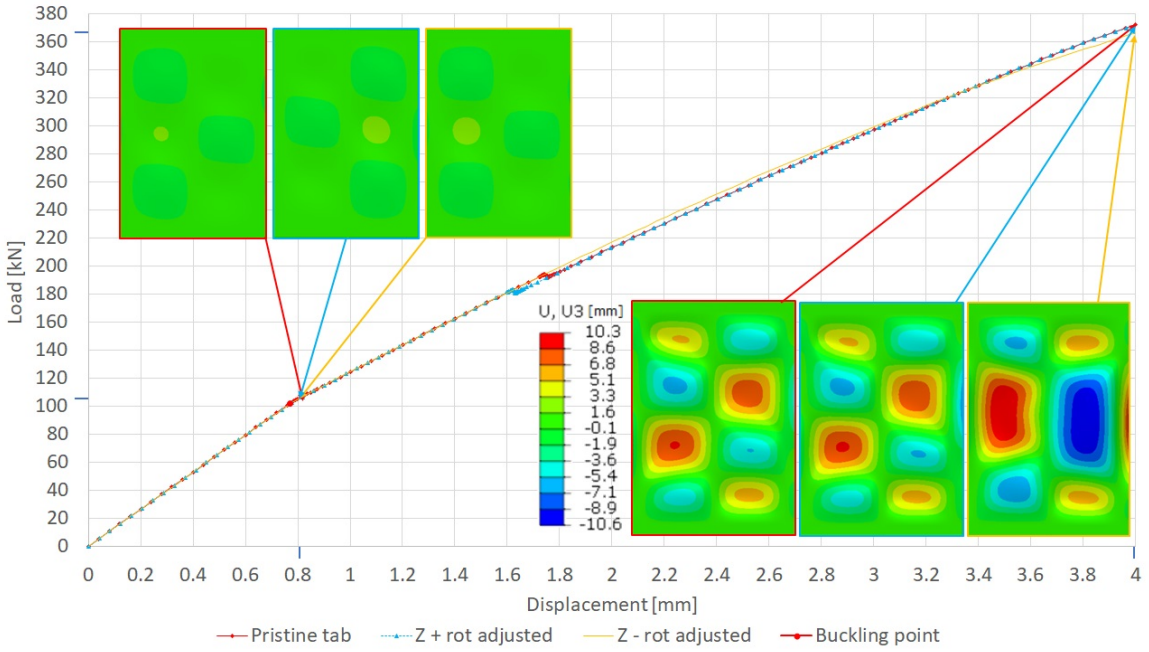

Figure 4.36: Comparison in terms of load-displacement curves and skin out of plane deflections between the pristine panel model and the panel models with asymmetric load introduction along its width

Although not visible in this graph due to the scale chosen to account for the highest deflections noticed, the models with loading imperfection buckled slightly sooner than the $Pristine$ one. This behaviour was expected, as the former models have more load on one of their panel bays. Also as expected, buckling first occurred in the skin bay under compression. This meant that for the $Z+rot$ model skin buckling first occurred in the right skin bay, while in the $Z-rot$ model skin buckling first occurred in the left skin bay. This aspect is shown in figure 4.37, where the skin out-of-plane deflection are shown for these three models for the same time step, together with their corespondent panel load and displacement.

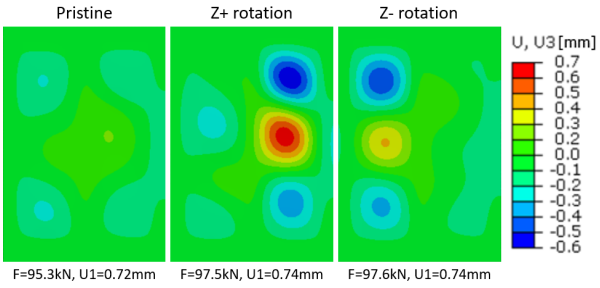

Figure 4.37: Comparison in terms of skin out-of-plane deflections between the pristine panel model and the panel models with asymmetric load introduction along its width

As it can be seen from this figure, while the pristine panel has not yet buckled, buckling pockets have already occurred in the more loaded skin bays of the models with asymmetric loading. The difference in skin buckling pocket deflection magnitude between these two models with asymmetric load introduction mostly comes from the slightly higher load and displacement at this time step in the $Z+rot$ model, especially as the skin pocket deflections grow rapidly during the initial buckling process.

When looking at figure 4.36, one can observe that the load-displacement response of all three models are very similar. The only load-displacement difference between the $Pristine$ model and the model with the left panel bay loaded mode $Z - rot$ was due to a different skin buckling pattern occurring in the latter. Similarly, the only load-displacement difference between the $Pristine$ model and the model with the right panel bay loaded mode $Z + rot$ was due to a different load level at which secondary buckling ocurred, these models having the same initial and final skin buckling pattern. The difference between the loads at which the secondary buckling occurs between the $Z + rot$ and $Pristine$ models likely comes as a result of the load introduction asymmetry, combined with the asymmetric stringer geometry as well.

Regarding the skin out-of-plane displacements, after buckling occurs the deflections magnitude are higher in the models with asymmetric load introduction. This can be already noticed when looking at the skin out-of-plane deflections shown in this figure. Interestingly however, the larger skin deflections within the models with asymmetric load introduction were found the panel bays less loaded.

PANEL FE MODEL ASYMMETRIC LOADING ALONG ITS HEIGHT

For the panel's asymmetric load introduction along its height, a $0.1mm$ difference between the bottom edge of the skin and the highest cap points was chosen. Taking into consideration the panel's height, the aforementioned $0.1mm$ difference can be considered as a pretty severe asymmetry in the load introduction and it was chosen considering more that the panel edges might not be perfectly parallel, rather than as asymmetric load introduction by the testing machine. This is due to the fact that introducing such a high difference in displacement along the panel's height would imply a really poor alignment of the load introduction surfaces of the testing machine.

Similarly as before, using the the panel's height of $32.884mm$, the angle to obtain a $0.1mm$ displacement difference along the panel's height would be $atan0.1mm/32.884 = 0.003040983rad$ ($0.174235503°$. This angle is used to impose positive and negative rotations around the Y axis, a positive rotation introducing more load in the skin than the stringers, while a negative rotation introduces more load in the stringers than in the skin.

The approach described above to introduce a pure compression load at the end of the rotation step had the same outcome, the $0.1mm$ difference being with either the skin, or the stringer side being in tension.

While in the previous case the asymmetry in the load taken by the panel during the rotation step was due the asymmetry of the stringers, in this case the difference in the load taken by the panel as a function of the rotation applied would be higher, as the skin is considered to be stiffer than the stringers. This would imply that the panel takes more compression load when a positive Y rotation is applied, as this rotation would compress the skin significantly more.

Also as for the previous load introduction asymmetry, at the end of the rotation steps there was a small displacement along X axis found in the reference point, the load-displacement curves of the compressive step of these models being also adjusted such that they begin from a $0kN$ load and $0mm$ displacement. The offset used to adjust the load-displacement curve of the model with a positive Y rotation was $0.074846mm$, while for the model with a negative 'Y" rotation the offset used was $0.0245459mm$. The difference between these two values is significantly higher than the one observed during the case of asymmetric loading along the panel's width. This is expected as the asymmetry between loading the skin, or the stringers more is also higher than loading the left, or the right panel bay more.

PANEL SENSITIVITY TO ASYMMETRIC LOADING ALONG ITS HEIGHT

The load-displacement curves and skin out-of-plane deflections of the models with asymmetric load introduction along the panel's height are compared with the ones of the $Pristine$ model in figure 4.38.

Also similarly as for the previous case, skin the out-of-plane deflections near the buckling point of the three models were taken for the same time step and shown in figure 4.39. This time step was slightly larger, due to the fact that as the applied rotation led to a smaller averaged compressive displacement, buckling also ocurred slightly later during these analyses. In this figure, as expected, buckling occurs earlier in the model with a positive rotation around the Y axis, as in this case the skin takes more load than the stringers. On the other hand, when the stringers are loaded more than the skin, buckling occurs later than in the $Pristine$ model.

Similar as in the case of asymmetric load introduction along the panel's width, also in this case the load-displacement responses of the models with asymmetrical loading are very similar to the one of the $Pristine$ panel model, small the mis-matches between them being also for the same reasons.

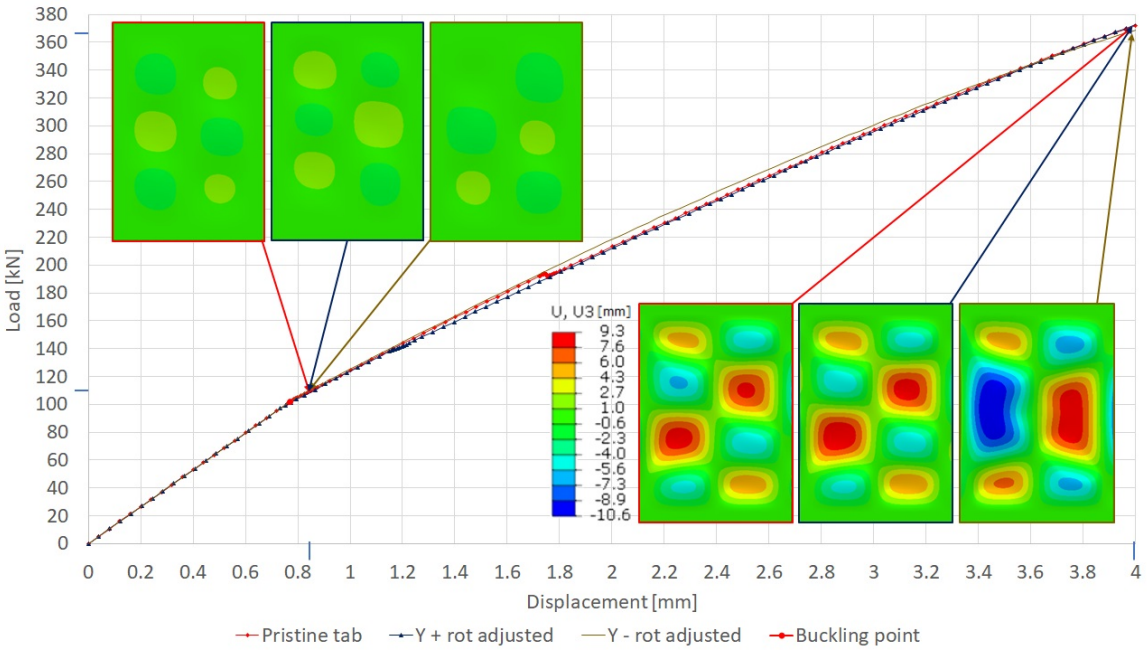

Figure 4.38: Comparison in terms of load-displacement curves and skin out of plane deflections between the pristine panel model and the panel models with asymmetric load introduction along its height

When looking at the first set of skin out-of-plane deflections from the above figure, one can notice that the initial 3 half-waves buckling pattern of the panel models with asymmetric load introduction width differ form the ones of the model with uniform load introduction. While the two panel models with asymmetric load introduction show an identical initial buckling pattern between them, this pattern is opposite with respect to the initial buckling pattern of the panel model with uniform load introduction.

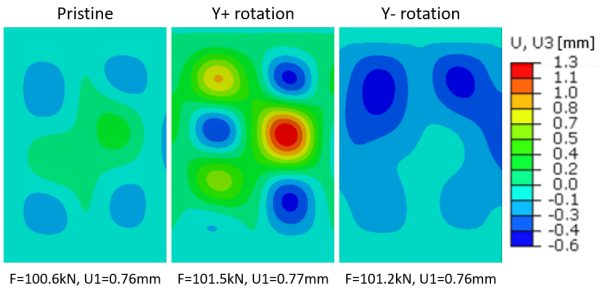

Figure 4.39: Comparison in terms of skin out of plane deflections between the pristine panel model and the panel models with asymmetric load introduction along its height

Secondary buckling occurs only when the skin is loaded more than the stringers, the resulting buckling pattern being identical with the one of the $Pristine$ model. The difference in the load levels of these two models for which secondary buckling occurs is $55kN$, which is significantly higher than for the previous case of asymmetrical load introduciton along the panel's width. This implies that the asymmetrical load introduction along the panel's height could have a stronger influence over the panel's skin buckling behaviour.

On the other hand, loading the stringers more does not lead to any secondary buckling, the $Y-rot$ model showing a 3 half-waves buckling pattern throughout the whole analysis. This model also showed the highest skin out-of-plane deflections at the end of the analysis, owing to the lower number of half-waves.

4.3.4 PANEL SENSITIVITY TOWARDS ITS IMPERFECT SHAPE

Often seen in both thermoset and thermoplastic stiffened panels, the resulted shape during the manufacturing process does not exactly match the nominal one, with significant deviations not being uncommon. The bulk of these deviations occur during the cooling stage of the manufacturing process and it comes as a result of different CTEs of the material/parts of a panel. These deviations also tend to be proportional with the processing temperature, making this panel more susceptible to these types of deviations, as the melting temperature of $PEKK$ (≈340° [37]) in particular is very high when compared to the processing temperatures of thermoset composites (generally lower than 220° for epoxies).

The effect of the real panel skin shape over the panel's compressive behaviour can have a significant impact, particularly for this panel which showed multiple signs of its very sensitive buckling behaviour. Therefore, especially as the occurring buckling pattern would also influence the skin-stringer de-bond growth, the influence of the real skin shape over the compressive behaviour of the panel was also studied.

PANEL DIC SKIN OUT-OF-PLANE DEFORMATION MEASUREMENT

The panel's skin shape is measured using a $3D$ Digital Image Correlation (DIC) measuring system, the measurement being done from both sides of the panel. In order to measure the panel's deformation through $3D$ DIC, the panel had to painted with a speckle pattern, as it can be seen in figure 4.28. To measure the panel's skin imperfection, the $3D$ system uses triangulation to measure out-of-plane deformations, instead of tracking used for the $2D$ in-plane displacement. The out-of-plane skin deformation of the panel can be seen in figure 4.40. In this figure the skin deflections sense are the same as previously used one, with positive deflections being towards the stringers.

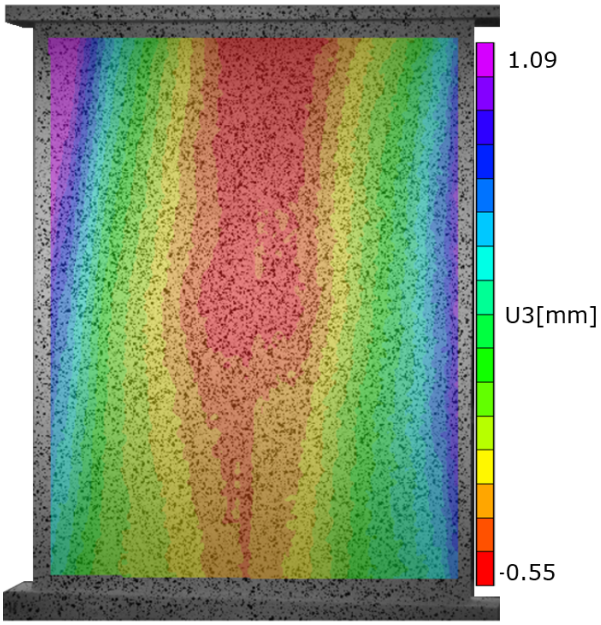

Figure 4.40: Panel DIC skin out of plane deformation/imperfection measurement

Important to mention here is that the DIC measurement scale is not according to a fixed reference point, it being determined relative to the panel's skin imperfection, using the deformation's amplitude. In other words, as the panel was centered to sit with the middle stringer's web along the $U3/Z$ axis and as the skin is curved around the stringers, more skin measurement points are laying closer to the highest deflection towards the stringer. Due to this reason the scale is not centered around a point of $0mm$ deflection and the skin deflection towards the stringer seems to be higher in magnitude.

As it can be seen from this figure, the skin is curved around the panel. As discussed before, this comes from the manufacturing process, due to the skin-webs butt-joints having a higher CTE than the skin laminate. This higher CTE of the filler results in a tendency to compress the top surface of the skin, bending the skin around the stringers and resulting in the general curvature seen here. Besides this general curvature, a higher deflection in the middle of the panel away from the stringer can be noticed. This is due to the existent debond between the middle stiffener and the skin shown in figure 4.1, as well as the means to extend the debond to the desired length. There is also an asymmetry that can be noticed at the top of the left stringer, the deformation pattern here being oblique on the stringer's web.

As the panel's skin imperfection is relatively large, its influence on the panel's compressive behaviour was also studied. To introduce this skin imperfection in the panel's FE model there were two main approaches considered. One of them was to implement the skin imperfection in the model definition itself, while the other was to introduce it as an imperfection, using the same procedure as the one earlier used to study the influence of multiple buckling patterns. Out of these two imperfection introduction methods, the latter was chosen, as it was both easier to implement it and as it also represented the real panel's geometry better. This was due to the fact that using only the skin deformation measured from the skin's side implies that all the other points without measurements would have had to be moved as well. As an example, using these measurement points on the skin's bottom would have meant that only the region from the bottom of the skin would be adjusted according to the measurement taken. In this case all the other FE model nodes laying outside the measured area from figure 4.40 (including the stringer side of the panel) would have needed adjustments made based on the initial panel geometry and the DIC measurements taken. This would have represented a relatively complex procedure, which would have been highly simplified if a $3D$ scan of the panel would have been available. If a $3D$ scan of the panel would have been made, the panel's FE model could have been built based on the $3D$ scan. This would have meant that not only the imperfect shape of the whole panel would have been included, but also any thickness variations within it. However, here a simpler procedure was

chosen based only on the skin imperfection measured from the skin side of the panel.

METHOD USED TO INTRODUCE THE SKIN OUT-OF-PLANE DEFORMATION MEASUREMENT IN THE FE MODEL

The approach taken here was to apply the measured imperfection by applying displacements on the bottom of the FE panel model's skin. This has the advantage of keeping the panel's size unchanged, while the areas without measurements are also automatically adjusted. This adjustment comes from leaving these areas to move freely as a result of the displacements applied on the bottom side of the skin. For example this would imply that the stringer webs would remain locally perpendicular to the skin at their intersection point. In other words, as the only panel constraints applied are the bottom skin measured displacements, the rest of the panel would deform as well as a result of these displacements.

The measurements points Z coordinates were applied as displacement BC in a separate FE model, with identical panel geometry, in a $Static, General$ analysis loading step. The analysis procedure used was not the previously used $Dynamic, Implicit$ one, as the nodal coordinates resulting from such a procedure cannot be further included in another analysis as an imperfection shape. Non-linear geometry was also enabled, the analysis being over a time period of 1, with a both an initial and a maximum increment of 1. The analysis was defined with only one increment as convergence issues, or concerns about its accuracy are none, the panel being completely unconstrained.

The skin displacements were introduced in the analysis by modifying the Abaqus analysis input file, which contains all the information needed for the Abaqus solver. To modify the Abaqus input file, a script was used to generate the syntax of the node sets containing the bottom skin nodes for which displacements were applied. The same script was also used to generate the syntax of the displacement boundary conditions applied to these skin node sets. The description of the script used, some implementation details and the code itself is shown in appendix D.

Using this script, an Abaqus input file was modified by introducing the skin measured Z coordinates as displacements along the Z axis in the FE model. The comparison between the DIC measurement shape and its FE model implementation can be seen in figure 4.41.

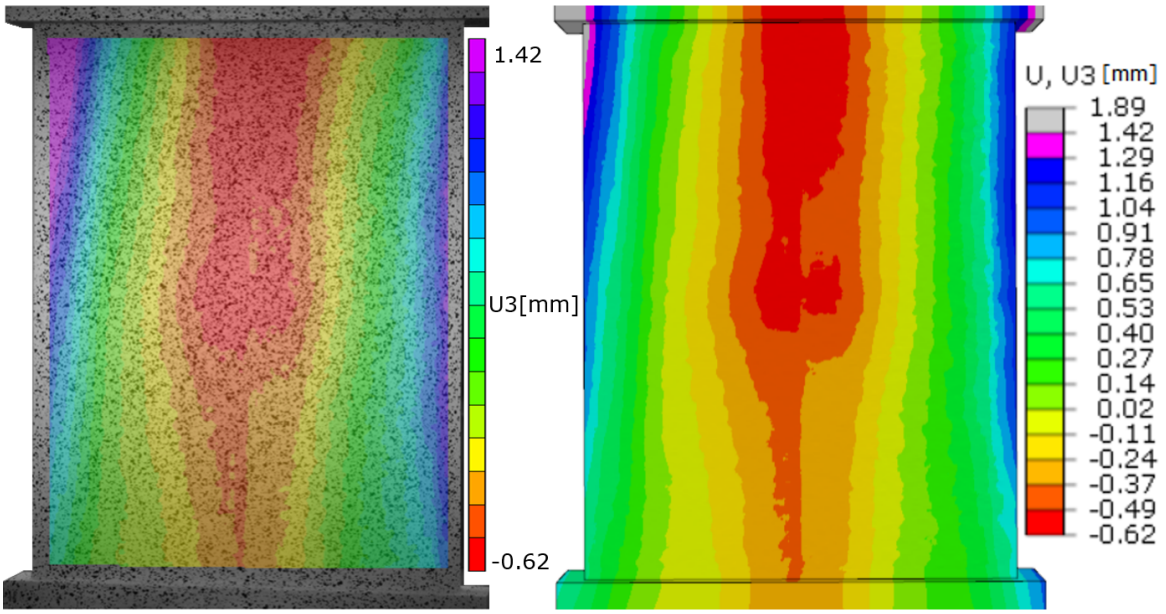

Figure 4.41: Comparison between the DIC measured skin imperfection (left picture) and its FE model implementation (right picture)

As in can be seen from these figure, the scales of the DIC skin measured imperfection and its FE implementation are adjusted such that a better comparison can be made between them. It can be seen from this figure that the implemented DIC measurement in the FE model is very similar with the DIC skin imperfection, the minor differences mostly coming from either a difference between the scales of the two models, or from the averaging used for the FE skin imperfection implementation. The difference between the maximum nega-

tive deflections between figure 4.40 and 4.41 came from the DIC measurement software neglecting extreme points, which is explained in more detail in appendix D.

Using the deformed shape of the panel shown in figure 4.41 as an initial imperfection, the compressive behaviour of the panel with an imperfect shape was studied. It was found during this study that the compressive behaviour of this model was very similar with the ones previously shown for the $Pristine$ and $Buckling$ 3+ models in figure 4.35, therefore here only the few relevant aspects are mentioned.

The main feature shared by this model with the $Buckling$ 3+ was an identical skin buckling pattern and a near identical load-displacement curve. The only mis-matches in the load-displacement curves were due to the gradual buckling in the latter, as the buckling point of the FE model with the imperfection included was slightly higher than the one of the $Pristine$ model. This aspect is most likely due to its small curvature along its width, which increases the panel's cross-section moment of inertia, therefore the panel's stiffness as well.

Secondary buckling event occurs in the model with the DIC imperfection at a load around $163kN$, which is roughly $30kN$ lower than the secondary buckling event occurring in the $Pristine$ model. As the panel FE model with the real skin imperfection implemented should be the most relevant, this lower load secondary buckling event could have a significant effect when damage is modeled, as it could promote de-bond growth at lower load levels.

Regarding the buckling behaviour of the panel with the DIC imperfection applied, modeling the resin tabs, or using tab equivalent boundary conditions also resulted in some potentially important differences. When using the tab equivalent boundary conditions, the secondary buckling event occurs slightly earlier, as shown in figure 4.42/

In this figure a skin out-of-plane deflection comparison between the $Pristine$, DIC imperfection and DIC imperfection with tab equivalent boundary conditions is shown. As mentioned earlier, here it can be seen that for the same load level, the model with the DIC imperfection implemented and with tab equivalent boundary conditions undergoes secondary buckling earlier than the other two. The load difference is relatively small, at around $8kN$ between the secondary buckling events occurring in the models with the DIC shape imperfection introduced, the one with tab equivalent boundary conditions being lower. However, after secondary buckling occurs in both models with the imperfection included, the buckling pattern resulted is the same, the main difference being the load at which this event occurs.

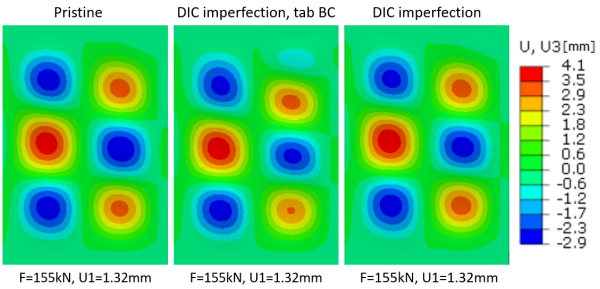

Figure 4.42: Panel DIC skin out of plane deformation/imperfection measurement

CONCLUSIONS

Studying the panel's undamaged behaviour revealed a number of important aspects. First, it found that using tab equivalent boundary conditions might not be a reliable option in capturing the panel's damaged behaviour, as it could significantly influence this panel's skin buckling behaviour.

Second, it was found that small skin imperfections could make a significant difference in what concerns the panel's skin buckling pattern. It was found that small skin buckling pattern based imperfections of $0.2mm$ in amplitude can change the panel's buckling behaviour from its nominal one when its skin is perfectly flat.

Third, it was found that asymmetric load introduction could also have a major impact on the panel's buckling behaviour. Among the observed effects were changing the panel's buckling pattern load, changing the load at which secondary buckling occurs, or preventing the secondary buckling pattern from occurring altogether.

Last, studying the influence of the measured panel's imperfection also confirmed the high sensitivity of the panel towards different buckling patterns, as the measured imperfection also changed the panel's buckling behaviour.

The main point to take form this study is that the panel's skin buckling behaviour is highly sensitive to the ends boundary conditions, skin imperfections, or asymmetric load introduction. As a strong relation between the de-bond growth and the panel's skin buckling pattern is expected, all these aspects could play a major role in the panel's failure load. Given the panel's skin buckling high sensitivity to different factors, the presence of the damage itself was also expected to play a significant role in the panel's skin buckling behaviour.

4.4 DAMAGED PANEL SENSITIVITY STUDY

The previous sensitivity study on the panel's undamaged behaviour revealed its high sensitivity towards different buckling patterns, as a function of multiple factors. However, the damage itself could also have an influence over both the panel's global behaviour, therefore further influencing its failure load. With that being said, the same sensitivity studies performed in the previous section 4.3, except the one for tab equivalent boundary conditions, are also be performed in this section. Furthermore, a sensitivity study regarding the damage itself and the modeling parameters used was also done. These involve different damage sizes, as well as different material properties to describe the skin-stringer separation. The model with the tabs modeled are considered to be more representative for the panel as it can influence its buckling behaviour, therefore this model was used in this section.

SKIN-STRINGER DE-BOND DAMAGE INTRODUCTION IN THE PANEL'S FE MODEL

In order to model the skin-stringer de-bond damage in the 3-stringer panel, the same approach as used before in modeling the 1-stringer's de-bond and the DCB de-bond described in sections3.1 and 3.2 is used. In a similar way to the 1-stringer panel, also for the 3-stringer panel a conservative maximum de-bond length was defined. This maximum de-bond length was chosen to be $280mm$, as this length is greater than the panel's half-length and it can be assumed the de-bond growth would become unstable before reaching this size, leading to complete skin-stiffener separation and ultimately to panel collapse. The cut made was also centered along the panel's length and it can be seen in figure 4.43

Similar as for the previous 1-stringer model, a trapezoidal shaped cut was made in the skin-filler butt-joint, leaving the skin intact and it had a negligible height of $5E^{-4}mm$. Using this cut, top and bottom surfaces were defined for which the $surface-to-surface$ contact behaviour with a $VCCT$ interaction property is defined. The $VCCT$ contact behaviour is defined in the same manner as the previous ones for the DCB and 1-stringer specimen, using the same material fracture properties and damage model implementation and with an initial clearance of $5E^{-6}mm$. Also for this analysis, a node set defining the bonding nodes needed to be specified. This node set was defined such that a de-bond along all the filler's width with a length of $70mm$ wass introduced in the model. This de-bond, like the cut used to define the VCCT contact, is centered along the panel's length.

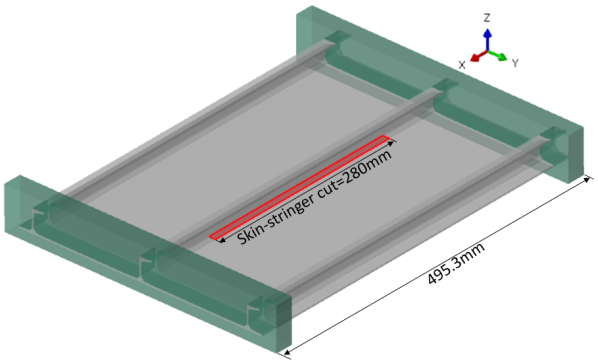

Figure 4.43: Panel de-bond cut

The de-bond length and shape was also verified, using its C-scan shown in figure 4.8. In this figure the left and bottom scales are in mm and they represent the width and the length scales respectively. The right scale represents the strength of the returned signal, which is used to determine if there is continuity in the butt-joint or not. As for butt-joint continuity the strength of the returned signal should be 0, or close to 0, the undamaged butt-joint appears colored in white or blue. This can also be verified by measuring the width of the area in the aforementioned colors. Using the white horizontal lines, one can notice that the width of this area is roughly $12mm$. This width is slightly smaller than the theoretical $14.484mm$ one, this difference likely coming from the very small material quantity at the butt-joint edges, where the radius meets the skin. This low amount of material can be seen in figure 4.20 showing the nominal geometry model. Using now the vertical white lines, one can notice that the de-bond length is indeed roughly $70mm$ when the areas where the de-bond spread along all the panel's width is considered. When a conservative approach is taken, the width of the de-bond can be considered to be roughly $74mm$ as this length would include all the areas that seem to be partially de-bonded. This de-bond length also includes the areas in dark blue representing a relatively low returned signal strength, thus possibly a de-bond. This de-bond length is also set to be included in the de-bond length sensitivity study, while for the rest of this sensitivity study the de-bond length used was $70mm$.

With the damage included, also the simulation was modified slightly. As the panel is expected to fail for a displacement far smaller than $4mm$, the displacement is lowered to $3mm$. Furthermore, the maximum increment allowed was lowered to 0.005 to improve the accuracy of the model with damage included.

4.4.1 DAMAGED PANEL'S COMPRESSIVE BEHAVIOUR

The load-displacement curve and skin out-of-plane deflections of the damaged panel is compared with the ones of the panel without damage in figure 4.44. In this figure also the de-bond pattern and de-bond lengths associated with the damaged panel's skin out-of-plane deflections are shown. These are placed at the left side of the figure and numbers are also used to identify the skin out-of-plane deflections and their corresponding de-bond patterns and lengths.

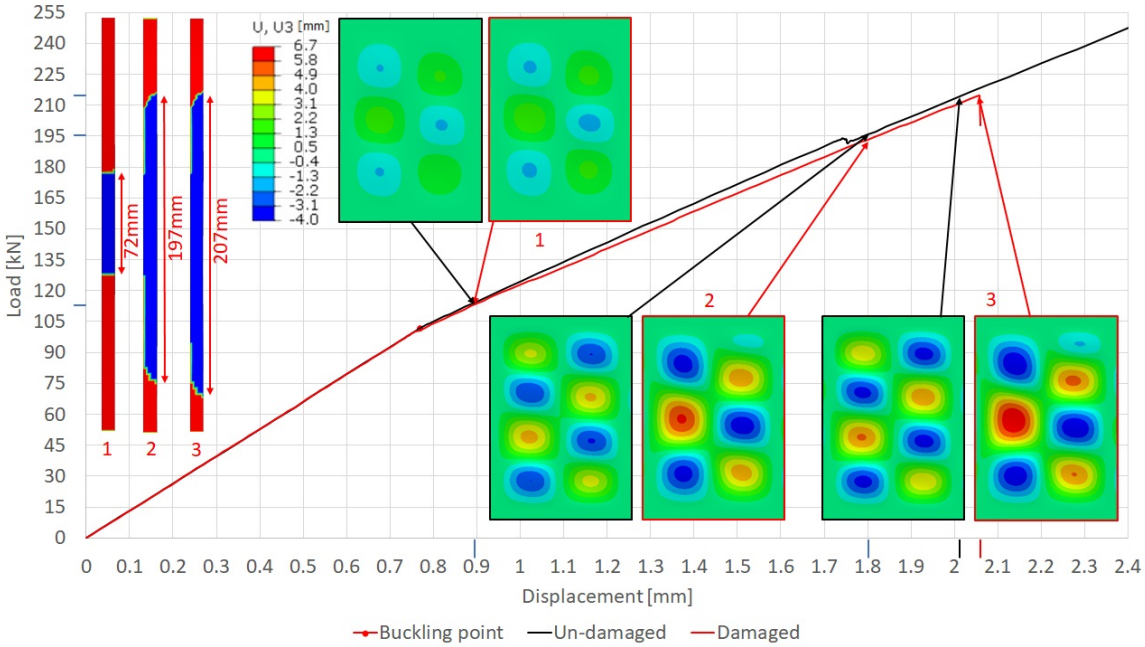

Figure 4.44: Panel's compressive behaviour with de-bond damage included

As it can be seen in this figure, the initial stiffness is the same between the two models, the de-bond having a negligible impact over this aspect. A small difference in stiffness can be seen immediately after buckling, the load-displacement curve of the $Damaged$ model being slightly lower.

Soon after buckling, at a load of $114kN$, the de-bond starts to grow, from the skin side with a buckling pocket deflecting away from the stringer. As the de-bond grows, it also leads to further divergence of the two load-displacement curves. This softening behaviour being best seen towards the end of the load-displacement curve. The de-bond growth manner is logarithmic, as the de-bond growth decreases rapidly as the load increases, this behaviour being counter-intuitive. The de-bond starts to grow in an unstable manner after reaching a length of $207mm$, at a load around $215kN$, which gives the panel's failure load. The analysis also crashes at this point, as the de-bond started to grow also on the side of the buckling pocket deflecting towards the stringer.

The occurring buckling pattern after the secondary buckling events is different between these two models and so is the load at which these occur. The load at which secondary buckling events occurs for the $Un-damaged$ model is around $193kN$, while for the $Damaged$ model it gradually starts from a load around $180kN$. The buckling pattern occurring after the secondary buckling event in the damaged panel is identical with the one occurring when the DIC measured imperfection is implemented. The different buckling patterns between these two models shows that the damage itself can also interfere with the skin's buckling pattern, therefore influencing the panel's global behaviour.

As expected, also the magnitude of the skin out-of-plane deflections is larger for the damaged panel. Furthermore, the largest magnitude is seen for the positive pocket deflection (towards the stringer), which is consistent with the previous findings.

When looking at the de-bond shapes, one can notice that there is a certain de-bond growth front, dictated by the existent buckling pattern. This de-bond pattern comes as a result of the adjacent buckling pocket deflecting away from the skin. This type of deflection induces a strong $Mode\ I$ separation component, which promotes skin-stiffener separation in its proximity. Interesting to notice is that on the other side of the stringer,

where the skin pocket is deflecting towards the stringer, there was still a line of nodes attached. With that being said, the de-bond growth is not along all the butt-joint's width, as the de-bond buckling pocket deflecting towards the stringer prevents the separation at this side. This is due to the fact that this deflection tends to close the de-bond and in its proximity it counteracts the tendency of the adjacent buckling pocket to open the de-bond and promote its growth.

Another aspect that can be noticed when looking at these de-bond growth fronts is the significance of the secondary buckling event. As the de-bond grows in the panel bay in which secondary buckling occurs, the de-bond growth front changes according the the buckling pattern occurred after this event. In this case, as the buckling pocket adjacent to the initial de-bond deflecting away from the stringer migrates downwards, so does the de-bond growth front. This can be noticed when looking a the 2 and 3 de-bond patterns, were it can be seen that the de-bond grew more downwards.

Similarly as in sections 3.1 and 3.2, where the DCB and 1-stringer specimens were studied, also for the 3-stringer panel the FE model including damage was analysed in terms of energies. For this model the expected behaviour in terms of energies was found up to the point of unstable de-bond growth, similarly as for the 1-stringer specimen. This means that the total internal energy component $ALLIE$ equaled the energy associated with the total work done by the model $ALLWK$, rendering also an energy balance $ETOTAL$ constant and near 0 prior unstable de-bond growth. After unstable de-bond growth occurred, this FE model showed a similar behaviour in terms of energies as the 1-stringer model.

As previously mentioned, when requesting the $SERR$s of the model the some energy components do not appear in the model's energy output. In order to analyse the model in terms of energy another ran was needed, in which the $SERR$s were not requested. Surprisingly, it was found at this stage that requesting the $SERR$s made the model crash when unstable de-bond growth was reached, while not requesting these led to a complete analysis. This aspect is particularly odd, as simply requesting different history outputs from the analysis should not influence the outcome of the simulation. The complete analysis also confirmed that the previous incomplete analysis crashed due to the unstable de-bond growth occurring at the load at which the initial one crashed. Due to this reason the load-displacement curves of these two analyses perfectly match, the failure load being confirmed by the later one to be around the previously found $215kN$ value. As this previous analysis was completed, the manner in which the FE model of the panel collapses could also be shown in more details.

PANEL COLLAPSE

Panel collapse occurs when unstable de-bond growth is reached, as nodes preventing the de-bond from reaching the adjacent panel bay begin to detach.. This aspect can be better seen in figure 4.45 showing the skin out-of-plane deflections and de-bond evolution when the point of unstable de-bond growth is reached.

As it can be seen from this figure, at the left side with respect to the middle stringer, the skin buckling pocket deflecting towards the stringer prevents the de-bond growth. At this side the measured de-bond length is still the initial one, at $70mm$. However, as soon as unstable de-bond growth starts, the nodes from this node line begin to detach as well. It can also be noticed from this figure that the skin buckling pocket deflecting away from the stringer is not large enough to generate de-bonds of such lengths alone. In all the four pictures shown in this figure there are skin deflections with a positive sign next to de-bonded regions, which means that in these areas these skin deflections alone could not have led to skin-stiffener separation. The answer on why the de-bond also grew over these areas was found by looking at the panel out-of-plane deflections from the stringer side. The stringer out-of-plane deflections for two load levels in the unstable de-bond growth region are shown in figure 4.46.

In this figure, the first row of stringer views are taken from the same load step as the bottom right picture from the previous figure 4.45. Also, the elements below the skin-web butt-joint have been removed in order to see easier the skin-stiffener separation. In the first view from this row, one can notice that the de-bond growth is not only promoted by the skin buckling pocket deflecting away from the stringer, but also by the stringer itself deflecting away from the skin. This stringer deflection at this side has two main causes. The first one is the existent de-bond in the middle region, which allows the stringer to deflect freely at this region. The second cause is that due to the skin buckling pattern, after the de-bond reaches a certain length, the stringer is only attached in regions that promote its deflection upwards. This can also be seen in this first view from the first row of pictures, as the areas in which the stringer is still attached are pointing upwards at both the stringer edges, as they follow the adjacent skin buckling pattern.

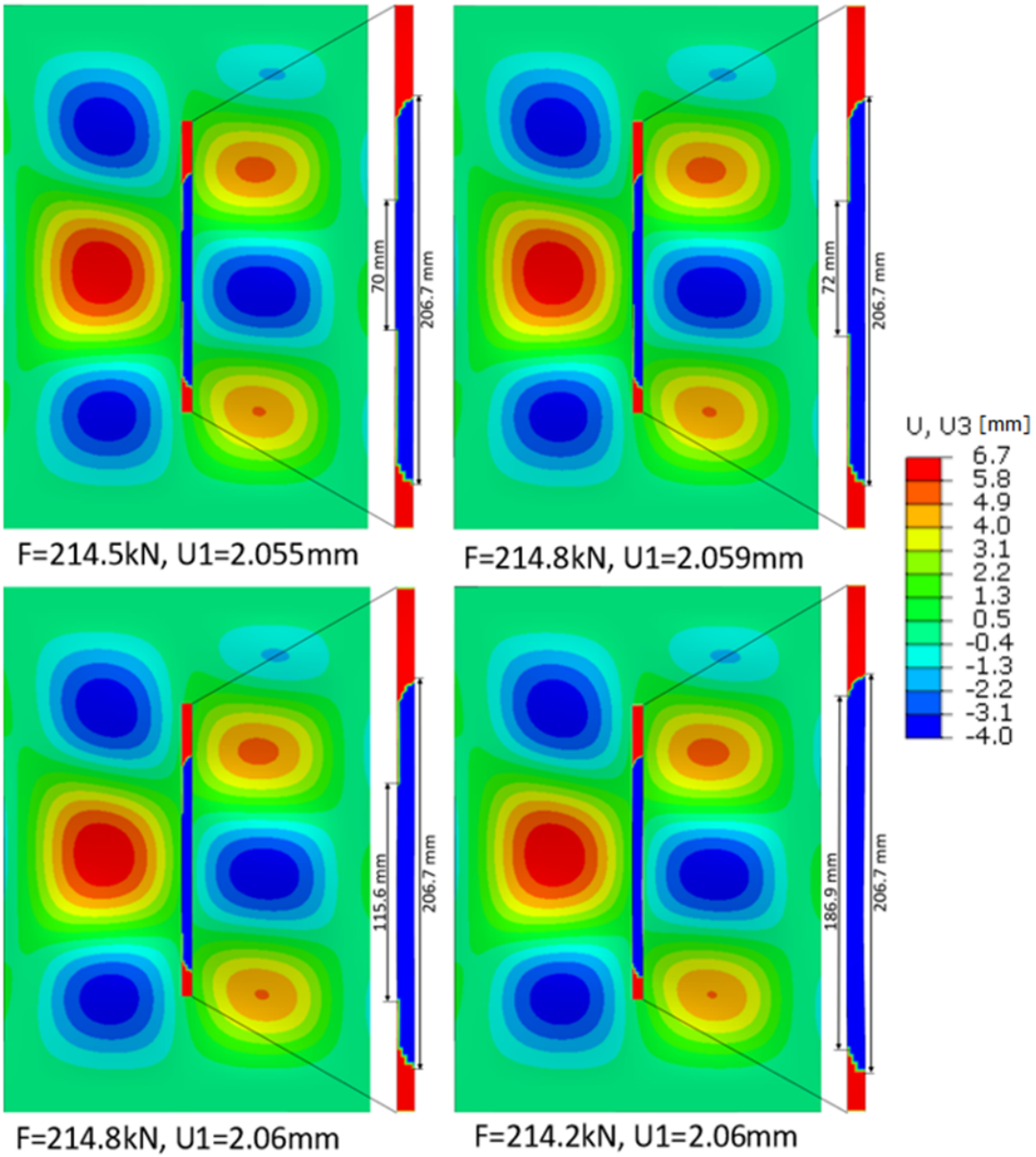

Figure 4.45: Panel skin out-of-plane deflections and de-bond evolution at unstable de-bond growth

In the second view form this row it can be seen that, although from figure 4.45 at the same load level the de-bond also reached this side, the separation is still not seen. Furthermore, it can also be seen that the adjacent skin buckling pocket deflecting towards the stringer still pushes against the skin-web butt-joint at this side, keeping the skin in contact with the stringer, although separation already occurred. This suggests that the de-bond growth at this side was not under mode I, but rather under *Mode II* or *Mode III*. This also implies that, while the de-bond growth might be governed mainly by the *Mode* 1 fracture toughness, the shear modes might be the ones governing when the unstable de-bond growth occurs, therefore the panle's collapse as well.

When looking at the last view from this first row, one can notice that a significant *Mode III* component could also appear during the unstable growth, as the stringer both rotates and tends to deflect sideways, inducing thus also a tearing, or *Mode III* component.

As it can be seen from the load level from which the second set of stringer views were taken, the panel collapse has already begun, the load drop being significant with respect to the panel's failure load. In the first view

from this row, one can notice that the cap deflection significantly relaxed, as the de-bond growth allowed a less constrained stringer movement. This can also be noticed from the last view from this row, where a higher lateral deflection can be noticed for this stringer cap. In this last view from the second row it can also be seen that the stringer rotation is significantly smaller, as the whole stringer deflects sideways. This aspect can best be seen when looking at the side deflection of the skin-web butt-joint, which is significantly higher in the cross-section view from the second row.

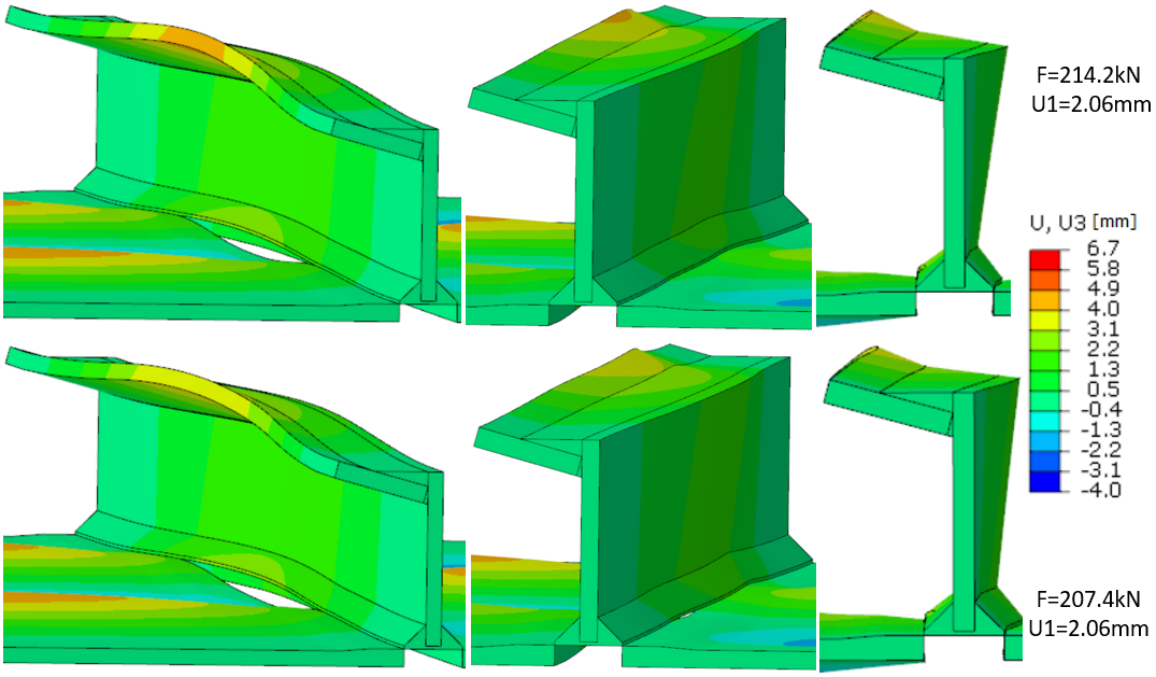

Figure 4.46: Views on the middle stringer deflections for two load levels at unstable de-bond growth

While a de-bond opening could not be seen in the second stringer view from the first row, same is not the case for the second row. Here a small de-bond opening can be seen in the proximity of the skin buckling pockets deflecting away from the skin. As previously mentioned, these two adjacent pockets deflection away from the skin tend to merge, leading ultimately to a large pocket across the middle stringer. When the maximum allowed de-bond length is reached, the stringer also buckles and deflects sideways. This tendency of the stringer to buckle and deflect sideways can be considered to significantly influence the de-bond growth only at higher load levels. Regardless, its influence on when the de-bond growth becomes unstable is unclear, as multiple buckling patterns can result in different tendencies of the stringer to deflect sideways.

The panel skin out-of-plane deflections at the *FE* model collapse are shown in figure 4.47, together with the load level and the panel's compressive displacement.

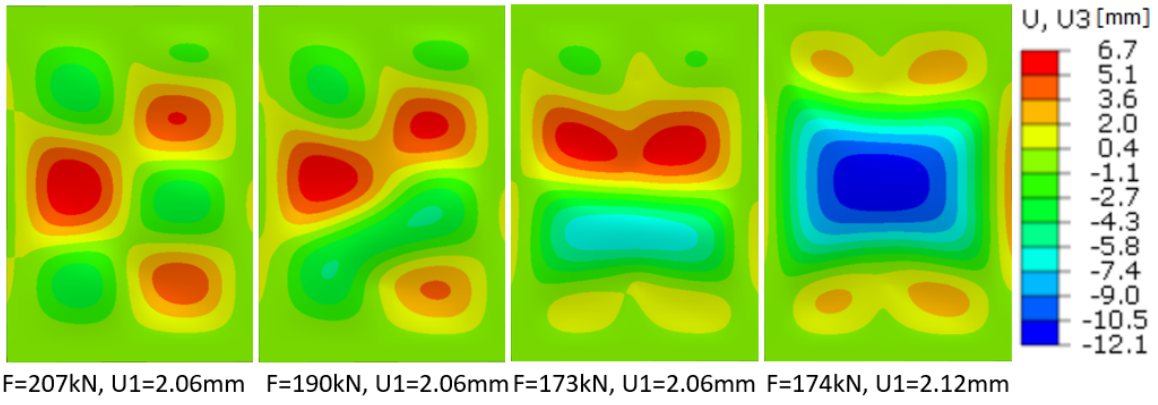

Figure 4.47: Panel FE model collapse

As mentioned earlier, the lower skin buckling pockets deflecting away from the stringer tend to unite and form a continuous buckling pocket across the panel's width. The same tendency is also seen for the buckling pockets deflecting towards the stringer, these also tending to form a single buckling pocket across the panel's width. However, this buckling pocket deflecting towards the stringers cannot be uniform across the panel's width, as the middle stringer impedes this type of buckling pattern. This is best seen in the third skin out-of-plane deflection picture form this figure, as below the stringer the skin out-of-plane deflection magnitude towards the stringer is lower than in the adjacent skin bays. As the deflection towards the stringer is impeded, the panel's skin deflects away from the stringer, forming a uniform buckling pocket in the middle of the panel. This uniform buckling pocket across the panel's width can be seen in the last skin out-of-plane picture from the above figure.

The unstable nature of the de-bond growth can also be seen from these load levels and panel compressive displacement reached, as the whole transition occurs for a panel displacement difference smaller than $0.06mm$, with a significant load drop. However, it has to be stated that this is just the failure seen in the FE model taking into account only the existent de-bond between the middle stringer and the skin. With that being said, most of this behaviour is unlikely to be noticed during the experimental test. This is due to the fact that in the experimental test the stringer-skin de-bond length is not limited and also due to the fact that other failure modes are likely to occur at this point. Among the other possible failure modes that are likely to occur are de-bonds at different locations within the stringers, as well as cap crippling.

EVOLUTION OF THE DE-BOND GROWTH MODE

Similar as for the previous DCB and 1-stringer specimen FE models, the de-bond opening modes during the analysis was studied by comparing the models $SERR$s. The strain energy release rate $SERR$ components also reveal the importance of the buckling pattern and of the buckling pockets deflecting away from the stringers. The $SERR$ components, or fracture toughness G components, for this model are shown in figure 4.48.

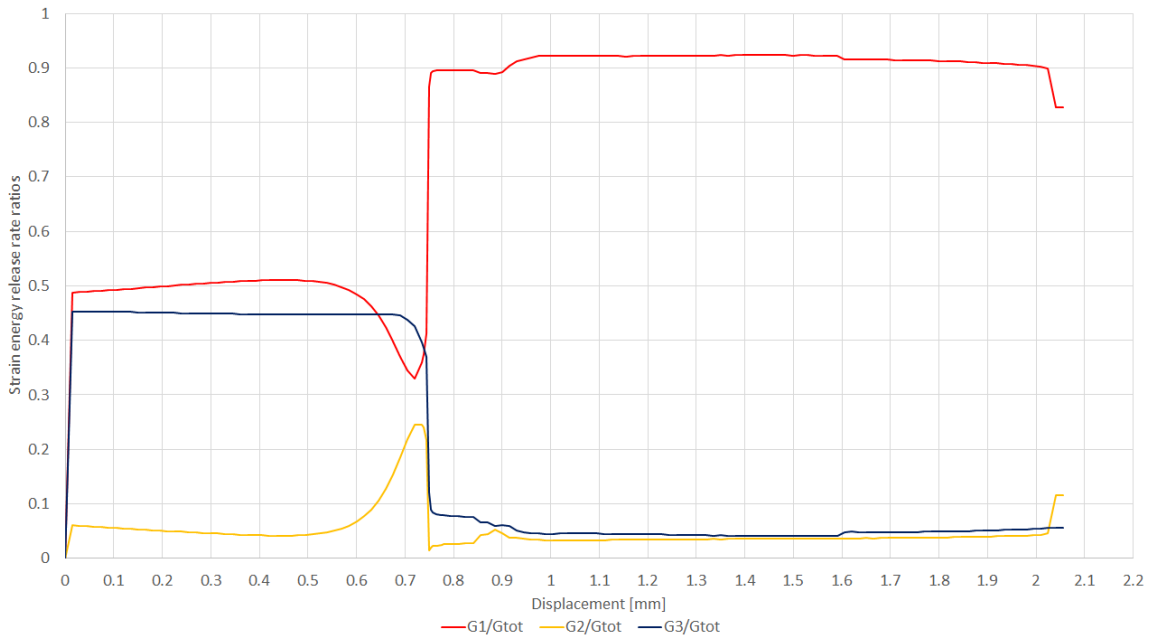

Figure 4.48: Panel's strain energy release rate componets (SERR, or G)

Here it can be seen that at the beginning of the analysis, the dominant component is $Mode\ I$, it being close to 0.5/1 at this point. $Mode\ I$ is followed closely $Mode\ III$, which sits constant at around 0.45/1 until the proximity of the buckling load/displacement is reached. $Mode\ II$ component is the lowest, starting from roughly 0.06/1 and decreasing until the proximity of the buckling load/displacement is reached.

While the $Mode\ III$ component is relatively flat in the initial linear-elastic, or pre-buckling stage, same is not the case for the mode I and II components. In this initial stage, there is a change between $Mode\ I$ and $Mode\ II$ components, with the former slightly increasing as the latter decreases by an equivalent amount.

Important to mention here is that the ratios before the buckling point are without de-bond growth, representing only the loading type of the skin-filler inter-phase. This behaviour however changes significantly as the buckling load/displacement is reached, as significant changes can be seen for all three mode components.

Upon reaching the buckling point, there is a high increase in $Mode\ II$ component, which is compensated by the $Mode\ I$ and $Mode\ III$ components. However, after buckling occurs, there is a massive spike in the $Mode\ I$ component, which is compensated by massive drops in the $Mode\ II$ and $Mode\ III$ components. Immediately after buckling, the $Mode\ I$ becomes clearly dominant, as now its value is around 0.9/1, with the $Mode\ III$ component is roughly 0.08/1. This confirms the tendency of buckling pattern to load the de-bond under a dominant $Mode\ I$. From this point until the point where the de-bond starts to grow (U=0.885mm), the only growing component is $Mode\ II$, with the other two decreasing. As soon as the de-bond starts to propagate, there is another small increase in the $Mode\ I$ component, now reaching a value around 0.92/1, with the other two components decreased. After this point the values of the three components remain roughly constant, until the point of unstable de-bond growth was reached.

Having a dominant mode I component in the region of stable de-bond growth is in agreement with the aforementioned observations regarding the buckling pattern and the de-bond pattern. Namely, the dominant $Mode\ I$ component is given by the buckling pocket adjacent to the initial de-bond and deflecting away from the stringer. This particular buckling pocket tends to separate the skin from the stringer and as a result the de-bond growth front is curved according to this particular buckling pattern.

The point of unstable de-bond growth is marked by a change between the $Mode\ I$ and $Mode\ II$ componets, as the latter grows. After this event the $Mode\ II$ component grows up to a value slightly higher than 0.1/1, while the $Mode\ I$ component drops to a value slightly higher than 0.8/1. This increase in the $Mode\ II$ component associated with a drop in the $Mode\ I$ component might be due to the stronger tendency of the skin and stringer to deform separately, which increases the sliding component along the longitudinal direction of the $VCCT$ region. This high increase in the $Mode\ II$ component when unstable de-bond growth is reached adds further support to the previously made affirmation, namely that unstable de-bond growth, thus the panel's failure load, is mainly $Mode\ II$ dependent.

Another reason for this significant $Mode\ II$ component increase could be simply the transition region between a skin buckling pattern with multiple half-waves in the two skin bays, to a skin buckling pattern having only one large, global half-wave in both the skin bays. This latter skin buckling pattern occurs in the FE model after as all the remaining bonded nodes detach and the panel is considered collapsed.

4.4.2 DAMAGED PANEL'S FAILURE LOAD SENSITIVITY TOWARDS DIFFERENT BUCKLING PATTERNS

In a similar way as for the panel's undamaged behaviour and sensitivity towards different buckling patterns from the previous sections, the same study is also repeated here, but now with the skin-stiffener de-bond damage taken into account.

For this study a buckling eigenvalue analysis was conducted again to obtained the deformed panel shape for the new panel mesh, the one with the $VCCT$ cut included. In order to obtain the same buckling shapes as for the panel without damage included, the surfaces created to simulate a de-bond using $VCCT$ were tied, such that the buckling behaviour of the undamaged panel is mimicked for this new mesh. In this tie constraint a $surface-to-surface$ discretization method was used, without adjusting the slave node's initial position and with a specified tolerance of 0.01. This custom tolerance is used to be sure that all the desired nodes were tied together and it was chosen based on the mesh size in the cut area. As expected, using a tie constraint in this cut area led to negligible differences in terms of buckling load and displacement eigenvalues. With the desired buckling deformed shapes also obtained for the new mesh configuration, the same type of deformed shapes are applied as in the previous study, using the same ± 0.1 amplitude for the first two buckling patterns.

As the sensitivity of the undamaged panel for the same cases was already studied, the compressive behaviour of the damaged panel was compared with both its undamaged behaviour for the same case, together with the compressive behaviour of the $Damaged$ panel model. Similarly as for the undamaged panel sensitivity study, the panel's compressive behaviour was compared in terms of load-displacement response, skin out-of-plane deflections, plus also de-bond pattern and length.

DAMAGED PANEL SENSITIVITY TOWARDS THE FIRST BUCKING MODE

When a +0.1 amplitude of the first mode was applied, the model's response was near identical with the one previously described for the *Damaged* model.

In terms of buckling pattern and skin out-of-plane deflections, the differences between these two models were negligible, as both had the same buckling pattern and negligible differences in skin out-of-plane deflections. Furthermore, the de-bond pattern and length were also very similar, with the differences in de-bond length being only in range of a few millimeters for the same load level.

Surprisingly, the $Buckling3+\ damaged$ model had a higher failure load than the *Damaged* one, as it failed at around $217kN$, compared with the $215kN$ failure load of the *Damaged* one. The only other minor difference between these two models was the gradual buckling of the model with the initial buckling imperfection applied, which was expected.

On the other had, when a -0.1 amplitude of the first mode was applied, the model showed collapse at a load significantly earlier than the *Damage* model. The panel compressive behaviour of this case is shown in figure 4.49.

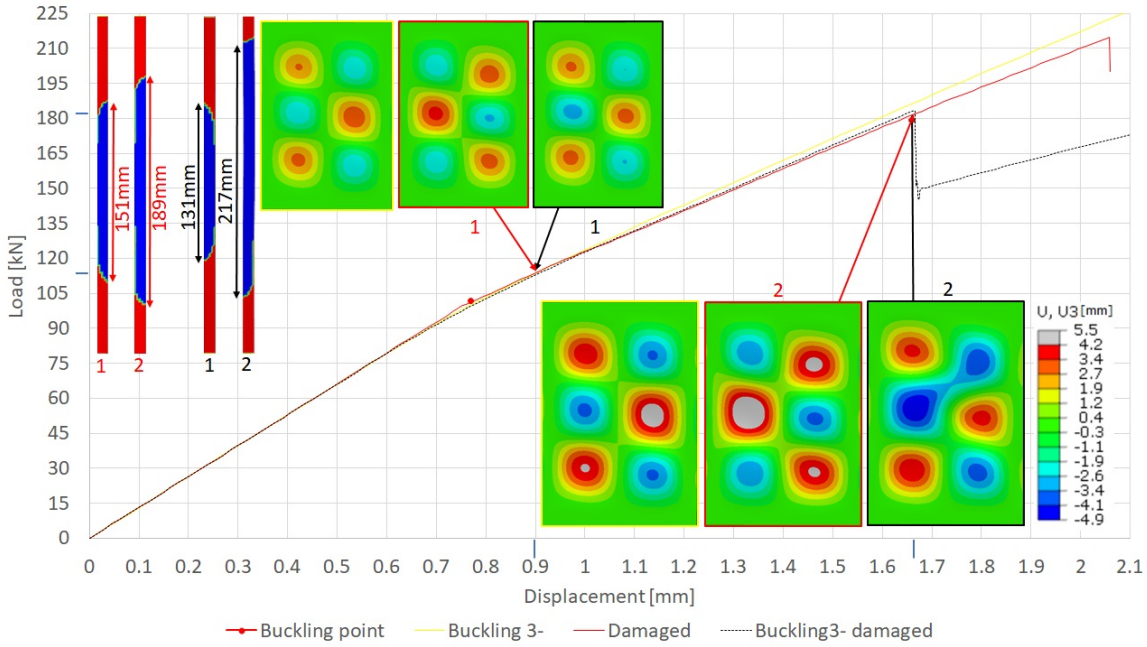

Figure 4.49: Panel's compressive behaviour with a 'negative' 3 half-waves buckling pattern

As expected, the de-bond pattern in the $Buckling3-\ damaged$ is opposite than in the *Damaged* model, owing to the introduced imperfection. Having this particular buckling pattern had a huge impact on the panel's failure, as in the *FE* model with this buckling pattern failure is reached at load around $183kN$, which is roughly $34kN$ lower than the failure load seen in the *Damaged* model. While the curves of the $Buckling\ 3-$ and $Buckling3-\ damaged$ models perfectly overlap until the de-bond starts to grow in the latter model, after this point there are more similarities between the latter and the *Damaged* model in terms of load-displacement response.

The skin buckling pockets deflecting away form the stringers in the $Buckling3-\ damaged$ model were larger than in the other two models, while the skin pockets deflecting towards the stringer were smaller than than in the other two. This implies that this particular buckling mode promotes larger skin out-of-plane deflections away from the stringer, particularly when damage is also included, therefore increasing the strength of the *Mode I* separation component. At the same time, the lower skin pocket deflections towards the stringer could also play a role in this lower failure load. However, initially the de-bond length in the $Buckling3-\ damaged$ model was smaller than the one in the *Damaged* panel for the same load levels, which suggests that these skin out-of-plane deflections in this case did not necessarily promote faster de-bond growth.

From this figure also the strong relation between the de-bond growth front and the buckling pattern can be

observed, as well as the slightly difference panel collapse than in the *Damaged* model. In this model the skin buckling pocket deflecting away from the stringer is on the opposite side with respect to the middle stringer, which results in a mirrored de-bond pattern for the $Buckling3-damaged$ model when compared with the *Damaged* model. Furthermore, the collapse in this panel is given by the tendency of the middle skin buckling pocket deflecting away from the stringer to unite with its upper corresponding pocket from the adjacent bay. This is different than in the *Damaged* model where the the middle pocket, merged with its lower corresponding pocket from the adjacent bay. This aspect can be seen by comparing the skin out-of-plane deflections from figures 4.44 and 4.49.

DAMAGED PANEL SENSITIVITY TOWARDS THE SECOND BUCKING MODE

The compressive behaviour of the model with an initial imperfection based on the second buckling mode with an +0.1 amplitude applied is shown in figure 4.50.

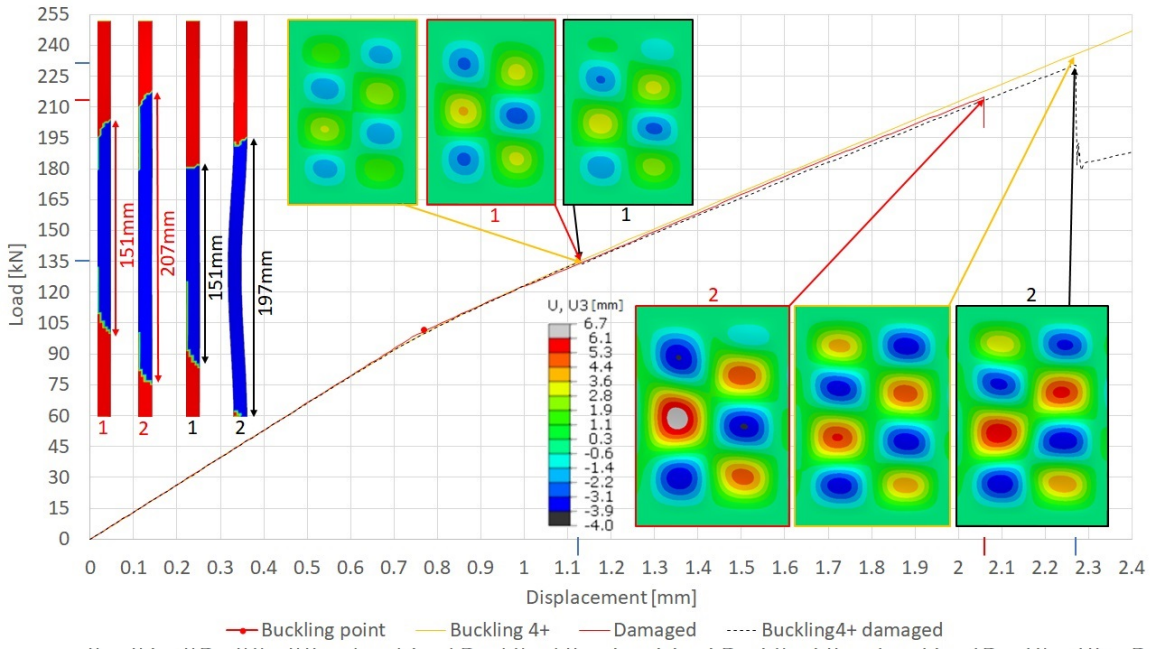

Figure 4.50: Panel's compressive behaviour with a 'positive' 4 half-waves buckling pattern

As expected, this different skin buckling pattern also had a strong influence over the de-bond pattern. Having a 4 half-waves buckling pattern means that now the skin buckling pocket deflecting away from the stringer is no longer centered along the panel's length, which means that also the de-bond pattern is no longer centered along the panel's length either. The de-bond length is initially the same between the $Buckling4+ damaged$ and the *Damaged* model, while for higher loads the de-bond length is smaller in the former.

This de-bond growth is promoted by the skin buckling pocket deflecting away from the skin with the highest magnitude, which is the lower one of the right. The higher deflection magnitude in this particular skin buckling pocket was not an aspect related to the damage included, but an inherent behaviour for the initial imperfection applied.

When comparing the last set of skin out-of-plane deflections from figure 4.50, one can notice that the skin deflection magnitude of the $Buckling4+ damaged$ model is significantly lower than the ones of the other two models, due to the tendency to have lower skin out-of-plane deflection magnitudes for higher number of half-waves. This difference in skin out-of-plane deflections magnitude could also explain why in the $Buckling4+ damaged$ model a lower de-bond length and a higher $230kN$ load level before unstable de-bond growth is seen .

While introducing a +0.1 imperfection amplitude of this second buckling mode delayed the panel's collapse significantly, quite the opposite was observed when a -0.1 imperfection amplitude was applied. The compressive behaviour of the model with an initial imperfection based on the second buckling mode with a -0.1 amplitude is shown in figure 4.51.

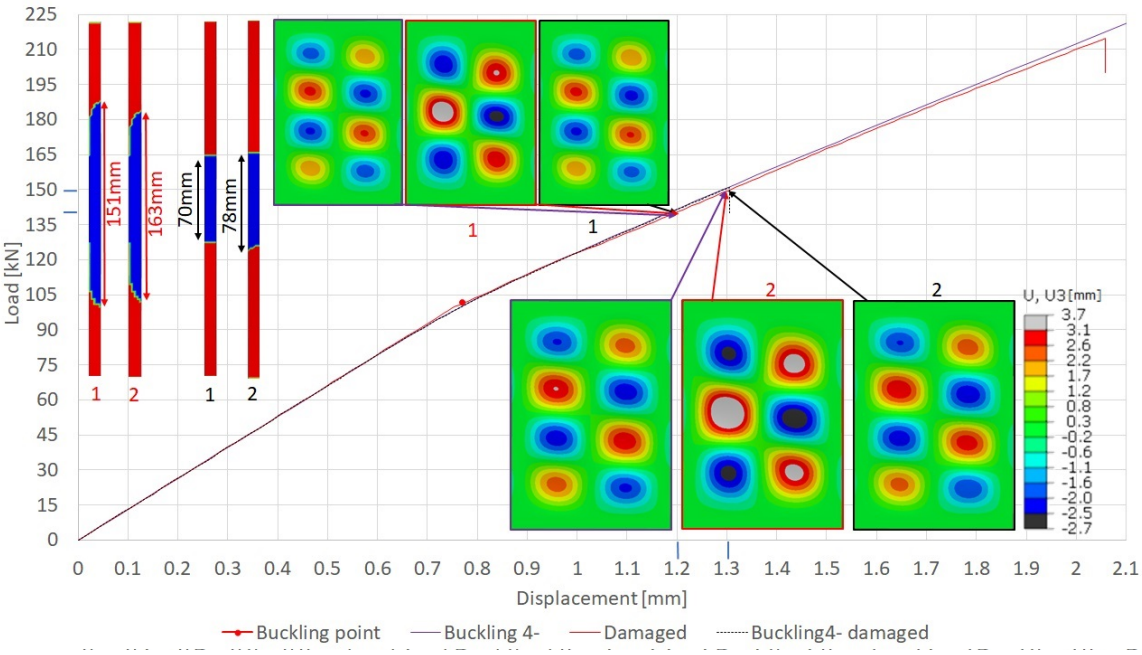

Figure 4.51: Panel's compressive behaviour with a 'negative' 4 half-waves buckling pattern

As it can be seen from this figure, this skin buckling pattern seems to be the most critical one, as the $Buckling4-damaged$ model fails at a load of $151kN$. This failure load is smaller than the one of the $Damaged$ model by roughly $66kN$, which implies that the failure load could decrease by more than 25%, due to a different skin buckling pattern only.

This buckling pattern also gives a highly different de-bond growth, as the de-bond growth is significantly delayed with respect to all the other models previously shown. However, soon after de-bond growth starts, it becomes unstable after reaching a small de-bond length of only $78mm$, while for all the previous models shown unstable de-bond growth occurred for de-bond lengths around $200mm$ or higher.

Similarly with the previous case, also for this $Buckling4-damaged$ model the skin out-of-plane skin deflections magnitude is significantly lower than the one of the $Damaged$ model. While this difference with respect to the $Damaged$ model is relatively high, same is not the case when compared with the $Buckling$ 4+ model, the skin out-of-plane deflections between these two models being negligible. With the skin out-of-plane deflections at which unstable de-bond growth is reached are significantly different than the previous one, it reveals that there are also other factors governing the unstable de-bond growth. As the panel with the de-bond growing in the left panel bay for a 3 half-waves buckling pattern also had a significant lower failure load, it would seem that a de-bond growing in this panel bay could be more critical. This behaviour is not unlikely, given the asymmetric stringer geometry of this panel, this bay also being the weaker one, containing only one of the three stringer caps.

4.4.3 DAMAGED PANEL SENSITIVITY TO ASYMMETRIC LOADING

In this section the sensitivity study done for the undamaged panel model shown in section 4.3.3 is repeated for the damaged panel. The load introduction asymmetry is mimicked in the same manner as in the aforementioned previous section, therefore only the different aspects with respect to that sensitivity analysis are mentioned. The biggest difference for these asymmetric load introduction cases is that in the first step in which the rotation was applied to introduce the asymmetry, the analysis step was increased from 0.1 to 0.5 from a total time step of 1. This change had no effect in terms of the accuracy of the analysis, while the CPU time was significantly improved.

DAMAGED PANEL SENSITIVITY TO A HIGHER LOAD IN THE LEFT PANEL BAY

The compressive behaviour in the case where the left panel bay is loaded more was almost identical with the one of the $Damaged$ model, therefore only significant difference is mentioned here.

This main difference with respect to the $Damaged$ model was that the initial skin buckling pattern was

kept until unstable de-bond growth occurred at a load level of $214kN$ (compared with the $215kN$ one of the $Damaged$ model). This particularity of the buckling behaviour is also the same as in the case where this asymmetrical load was studied without the damage included.

DAMAGED PANEL SENSITIVITY TO A HIGHER LOAD IN THE RIGHT PANEL BAY

The compressive behaviour in the case where the right panel bay was loaded more than the left one was highly similar with the presented in section 4.4.2 for a -0.1 amplitude of the first buckling pattern.

The buckling pattern was the same as the previously shown one for the $Buckling\ 3-$ and $Buckling3-damaged$ models from figure 4.49. However, the damage did influenced the skin's buckling behaviour at higher loads, as for the model including damage the secondary buckling event is no longer seen. The failure load of this model is the same with the one of the $Buckling3+\ damaged$ model, at around $183kN$, which would suggest that the main cause for this earlier failure when compared with the $Damaged$ model could be mainly due to the skin's buckling pattern.

DAMAGED PANEL SENSITIVITY TO A HIGHER LOAD IN THE SKIN

The model with its skin loaded more gave roughly the same compressive and buckling response as the $Damaged$ model, despite having a different initial buckling pattern when the damage was not included. Loading the skin more seemed to delay the secondary buckling event, it showing signs of appearing only near the failure load, at around $217kN$. However, at failure the panel still showed a pure 3 half-waves buckling pattern in both panel bays.

As expected, the magnitude of the skin out-of-plane deflections of this model for the same load level were slightly higher than the ones of the $Damaged$ model, which also correlated with slightly higher de-bond lengths for this model. However, the higher skin deflections magnitudes of the pockets towards, the stringers, as well as the delay of the secondary buckling was likely the cause of the slightly higher failure load seen in this model when compared with the $Damaged$ one.

DAMAGED PANEL SENSITIVITY TO A HIGHER LOAD IN THE STRINGERS

While loading the stringers more for the panel whiteout damage gave a different buckling pattern than the one of the $Damaged$ model, when the de-bond was included the buckling behaviour matched the one of the $Damaged$ model. Due to this reason, the compressive behaviour of the model with its stringers loaded more was very similar with the one of the $Damaged$ model.

Loading the stringers more seemed to lower the secondary buckling load in this model, as well as to give a lower skin out-of-plane deflection magnitude. These two aspects also led to generally lower de-bond lengths for the same load level, as well as to a higher failure load, at roughly $223kN$, compared with the $215kN$ one of the $Damaged$ model. This higher failure load was somewhat expected, as lower skin out-of-plane deflections were also seen for the same loading case without damage.

4.4.4 DAMAGED PANEL SENSITIVITY TO DE-BOND LENGTH

With the initial de-bond of roughly $42mm$ being extended to mimic a realistic crack surface, the $70mm$ desired de-bond length might not have been accurately reached. As the initial de-bond length could also play a significant role in the panel's failure load, different de-bond lengths of $66mm$ and $74mm$ were also simulated using the existent model. Regarding the modeling aspect, these different de-bond lengths were simply modeled by adding or removing nodes from the set used by the Abaqus $VCCT$ method to define the de-bond front, such that the initial de-bond would measure either $66mm$ and $74mm$.

As expected, the main difference between these three models was their failure load. Having an initial de-bond length of $66mm$ gives a higher failure load by roughly $3kN$, while having an initial de-bond length of $74mm$ gives lower failure load by roughly $2kN$, compared with the failure load of roughly $215kN$ for an initial de-bond length of $70mm$. The de-dond lengths for the same load levels were also identical, while the de-bond length at which unstable growth occurs was only the same for the model with de-bonds of $70mm$ and $74mm$, for the $66mm$ one being slightly higher. This slightly higher de-bond in this latter model is mostly owing to the de-bond growing downwards, as its driven by the migrating skin buckling pocket deflecting away from the stringers after the secondary buckling event.

4.4.5 DAMAGED PANEL SENSITIVITY TO THE MATERIAL DAMAGE MODEL PARAMETERS

The material damage model parameters of the $VCCT$ damage model used were the measure fracture toughnesses and the BK coefficient for the mix-mode fracture propagation criterion.

In measuring fracture toughnesses significant errors can occur, especially for the $Mode\ II$ and $Mode\ III$ fracture toughneses, for which a unique measurement standard as for the $Mode\ I$ fracture toughness does not exist. This can also be verified by checking the measurement technique standardized by the most relevant authorities. While standardization authorities like $ASTM$, ISO, or EN chose the DCB specimen to measure the $Mode\ I$ fracuture toughness [38, 60, 61], same is not the case for $Mode\ II$ fracture toughness. For $Mode\ II$ fracture the $ASTM$ standard uses the ENF test [62] (End-Notched Flexure) and the ISO standard uses the $C-ELS$ test [63] (Calibrated-End-Loaded Split). While for $Modes\ I$ and $Mode\ II$ there are standardized methods to characterize their corresponding fracture toughnesses, same is not the case for the $Mode\ III$ opening, although a great number of methods were proposed [64–66], all coming with their own shortcomings. With that being said, it is important to asses what could be the compressive behaviour of the panel if the fracture toughness values are altered. For this sensitivity study, a measurement error of ±10% for each fracture toughness value was simulated. For the nominal value of $1.41 kJ/m^2$ for the $Mode\ I$ fracture toughness, this meant changing this value by $\pm 0.141\ kJ/m^2$, while for the nominal values of $2.2 kJ/m^2$ for both the $Mode\ II$ and $Mode\ III$ fracture toughness, this meant changing these values by $\pm 0.22 kJ/m^2$. As a reminder, the value of the $Mode\ III$ fracture toughness is assumed to be equal to the one of the $Mode\ II$ fracture toughness, as a measured value for this $Mode\ III$ was lacking for the APC lamina [36].

DAMAGED PANEL SENSITIVITY TO $Mode\ I$ FRACTURE TOUGHNESS

The compressive response of the panel models with a ±10% difference in the $Mode\ I$ fracture was negligible, having the same failure load around $215 kN$ like the $Damaged$ model. The only minor differences were seen in the de-bond length for the same load level, but a clear trend as a function of the $Mode\ I$ fracture toughness could not be defined.

DAMAGED PANEL SENSITIVITY TO $Mode\ II$ FRACTURE TOUGHNESS

Modifying the $Mode\ II$ fracture toughness by ±10% led to a difference of $\pm 4 kN$ in the panel's failure load, the relation between these being proportional. Similarly as varying the $Mode\ I$ fracture toughness, although differences in the de-bond length for the same load level were observed, a clear trend as a function of this fracture toughness could not be defined. The higher influence of the $Mode\ II$ fracture toughness was also suggested earlier based on the de-bond growth behaviour and the mode openings ratios when unstable de-bond growth is reached.

DAMAGED PANEL SENSITIVITY TO $Mode\ III$ FRACTURE TOUGHNESS AND BK COEFFICIENT

A study on the influence of the mode III fracture toughness was also done in the same manner as for the other two, by varying the initial value by ±10%. However, the results were identical with the ones of the $Damaged$ model previously shown in this section, hence these results are not shown here. This would also imply that the tendency of the stringer to deflect sideways could indeed be not important in inducing unstable de-bond growth, therefore irrelevant for the panel's failure load. A similar study was also done for the BK coefficient η used in the $VCCT$ material parameters, but as very similar results were found these were also not shown here.

4.4.6 DAMAGE PANEL SENSITIVITY TOWARDS ITS IMPERFECT SHAPE

The behaviour of the panel with damage and the same shape as described in section 4.3.4 was also studied. As a reminder, another analysis had to be done to generate this imperfect shape based on DIC skin imperfection measurement, as again the mesh configuration slightly changed due to the damage included. For this analysis to introduce the imperfection, similar with the one to determine the shapes to induce different buckling modes, discussed in section 4.4.2, the surfaces between which the $VCCT$ contact behaviour were tied.

The compressive behaviour of the panel with this imperfect shape was highly similar with the one of the $Damaged$ model, the main difference being a slightly higher failure load. In this case the failure load was around $221 kN$, which is roughly $6 kN$ higher than the one of the $Damaged$ model. This slightly higher failure load was associated with the lower skin out-of-plane deflections than the one of the $Damaged$ model. In terms of de-bond lengths, the ones of this model are also slightly lower than the ones of the $Damaged$ model for the same load levels and also at the point of unstable de-bond growth.

4.4.7 DISCUSSION ON THE DAMAGED PANEL'S SENSITIVITIES

The sensitivity study of the panel with damage included revealed a number of important aspects concerning the panel's compressive behaviour. Table 4.11 shows the de-bond growth initiation load F_{ini} and displacement U_{ini}, together with the load F_{udg}, displacement U_{udg} and de-bond length when the unstable de-bond growth is reached for all the models discussed in section 4.4. In this panel the most critical values are highlighted in red font, while the most 'beneficial' ones are highlighted using a green font.

Panel model	De-bond start		Failure (unstable crack growth)		
	F_{ini} [kN]	U_{ini} [mm]	F_{udg} [kN]	U_{udg} [mm]	De-bond [mm]
Damaged	114	0.9	215	2.06	207
Buckling 3-	114	0.9	183	1.665	191
Buckling 3+	113	0.9	217	2.09	211
Buckling 4-	147	1.26	151	1.32	78
Buckling 4+	132	1.1	230	2.27	173
Higher skin load	112	0.89	217	2.09	215
Higher stringer load	117	0.92	223	2.15	201
Higher right bay load	118	0.94	183	1.66	189
Higher left bay load	115	0.91	214	2.05	213
+10%G1	115	0.91	215	2.06	203
-10%G1	114	0.9	215	2.06	209
+10%G2	114	0.9	218	2.1	209
-10%G2	114	0.9	211	2.01	205
±10%G3	114	0.9	215	2.06	207
±10%η	114	0.9	215	2.06	207
66mm de-bond	114	0.9	218	2.1	217
74mm de-bond	114	0.9	212	2.03	207
DIC imperfection	115	0.91	221	2.13	205

Table 4.11: Damaged panel's de-bond growth behaviour and failure load summary

Most of the models showed de-bond growth initiation around a load of $114kN$, a failure load around $215kN$ and a de-bond length prior unstable growth around $207mm$. These mean values were found mainly for the models which showed the same skin buckling pattern as the $Damaged$ model.

When looking at this table, it can be noticed that the occurring skin buckling pattern has the highest influence on the panel's failure load. Loading the right panel bay more than the left one also had a high impact on the panel's failure load, but this was mostly as in this case the same buckling pattern as in the $Buckling\,3-$ case was observed, therefore the identical failure load.

Besides the occurring skin buckling pattern the other aspects that could lower the panel's failure load are a slightly lower $Mode\,II$ fracture toughness and a larger de-bond length.

Important to mention here is that for the models with the same skin buckling pattern and no other parameter modified, namely for the $Damaged$, $Buckling\,3+$ and $DIC\,imperfection$ models the failure load differences are relatively small. This would imply that when the panel's measured skin imperfection is not accounted, the failure load would be relatively similar, provided that the skin's buckling pattern is correctly captured.

Out of these models, the best prediction is considered to be given by the $DICimperfection$ model, as it represents best the real state of the panel. Therefore this model was further used for the test-simulation correlation. While the skin-stiffener separation was here considered to be the critical failure mode, leading to the panel's collapse, other failure modes were also assessed.

ADDITIONAL FAILURE CHECKS

Laminate strength was assessed using the Abaqus Hashin 2D, Tsai-Wu and Tsai-Hill criteria [67–69], for which the material strengths shown in table 3.2 were used. These failure criteria were used for the undamaged model with the DIC imperfection applied, as for the panel with damage neither of the above criteria were satisfied. In what follows the load levels at which material failure was predicted by the aforementioned criteria in the panel model without damage are shown.

The first damage was predicted by the Tsai-Wu criteria, relevant for the matrix tensile damage, at a load level around $230kN$ in the first ply of the middle stringer's web. The Hashin criteria also predicted the same type of damage, in the same location, but for a higher load level, at around $248kN$. Next, matrix compressive failure was predicted by the Hashin criteria at a load lever around $298kN$, while fiber compressive fracture was predicted at a load level above $320kN$. Considering that no laminate strength failure was predicted by the criteria used before the panel's collapse due to skin-stringer separation and that the relevant compressive laminate strengths are reached for load levels with roughly 50% higher than the expected one given by skin-stringer separation, laminate strength failure is not considered critical for this panel.

The assessment of butt-joint strength strength was not thoroughly done for this project. However, the likelihood of this failure mode to occur prior skin-stringer de-bond was evaluated based on the previous knowledge within Fokker [70]. As for a 5-stringer panel under simply supported boundary conditions, the displacement at which butt-joint failure was predicted was above $3.3mm$, it was considered that butt-joint strength as a result of the purely compressive load applied would not be exceeded. Furthermore, the filler stresses were also verified for the model with nominal geometry and tensile stresses above the transversal strength of the APC were only found for load levels above $230kN$. The nominal panel geometry here was used since the simplified one gave significantly lower stresses and since it is also more representative for the real panel from this aspect.

The transverse strength of the APC lamina was used here as an estimation, as a butt-joint material's allowable for transverse tension was not defined. Also not defined is an allowable of the butt-joint's material compressive strength, therefore a comparison in this aspect could not be done. As a reference only for a load level of $230kN$ the highest principal stresses seen in the skin-web butt-joints are around $100MPa$ and -$186MPa$.

The strength of the resin cast material was also checked and stresses over the conservative allowable of $35MPa$ [58] were not found in the FE model.

Concluding, the predicted critical failure mode of this panel with an initial skin-stringer de-bond is skin-stringer separation.

5 | 3-STRINGER PANEL TESTING

With the panel behaviour studied under various conditions, without and with damage in sections 4.3 and 4.4 enough confidence in the panel model was built to proceed towards testing. With the prediction shown in section 4.4.6 considered the base one and the most likely to be accurate in ideal conditions, the test instrumentation and plan could be prepared. Here by ideal conditions it is meant that the same buckling pattern is seen in the *FE* panel model and during the panel test, that uniform load introduction in seen during the test, that the assumed de-bond length is correct and that material fracture data is accurate. In what follows, the test instrumentation and plan is presented in section 5.1, the test results are shown and discussed in section 5.2, while the correlation between the panel *FE* model and the test is shown in section 5.3.

5.1 PANEL TEST INSTRUMENTATION AND TEST PLAN

While retrieving data from a *FE* model is a generally an easy process, measuring the desired quantities during an experimental test can be cumbersome. Preparing the test instrumentation is a process that requires special attention, as every destructive test is an unique event and any measurement error could lead to poor simulation-experiment correlation. Furthermore, care must be taken when doing a simulation-experiment correlation, as the exact same quantities need to be compared between the test and the *FE* simulation. Even after the quantities to be compared between the simulation and experiment are defined, care must be taken to accurately measure these quantities during the experimental test and also to correctly extract them from the *FE* model. In what follows in this section, the measures took to prepare the test instrumentation and the *FE* model for a good simulation-experiment correlation are described.

5.1.1 PANEL TEST INSTRUMENTATION

The panel's measuring instrumentation here was mainly meant for correlation purposes. The instrumentation used during the test contained:

- 7 strain gauges
- 5 displacement transducers
- 2 3D DIC systems
- 2 high speed cameras
- 2 regular cameras

In what follows, the purpose and details about each of the aforementioned measuring equipment is given.

STRAIN GAUGES

The strain gauges distribution is meant such that it satisfies three criteria:

1. provide the means of correlation between the simulation and the experiment
2. check and/or measure if there is any asymmetry in the load seen by the panel's sides
3. check and/or measure if there is any load redistribution between the stringers

The first criteria is important due to the fact that having only a correlation in terms of panel load-displacement curve does not necessarily mean that the *FE* model is able to capture the panel's behaviour accurately. Often a poor correlation in terms of strain-panel load, or strain-panel displacement is observed, although a good correlation in terms of panel load-displacement curve is achieved. Furthermore, verifying if there is a good correlation in both terms of load-displacement and strain-panel load/displacement gives more information about the robustness of the *FE* model.

The second criteria is also important in verifying the conditions of the experimental test. It is relatively common that the test machine introduces the load with a certain degree of asymmetry and this aspect could have a significant influence over the structure's behaviour, case also valid for this panel as previously shown. Moreover, even in the case of a uniform load introduction, the panel sides might take the load differently, due to possible manufacturing imperfections, which could make one skin bay behave stiffer than the other. Due to this reason, having strain gauges mounted at the sides of the panel would give a measure on how much compressive load is seen by either of these sides independently.

The last criteria is meant to reveal if load redistribution occurs between the stringers as the de-bond grows. This is relevant in understanding how this panel behaves when loaded under compression.

In order to define the locations of the strain gauges, the strain gauge type must be known, in order to use its dimensions when determining their positions. The strain gauge type used was $Kyowa\ KFRP-5-350-C1-3$ [71], which is a special type of strain gauge design for use with composite materials. This strain gauge had a gauge dimension of $5mm$X$1.5mm$ (LxW of the measuring area) and a base dimension of $15mm$X$5mm$ (LxW of the whole strain gauge), while the allowed elongation at room temperature is 2.2%. More information about the strain gauges used can found in the manufacturer's website [71]. Using the base dimension of the strain gauges and also analysing the FE model' surface strains, the strain gauge locations shown in figures 5.1 and were used.

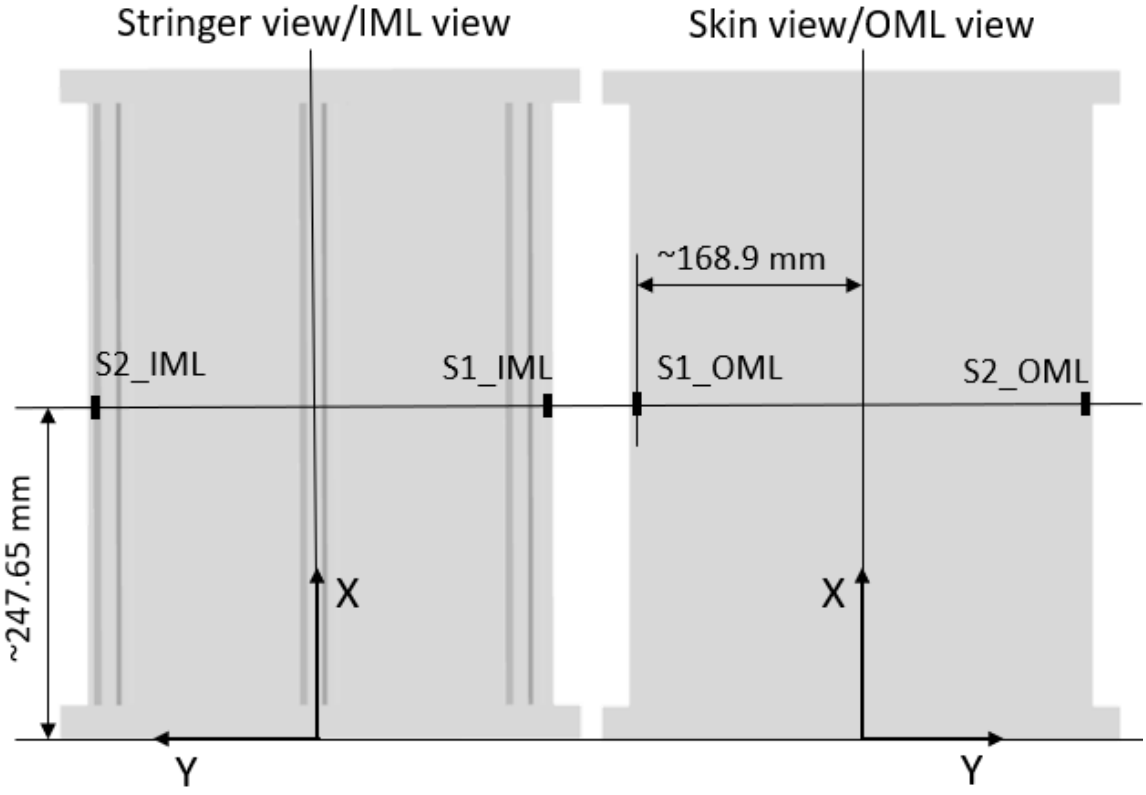

Figure 5.1: Panel strain gauges locations StringerIML and SkinOML views

Important to mention here is that these locations were verified in the panel FE model to have a low surface strain gradient along the panel's length and width. Small strain gradients are desired for mounting strain gauges, as the strain error due to small strain gauge positioning error are reduced. In other words, positioning the strain gauges in an area of high strain gradients would lead to significant differences in the strain values measured as a function of their position within that area of high strain gradients. Therefore, finding these areas of low strain gradients and mounting the strain gauges there is more likely to reduce the errors due to poor correlation of the locations where the strain are measured during the test and from where they are extracted from the FE model.

As it can be seen from this figure, the strain gauges mounted on the panel's skin at the sides are in a back-to-back configuration. Using this configuration the pure membrane strain along the panel's length can be determined. This configuration is used to eliminate additional strain due to bending, by averaging the strain values given by the pair of back-to-back strain gauges. The position of the skin strain gauges relative to the middle of the panel was calculated such that $1mm$ remains between the panel's edge and the edge of the strain gauge base. This relatively small margin is also needed to avoid mounting the strain gauges on the skin side over the glass plies below the stringer.

A schematic of the strain gauge positioning on the skin side is shown in figure 5.2, together with the position

of the web strain gauges. In this figure, the position of strain gauge base (shown in black) and of measuring gauge (shown in red) with respect to the glass plies and skin edge is shown. Also from this figure it can be seen that the web strain gauge was chosen to be at the mid-point between the skin-web butt-joint radius and the web-cap butt-joint radius. This location was chosen in order to be sure that the strain gauges are mounted on the webs, without covering any part of the butt-joints. The web strain gauges position was chosen to be on the cap side of the stringer, in order to impede as little as possible the views of the DIC cameras. This was chosen despite the higher difficulty to mount the web strain gauges below the cap, since a better view of the DIC cameras was desired. Furthermore, the error due to any small positioning errors would not lead to significant differences in the strain measurement, as based on the FE model analysis this area has a small strain gradient. An iso-metric view of the panel's strain gauges locations can be seen on figure 5.3. As it can be seen from this figure, the web strain gauges are placed a the panel's bottom, minimizing thus the length of the strain gauges wires. The distance from the strain gauge base to the panel's edge was taken to be $15mm$ from the panel's tab, which gives roughly $40.4mm$ from the panel's edge

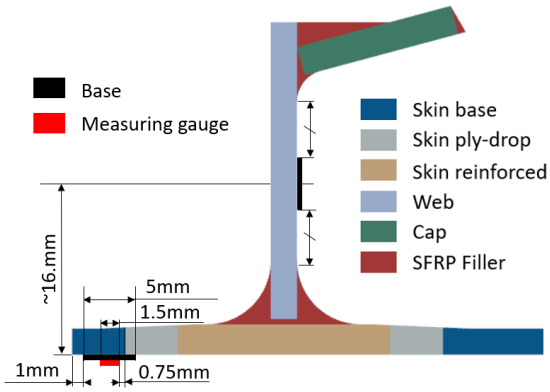

Figure 5.2: Schematic of the skin and web strain gauge locations

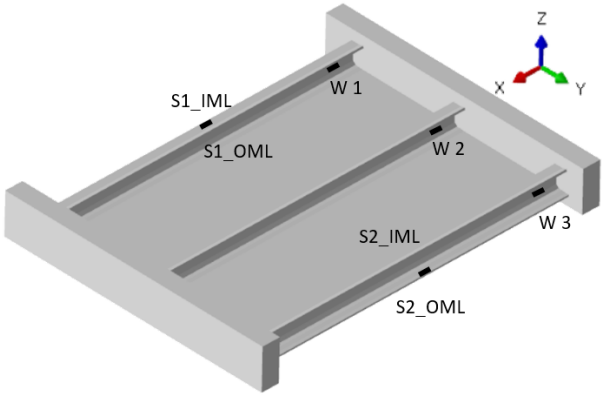

Figure 5.3: Iso-metric view of the panel's strain gauges locations

A comparison between the strain gauges position on the panel and their corresponding locations in the FE model is shown in table 5.1. The '~' sign is used in this table to either account for any errors in positioning the strain gauges on the panel, or for any positioning error in the FE model due to the mesh size. However, as these errors are relatively small, no major errors are expected due this type of panel test-FE model positioning errors between the strain gauges and the FE model's strain extraction nodes. Also, in the FE panel's model the measuring gauge of $5mm$ x $1.5mm$ was also accounted. This was done by averaging the strains from the nodes falling withing this area from the their location in the FE model.

Strain gauge ID	X coord [mm]		Y position		Z coord [mm]	
	Panel test	Panel FE model	Panel test	Panel FE model	Panel test	Panel FE model
S1_IML	~247,65	~247,65	~3.5mm from edge	~3.3mm from edge	~2.484	2.484
S1_OML	~247,65	~247,65	~3.5mm from edge	~3.3mm from edge	0	0
S2_IML	~247,65	~247,65	~3.5mm from edge	~3.3mm from edge	~2.484	2.484
S2_OML	~247,65	~247,65	~3.5mm from edge	~3.3mm from edge	0	0
W1	~46	~46.4	web 1 cap side	web 1 cap side	~16	~16.3
W2	~46	~46.4	web 2 cap side	web 2 cap side	~16	~16.3
W3	~46	~46.4	web 3 cap side	web 3 cap side	~16	~16.3

Table 5.1: Panel test/FE model strain measurement/extraction points

Due to the $2mm$ mesh seed used, 4 nodes along the length were used to average the strain values. For this mesh configuration using 4 nodes along the length to average the strain is equivalent to an approximate measuring gauge of $6mm$, which is $1mm$ more than the measuring gauge of the strain gauges used in the experimental test. Regardless, this was chosen since using 3 the nodes line would not have been centered around the points shown in table 5.1, while 2 nodes would have gave a small $2mm$ measurement area. This

aspect can be better be seen in figures 5.4 and 5.5, where the nodes used and the coordinates at edge nodes are shown.

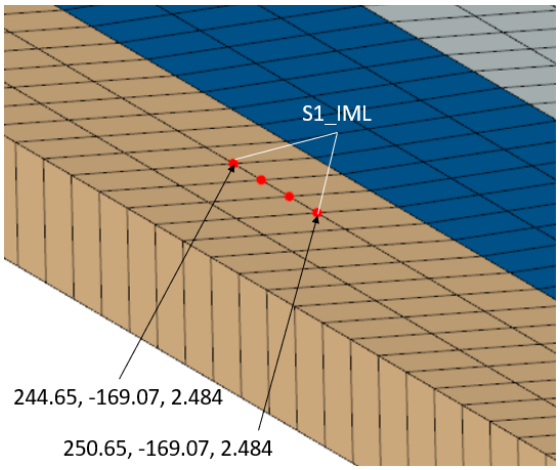

Figure 5.4: *S1_IML* strain gauge associated nodes in the panel FE model

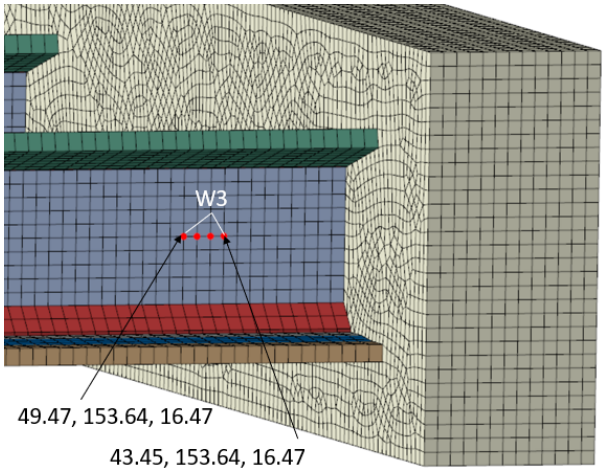

Figure 5.5: *W3* strain gauge associated nodes in the panel FE model

In order to avoid measurement errors, the panel areas where the strain gauges had to be mounted were sandpapered to remove the *DIC* speckled pattern and the initial primer. This was done such that the strain gauges could be mounted directly on the laminate material and making sure to remove as little as possible from the laminate material itself. Care was taken also to avoid breaking, or pulling, the strain gauges wires, by soldering them on soldering pads. Figure 5.6 shows the mounting details of the *S2_IML* and *S2_IML* skin strain gauges.

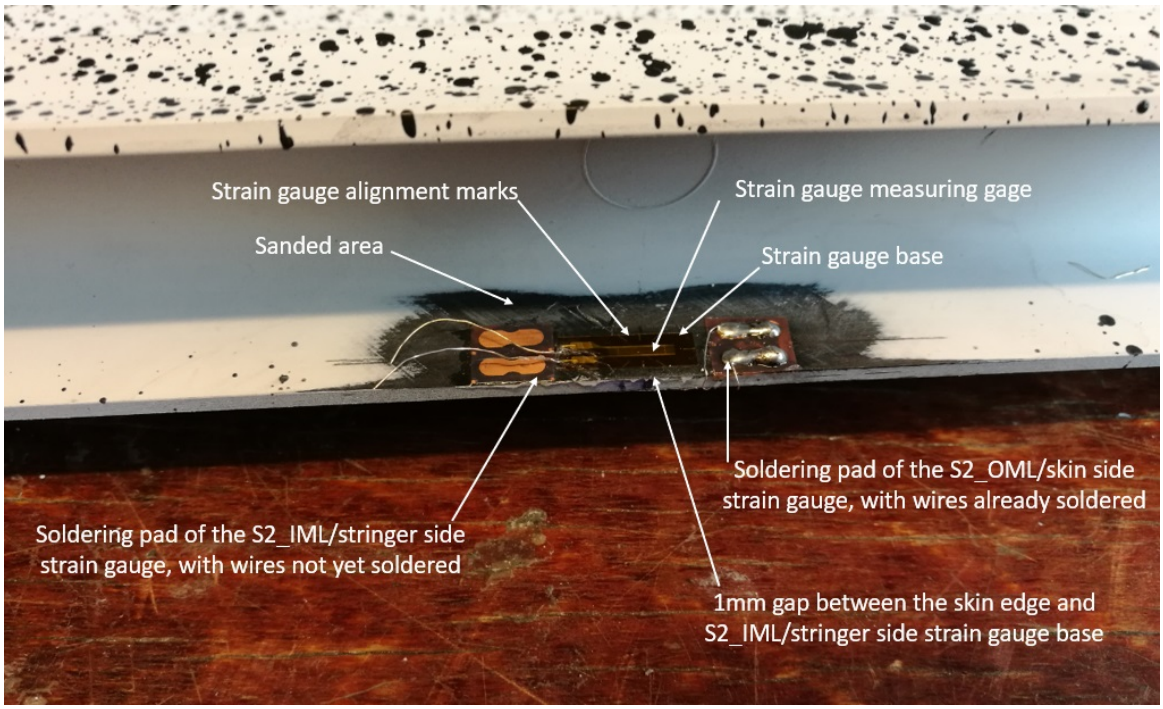

Figure 5.6: *S2_IML* and *S2_IML* skin strain gauge mounting details

The soldering pad of the *S2_OML* strain gauge was also mounted on the stringer side of the panel, in order to keep the skin side as clear as possible for the 3*D DIC* measuring system. Moreover, the panel's skin was repainted with speckled pattern over the skin side strain gauges and sandpapered area. In soldering the wires

of the $S2\_OML$ strain gauge, care was taken to cover the skin's edge with a layer of glue, such that contact between the wires and the panel was avoided. This was done since in that area the carbon fiber was exposed and since carbon fiber is a conductive material, it could alter the strain gauge measurement if its lead wires come into contact with it. Similarly, care was also taken to avoid contact between the lead wires of the strain gauges with the exposed carbon laminate for all the rest of the strain gauges mounted. In the process of sandpapering the areas for the skin side strain gauges, it was noticed that at the edge where the $S1\_OML$ had to be mounted there was not enough space to position it completely on the pure carbon laminate. This aspect can be seen in figure 5.7, where the skin side strain gauges can be seen mounted on the panel.

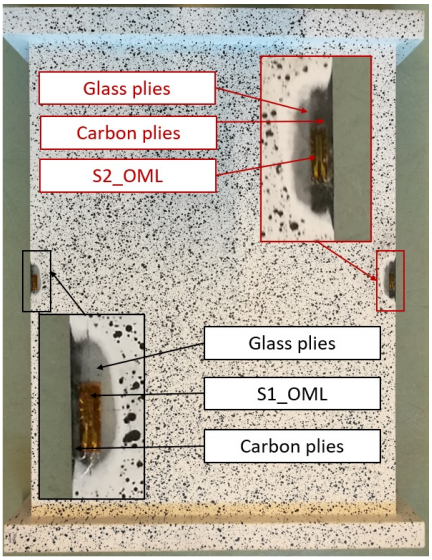

Figure 5.7: $S1\_OML$ and $S2\_OML$ skin side strain gauges

Figure 5.8: Web strain gauges mounted on the panel

In both sandpapered areas a dark grey area, corresponding to the carbon plies and a light gray area, corresponding to the glass plies can be seen. For for the right bay the strain gauge falls within the estimated distance, as also the strain gauge base falls inside the carbon plies area, not only the measuring gauge as initially estimated. This is most likely due to the glass plies being either over a smaller width, or slightly displaced towards the middle of the panel.

On the other hand, on the left side bay the strain gauge base falls almost completely on the glass plies, the measuring gauge being entirely on this glass plies area. This is partially as an outcome of the smaller panel width, as this edge distance at this side was thought to be cause of the shorter width. However, as the width is only smaller by $1.2mm$, considering the measuring gauge width of $1.5mm$ and the theoretical $0.75mm$ gap between it and the glass plies, the measuring gauge still should not have fallen completely on the glass plies. The other possible reasons on why this happened are the glass plies being closer to the panel edge than in theory, the strain gauge being positioned with an edge distance larger than $1mm$, or a combination of the two. Regardless, as the strain gradient in the FE model was small, the nodes corresponding to the $S1\_OML$ and $S1\_IML$ were left to their initial positions, considering the nominal width.

The strain gauges mounted on the webs of the panel can be seen on figure 5.8. As it can be seen from this figure, the soldering pads were mounted towards the middle of the panel, although there was enough space for these towards the end of the panel. Mounting the soldering pads towards the end of the panel would have resulted in a cleaner wire management, as the wire on the panel would have been shorter and also already pointing towards the bottom of the panel. However, mounting the soldering pads in that narrow area below the cap can be difficult due to the space constraints, therefore the soldering pads of the web strain gauges were mounted towards the panel's middle.

DISPLACEMENT TRANSDUCERS

The displacement transducers used were $LVDT$ type (Linear Variable Differential Transformer) and their purpose was to give a better panel displacement measurement than the one given by the testing machine.

Due to various plays and stiffnesses of the components between the panel and the machine's measurement cell, the displacement given by it tends to be higher than the one measured between its load introduction surfaces. Due to this reason, $LVDT$s (or other displacement transducers) are commonly used to give a better measurement of the panel's true compressive displacement. Moreover, here the 5 $LVDT$s were also used to measure any asymmetry in the machine's load introduction. Figure 5.9 shows the $LVDT$s locations used to measure the panel's sides shortening and asymmetric load introduction.

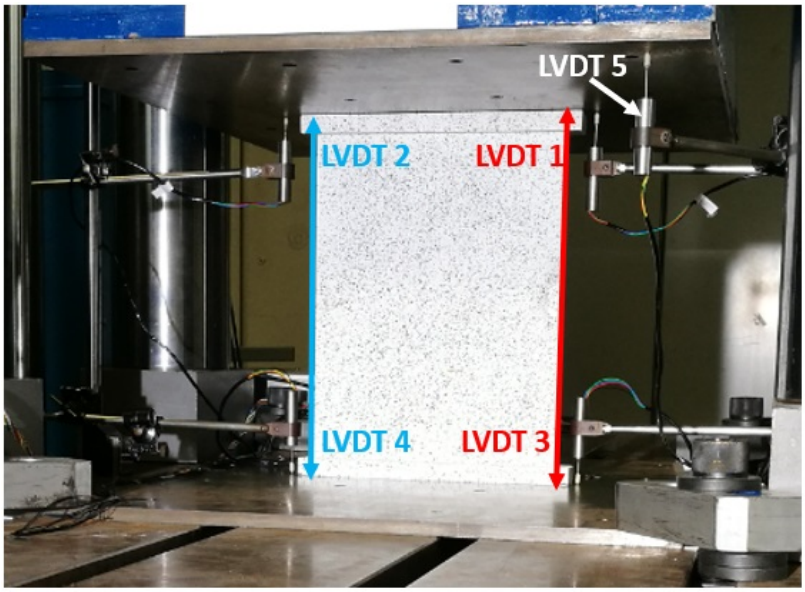

Figure 5.9: LVDTs used to measure the panel's side shortening and asymmetric load introduction

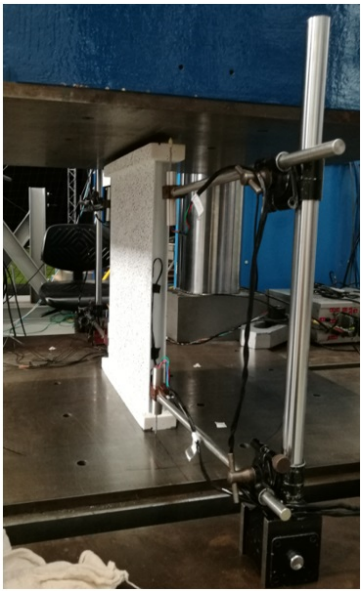

Figure 5.10: LVDTs mounting support and location

Measuring the panel shortening at each side gives an indication about both the panel's average shortening, as well as about any asymmetric load introduction. The panel's side shortening was chosen to be measured using $LVDT$s on both the lower and upper loading plate, since this approach potentially measures the panel's shortening with higher accuracy. Using $LVDT$s to measure just the displacement of the upper loading plate could lead to errors if the lower plate also deforms under loading. With the first 4 $LVDT$s an asymmetric load introduction along the panel's width could be measured. In order to also have an estimate on the asymmetric load introduction along the panel's height, a fifth $LVDT$ measured the upper's plate displacement at one of its corners. Comparing the displacement reading given by this $LVDT$ 5, with the ones given by the $LVDT$ 1 and 2 during the test would give indications about the asymmetric load introduction along the panel's width. The $LVDT$s supports were mounted on the test machine's frame outside the testing area, such that their reading was as little as possible influenced by any small machine vibrations or by the lower plate deforming under load. In figure 5.10, the $LVDT$ 1 and 3 support and its position on the test machine's frame is shown.

DIC SYSTEMS

The two DIC systems used were meant to monitor the deformations of the panel from both the skin and stringer side. These views correspond with the ones shown in figure 5.1, where the skin side and stringer side skin strain gauges locations were shown. Figure 5.11 and 5.12 shows the two DIC systems set-ups used during the test.

As the used testing machine's loading plates were $1m$X$0.75m$, with the panel sitting in the centre of if there was not sufficient light for the DIC systems to be able to measure displacements accurately. To alleviate this issue each DIC system had its own light system to provide the desired lighting conditions. The stringer side DIC system's light source can be seen in figure 5.11, it being turned off at the moment when the picture was taken, while the skin DIC system's light can be seen turned on in figure 5.12. As it can be seen form these figures, the two DIC systems have different orientations, as the one measuring the panel's displacements form the skin's side was mounted horizontally, while the one measuring the panel's displacements from the stringer side was mounted vertically. The latter one was mounted vertically due to space constraints, as the area behind it was designated for the people attending the test and operating the high speed cameras.

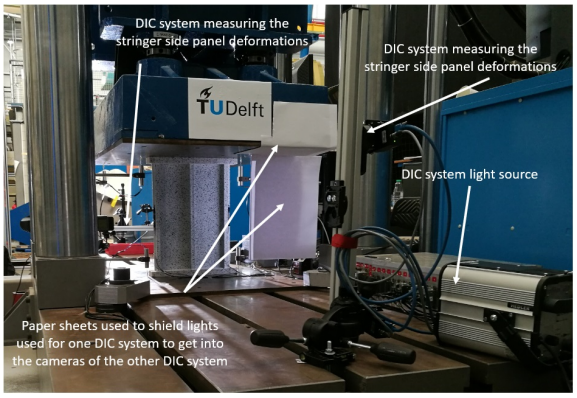

Figure 5.11: DIC system set-up measuring the panel's stringer side displacements

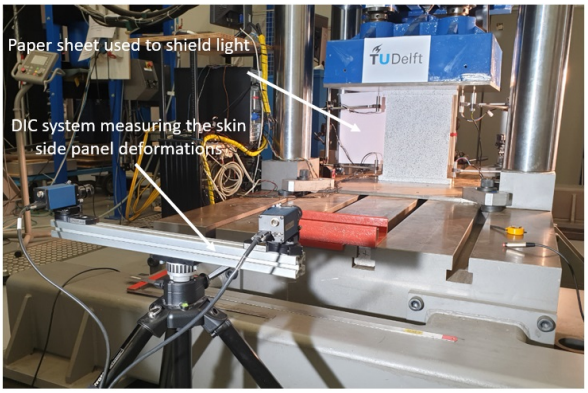

Figure 5.12: DIC system set-up measuring the panel's skin side displacements

As the two light sources used for the *DIC* systems opposed each-other, they interfered with opposing *DIC* system. To prevent the light used for one *DIC* system to pass trough the test bench area and disturb the camera of the *DIC* system from the other side, paper sheets were mounted on the upper plate to dim the light passing trough. Two of these paper sheets can be seen hanging from the upper loading plate in both figures 5.11 and 5.12. However, this was not sufficient, as the upper plate's surface still reflected a high amount of light towards the stringer side *DIC* system. To alleviate this issue, a paper sheet was also taped to the reflective area of the upper loading plate, such that the strong light source next to the panel was no longer seen in the stringer side *DIC* measuring system.

HIGH SPEED CAMERAS

Two high speed cameras were used to capture de-bond growths, one provided by Fokker, one provided by the faculty's lab. These were both mounted such that they would capture the de-bond growing from the cap side, based on the predicted buckling pattern occurring of the model with the *DIC* imperfection included. The views of these two cameras can be seen in figures 5.13 and 5.14.

Figure 5.13: TUD high speed camera view

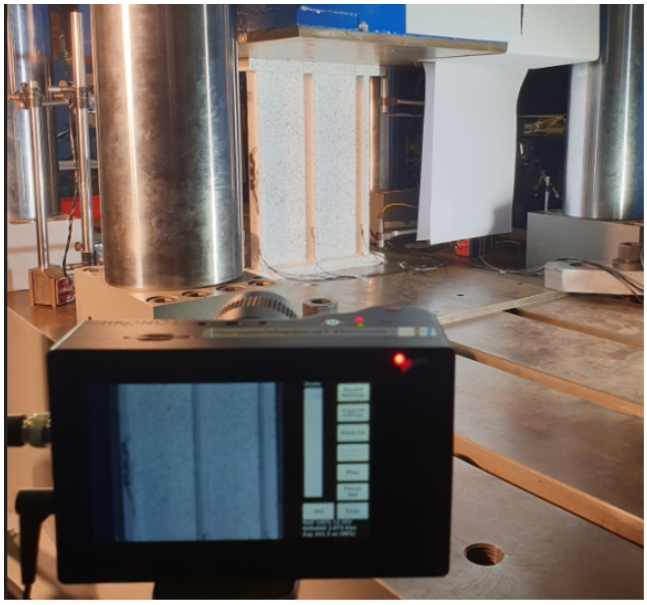

Figure 5.14: Fokker high speed camera view

As the frame rate of these high-speed camera was very high >10000Hz, the amount of time available was also limited due to limited memory. The available memory limitations in this case, with the used frame-rate, led to a recording time of around 3 seconds. Also, these two cameras were operated individually, with its operator

choosing when to trigger the camera. When the camera is triggered, a video of around 3 seconds prior to the triggering point is saved on its memory card. The aim of these cameras was to capture a de-bond growth events, as well as the panel's final collapse.

REGULAR CAMERAS

During this experimental test, a set of 3 *GoPro*s were used. Two of these were following the middle stringer from two side views, such that the de-bond growth could be monitored from both stringer sides. The views of these two *GoPro*s on the panel can be seen in figures 5.15 and 5.16

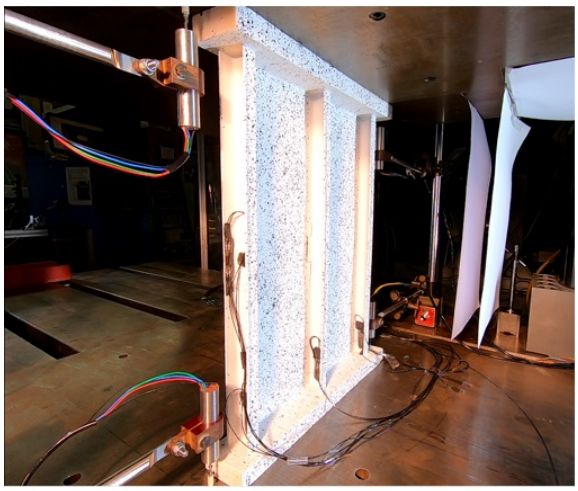

Figure 5.15: GoPro view on the panel's de-bond from the cap side

Figure 5.16: GoPro view on the panel's de-bond from the non-cap side

These two *GoPro*s only recorded the panel at higher load levels, as the collapse was also desired to be captured on these cameras. A third *GoPro* was used to asses a method to measure the asymmetric load introduction of the machine. This method consisted in taping a laser on the upper test-bench of the testing machine and a millimetric paper on its lower frame, assessing the asymmetric load introduction by following the laser's dot displacement on this paper. By aligning the laser beam such that it would fall perpendicularly on the millimetric paper and by knowing the distance between the laser beam source and the millimetric paper, together with the length and width of the load introduction plate, the asymmetric load introduction could be assessed both qualitatively and quantitatively. Out of these two assessment types, probably the most reliable one is the qualitatively one, as for the quantitative one multiple factors can come into play. Among these, one of the simple ones than can be mentioned is the accuracy of the test-bench displacement, which also has to be accounted for in the distance between the laser beam and the millimetric paper.

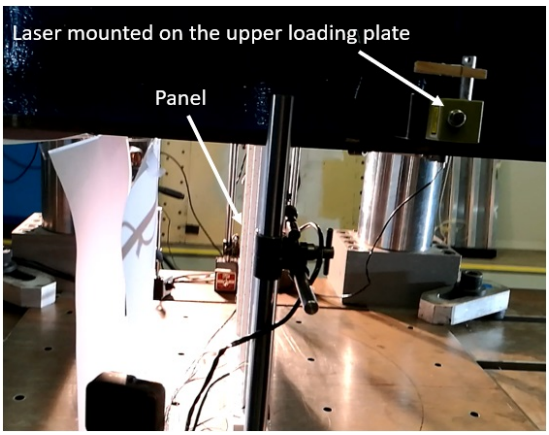

Figure 5.17: Laser mounting location

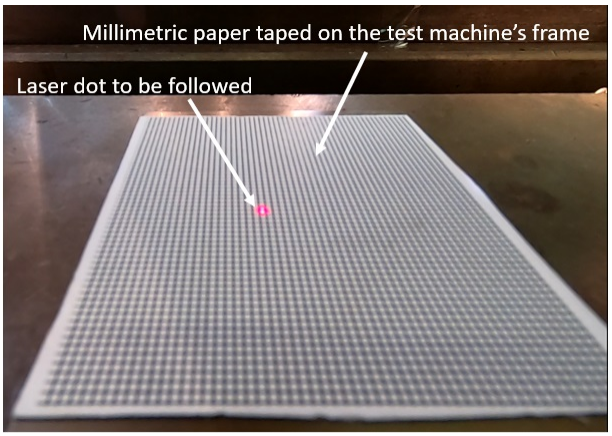

Figure 5.18: Laser dot on the millimetric paper

The laser mounted on the upper test-bench of the testing machine can be seen in figure 5.17, while its beam on the millimetric paper can be seen on figure 5.18, which is also the view of the $GoPro$ monitoring it.

5.2 EXPERIMENTAL TEST RESULTS

The test was conducted on the $MTS3500$ compression testing machine at the faculty's lab. A picture of the test machine can be seen in figure 5.19, with its test-bench loading plates features and dimensions being shown in figure 5.20

Figure 5.19: MTS3500 compression testing machine at the TUD ASM lab

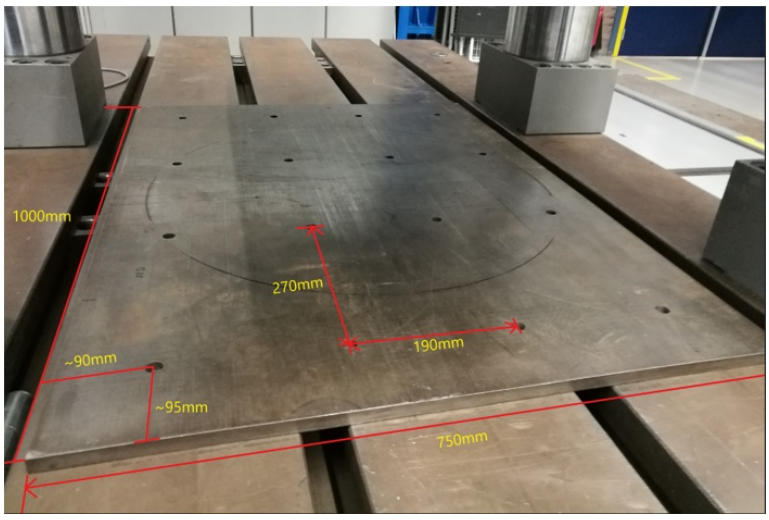

Figure 5.20: Test bench loading plates features and dimensions

A $Keithley$ 2701 [72] data acquisition system was used to log the displacement and load given by the testing machine, as well as the LVDTs and strain gauges data with a frequency of $3Hz$. As the same data acquisition card was used to log the aforementioned quantities, the synchronisation between them was automatically done, while the synchronisation between these and the other measuring equipment was done based on time. The same log frequency was used for the DIC systems, while frame-rate used for the $GoPro$s was $60Hz$, or $60fps$, with a resolution of $1920p$x$1080p$ (Full HD).

The test machine's loading speed was chosen to be $0.1mm/min$, since the panel's failure was predicted at a panel compressive displacement of roughly $2mm$. This loading rate also complies with the $quasi-static$ simulation environment and it also gives a reasonable testing time of 20+ minutes.

Prior to the destructive testing, the panel was loaded and unloaded several times up to a load around $30kN$. This load level was chosen such that skin buckling would not occur and such that the settling usually seen at the beginning of the load-displacement curve would be reduced. These settling events usually occur in the panel's load-displacement curves at the beginning, since plays within the testing machine can come into play, as well as small fiber rotations within the panel. Before this loading-unloading stage, all the equipment was verified and calibrated. In this calibration process, the constant factor with which each $LVDT$ voltage had to be multiplied was recorded, each of them being slightly different. After a few loading-unloading cycles up to a load of $30kN$, the panel final testing begun.

In what follows, the test summary is presented:

- $\approx 88kN$: a possible de-bond growth tick
- $88kN$-$93kN$: panel gradually buckles, a clear skin 3 half-waves buckling pattern was seen $93kN$
- $94kN$-$133kN$: rare de-bond ticks, large visible growth at $133kN$
- $137kN$-$145kN$: small de-bond ticks are becoming more frequent, large visible de-bond growth at $145kN$
- $145kN$-$185kN$: small and big de-bond ticks with increased frequency, large visible de-bond growth at $185kN$
- $185kN$-$206kN$: big ticks, clearly audible and barely visible de-bond growth at roughly $206kN$
- $206kN$-$222.35kN$: clear ticks with increased frequency, panel fails explosively at the load of $222.35kN$

PANEL DE-BOND GROWTH

The panel seemed to experience small de-bond growths during the gradual buckling stage, small and rare ticks being heard during these load levels. As the panel took more load, the ticks also increased in their frequency and clearness until the panel's collapse. However, the de-bond growth was not constantly stable, as it had several fast de-bond bursts at load levels of $133kN$, $145kN$, $185kN$ and $206kN$. In between these de-bond growth bursts, the gap between the skin and the stiffener constantly increased, without any sign of de-bond growth.

The change in the skin out-of-plane deflections measured by the DIC systems can best be seen for the de-bond growth occurring at a load level of $145kN$, or $185kN$, the former being shown in figure 5.21 below. The impact of these two can also be seen on the $LVDT$ and strain recordings, while the other ones at $133kN$, or $206kN$ are barely visible on DIC and strain recording, while their influence was too small to be observed on the $LVDT$ data.

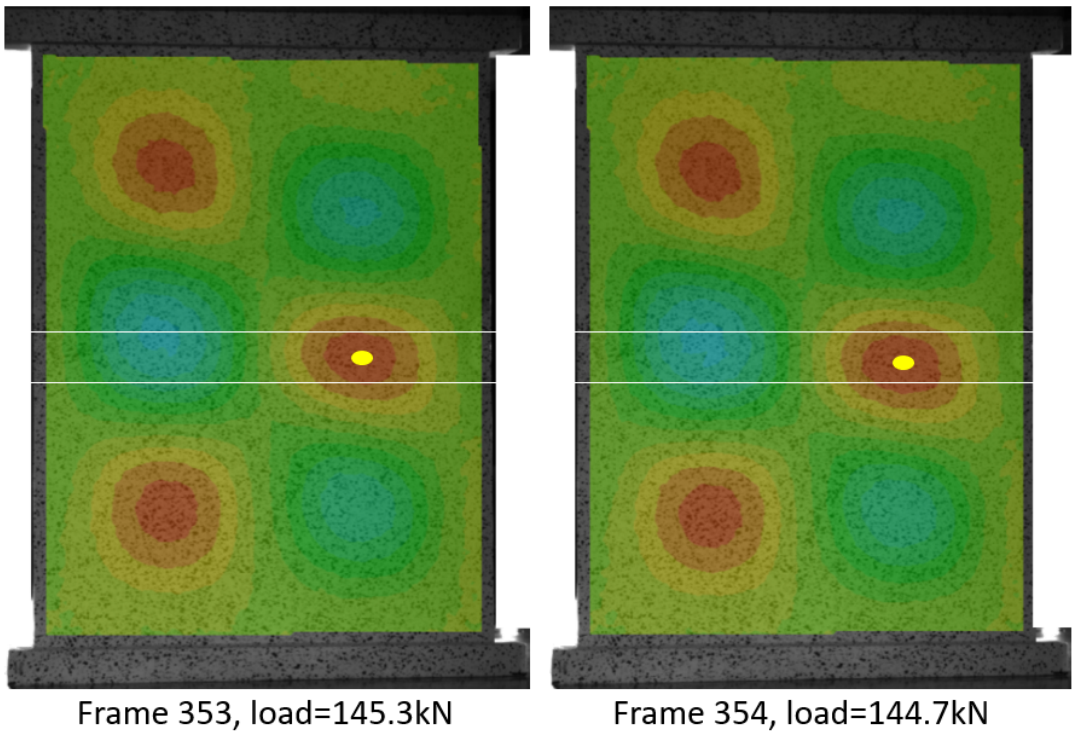

Figure 5.21: Buckling pattern moving slightly downwards as a result of de-bond growth at a load of $145kN$

In this figure the white lines are meant to help tracking the first skin buckling pocket deflecting away from the stringer (the first red one) from the right panel bay. The buckling pocket to be followed is also marked with a yellow dot. The panel loads and frame numbers from the video showing the DIC measured skin out-of-plane deflections are also shown for the two pictures in this figure.

Here it can be seen that the panel's skin buckling pattern is migrating downwards. Another aspect that can be noticed when comparing the two skin out-of-plane deflections from figure 5.21 is that in the second picture the deflections seem to be slightly larger. This behaviour is to be expected, as it comes as a result of the skin separating more from the stringer and allowing thus greater skin out-of-plane deflections.

The de-bond growths at the load levels of $185kN$ and $206kN$, were also similar to the one at $145kN$, as the de-bond in these cases also propagated downwards. Same is not the case for the one at $133kN$, as the de-bond propagated upwards in this case.

PANEL COLLAPSE

After the panel's explosive failure, there were extensive butt-joint failures found within the panel. Not only the middle stringer separated from the panel's skin, but the other two stringers as well. Furthermore, there were also butt-joint failures between the stringer webs and caps, as well as web and cap fractures. While

delaminations were found at the panel skin's surface, the skin appeared to be relatively intact after the panel's collapse. In what follows, the failure of the panel is described.

1. the skin buckling pockets deflecting away from the stringer unite below the middle stringer as the de-bond reached the other panel bay, a crack in the middle stringer's web initiates and the de-bond propagates upwards, as it can be seen from figure 5.22
2. web crack propagates across the middle stringer's web and into its cap, with web-cap de-bond also occurring at the same time for this stringer, skin-stringer separation occurs in stringer 1, as shown in figure 5.23
3. web and cap fracture on the first stringer occurs, with skin-stiffener separation now also in the stringer 3, as it can be seen in figure 5.24
4. extensive de-bond between all the stringer caps and webs, as the skin completely separates from the stringers, with skin and cap delaminations and stringer web-cap de-bonds, as it can be seen from figure 5.25

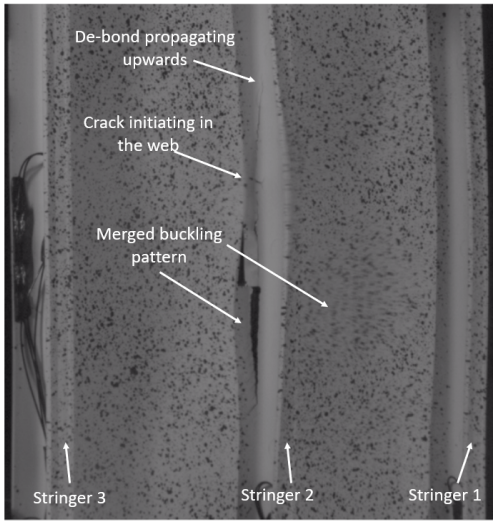

Figure 5.22: Panel collapse: skin buckling patterns merge, crack initiates in the middle stringer web, de-bond propagates upwards

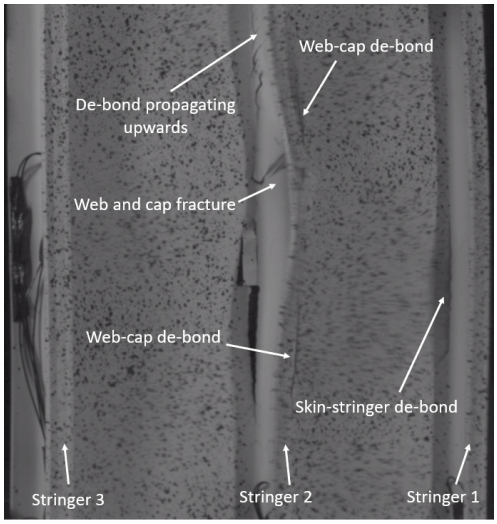

Figure 5.23: Panel collapse: web and cap fracture, web-cap de-bond and stringer de-bond propagating upwards in stringer 2 and skin-stringer 1 de-bond

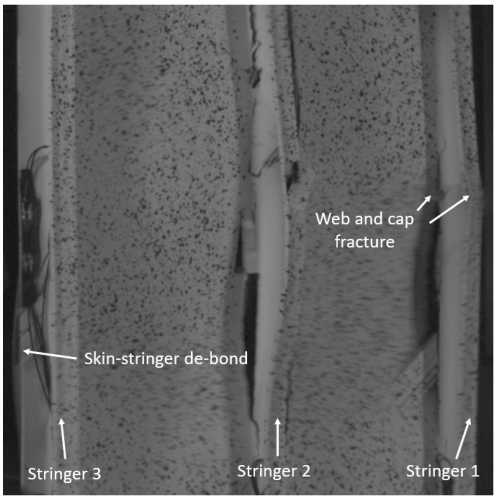

Figure 5.24: Panel collapse: web and cap fracture in stringer 1, skin-stringer 3 de-bond, de-bond propagating upwards

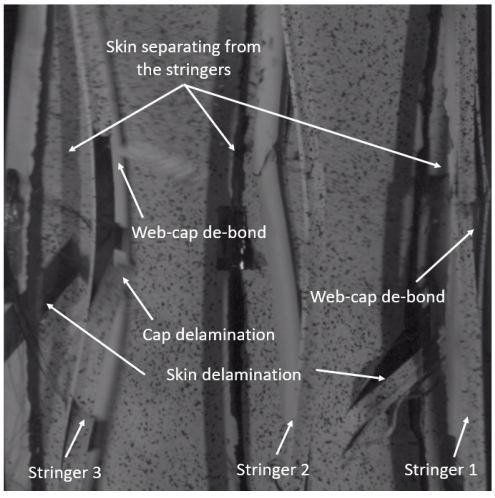

Figure 5.25: Panel collapse: skin-stringers total separation, skin and stringer 3 cap delaminations and stringer 1 and 3 web-cap de-bonds

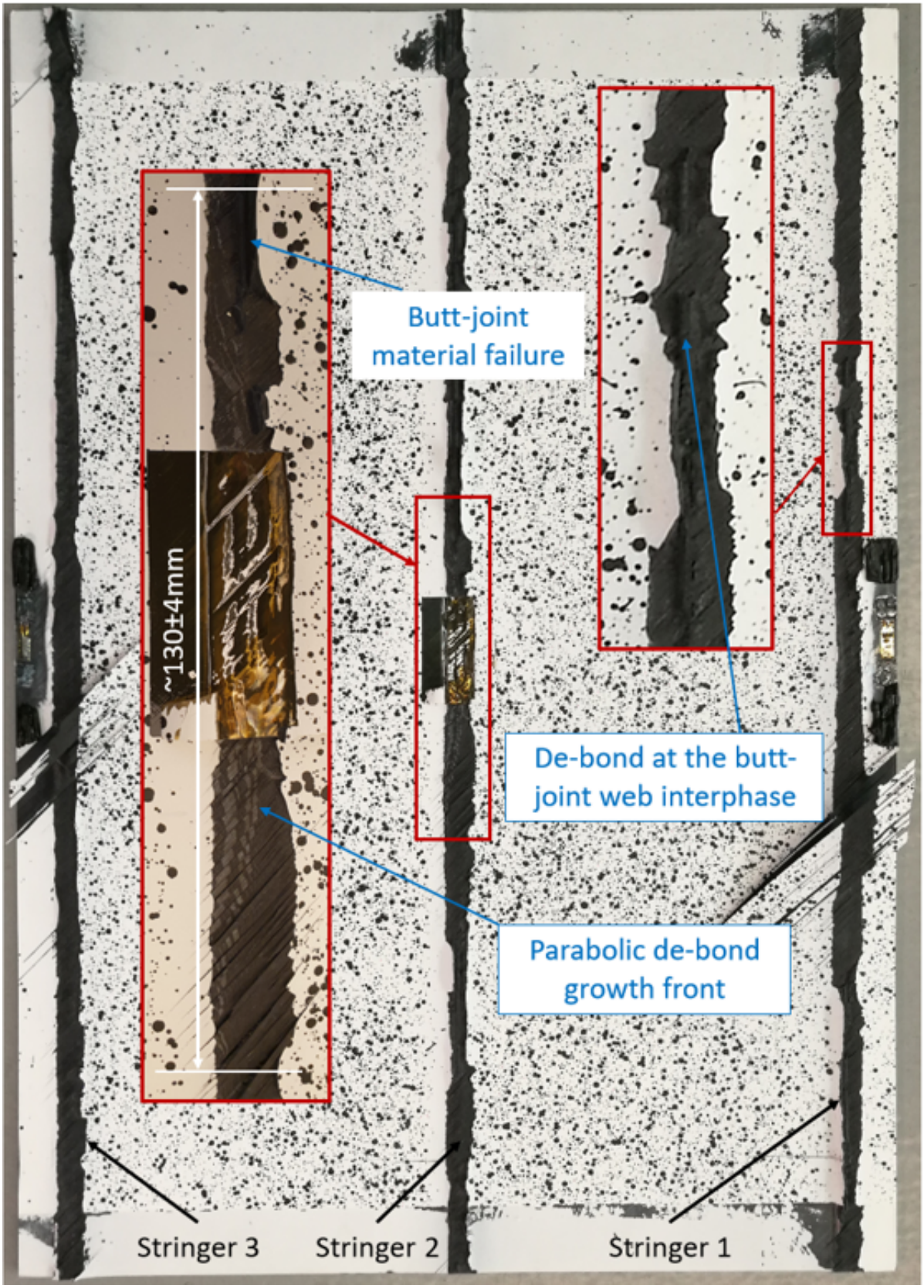

Figure 5.26: De-bond length and growth front seen on the panel's skin after collapse

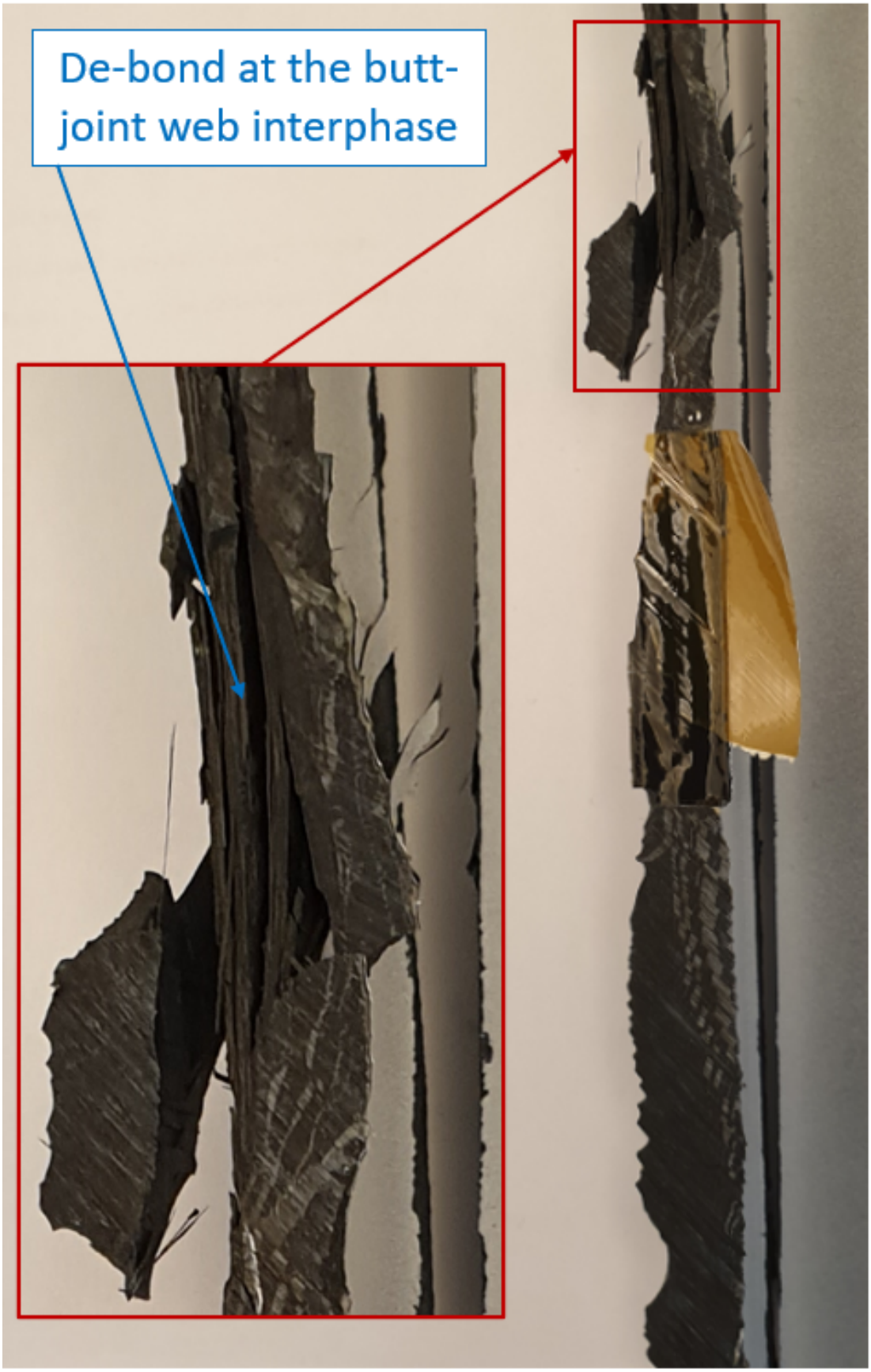

Figure 5.27: Fracture surface of the middle stringer, web de-bond surface and delaminations

The de-bond length at failure failure was roughly $130 \pm 4mm$ (based only of post-test observations) and the de-bond only propagated on the middle stringer side, were the adjacent skin buckling pocket deflected away from the skin. This de-bond growth at failure is less than twice the initial one of roughly $70mm$. Based on post-test observation the de-bond growth front was parabolic, with the de-bond growing more towards the bottom of the panel. This tendency of the de-bond to grow towards the bottom of the panel corresponds with the downwards migration of the skin buckling pattern deflecting away from the skin, as a result of the secondary buckling event. The de-bond growth front can be seen on the panel's skin after the panel's collapse, shown in figure 5.26

As it can be seen from this figure, the panel's skin is roughly intact after the panel's collapse, with delaminations mainly at the surface. In this figure it can be also noticed that the skin-stringer failure at panel collapse is partially due to de-bonds occurring at the skin-web butt-joint's inter-phase with the skin, partially due to material failure in the skin-web butt-joint, with small areas of de-bonds at skin-web butt-joint inter-phase with the webs also existing.

The skin-web butt-joint de-bond failure is characterised by a relatively smooth fracture surface. These fracture surfaces were the most abundant type found on the panel's skin after the panel's collapse. The material failure instead were characterised by a rugged fracture surface, these fracture types being the second most abundant type. Last, the fracture surfaces of the de-bonds between the skin-web butt-joints at the inter-phase with the webs were characterised by the butt-joint being partially still attached to the skin, including the area between the web and the skin. However, these fracture surfaces were only found together with the ones of the for material failure.

The fracture surface of the middle stringer can be seen on figure 5.27. In this figure the delaminated web can be seen clearly, which means that in these regions the web de-bonded from the skin-web butt-joint. These delaminations are thought to occur only after the panel's collapse begun, as they lie beyond the observed de-bond growth front. Furthermore, skin-web butt-joint lateral de-bonds at the filler-web interface can also be spotted, together with the mirrored de-bond pattern shown in figure 5.26.

PANEL LVDT DATA AND LOAD-DISPLACEMENT CURVE

The load-displacement curves using the $LVDT$ displacements read from the upper loading plate can be seen in figure 5.28.

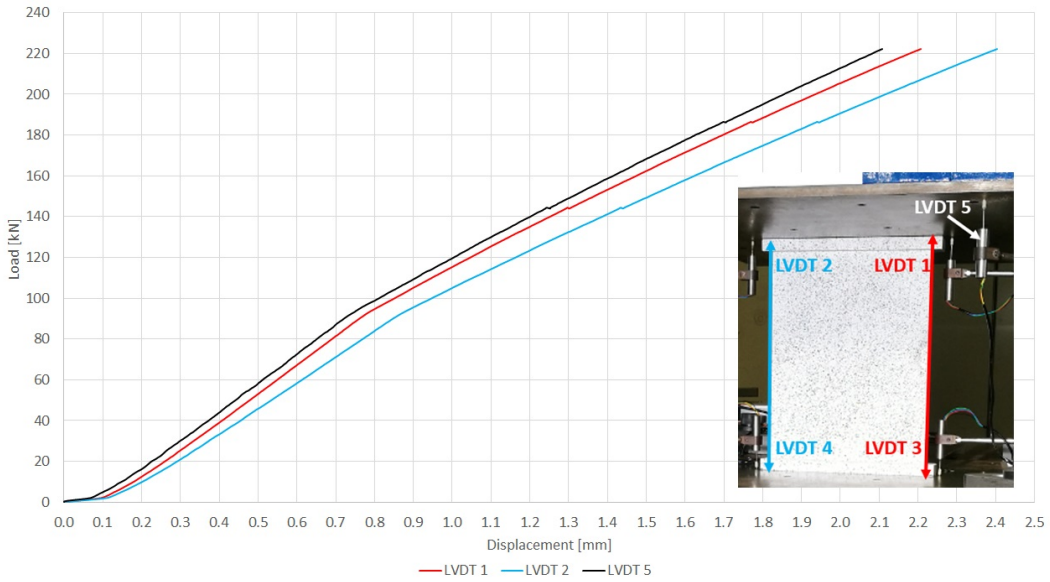

Figure 5.28: Load-displacement curves using the upper plate LVDTs displacement readings

Remembering the positioning of the $LVDT$s from figure 5.9, it would seem from the above figure that the left panel bay (when looking from the skin side) was deflecting more than the right bay. In this figure it can also be seen that the right side of the panel appears to be stiffer. This right panel bay was also the one

containing two stinger caps, which could have also played a small role in this stiffness difference. A small difference was however to be expected, since the panel's ends were not exactly parallel with respect to each-other, as previously shown in figure 4.12. Due to the un-parallel machining, this left side of the panel is also expected to be compressed more. Moreover, as the left bay of the panel should compress more, it should also develop a greater reaction force, therefore the displacement read on this side should also be slightly smaller than the one read on the right panel bay. However, this was not seen in the $LVDT$ displacements, on the contrary, the displacement read on this left side being greater than the one of the right side, despite the left side compressing earlier. This load case corresponds with the one shown in section 4.4.3, for which a similar failure load as the one seen in the model with uniform load introduction.

The magnitude of the asymmetric load introduction based on the $LVDT$s measuring the displacement of the upper loading plate was really close to the $0.2mm$ one previously simulated simulated, the exception here being that this difference is purely compressive, unlike in the asymmetric load introduction sensitivity studies previously shown in section 4.4.3.

For a more accurate assessment of the asymmetric load introduction along the panel's height, the $LVDT$ 5 was compared with the $LVDT$ 1, as errors due to the asymmetric load introduction along the panel's width would occur if the comparison was made against the displacement given by $LVDT$ 2. When comparing the displacements given by $LVDT$ 5 and $LVDT$ 1, a small load asymmetry can be seen, the skin seeming to take slightly more compression. This load case corresponds to the one with the stringers taking more load shown in section 4.4.3, for which a load slightly higher than in the case of uniform load introduction was also seen. Assuming a distance of $400mm$ between the two $LVDT$s along the loading plate's length, the corresponding angle for a $0.1mm$ displacement difference would be $atan 0.1mm/400mm = 0.00025rad$. Using this angle, the difference in displacement between the bottom of the skin and tip of the caps can be estimated, using the panel's height of $32.884mm$. This difference would be $tan(0.00025) \cdot 32.884mm \approx 0.008mm$, which can be considered negligible. Furthermore, even if the angle would have been calculated by considering the difference between $LVDT$ 2 and $LVDT$ 5, this difference would still have been negligible.

Besides the difference in stiffness and the magnitude of the recorded displacement at the end of the test, the three displacement readings of the upper loading plate have the same main 4 features. The first of this features is the initial settling region, up to a displacement around $0.1mm$ for $LVDT$ 1 and $LVDT$ 2, while this region ends slightly sooner for the $LVDT$ 5. Then, the initial pre-buckling linear region follows. The initial stiffnesses based on the load-displacement curves using $LVDT$ 1, $LVDT$ 2 and $LVDT$ 5 were $137.98kN/mm$, $124.19kN/mm$ and $140.33kN/mm$ respectively, these stiffnesses being taken between the loads of $10.44kN$ and $87.67kN$. After this linear region all these $LVDT$ based load-displacement curves showed a change of slope around a load of $93kN$, which corresponded with the buckling load of the panel. This buckling load was smaller than the one from the FE model eigenvalue analysis and the previous compressive behaviour simulations, where the panel buckled at loads around $100kN$. This smaller buckling load could be due various reasons, among which the de-bond damage inflicted, or different panel thicknesses imperfections could be mentioned. Different stiffnesses can also be seen in post-buckling, as the stiffnesses taken between $100.43kN$ and $140.93kN$ gave stiffnesses of $99.86kN/mm$, $91.14kN/mm$ and $102.7kN/mm$ using the displacements of $LVDT$ 1, $LVDT$ 2 and $LVDT$ 5 respectively.

Furthermore, two small load drops can be seen at loads around $145kN$ and $187kN$. This load drops correspond with the significant de-bond growths, which were clearly audible and also visible. After the last load-drop, the stiffneses between $191.09kN$ and $222.33kN$ of the $LVDT$ 1, $LVDT$ 2 and $LVDT$ 5 were $82.69kN/mm$, $78.1kN/mm$ and $88.63kN/mm$ respectively.

Small displacement readings were also measured on the lower loading plate, as it can be seen from figure 5.29. Here, also the displacements recorded of the bottom loading plate on the left side of the panel were higher than the ones measured on the right side. A significant part of the displacement is recorded for a negligible load increased for both lower plate $LVDT$s. This could be the area in which a firm contact between the panel and the bottom loading plate and between the bottom loading plate and the machine's frame was established. Both of these curves appear to share the same three big regions. In the first region the displacement grows for a negligible load, for $LVDT$ 3 until near a $0.04mm$ displacement, while for the $LVDT$ 4 until near a $0.06mm$ displacement. After this follows a region of roughly linear growth, which for $LVDT$ 3 ends around a displacement of $0.048mm$, or a load of roughly $20kN$, while for $LVDT$ 4 ends around a displacement of $0.082mm$, or a load of roughly $10kN$. Last, for both $LVDT$s the displacement grows exponentially, with a faster growth for $LVDT$ 3. This faster growth also suggests that this right panel bay is stiffer than the left one, or that the panel is asymmetrically loaded. At the end of this exponential displacement growth a difference of roughly $0.05mm$

can be seen between the $LVDT$ readings, with $LVDT$ 4 positioned at the left side of the panel showing the higher displacement. This higher $LVDT$ 4 displacement suggests a higher compression on the left side of the panel, as this side seems to be pushed harder against the lower plate, but it could also come from the higher displacement seen in the $LVDT$ 2 readings.

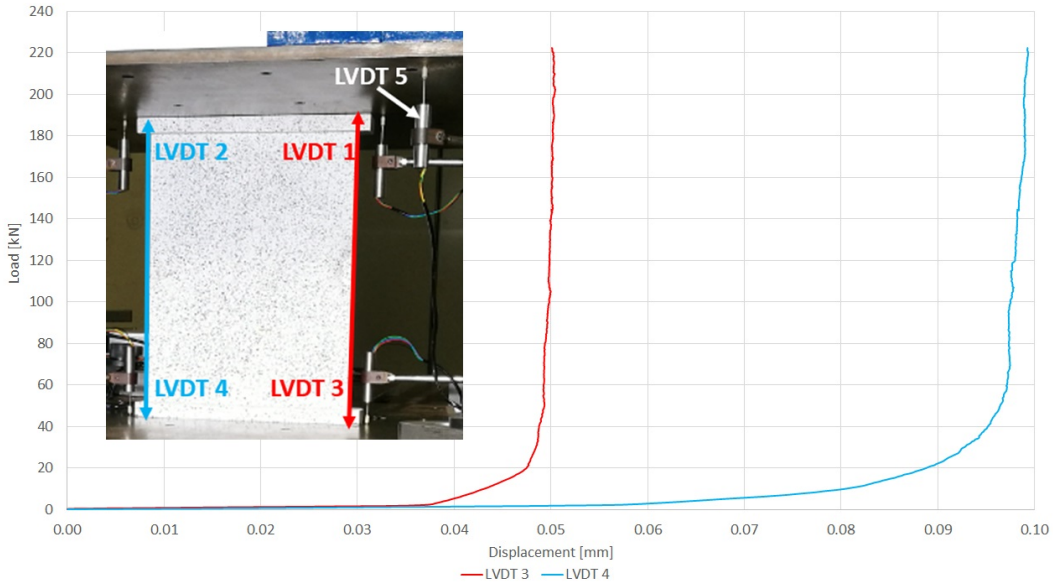

Figure 5.29: Load-displacement curves using the lower plate LVDTs displacement reading

While analysing the different displacement of $LVDT$ 1 and $LVDT$ 2 mounted on the upper test bench and of $LVDT$ 3 and $LVDT$ 4 gave a good indication on the asymmetric load introduction along the panel's width, accounting for all 4 of them can give an even more accurate assessment. By subtracting the displacements of $LVDT$ 3 from the one of $LVDT$ 1 and the one of $LVDT$ 4 from the one of $LVDT$ 2, a clearer picture on the panel's side shortening can be obtained. The load-displacement curves using these differences are shown in figure 5.30, there the labels Right-Hand Side (RHS) and Left-Hand Side (LHS) are according to a panel skin view.

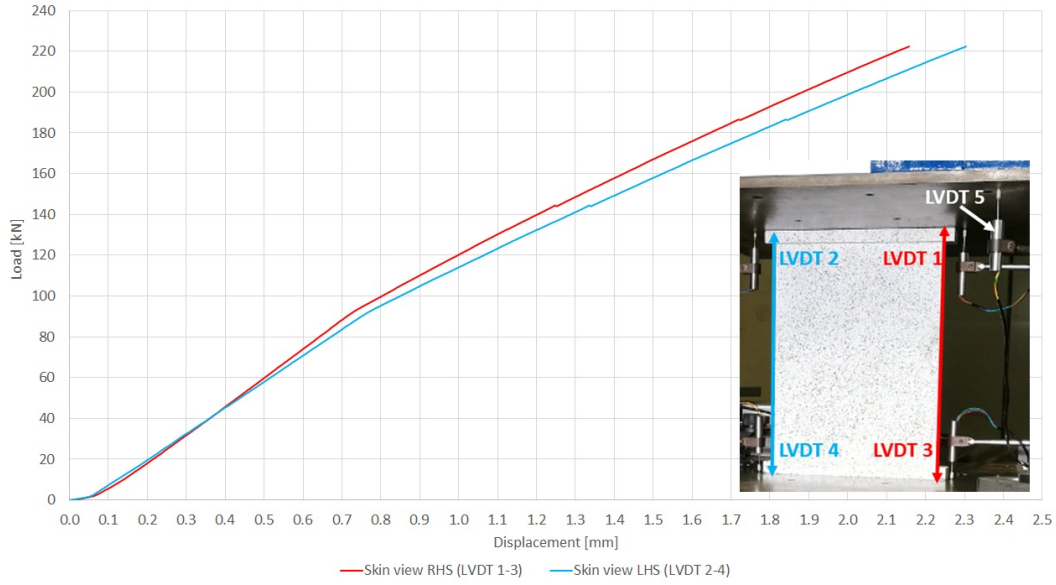

Figure 5.30: Load-displacement curves using the upper and lower plate LVDTs displacement readings

The displacement differences between the panel's sides also show that the right panel bay deforms less than the left one, the displacement difference at the end being around $0.15mm$. As the distance between the two $LVDT$ lines is greater than the width of the panel, the difference between the panel side shortening would be even smaller, close to one of $0.1mm$. The stiffenesses also slightly changed, as the right panel bay shows an stiffness of $139.51kN/mm$, $99.91kN/mm$ and $82.65kN/mm$ for the load intervals of $10.43kN$-$87.67kN$, $100.43kN$-$140.93kN$ and $191.09kN$-$222.33kN$ respectively, while the left panel bay showed stiffnesses of $127.5kN/mm$, $91.29kN/mm$ and $78.18kN/mm$ for the same load intervals. Using these averaged left and right panel side shortenings, the panel's experimental load displacement curve was plotted and shown in figure 5.31, together with the DIC measured skin out-of-plane deflections. Important to mention here is that the skin DIC measurement have an inverted deflection sign with respect with the previous shown FE models. Therefore, the deflections in red depicts skin buckling pockets deflecting away form the stringers, while the blue ones depict skin buckling pockets deflecting towards the stringers.

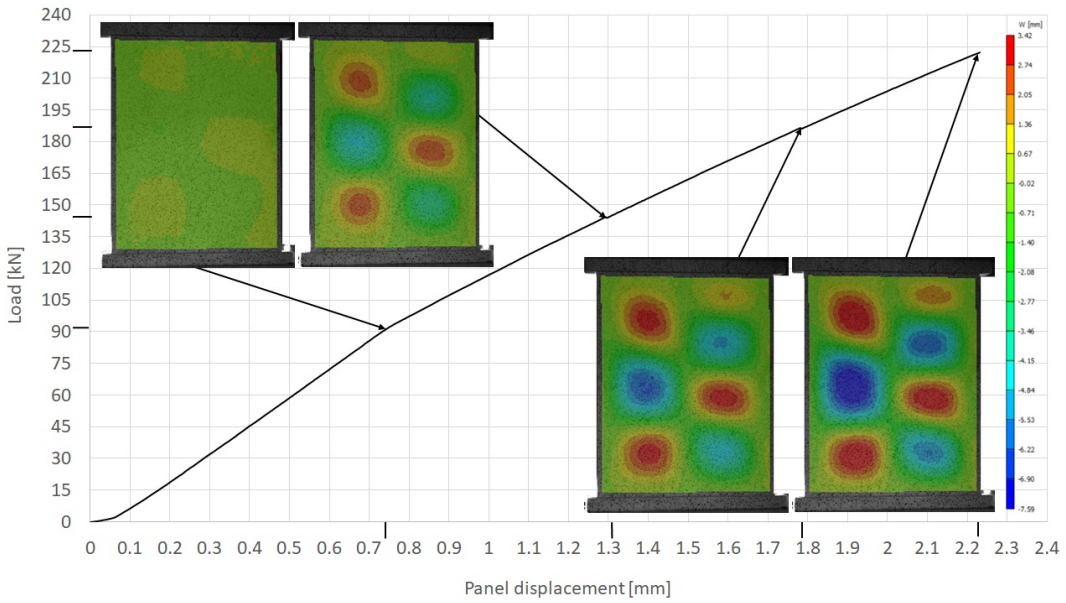

Figure 5.31: Panel's load-displacement curve using the averaged side shortening and DIC measured skin out-of-plane deflections

As it can be seen from this figure, an initial 3 half-waves buckling pattern was initially seen in the panel's skin. This buckling pattern changes around a load of $140kN$, when a secondary buckling event occurs in the panel's right bay, leading to a 4 half-wave buckling pattern. Using the averaged left and right panel bay shortenings, the panel stiffnesses taken in the $10.43kN$-$87.67kN$, $100.43kN$-$140.93kN$ and $191.09kN$-$222.33kN$ load intervals are $133.25kN/mm$, $95.41kN/mm$ and $85.35kN/mm$ respectively. The skin out-of-plane deflections spread from $3.24mm$ for the buckling pockets deflecting away from the stringers, to -7.59mm for the buckling pockets deflecting towards the stringers. This means that the pockets deflecting away from the stringers have a deflection magnitude smaller than half of the ones deflecting towards the stringers. This also implies that the tendency of the skin buckling pockets deflecting towards the stringers to prevent the de-bond from opening under mode I and promote de-bond growth is higher than the tendency of the skin buckling pockets deflecting away from the stingers to do the opposite.

PANEL STRAIN GAUGE DATA

The higher loading of the panel's left side (skin view) suggested by the $LVDT$ displacement analysis was also confirmed by the strain gauges recordings, as it can be seen in figure 5.32, showing the skin strain-load curves using the strain in microstrain units ($\mu\epsilon = \epsilon \cdot 10^6$).

As it can be seen form this figure, the strain readings of the $S1\_IML$ and $S1\_OML$ strain gauges, which are also on the same side as $LVDT$ 2 and 4 shown in figure 5.30, showed significantly higher strains than the $S2\_IML$ and $S2\_OML$ ones from the other side of the panel. However, the magnitude of the difference is greater than the expected one based on the asymmetric load introduction, therefore the panel bays inherently load up

differently, most likely due to the asymmetric stringer caps. Considering the asymmetric load introduction along the panel's width represented a difference of only $0.2mm$ at the end of the averaged $2.22mm$ failure displacement and that the differences in the strain readings between the panel's sides were roughly 40%, this significant difference in strain readings could not have come from the asymmetric load introduction alone.

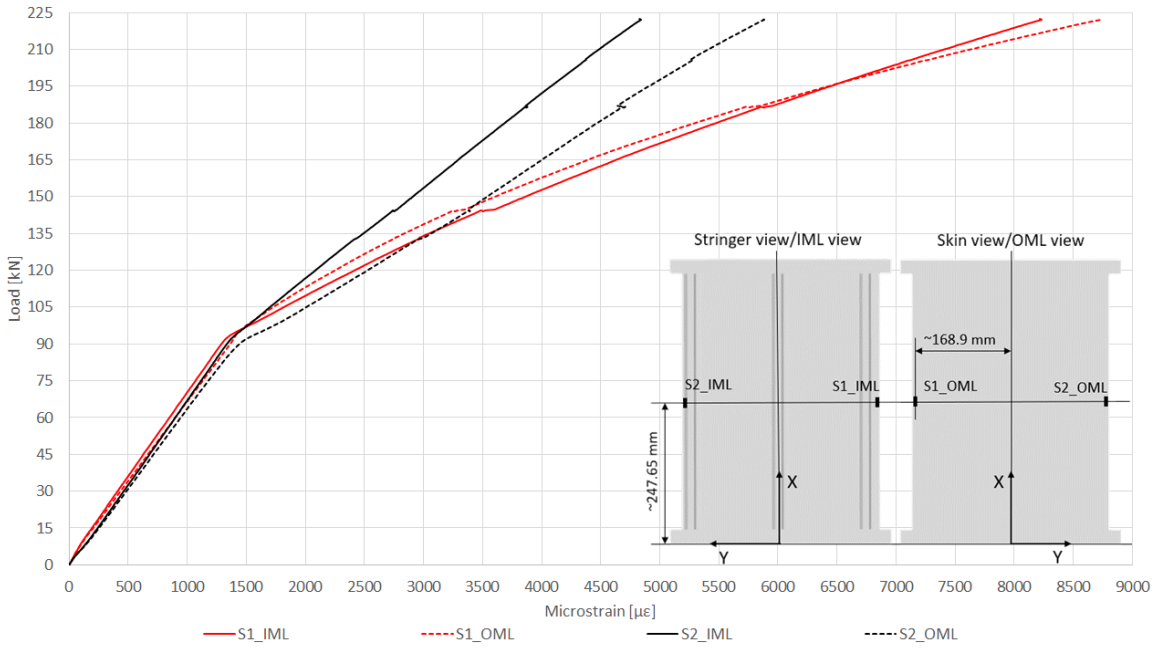

Figure 5.32: Panel's skin strain gauge recordings

When looking at the $S1\_IML$ and $S1\_OML$ pair of back-to-back strain gauges, one could see that in the initial stage they showed the same strain readings. The load-microstrain curves of these two strain gauges tend to separate, as the load approaches the buckling load, the response of the $S1\_IML$ strain gauges appearing to be slightly stiffer. The slope of the $S1\_IML$ load-microstrain curve also changes earlier at a load around $92kN$, while the $S1\_OML$ load-microstrain curve's slope changes around a load of $96kN$. These changes in slope correspond with the panel skin's buckling and after this event initially the strain response of the $S1\_OML$ strain gauge is slightly stiffer. This change suggests that, at this side, before the panel's skin buckling the inner side of the skin (closest to the stringers) is loaded more compared the opposite side of the skin, while after skin buckling vice-versa occurs. The two large de-bond growths at $145kN$ and $185kN$ can also be seen on these two, $S1\_IML$ and $S1\_OML$, load-microstrain curves, identifying with significant microstrain increases for negligible load changes. These two curves intersect each-other again at a load around $196kN$, which suggests some bending in the panel's skin. Since the $S1\_IML$ strain value is smaller than the $S1\_OML$ one, inner skin side seems to be in tension, while the outer skin side is in compression, hence the higher strain reading for this side.

When looking at the load-microstrain curves of the $S2\_IML$ and $S2\_OML$ pair of back-to-back strain gauges, one can notice that the same initial trend as for the $S1\_IML$ and $S1\_OML$ is observed. Also for this pair, the initial response of the $S1\_OML$ strain gauge mounted on the inner side of the skin is stiffer than the one of the $S1\_OML$. A difference in the load level at which these the curve slopes change can also be seen here, as the slope change in the curve of the $S2\_IML$ strain gauge is at a load around $90kN$, while in the one of the $S2\_OML$ strain gauge is at a load around $93kN$. After skin buckling occurs, these curves keep diverging further, which suggests that some bending also occurs at this side of the skin. Moreover, the same bending as the one suggested by the $S1\_IML$ and $S1\_OML$ strain gauges is also seen here, as the $S2\_IML$ strain value is smaller than the $S2\_OML$ one. Same as for the $S1\_IML$ and $S1\_OML$ strain gauges, the two large de-bond growths at the load levels of $145kN$ and $185kN$ can also be seen on load-microstrain curves of the $S2\_IML$ and $S2\_OML$ strain gauge readings. Moreover, for these two $S2\_IML$ and $S2\_OML$ strain gauges, the small de-bond growth at $133kN$ and $206kN$ can also be noticed upon a closer inspection, although not as clearly as for the other two.

The load-microstrain curves from the three strain gauges mounted on the panel's webs are shown in figure 5.33.

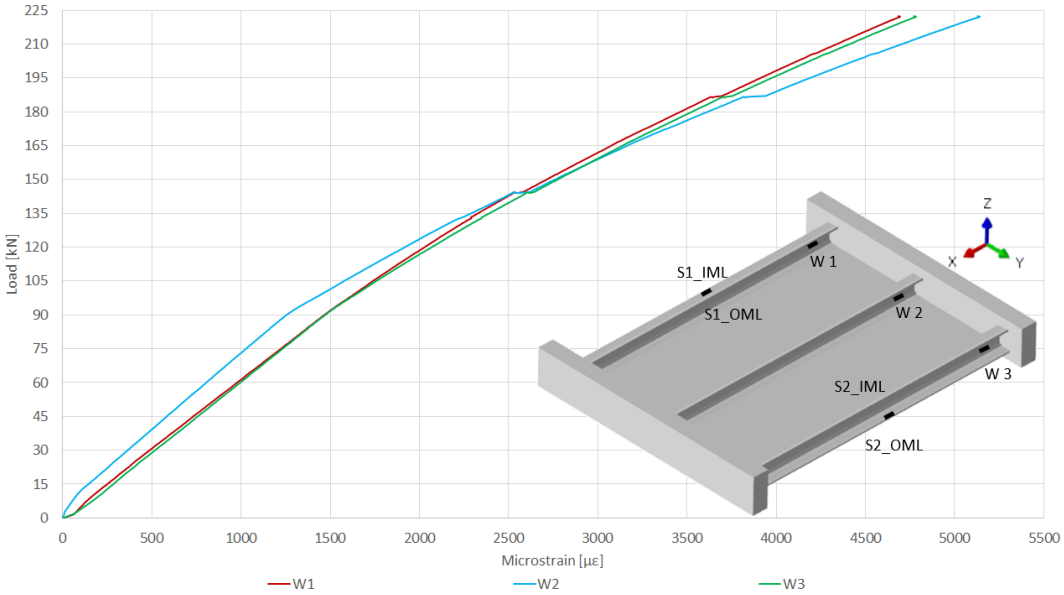

Figure 5.33: Panel webs strain gauge recordings

As it can be seen from this figure, the middle stringer loads up quite differently than the side stringers, while the difference between the strains seen in the side stringers is negligible. The middle stringer seems to take less load and to behave stiffer than the side ones prior to the panel's skin buckling. In this middle stringer the skin buckling event is also easier to observe, as the slope change in the other two side stringers is barely noticeable. The slope change in the load-microstrain curve from the $W2$ strain gauge mounted on the middle stringer is at a load level around $93kN$, which confirms the panel's skin buckling around this load level. After skin buckling occurs, the strain measured in the middle stringer increases at a faster rate than in the other two stringers, it becoming larger than the other two around a load of $160kN$. The de-bond growth events are also easier to see in the strain data of this stringer's web, as the de-bond growth occurs between the skin and this stringer's web. The two big de-bond growth events at $145kN$ and $185kN$ can be clearly seen in the strain data from all three stringer webs, their impact being larger on the middle stringer's web strain, as previously mentioned. Interesting to notice is that the strains recorded on the panel's webs seemed more sensitive to the de-bond growths, as the ones occurring at the loads around $133kN$ and $206kN$ can be also seen in these strain gauge data upon a closer inspection. However, these are only visible as small perturbations in the load-microstrain curves of the web strain readings.

5.3 CORRELATION BETWEEN THE PANEL FE MODEL AND EXPERIMENTAL TEST

A correlation between the panel and its model in terms of frequency was already made and shown in table 4.6 and figure 4.22 for the panel without tabs and in table 4.10 and figure 4.33 for the panel with resin tabs cast. While a significant load introduction asymmetry was observed during the experimental testing, the test-simulation correlation was done against the FE model with the DIC imperfection included since this was the best blind prediction. As one of the side goals of the thesis was also to asses the degree of accuracy that can be reached in predicting the panel's compressive behaviour without any test observation implemented, the correlation was done with the aforementioned model.

5.3.1 LOAD-DISPLACEMENT CURVES AND SKIN OUT-OF-PLANE DEFLECTIONS

Figure 5.34 shows the correlation between the load-displacement curves and skin out-of-plane deflections. For the experimental load-displacement curve, the averaged side shortening is used and a displacement offset of -0.055mm was also applied to overlap the two curves in their linear-elastic region.

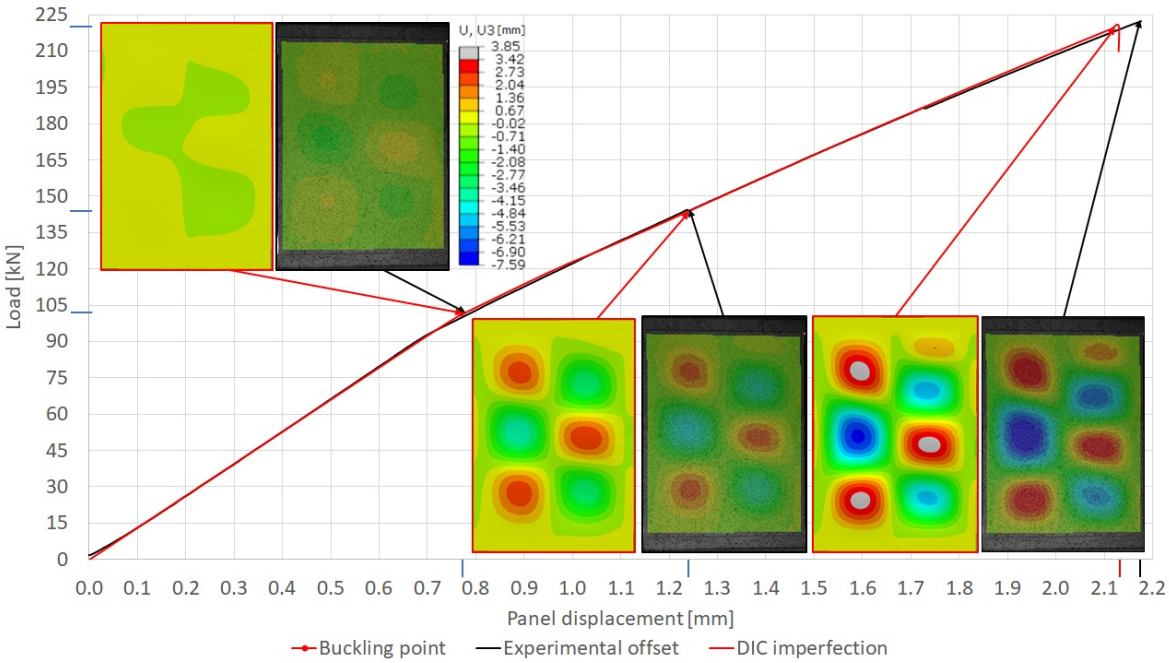

Figure 5.34: Correlation between the experimental and simulation load-displacement curves and between the skin out-of-plane deflections

As it can be seen from this figure, with the -0.055mm displacement offset used for the experimental curve, the correlation between the experimental and simulation load-displacement curves was extremely good. The difference between the stiffnesses seen in the FE model and during the test are shown in table 5.2.

Load interval [kN]	10-87	105-140	190-220
Panel FE model stiffness [kN/mm]	132.31	90.26	83.09
Panel experimental stiffness [kN/mm]	133.07	94.60	80.89
Relative error [%]	-0.58	-4.59	2.71

Table 5.2: Correlation between the experimental and simulation panel stiffnesses

As it can be seen form this table, the correlation in terms of initial stiffness was very good, around -0.6%, the minus sign meaning that the panel's FE model stiffness is slightly smaller than the experimental one. The correlation in terms of initial post-buckling stiffness was also good, here the relative error being slightly larger, at roughly -4.6%, with the experimental stiffness also being larger in the 105kN-140kN load interval. Last, the panel's experimental stiffness towards the end, for the 190kN-220kN load interval, was slightly smaller than the one of the panel's FE model, it being around 2.7%. This implies that the FE model predicts accurately the initial stiffness, slightly under-estimates the initial post-buckling stiffness and over-estimates the panel stiffness for higher load levels.

In terms of buckling load, the experimental one is slightly lower, as it can also be seen from the slope change of the two load-displacement curves shown in figure 5.34. The panel's experimental stiffness begins to change starting from a load around 87kN and stabilizes at a load around 93kN, while in the FE model the stiffness begins to significantly change from a load around 95kN and stabilizes at a load around 104kN. This gives, in an averaged sense, a difference in buckling load of roughly 10kN. The difference in buckling load is significant and it could have been given by the panel's skin thickness differences, the panel's real shape favouring a lower buckling load than the one seen in the FE model, or due to the asymmetrical load introduction. As a reference, for the models where a shape imperfection based on the first buckling mode was imposed, the significant change in stiffness occurred at a load level around 81kN. This shows the panel's buckling load's high sensitivity to shape imperfections, which could be also valid for slightly different panel skin thicknesses.

The difference in buckling loads can also be seen in the first set of skin out-of-plane deflections from this figure. While in the test at a load level around 100kN there is a clear skin 3 half-waves buckling pattern

formed, in the FE model the buckling pattern barely begun to form. The secondary buckling event occurs in both the test and in the FE model around the same load level around $145kN$, it being slightly easier to see in the test DIC data as it also formed slightly sooner.

This buckling shape can only be indirectly seen forming in the FE model in the second set of skin out-of-plane deflections form this figure. Here it can be noticed that the upper skin buckling pockets in the FE model are not vertically aligned. The skin pocket in blue (in the right skin bay, deflecting towards the stringer) is lower than the one across the stringer of the opposite sign. This happens since another skin buckling pocket started to from above it, pocket that can be clearly seen in the last set of skin out-of-plane deflections.

In this last set of skin out-of-plane deflections, it can also be seen that the model gives slightly higher deflections magnitude for the buckling pockets deflecting away from the stringer, while the magnitude of the pockets deflecting towards the stringer seems to be smaller than the one seen during the test. The highest skin buckling deflection away from the stringer during the test was $3.42mm$, while in the model the highest deflection was $3.85mm$. On the other hand, for the opposite deflection the highest value seen in the test was -7.59mm, while in the model the highest value was -7.13mm. However, these extreme values were taken for the failure loads seen during the test and in the simulation and these failure loads are not identical. Furthermore, as previously discussed in section 4.3.4, the DIC scale is not accounting for the extreme values measured, with expected errors less than -0.1mm compared with the measured value being expected. The load levels at which these maximum skin out-of-plane deflection were taken also have a significant impact, as the panel's collapse was predicted at a slightly lower load level. Considering that the model overestimates the magnitude of the skin deflections away from the stringer and underestimates the skin deflections towards the stringer, if the model predicted the same failure load as the experimental one, the magnitude of the overestimation would have increased, while the magnitude of the underestimation would have decreased. Overall, the model's accuracy in capturing the skin out-of-plane deflections can be considered relatively good, while its accuracy in capturing the panel's skin buckling pattern was very good.

The difference in the failure loads predicted by the model and the experimental one was around $2kN$, the exact model prediction being $220.5kN$, while the experimental one was $222.3kN$, giving a relative error of -0.8%.

5.3.2 DE-BOND GROWTH

Similarly as in the panel's FE model, the first clear signs of de-bond growth were observed for loads slightly higher than the buckling load, meaning that the model's prediction of de-bond growth soon after skin buckling occurs was correct. While during the experiment there were no signs of extensive de-bond growth until the one at a load around $133kN$ and the bigger one at a load around $145kN$, same was not seen in the model. The de-bond growth seen in the FE model was plotted against the panel load in figure 5.35, where the de-bond length estimate at failure based on post-test observation was also marked with a marked red dot.

As it can be seen from this figure, the model predicts a fast initial de-bond growth, starting from a load around $115kN$. This fast initial de-bond growth tends to stabilize as the load increases, until it becomes unstable at the failure load. However, nor the fast initial de-bond growth, nor the relatively stable de-bond growth manner was not observed during the panel test. On the contrary, although the de-bond started to grow relatively soon after buckling occurred, there was no sign of significant de-bond growth until a load around $133kN$.

Also during the test, 4 significant de-bond growths were observed, which can be described as qusi-unstable. Moreover, in the model the de-bond growth rate decreases as the load level increases, which was also not in agreement with the experimental data. In the experimental test, a more intuitive de-bond growth rate behaviour is observed, with clear signs of de-bond growth rate increasing proportionally with the load. This behaviour was suggested by the ever increasing frequency of de-bond growth ticks recorded with higher load levels, their strength also increasing with higher loads. Last, the de-bond length at which the FE panel model showed failure overestimated the panel's de-bond length at failure. While the panel's FE model predicted a de-bond length of $205mm$ at the panel's collapse, the observed one post test was roughly $130mm$. Again, it has to be stressed that the experimental de-bond length was assessed post-test, meaning that the aforementioned de-bond length estimation could have been inaccurate.

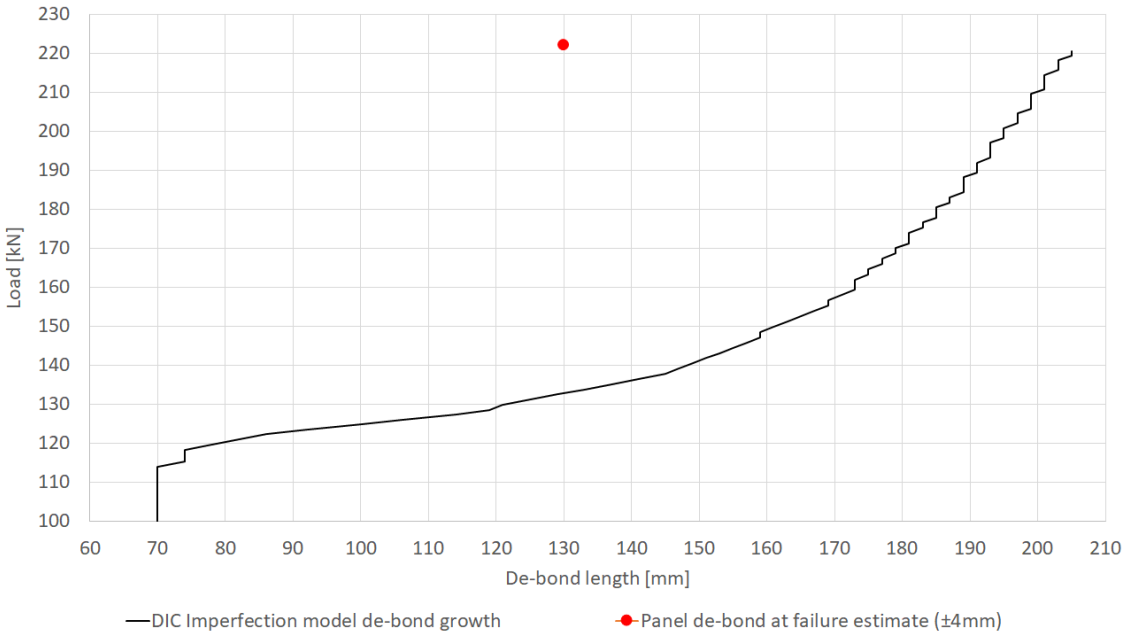

Figure 5.35: Comparision between the panel's FE model de-bond growth and panel's de-bond length estimate at failure

However, while the model was not able to predict the de-bond behaviour quantitatively, some qualitative aspects of the de-bond growth were successfully captured. As previously mentioned, the experimental testing confirmed that the de-bond tends to grow only after the panel buckles. Furthermore, the parabolic nature of the de-bond growth front was also successfully predicted by the model, as it can be seen for example when looking at figures 5.26 and 4.44.

Moreover, the tendency of the de-bond to grow only on one panel side, seen in all the models discussed in section 4.4, was also seen during the experimental test. Figure 5.36 shows both sides of the middle stringer just before the panel's collapse. As it can be seen from this figure, while the de-bond is clearly open and visible from the cap side, same is no the case for the other stringer side. This suggests that indeed the skin buckling pockets deflecting towards the stringers tend to prevent the de-bond from opening in their proximity, suppressing thus de-bond growth on their corresponding side of the stringer. However, the width of the de-bond below the stringer was likely not accurately captured, as in the model the de-bond grew until the edge of the skin-web butt-joint, while in figure 5.26 it can be seen that the de-bond barely passed the butt-joint's half-width.

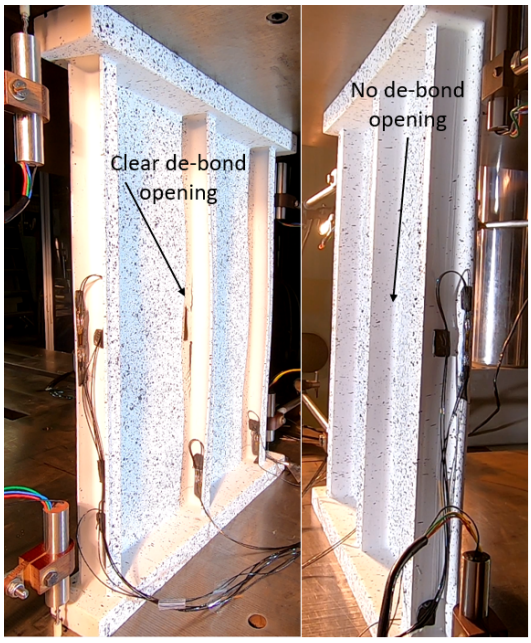

Figure 5.36: De-bond views from both stringer sides

5.3.3 PANEL STRAINS

While the previous test-model correlations gave good understanding on the fidelity with which the FE model captures the panel's compressive behaviour, a good correlation in terms of strains is also necessary in order to asses the robustness of the panel's FE model. The correlation between the $S1\_IML$ and $S1\_OML$ strain gauges from the test and from the $DIC\ imperfection\ FE$ model in terms of load-strain curves can be seen in figure 5.37.

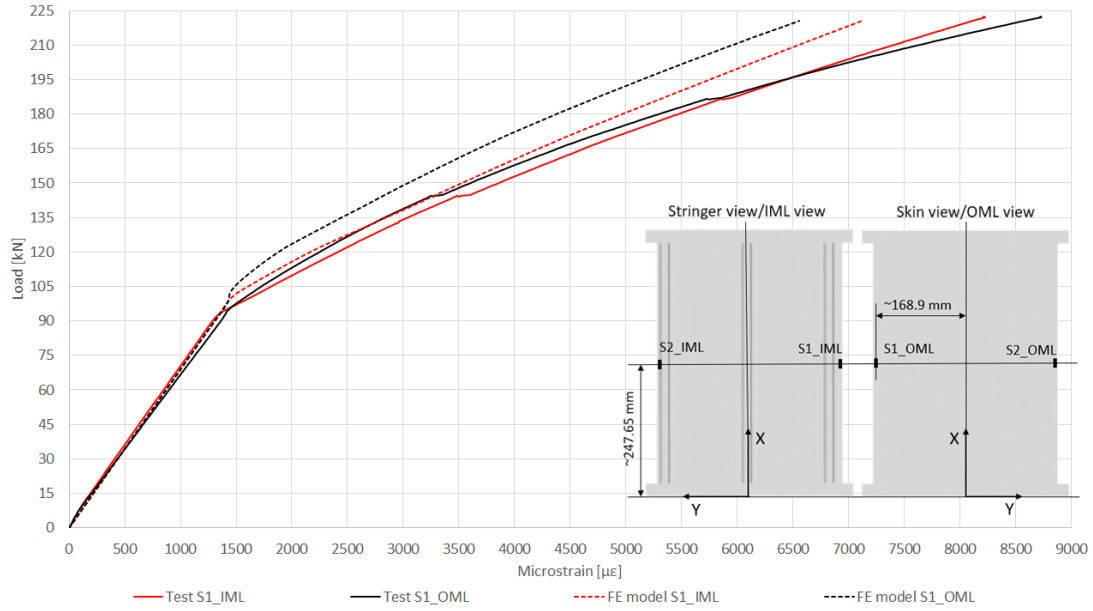

Figure 5.37: Correlation between the $S1$ strain data from the test and from the 'DIC imperfection' FE model

As it can be seen from this figure, in the initial, linear-elastic part the correlation between the strains seen in the test and in the FE model is relatively good. One difference that can be noticed here is that, while in the FE model the same strains are seen on both the top and bottom ply of the skin, same is not the case in the experimental test. This small difference could be given by a strain gauge positioning error on the panel and its corresponding nodes on the panel FE model from which the strains were taken. Also, for this particular pair of strain gauges the $S1\_OML$ one had to be positioned on the glass plies on the panel, while in the FE model it was on the $C/PEKK$ plies. Another possible cause could be an asymmetric load introduction, but since the estimated asymmetric load introduction along the panel's height was considered negligible, its impact on the strains measured by this back-to-back pair should be negligible as well. A small bending component could have also caused a similar behaviour, but since this region is before the panel's skin buckled, the skin bending expected is also negligible.

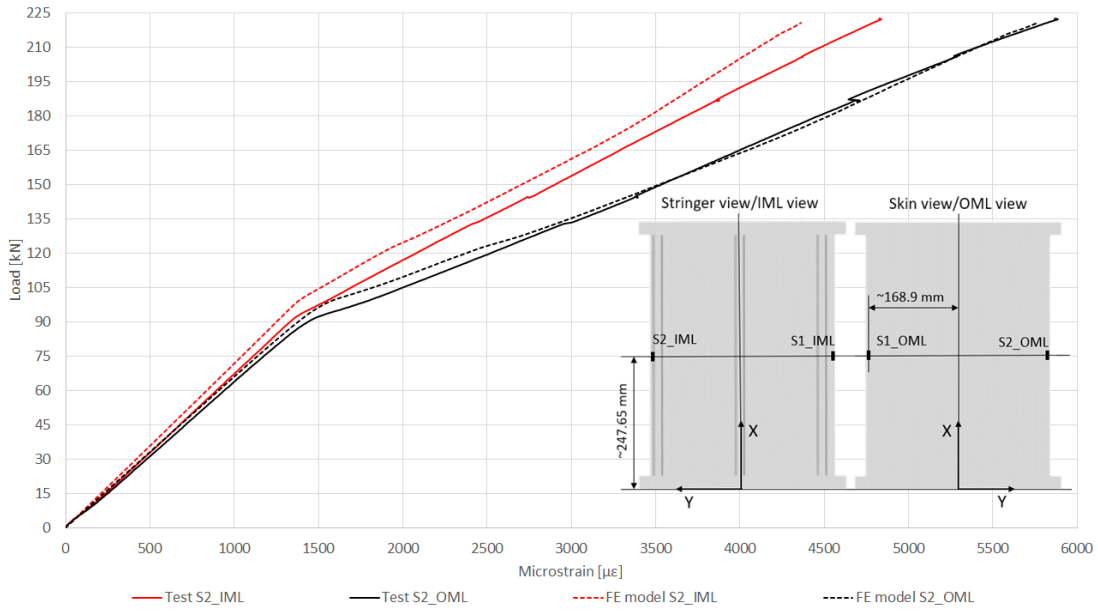

Figure 5.38: Correlation between the $S2$ strain data from the test and from the 'DIC imperfection' FE model

The higher buckling load given by the FE model can also be seen here, the load-microstrain curves using the strain from the FE model having the slope change associated with the panel's skin buckling later than the curves using the strains measured during the test. A good match between the curve slops was also seen immediately after buckling, the test-model strains starting to significantly diverge after the significant debond growth seen in during the test around a load level of $145kN$. After this point, especially the correlation between the strains seen at the $S1\_OML$ location in the test and in the the FE model degrades. This is due to the fact the in the test, the $S1\_OML$ strain increases faster than the $S1\_IML$, aspect which was not seen in the FE model. Due to this aspect, the difference between the strain values from the FE model and from the test for the $S1\_OML$ was significantly grater than the one seen for the $S1\_IML$ location. These differences are of approximately -2000$\mu\epsilon$ for the $S1\_OML$ and approximately -1100 $\mu\epsilon$ for the $S1\_IML$. These values were taken for the same load level of $220.5kN$, the minus sign meaning that the strains seen in FE model are smaller. Considering that the load-microstrain curves from the FE model and from the test have similar post-buckling slopes, most likely the correlation in terms of strains would have been significantly improved had the FE model predicted the buckling load more accurately. This was also valid for the $S2\_IML$ and $S2\_OML$ locations, as it can be seen from figure 5.38.

Interestingly to notice in this figure is that the strains in the top and bottom ply of the skin seen in the FE model at these locations were not identical, not even before the panel's skin buckled. This implies that the skin at this locations slightly bends as the load increases, the strain values diverging before the panel's skin buckles. The skin's bending increases even more after the skin buckles, as the strain values diverge even further. This behaviour was also seen during the test, although the bending component seems to be smaller, the two load-microstrain curves being closer. Here the differences for the same $220.5kN$ load are significantly smaller, with roughly -500$\mu\epsilon$ at the $S2\_IML$ location and less than -100$\mu\epsilon$ at the $S2\_OML$ location. Besides capturing the panel's buckling load with increased accuracy, here the correlation would have also been significantly improved if the correlation in the initial linear-elastic part was better. The correlation between the FE model and the test strains before skin buckling for the $S2\_IML$ and $S2\_OML$ locations is slightly poorer than the one at the $S2\_IML$ and $S2\_OML$ locations. Unlike in the previous case, the positioning errors between the test and the FE model strain measuring points could not be the only reason for this significant mis-match, the skin bending seen in the FE model probably being slightly different than the one seen during the test.

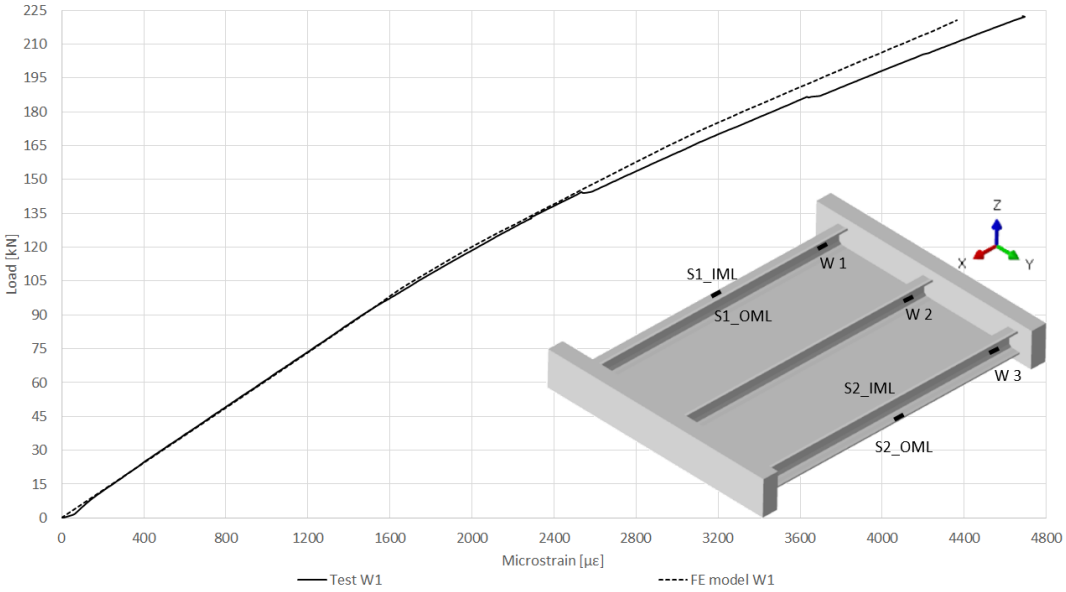

Figure 5.39: Correlation between the $W1$ strain data from the test and from the 'DIC imperfection' FE model

The importance of the bending component for the skin measured strains can also be indirectly seen in the correlation of the web strains. For the strain gauges mounted on the stringer webs, the bending component was smaller since their location was towards the bottom of the panel, unlike the skin strain gauges which were mounted at the panel's mid-length. The smaller bending component at the web strain gauges locations

also translated into a general better correlation between the test and FE model strains seen at these locations. The correlation between the test and FE model strains at the $W1$ location can be seen in figure 5.39.

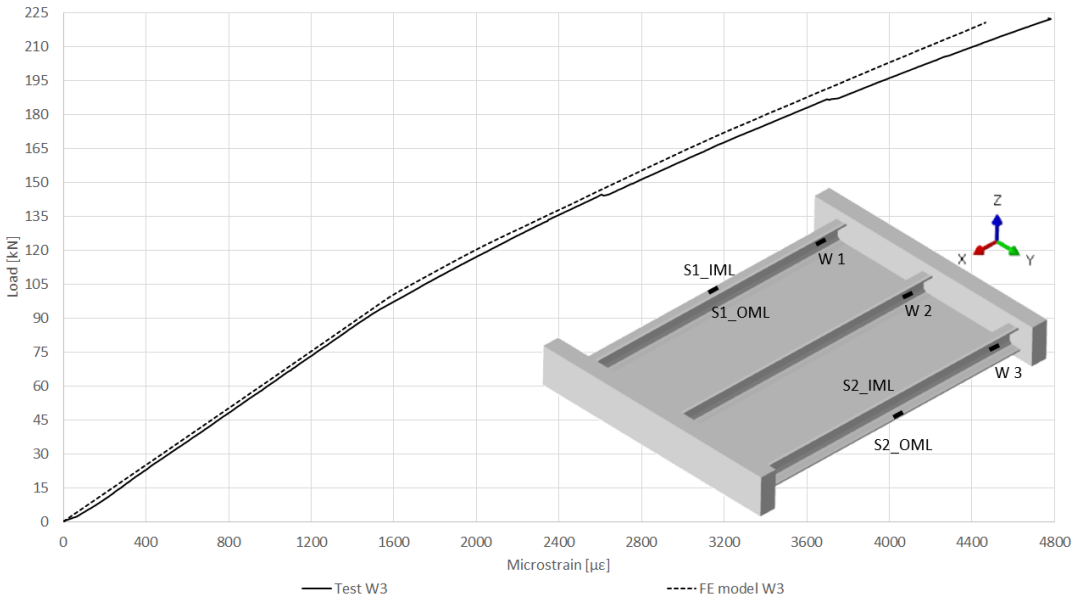

Figure 5.40: Correlation between the $W3$ strain data from the test and from the 'DIC imperfection' FE model

As it can be seen from this figure, the model was able to accurately predict the $W1$ location web strains before and after skin buckling, as the two curves overlap in these regions. However, the model was not able to accurately predict the stiffness changes related to the de-bond growth. This can be seen after a load around $145kN$, at which the first big de-bond growth event occurred in the test. After this point the two curves not only cease to overlap, but the a significant slope difference was also seen. The two curves stray apart even more after the second large de-bond growth around a load of $185kN$, the strain difference around a load of $220.5kN$ being roughly -300 $\mu\epsilon$. The same trend as for the $W1$ strain gauge location was also seen for the $W3$ strain gauge location, also with the same strain difference at a load around $220.5kN$, as it can be seen from figure 5.40.

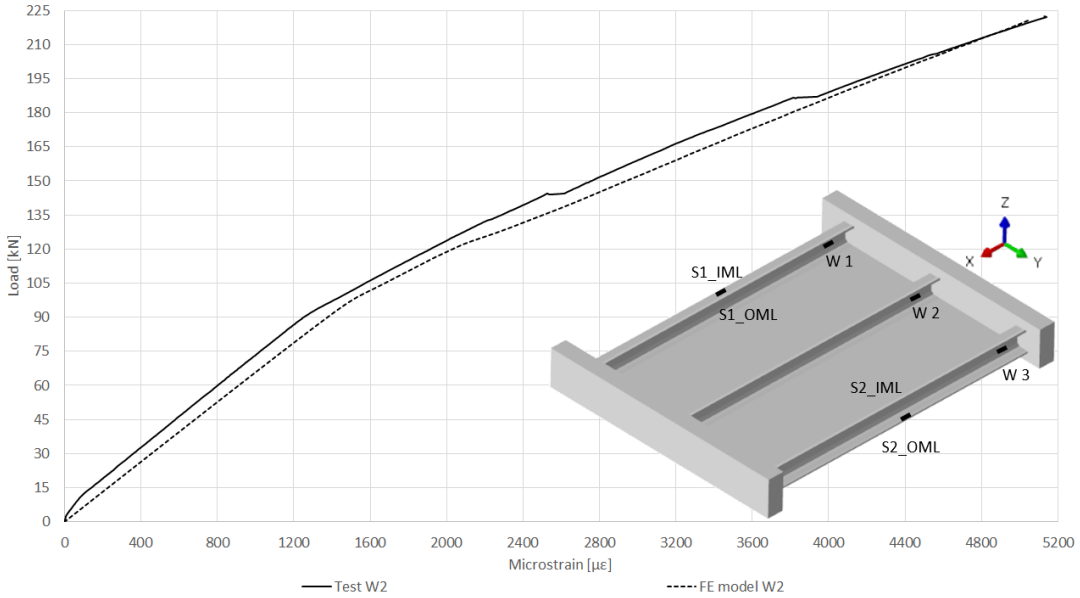

Figure 5.41: Correlation between the $W2$ strain data from the test and from the 'DIC imperfection' FE model

By far the poorest correlation between the three web locations is seen for the $W2$ location (shown in figure 5.41), which represents the middle stringer, hence the one with the skin-stiffener separation damage. Opposite to the other two $W1$ and $W3$ locations, in this case there was an offset between the two curves in the initial liner-elastic part, with the two curves overlapping at the end. This offset came from the significantly stiffer response seen in the test up to a load level around $12kN$, which resulted in an offset between the test and FE model results. Similarly as for the other two web strains, there was a good match between the slopes of the curves, with the change in stiffness due to the de-bond growth also not accurately predicted for this damaged stringer web strains. This mis-match was even more important considering that the de-bond length at failure seen after the test was considered significantly smaller than the one seen in the FE model. Therefore, the difference in slopes for the same de-bond lengths would have been even greater, this being also valid for all the other load-strain correlation curves.

DISCUSSION

Overall, the correlation between the test and the panel FE model can be considered as very good, the model accurately capturing most of the particularities of the panel's compressive behaviour. The load-displacement behaviour of the panel was captured with high accuracy and so were the panel stiffnesses, especially in the initial linear-elastic region. Furthermore, also the panel's buckling behaviour and skin out-of-plane deflection were captured with good accuracy. Moreover, the qualitative aspects of the de-bond behaviour were also captured accurately by the FE model. Among these were the de-bond starting to propagate soon after skin buckling occurred, the parabolic de-bond growth, the strong relation between the panel's buckling pattern and the de-bond growth front, as well as the fact that the de-bond would not reach the entire butt-joint width prior the panel's collapse. The correlation in terms of strain was also relatively good, especially for the web strains before de-bond growth occurred in the test.

One of the small mis-matches in the correlation data was regarding the panel's buckling load, which was overestimated roughly by $10kN$ by the model, which gives a relative difference around +8.6% with respect with the experimental one around $93kN$. This earlier panel skin buckling also led to a significant mis-match between the strains seen during the test and the ones in the model.

The other significant mis-matches were mostly related to the quantitative aspects of the de-bond growth behaviour and its impact on the panel's compressive response, especially on its stiffness and measured strains. The de-bond growth was overestimated by the model, the de-bond magnitude at the panel's collapse considered to be larger by approximately 60%, the FE model prediction being $205mm$, compared with the $130\pm4mm$ observed on the panel. While the model seemed to overestimate the de-bond growth, the panel stiffness loss and the significant strain increase as a result of the de-bond increase was underestimated by the FE model. These mis-matched were likely caused by not accounting for other failure modes which might have occurred in the stringer during the de-bond growth, as well as due to the butt-joint mesh used. Another aspect of the de-bond behaviour that was not accurately captured by the FE model was its growing manner. While the model predicted logarithmic growth with increasing load, the more intuitive exponential de-bond growth with the load was observed during the test.

Concluding, the panel's FE model using the $VCCT$ damage model to capture the skin-stringer de-bond proved able to predict the panel's behaviour with a very good overall accuracy, with some room for improvement regarding the specifics of the de-bond growth and its impact on the panel's compressive behaviour. However, care must be taken when using this methodology to study similar panels, as skin-stringer separation needs to be the main failure mode leading to the panel's collapse. When other failure modes are likely to occur the methodology proposed would not be as effective, as the only type of damage included in this model was skin-stringer separation.

6 | CONCLUDING REMARKS

In this thesis, a methodology to study skin-stiffener separation under compression was developed based on the butt-joint failure mode 2, using the building-block approach to model separation at three different scales.

The first block in this approach 3.1 was to numerically model separation in the DCB specimen tested to measure the $Mode$ 1 opening fracture toughness of APC [36] material used for the panel's $PEKK$ thermoplastic carbon fiber laminates. First the experimental load-displacement behaviour of the DCB test was accurately captured using the $ASTM\ LEFM$ based MMB [39] analytical model, using the measured G_{IC} fracture toughness from the APC material qualification report. Then, the accuracy, robustness and feasibility of the numerical approaches tried to be used for the mesh size desired in the 3-stringer panel was assessed in terms of their load-displacement correlation with this analytical model. Out of the three separation damage models investigated, namely using cohesive elements, cohesive contact and $VCCT$ the latter was chosen as it proved the most robust model, having a good accuracy with coarse mesh sizes and good simulation times, without the need of altering the measured material's fracture toughness properties.

In the second block of this approach 3.2, the chosen $VCCT$ damage model was then validated using a 1-stringer specimen with a $70mm$ skin-stringer de-bond. While an old FE model existed for this specimen, the cohesive surface damage modeling approach used in this model was not able to accurately capture separation in the DCB specimen used at the first building block, therefore it was deemed not consisted with this modeling approach. Furthermore, the skin-web butt-joint at the inter-phase which the separation damage model was implemented also proved to give a poor correlation with the experimental load-displacement response of this 1-stringer specimen. This was due to a significant over-estimation of the butt-joint's cross-section area, which also gave a stronger skin-stringer connection. To alleviate this issue, a novel FE model of the 1-stringer specimen was built, in which the butt-joint's cross-section area was made identical with the nominal one and the element type used to mesh it were changed to ones better suited to capture bending. The $VCCT$ damage model proved to work really well for this improved model, giving an excellent correlation with its experimental load-displacement behaviour and an relative error for its failure load within 1%.

In the third and last block, the modeling strategy used to capture the compressive behaviour for the 1-stringer panel was applied to study the compressive behaviour of the 3-stringer panel 4. The modeling approach developed in the first two building blocks for the DCB and 1-stringer specimen showed several signs of good reliability also for the 3-stringer panel. These were the near identical compressive response of a model with the another model with the nominal butt-joint geometry, as the good correlation of the model's weight and free vibration frequency response with the experimentally measured correspondent values. With the FE model of the 3-stringer panel passing well these preliminary checks, skin-stringer separation was studied using the same damage model and parameters previously used to capture separation at the two lower scale levels in the 1-stringer specimen and DCB coupon. This skin-stringer separation study was carried covering a range of possible testing scenarios and studying the influence of several modeling details. This approach was chosen to get a deeper understanding on the influence of the damage on the panel's compressive behaviour, to identify the most severe scenario, to identify the best blind prediction which would be further used in the correlation with the experimental data, as well as to prepare the experimental testing of the panel. One of the most relevant finding at this stage was the high sensitivity of the panel's buckling behaviour to a number of factors. The panel's buckling response was found to be highly influenced by asymmetrical load introduction, by skin imperfections, by the modeling strategy used to capture the boundary conditions provided by the resin tabs used to aid the uniform load introduction, as well as by the damage itself. Besides the panel's buckling behaviour high sensitivity towards the aforementioned aspects, the damage itself was also found to interact particularly with the asymmetric load introduction, as the buckling pattern varied for the same loading scenario depending on if the de-bond damage was accounted or not. The highest impact on the panel's failure load was found to be its skin buckling pattern, owing to its tendency to promote skin-stringer de-bond from one panel bay or another. It was found that the buckling patterns that promote de-bond growth from the panel bay containing one of the three stringer caps could reduce the panel's failure load by more than 25%, when a less likely 4 half-waves buckling pattern occurs. Similarly, also a 4 half-waves buckling pattern could raise the failure load by roughly 7%, the difference in this case with respect to the pattern that drops the

failure load by more than 25%, being its opposite pocket deflection signs, which causes the de-bond to grow from the cap side of the stringer.

The panel test set-up proposed for the panel's experimental test was successfully applied to characterise the panel's compressive response and to asses the robustness of the proposed FE modeling approach 5. The correlation between the test data and the FE model's prediction was very good overall, validating thus the proposed method. The model proved to predict very well the panel's load-displacement curve (including the failure load), the buckling pattern, skin out-of-plane deflections, initial strain response, as well as few important aspects of the de-bond growth, like to location, growth front shape or initiation. At the same time, there was also room for improvement in predicting the panel's skin buckling load, the magnitude of the de-bond and the stiffness loss due to skin-stringer separation.

6.1 RECOMMENDATIONS FOR FUTURE WORK

MODE II AND MIXED-MODE FE STUDY

Starting from the first block of the building-block approach used, the capabilities of the Abaqus $VCCT$ damage model to accurately capture mode II separation should also be investigated. While the $VCCT$ damage model is perfectly able to accurately simulate separation under pure mode I, its capabilities to simulate separation under a pure mode II should also be studied. For developing this approach in particular, this should be done by using the ENF [62] test standard, which was also the test used to measure the mode II fracture toughness of the material used for the panel's laminates. Studying the capabilities of this damage model to simulate pure mode II separation might also give insight on why the de-bond growth seen in the panel's FE model was significantly different than the one from the test observations. Furthermore, as in reality the skin-stiffener de-bond grows under a mix from all three opening modes, this aspect should also be taken into account. Especially the modes I-II interaction can be easily studied and simulated using a MMB specimen [39], which is an already established and standardised testing method.

PANEL MESH REFINEMENT

As the mesh size used for the damage model was relatively coarse, a mesh refinement study could be used to asses the influence of the mesh size on the accuracy of the $VCCT$ damage model. While the mesh size used proved to be good enough when simulating pure mode I separation using a DCB specimen, same might not be the case for simulating other pure opening modes or the opening under a mix of these modes. In order to make this sensitivity study, a mesh refinement could also be done using a global-local approach, with a reduced allowed de-bond growth length based on the test observations.

SKIN-WEB BUTT-JOINT GEOMETRY STUDY/REFINEMENT

Another recommendation would be to study the influence of the skin-web butt-joint geometry, which could also influence the de-bond growth. While the panel general behaviour with the nominal and simplified geometry was studied and the model with simplified geometry behaved generally the same as the one with nominal geometry, the de-bond growth behaviour might be different with a skin-web butt-joint geometry closer to the nominal one. This could be done together with the previous recommendation, as taking the skin-web butt-joint geometry closer to its nominal geometry would also imply some mesh refinement due to its radius.

POSSIBLE CORRELATION IMPROVEMENT-ACCOUNT FOR THE SMALL LOAD ASYMMETRY ALONG THE PANEL'S WIDTH

As a secondary goal of the thesis was to asses the accuracy of the best blind prediction and as an asymmetric load introduction was observed during the test, the simulation-test correlation from section 5.3 was not done 'on equal terms'. In other words, the load asymmetry was not accounted in the FE model prediction. While the test-simulation correlation was reasonably good, a better quantitative assessment could be done by simulating the load asymmetry observed in the test in the FE model and then to re-do the correlation.

RECOMMENDATION IN APPLYING THIS METHOD TO FUTURE MODELS

Since the same modeling approach and the same damage model and parameters showed a very good accuracy at all three scales level treated in the building block approach used, the developed method to study skin-stringer separation is considered to be robust and an useful tool for other similar studies. For the same

material type as the one studied and for similar skin-web butt-joint geometries the developed modeling strategy is likely to readily work well for the studied scales, provided it falls under its applicability range. This means that skin-stringer separation should be the main failure mode, with as little possible occurrence of other failure modes prior collapse. Furthermore, care should be taken if the proposed method is desired to be used in panels with transverse stiffening as well, as the method was only proven using simple, longitudinal stiffened structures. However, when a different material is to be used, it would be highly recommended to verify the accuracy of the numerical method to capture the the simple $Mode\,1$ separation of the DCB specimen against both of the two analytical models used here. This can be extremely valuable as the shown DCB analytical models are very simple to implement and so is setting up a DCB FE model using the $VCCT$ damage model described and used in this report. With that being said, it is easy to verify if the proposed method is robust and yields a good accuracy for the new material system starting from the smallest scale.

IMPROVE THE PYTHON SCRIPT TO APPLY THE DIC MEASURED SKIN IMPERFECTION

One last recommendation would be to simplify and to improve the python script used to generate the files used to introduce the DIC measured imperfection into the panel's FE model. While the script works correctly, it use can be troublesome for someone who is not familiar with it, since it was quickly written to perform the task at hand and to verify this process. With that being said, the script cannot be described as user friendly yet, as there are a few important steps that can be simplified and automated. One of the improvements that can be done is automatically read the imperfection file and the Abaqus input file, with user aids for possible future coordinates alignment. Right now this process has a few manual inputs, used to identify the rows of the nodes coordinates in the Abaqus input file, which require the visual inspection of this input file. Some user aids to align the two coordinate systems can also be used, like the extreme values of the X and Y coordinates and/or a $3D$ plot of the DIC measured points. Furthermore, the script writes separate files for the FE model node sets and displacement boundary conditions applied, which are then used to manually modify an Abaqus input file. This process can also be simplified such that the Abaqus input file is modified automatically by the script. Last, but not least, the script can be highly simplified and re-organized, such that its structure becomes clearer, hence also easier to adjust, improve, or to check its proper functioning.

REFERENCES

[1] Ginger Gardiner. *Thermoplastic composites: Primary structure?* CompositesWorld, 2011. Available online: https://www.compositesworld.com/articles/thermoplastic-composites-primary-structure.

[2] Mike Favaloro. *Thermoplastic composites in aerospace – the future looks bright.* CompositesWorld, 2018. Available online: https://www.compositesworld.com/columns/thermoplastic-composites-in-aerospace-past-present-and-future.

[3] Chris Red. *Thermoplastics in Aerospace Composites Outlook, 2014-2023.* CompositesWorld, 2014. Available online: https://www.compositesworld.com/articles/the-outlook-for-thermoplastics-in-aerospace-composites-2014-2023.

[4] John Macdonald. *Using Thermoplastics in Aerospace Applications.* Aerospace & Defense Technology - Tech Briefs Media Group, 01 August 2018. Available online: https://www.aerodefensetech.com/component/content/article/adt/features/articles/32727.

[5] Arnt Offringa. *Thermoplastic composites in aerospace-Breakthrough Technologies for Advanced Manufacture.* Society for the Advancement of Material and Process Engineering (SAMPE), 25 February 2016. Available online: http://www.sampe.org.uk/assets/documents/pdfs/AS2016/Presentations/AS2016_01_Arnt_Offringa_Fokker.pdf.

[6] GKN Aerospace. Fokker Technologies. Website: https://www.gknaerospace.com/en/about-gkn-aerospace/fokker-technologies/.

[7] M. Rouse, D.C. Jegley, D.M. McGowan, H.G. Bush, W.A. Waters. *Utilization Of The Building-Block Approach In Structural Mechanics Research.* https://ntrs.nasa.gov/search.jsp?R=20050199405, 1 January 2005. Available online: https://ntrs.nasa.gov/search.jsp?R=20050199405.

[8] B.H.A.H. Tijs, C. S. Lopes, A. Turon, C. Bisagni, J. Waleson, J. W. Van Ingen, S. L. Veldman. *Virtual testing of thermoplastic composites: Towards a hybrid simulation-physical testing pyramid.* ECCM18 - 18th European Conference on Composite Materials Athens, Greece, June 2018. Available online: https://az659834.vo.msecnd.net/eventsairwesteuprod/production-pcoconvin-public/7fc7887fd5934b759f30b1652b61db30.

[9] Thermoplastic affordable primary aircraft structures, 2016-2020. Available online: http://www.tapasproject.nl/en/about-us.

[10] I. Baran, L.L. Warnet, R. Akkerman. *Assessment of failure and cohesive zone length in co-consolidated hybrid C/PEKK butt joint.* Engineering Structures Volume 168, pag. 420-430, 1 August 2018. https://doi.org/10.1016/j.engstruct.2018.04.089.

[11] J.W. van Ingen. *Thermoplastic Orthogrid Fuselage Shell.* Sampe Journal 52(5), pag. 7-15, September 2016. Available online: https://www.researchgate.net/publication/307926694_Thermoplastic_Orthogrid_Fuselage_Shell.

[12] B. Rietman, R. Akkerman. *Pull-off strength assesment of co-consolidated AS4/PEEK T-joints.* Curran Associates, 8th SAMPE Europe Technical Conference & Table Top Exhibition, pag. 163-170, 2013 (SETEC 2013). Available online: https://ris.utwente.nl/ws/portalfiles/portal/5524849/Setec2013_Rietman.pdf.

[13] K. Ilin, L.L.Warnet, B. Rietman, R. Akkerman, R.H.W. ten Thije. *Failure Modeling of Thermoplastic Butt-Joint Stiffened Panels by Quasi-Static Loading.* SIMULIA Community Conference, 2012. Available online: https://www.researchgate.net/publication/267706801_Failure_Modeling_of_Thermoplastic_Butt-Joint_Stiffened_Panels_by_Quasi-Static_Loading/stats.

[14] Z. Sápi, R. Butler, A. Rhead. *Filler materials in composite out-of-plane joints – A review.* Composite Structures Volume 207, pag. 787-800, 1 January 2019. https://doi.org/10.1016/j.compstruct.2018.09.102.

[15] H.M.Hsiao, I.M.Daniel. *Effect of fiber waviness on stiffness and strength reduction of unidirectional composites under compressive loading.* Composites Science and Technology Volume 56, Issue 5, pag. 581-593, 1996. https://doi.org/10.1016/0266-3538(96)00045-0.

[16] D. Wilhelmsson, R. Gutkin, F. Edgren, L.E. Asp. *An experimental study of fibre waviness and its effects on compressive properties of unidirectional NCF composites.* Composites Part A: Applied Science and Manufacturing Volume 107, pag. 665-674, April 2018. https://doi.org/10.1016/j.compositesa.2018.02.013.

[17] P. Davidson, A.M. Waas, C.S. Yerramalli, Karthick Chandraseker, Waseem Faidi. *Effect of Fiber Waviness on the Compressive Strength of Unidirectional Carbon Fiber Composites.* 53rd AIAA/ASME/ASCE/AHS/ASC Structures, Structural Dynamics and Materials Conference, 2012. Available online: https://pdfs.semanticscholar.org/d4b8/37ce6c7c2a8fa39fe0e78665b0d987897014.pdf.

[18] D. O'Hare Adams, M.W. Hyert. *Effects of layer waviness on the compression fatigue performance of thermoplastic composite laminates.* International Journal of Fatigue Volume 16, Issue 6, pag. 385-391, August 1994. https://doi.org/10.1016/0142-1123(94)90450-2.

[19] J. Chen, D. Fox. *Numerical investigation into multi-delamination failure of composite T-piece specimens under mixed mode loading using a modified cohesive model.* Composite Structures Volume 94, Issue 6, pag. 2010-2016, May 2012. https://doi.org/10.1016/j.compstruct.2011.12.030.

[20] Dassault Systèmes Simulia. Abaqus Unified FEA. Available online: https://www.3ds.com/products-services/simulia/products/abaqus/.

[21] GKN-Fokker. *TW-14-140 - TAPAS2, test plan gridpanels: compression tests and in-plane shear tests.* GKN-Fokker internal report, 2016.

[22] R. Vescovini, C.G. Dávila, C. Bisagni. *Failure analysis of composite multi-stringer panels using simplified models.* Composites Part B: Engineering Volume 45, Issue 1, February 2013, pag. 939-951, 2013. https://doi.org/10.1016/j.compositesb.2012.07.030.

[23] A. Riccio, A. Raimondo, G. Di Felice, F. Scaramuzzino. *A numerical procedure for the simulation of skin–stringer debonding growth in stiffened composite panels.* Aerospace Science and Technology Volume 39, pag. 307-314, December 2014. https://doi.org/10.1016/j.ast.2014.10.003.

[24] A.C. Orifici, I. O. Z. Alberdi, R.S. Thomson, J. Bayandor. *Compression and post-buckling damage growth and collapse analysis of flat composite stiffened panels.* Composites Science and Technology Volume 68, Issues 15–16, pag. 3150-3160, December 2008. https://doi.org/10.1016/j.compscitech.2008.07.017.

[25] A. Riccio, M. Damiano, A. Raimondo, G. Di Felice, A. Sellitto. *A fast numerical procedure for the simulation of inter-laminar damage growth in stiffened composite panels.* Composite Structures Volume 145, pag. 203-216, 10 June 2016. https://doi.org/10.1016/j.compstruct.2016.02.081.

[26] A. Soto, E.V. González, P. Maimí, J.A. Mayugo, P.R. Pasquali, P.P. Camanho. *A methodology to simulate low velocity impact and compression after impact in large composite stiffened panels.* Composite Structures Volume 204, pag. 223-238, 15 November 2018. https://doi.org/10.1016/j.compstruct.2018.07.081.

[27] W. Sun, Z. Guan, Z. Li, T. Ouyang, Y. Jiang. *Modelling and simulating of the compressive behavior of T-stiffened composite panels subjected to stiffener impact.* Composite Structures Volume 186, pag. 221-232, 15 February 2018. https://doi.org/10.1016/j.compstruct.2017.11.079.

[28] N. Li, P. Chen. *Prediction of Compression-After-Edge-Impact (CAEI) behaviour in composite panel stiffened with I-shaped stiffeners.* Prediction of Compression-After-Edge-Impact (CAEI) behaviour in composite panel stiffened with I-shaped stiffeners, 2017. https://doi.org/10.1016/j.compositesb.2016.11.043.

[29] Wikipedia. Fracture Mechanics. Available online: https://en.wikipedia.org/wiki/Fracture_mechanics#/media/File:Fracture_modes_v2.svg.

[30] Abaqus 2017 user documentation. Crack propagation analysis. https://help.3ds.com/2017/english/dssimulia_established/simacaeanlrefmap/simaanl-c-crackpropagation.htm?contextscope=all.

[31] M.L.Benzeggagh, M.Kenane. Measurement of mixed-mode delamination fracture toughness of unidirectional glass/epoxy composites with mixed-mode bending apparatus. https://doi.org/10.1016/0266-3538(96)00005-X.

[32] M.E. Wu, R.C. Reuter Jr. Crack extension in fiberglass reinforced plastics, February 1965. Available online: https://apps.dtic.mil/dtic/tr/fulltext/u2/613576.pdf.

[33] J.R. Reeder, P.B. Chunchu, K. Song, D.R. Ambur. Postbuckling and Growth of Delaminations in Composite Plates Subjected to Axial Compression, February 2002. Available online: https://ntrs.nasa.gov/archive/nasa/casi.ntrs.nasa.gov/20030005487.pdf.

[34] Abaqus 2017 user documentation. Contact cohesive behavior. https://help.3ds.com/2017/english/dssimulia_established/simacaeitnrefmap/simaitn-c-cohesivebehavior.htm?contextscope=all.

[35] A.P. Mouritz. *Introduction to aerospace engineering: Chapter 5-Mechanical and durability testing of aerospace materials.* Woodhead Publishing Limited, pag. 91-127, 2012. https://doi.org/10.1533/9780857095152.91.

[36] GKN-Fokker. *TW-15-0143-Cover report Qualification of PEKK-FC materials 5.603/101from Cytec.* GKN-Fokker internal report, 2015.

[37] Solvay. ASD4 12K/APC (PEKK-FC) UD Tape. Available online: https://www.solvay.com/en/product/apc-pekk-thermoplastic-composite-tapes.

[38] American Society for Testing and Materials International (ASTM). ASTM D5528 - Standard Test Method for Mode I Interlaminar Fracture Toughness of Unidirectional Fiber-Reinforced Polymer Matrix Composites. https://www.astm.org/Standards/D5528.

[39] American Society for Testing and Materials International (ASTM). ASTM D6671 / D6671M - Standard Test Method for Mixed Mode I-Mode II Interlaminar Fracture Toughness of Unidirectional Fiber Reinforced Polymer Matrix Composites. https://www.astm.org/Standards/D6671.htm.

[40] A. Turon, P.P. Camanho, J. Costa, J. Renart. *Accurate simulation of delamination growth under mixed-mode loading using cohesive elements: Definition of interlaminar strengths and elastic stiffness.* Composite Structures Volume 92, Issue 8, pag. 1857-1864, July 2010. https://doi.org/10.1016/j.compstruct.2010.01.012.

[41] A.Turon, C.G.Dávila, P.P.Camanho, J.Costa. *An engineering solution for mesh size effects in the simulation of delamination using cohesive zone models.* Engineering Fracture Mechanics Volume 74, Issue 10, pag. 1665-1682, July 2007. https://doi.org/10.1016/j.engfracmech.2006.08.025.

[42] Abaqus 2017 user documentation. Mesh tie constraints, 2017. https://help.3ds.com/2017/english/dssimulia_established/simacaecstrefmap/simacst-c-tiedconstraint.htm?contextscope=all.

[43] Abaqus 2017 user documentation. Defining the constitutive response of cohesive elements using a traction-separation description, 2019. https://help.3ds.com/2017/english/dssimulia_established/simacaeelmrefmap/simaelm-c-cohesivebehavior.htm?ContextScope=all#simaelm-c-cohesivebehavior-regularize.

[44] Abaqus 2017 user documentation. Total energy output quantities, 2019. https://help.3ds.com/2017/english/dssimulia_established/simacaeoutrefmap/simaout-c-std-wholeandpartialmodelvariables.htm?contextscope=all.

[45] A.Soto, E.V.González, P.Maimí, A.Turon, J.R.Sainz de Aja, F.M.de la Escalera. *Cohesive zone length of orthotropic materials undergoing delamination.* Engineering Fracture Mechanics Volume 159, pag. 174-188, July 2016. https://doi.org/10.1016/j.engfracmech.2016.03.033.

[46] A.Turon, E.V.González, C.Sarrado, G.Guillamet, P.Maimí. *Accurate simulation of delamination under mixed-mode loading using a cohesive model with a mode-dependent penalty stiffness.* Composite Structures Volume 184, pag. 506-511, 15 January 2018. https://doi.org/10.1016/j.compstruct.2017.10.017.

[47] Abaqus 2017 user documentation. Contact formulations in Abaqus/Standard. https://help.3ds.com/2017/english/dssimulia_established/simacaeitnrefmap/simaitn-c-contactpairform.htm?contextscope=all.

[48] Abaqus 2017 user documentation. About general contact in Abaqus/Standard. https://help.3ds.com/2017/english/dssimulia_established/simacaeitnrefmap/simaitn-c-contactgeneralstd.htm?contextscope=all.

[49] Abaqus 2017 user documentation. Energy computations in a contact analysis. https://help.3ds.com/2017/english/dssimulia_established/SIMACAEEXARefMap/simaexa-c-contactenergy.htm?ContextScope=all.

[50] GKN-Fokker. *TW-18-0004 - FEM QA report cohesive zone analyses of 1-stringer specimen.* Fokker internal report, 2018.

[51] Cytec. HexForce 108 Fiber Glass Fabric. Available online: https://www.hexcel.com/user_area/content_media/raw/DSF_108.pdf.

[52] Arkema. KEPSTAN 7000 series thermoplastic material. Available online: https://www.arkema.com/export/shared/.content/media/downloads/products-documentations/incubator/arkema-kepstan-7000-tds.pdf.

[53] N.R.P. Koekoek. *FFTTT-18-005, 'ARF Stringer Compression test'.* GKN-Fokker internal document, 2018.

[54] Abaqus 2017 user documentation. Performance of continuum and shell elements for linear analysis of bending problems, 2017. https://help.3ds.com/2017/english/dssimulia_established/simacaebmkrefmap/simabmk-c-linbending.htm?contextscope=all.

[55] P .Koning. *ARF5341101C001, Catia model ,'TESTPANEL A, TRIMMED, FLAT'.* GKN-Fokker internal report, 2018.

[56] UBE. UPILEX. Available online: http://www.upilex.jp/en/upilex_grade.html.

[57] GKN-Fokker. *ARF 19-0004, issue 1 - Manufacturing data on TUD 3str panel WI -18-0076 and WI-19-0001.* Fokker internal report, 2019.

[58] Huntsman. RenCast® FC 52 Isocyanate / FC 52 Polyol casting resin. Available online: https://polyestershoppen.nl/download/polyurethaan-giethars/technische-data-119.pdf.

[59] MIT. Structural Mechanics Lecture 11: Buckling of Plates and Sections, 2013. Available online: https://ocw.mit.edu/courses/mechanical-engineering/2-080j-structural-mechanics-fall-2013/course-notes/MIT2_080JF13_Lecture11.pdf.

[60] International Organization for Standardization (ISO). ISO 15024. https://www.iso.org/obp/ui/#iso:std:iso:15024:ed-1:v1:en.

[61] European Committee for Standardization. DIN EN 6033. https://www.en-standard.eu/din-en-6033-luft-und-raumfahrt-kohlenstofffaserverstarkte-kunststoffe-prufverfahren-bestimmung-der-interlaminaren-en

[62] American Society for Testing and Materials International (ASTM). Standard Test Method for Determination of the Mode II Interlaminar Fracture Toughness of Unidirectional Fiber-Reinforced Polymer Matrix Composites. https://www.astm.org/Standards/D7905.htm.

[63] International Organization for Standardization (ISO). ISO 15114. https://www.iso.org/obp/ui/#iso:std:iso:15114:ed-1:v1:en.

[64] A.López-Menéndez, J.Viña, A.Argüelles, I.Viña, S.Rubiera. *Analysis of mode III interlaminar fracture toughness of laminated composites using a novel testing device.* Engineering Fracture Mechanics Volume 173, Pages 55-63, 15 March 2017. https://doi.org/10.1016/j.engfracmech.2017.01.021.

[65] Yangyang Ge, Xiaojing Gong, Anita Hurez, Emmanuel De Luycker. *Test methods for measuring pure mode III delamination toughness of composite.* Polymer Testing, Volume 55, Pages 261-268, October 2016. https://doi.org/10.1016/j.polymertesting.2016.08.025.

[66] Gabriele Cricrì, Michele Perrella, Salvatore Sessa, Nunziante Valoroso. *A novel fixture for measuring mode III toughness of bonded assemblies.* Engineering Fracture Mechanics, Volume 138, Pages 1-18, April 2015. https://doi.org/10.1016/j.engfracmech.2015.03.019.

[67] Abaqus 2017 user documentaiton. Damage initiation for fiber-reinforced composites. https://help.3ds.com/2017/english/dssimulia_established/SIMACAEMATRefMap/simamat-c-damageinitfibercomposite.htm?ContextScope=all.

[68] Z. Hashin. *Failure Criteria for Unidirectional Fiber Composites.* J. Appl. Mech 47(2), 329-334, Jun 01, 1980. Available online: http://oss.jishulink.com/caenet/forums/upload/2012/11/19/106/61053946809015.pdf.

[69] Abaqus 2017 user documentaiton. Plane stress orthotropic failure measures. https://help.3ds.com/2017/english/dssimulia_established/simacaematrefmap/simamat-c-failuremeasures.htm?contextscope=all.

[70] GKN-FokkerI. Lippers. *ARF 18-0013 'ARF compression test panels – panel design description, test proposal and FE test prediction'.* GKN-Fokker internal document, 2018.

[71] KYOWA. Composite material strain gauges. Available online: https://www.kyowa-ei.com/eng/product/category/strain_gages/kfrpb/index.html.

[72] Keithley Instruments. Test Equipment Solutions Datasheet. Available online: http://www.testequipmenthq.com/datasheets/KEITHLEY-2701-Datasheet.pdf.

A | 3-STRINGER PANEL CUT AND THICKNESS MEASUREMENT

In figure A.1 the 3-stringer panel cut from the initial 5-stringer panel is shown, together with the measured width of the 3-stringer panel. This measured width of the panel is $1.2mm$ less than the $344.8mm$ nominal one based on the stinger $20mm$ edge distance and $152.4mm$ stringer pitch. Figure A.2 shows the thickness measurement of the initial 5-stringer panel. In this figure red rectangles are used to highlight the measurements relevant for the 3-stringer panel. From this figure it can be noticed that the web thickness is slightly smaller than the nominal one, while the cap and skin thickness seem to be higher than the nominal ones. Also, here it can be noticed that the cap width is $0.25mm$ smaller than the ones used in this report, which was based on the Catia model definition of the 5-stringer panel [55]. However, this small difference is not thought to significantly influence the accuracy of the model.

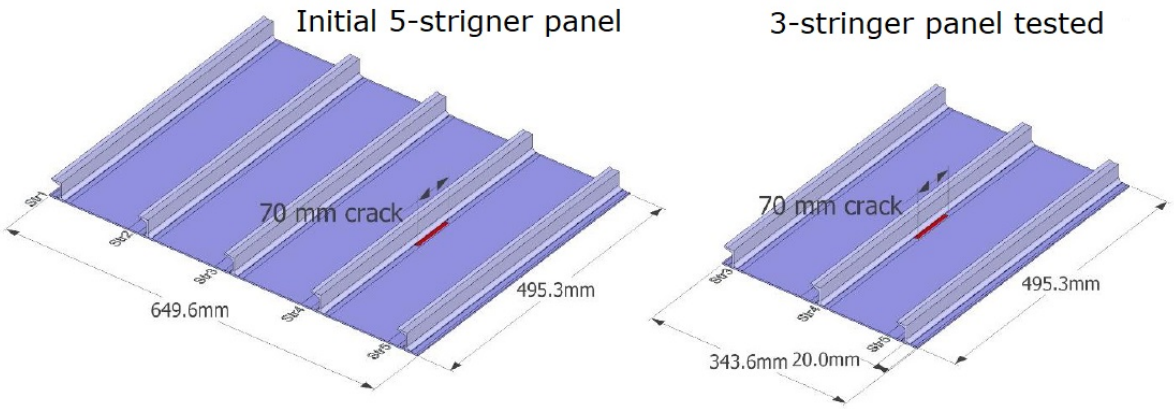

Figure A.1: 3-stringer panel area cut from the initial 5 stringer panel

		Before consolidation					After consolidation					
							Skin thickness			Web	Cap	
		W_web	t_web	W_cap	t_cap	Block	A	B	C	D	E	Step
Stringer	Location	[mm]	[mm]	[mm]	[mm]	[mm]	[mm]	[mm]	[mm]	[mm]	[mm]	[mm]
Str1	1	27.94	2.49	14.75	2.78	0.3	n.a.	n.a.	2.5	2.41	2.85	
Str1	2	27.94	2.53	14.76	2.8	0.4	n.a.	n.a.	2.54	2.42	2.87	
Str1	3	27.94	2.54	14.75	2.79	0.4	n.a.	n.a.	n.a.	2.42	2.86	
Str1	4	27.93	2.52	14.75	2.78	0.3	n.a.	n.a.	2.53	2.43	2.84	
Str1	5	27.94	2.54	14.76	2.77	0.35	n.a.	n.a.	2.53	2.43	2.85	
Str2	1	27.97	2.53	14.74	2.78	0.4	2.56	2.39	2.52	2.43	2.9	-0.17
Str2	2	27.96	2.55	14.75	2.81	0.3	2.59	2.44	2.54	2.42	2.85	-0.15
Str2	3	27.93	2.52	14.75	2.8	0.3	n.a.	n.a.	n.a.	2.41	2.83	
Str2	4	27.96	2.54	14.74	2.8	0.3	2.56	2.42	2.53	2.42	2.83	-0.14
Str2	5	27.92	2.53	14.75	2.81	0.3	2.57	2.42	2.53	2.43	2.83	-0.15
Str3	1	27.93	2.51	14.75	2.75	0.3	2.56	2.41	2.52	2.42	2.85	-0.15
Str3	2	27.93	2.52	14.75	2.75	0.3	2.57	2.43	2.54	2.42	2.8	-0.14
Str3	3	27.94	2.57	14.75	2.78	0.3	n.a.	n.a.	n.a.	2.42	2.8	
Str3	4	27.92	2.54	14.75	2.78	0.35	2.58	2.43	2.54	2.4	2.81	-0.15
Str3	5	27.93	2.52	14.75	2.77	0.3	2.56	2.42	2.54	2.43	2.84	-0.14
Str4	1	27.91	2.54	14.72	2.8	0.35	2.56	2.42	2.55	2.42	2.86	-0.14
Str4	2	27.9	2.5	14.71	2.78	0.3	2.58	2.44	2.52	2.4	2.81	-0.14
Str4	3	27.93	2.55	14.74	2.82	0.3	n.a.	n.a.	n.a.	2.4	2.82	
Str4	4	27.88	2.55	14.73	2.8	0.35	2.57	2.43	2.68	2.4	2.84	-0.14
Str4	5	27.9	2.52	14.74	2.8	0.35	2.56	2.42	2.62	2.43	2.85	-0.14
Str5	1	27.96	2.5	14.76	2.77	0.35	2.56	2.44	2.49	2.42	2.81	-0.12
Str5	2	27.94	2.54	14.76	2.8	0.3	2.57	2.46	2.57	2.4	2.81	-0.11
Str5	3	27.93	2.52	14.75	2.78	0.3	n.a.	n.a.	n.a.	2.39	2.79	
Str5	4	27.93	2.52	14.76	2.79	0.3	2.58	2.48	2.57	2.4	2.78	-0.1
Str5	5	27.93	2.53	14.76	2.79	0.3	2.54	2.43	2.56	2.4	2.8	-0.11
	Average	27.93	2.53	14.75	2.79	0.32	2.57	2.43	2.55	2.41	2.83	-0.14
	St dev	0.02	0.02	0.01	0.02	0.04	0.01	0.02	0.04	0.01	0.03	0.02
	Nominal	27.95	2.48	14.75	2.76		2.48	2.48	2.48	2.48	2.76	
	Deviation	-0.02	0.04	0.00	0.03		0.08	-0.05	0.06	-0.07	0.07	
	Max dev	0.02	0.09	0.01	0.06	0.40	0.11	0.00	0.20	-0.05	0.14	-0.10
	Min dev	-0.07	0.01	-0.04	-0.01	0.30	0.06	-0.09	0.01	-0.09	0.02	-0.17

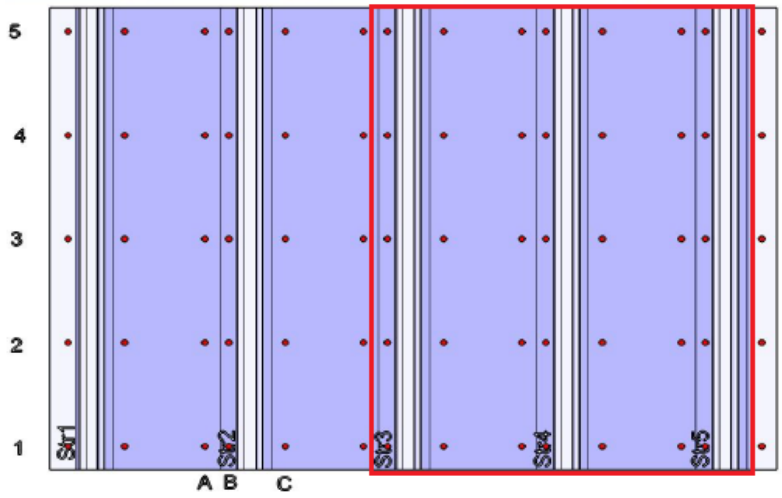

Requirements		CPT	0.138	
		Nom	Max	Min
	[Ply]	[mm]	[mm]	[mm]
Skin	18	2.48	2.68	2.29
t_Web	18	2.48	2.68	2.29
t_Cap	20	2.76	2.98	2.54
W_Web		27.95	28.2	27.7
W_Cap		14.75	15	14.5

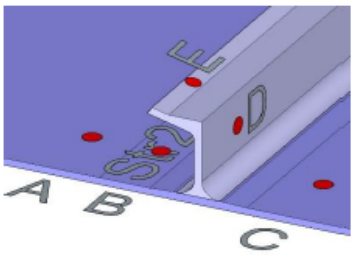

Figure A.2: 5-stringer panel thickness measurement

B | PANEL NDT UT SCANS

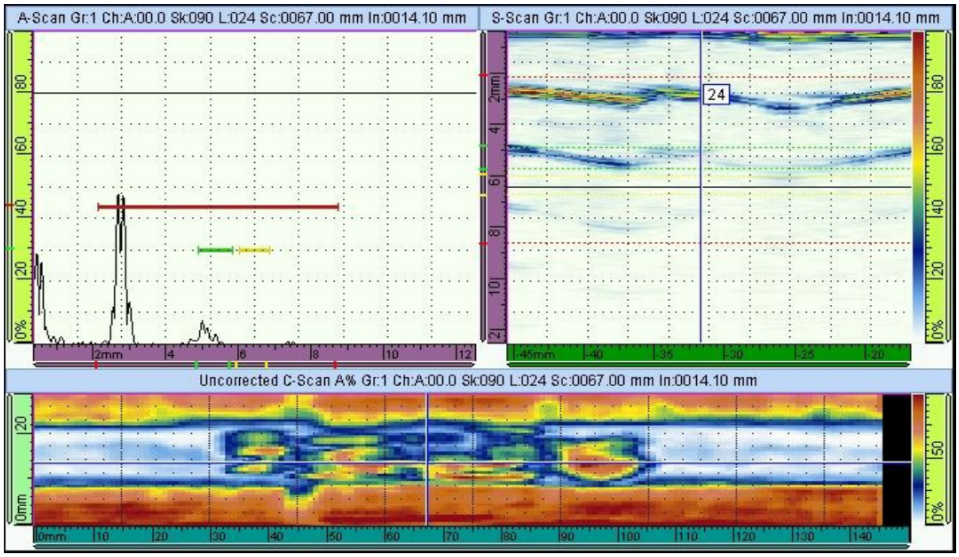

Figure B.1: Middle stringer's de-bond UT scan

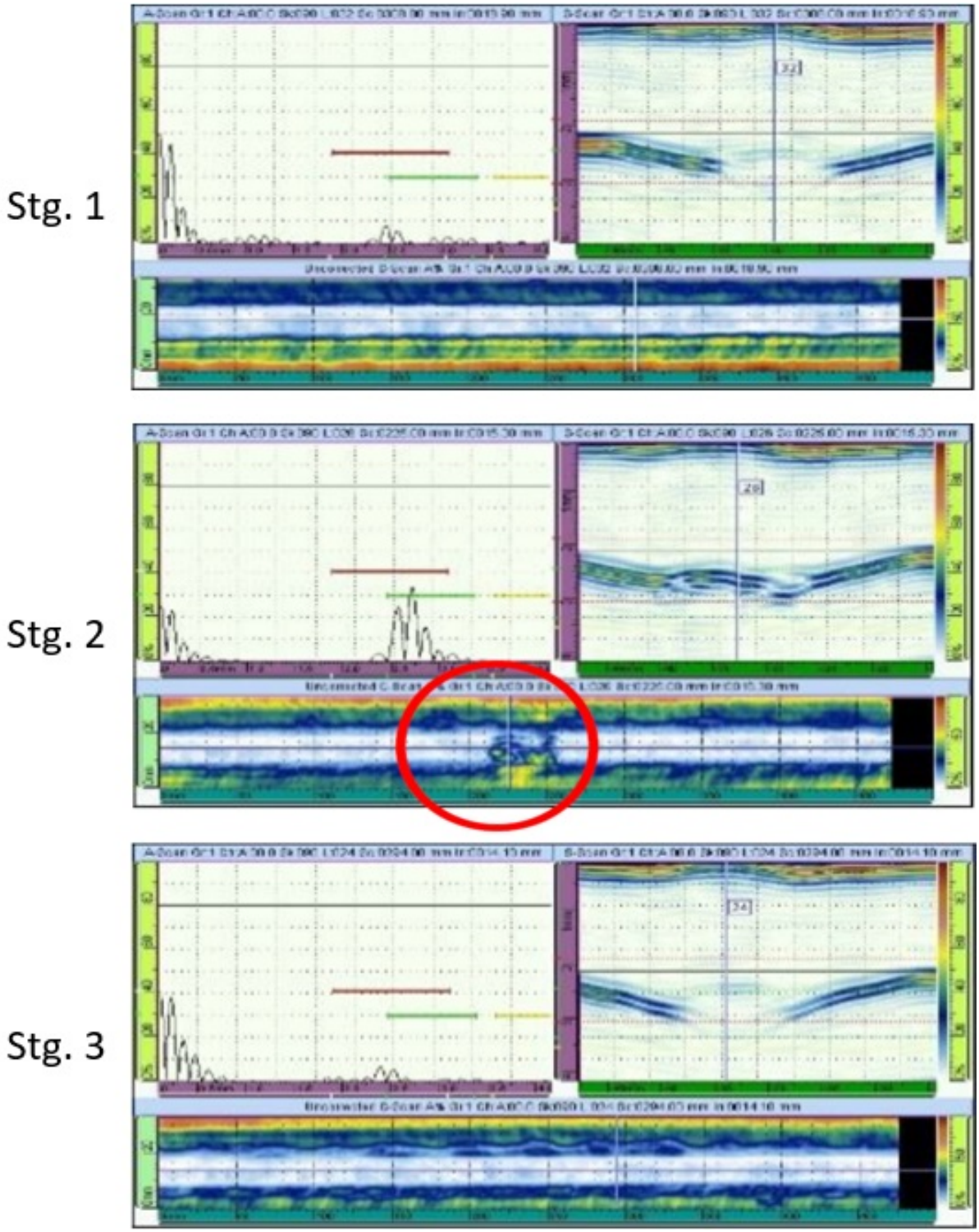

Figure B.2: UT scans of the stringers middle locations

C | Panel free vibration frequency response measurement

For the experimental measurement of the panel's free vibration frequency response, the panel (here without tabs) was suspended using two wires, such that the panel would have a minimum support. This minimum support is important to capture the panel's free vibration frequency response, as constraining the panel, for example by clamping one edge of it, would adversely influence the results. Measuring the panel's free vibration frequency response was done by exciting the panel's stringer side with a speaker over a certain range of frequencies, while a Polytec PSV 500 laser scanning vibrometer was scanning the skin side of the panel. The test set-up used to measure the panel's frequency response is shown in figures C.1 and C.2. Important to mention is that in these figures the panel with the resin tabs cast is shown, while the results in this section are for the panel without these tabs. However, the test set-up is almost identical with the one shown in this figures, the only small difference being in the way the panel was supported.

Figure C.1: Test set-up used to measure the panel with tabs frequency response

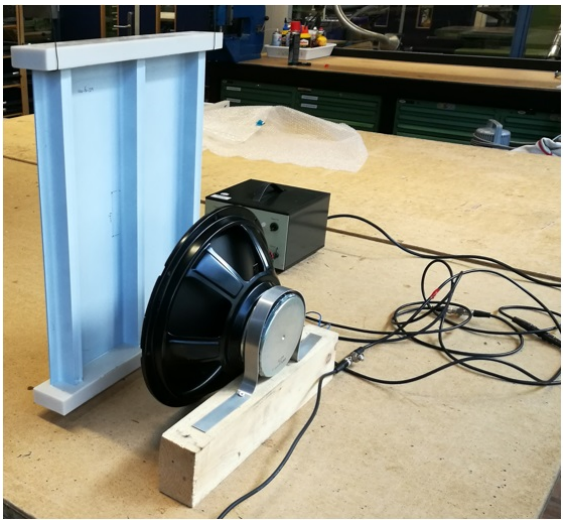

Figure C.2: Speaker used to excite the panel in the frequency response measurement

D | PYTHON SCRIPT TO INTRODUCE DIC MEASURED SKIN IMPERFECTION

In this appendix the script used to generate the syntax used to modify the Abaqus input file and to introduce the DIC measured skin out-of-plane deformation in the panel FE is described. The actual code used is also attached at the end of this appendix.

First, the measurement points are read from the DIC csv file containing the coordinates of the measured points on the panel's skin. These coordinates have to be adjusted prior to further use, as the coordinate systems of the DIC measurement and the one of the FE model are not identical. The first adjustment made was to change the X and Y axis between them, as in the DIC coordinate reference system the Y axis is along the panel's length, while in the FE model the X axis is along the panel's length. Furthermore, same as for the DIC $U3/Z$ 0 coordinate, also for DIC $U1/X$ coordinate the 0 coordinate is defined in a relative manner. As here the skin measurement area was centered inside the panel, this meant that the origin in the XY plane would be in the center of the panel, while the coordinate system of the FE model has the origin at the bottom of the skin below the middle stringer and at the end of the panel. This means that the X coordinates of the DIC measurement points also had negative X coordinates. Therefore, to align the DIC measurement points with the panel FE model nodes along the X axis, a length equal with half of the panel's length was added. This addition is made such that the origin of the DIC measurement points along the X axis is also at the panel's end and not at the middle of it. After the switch between the X and Y axis of the DIC measurement points, no further adjustment was needed to align Y axes of the two reference systems, as in the FE model the 0 coordinate of the Y axis also sits at the half width of the panel.

The Z coordinates of the DIC measurement system, is also adjusted, as in figure 4.40 the positive direction of the Z axis is away from the stringer, while in the FE model is the opposite. This was simply done by inverting the sign of the DIC measurement points Z coordinate, which concluded the alignment needed between the two reference systems. The alignment along the Z axis of the reference system was not done, since it is not necessary for the FE analysis. Summarizing, the steps to align the DIC measured points and the FE model nodes reference systems was to switch the X and Y axes of the measured points, add half the panel's length to the X coordinates of the measured points and to invert their Z coordinate.

With the alignment needed for the two reference systems being done and having the measurement points and the FE model node coordinates, the next step is to change the Z coordinate of the FE model nodes to the value of the Z coordinate of the measurement points. To implement this, for all the FE model coordinates with a 0 Z coordinate (representing the nodes at the bottom of the skin) a search in the XY plane is done among the DIC measured points. This search had the origin centered in the XY coordinates of the FE model node for which the Z coordinate is to be adjusted. If multiple measurement points are found in this area, the averaged Z coordinate of the found points is then applied to the respective node as a displacement boundary condition. The searched area is adjustable and the specified size must be within a certain limit, considering that the distances between of the measurement points along the X and Y axes is not the same with the one of the FE model skin nodes. With that being said choosing a small area might lead to no points found within the DIC measurement points, while choosing a large area might lead to inaccuracies. As the searched area is defined by looking for DIC measurement points using the FE model nodal X and Y coordinates, plus/minus a certain value (tolerance), the shape of the areas searched are rectangular. As this rectangular searched ares is defined by using the model nodal X and Y coordinates, plus/minus a certain value (tolerance), the FE model node is right at the centre of the searched area. With the nodes IDs for which the corresponding Z coordinate from the DIC measured points is applied as a displacement identified, the syntax of the nodes sets definition using their IDs is written in a csv file. Similarly, the syntax of the displacement boundary condition applied for each of these node sets is written in another csv file. This is due to the fact that in the Abaqus input file, the node sets and the boundary conditions are defined in different file regions. With these files generated, the Abaqus input file used to create the imperfection node file was modified and ran. Similar with the buckling eigenvalue analysis, a node file is requested for the deformed shape of the panel, which serves as an imperfection input file at the start of the analysis in which the compressive behaviour of the panel is studied.

The comparison between the resulted shapes using tolerances of $\pm 1mm$, $\pm 2mm$ and $\pm 5mm$ are shown in figure 4.40. These tolerances give square searched areas with lengths of $2mm$, $4mm$ and $10mm$, therefore searched areas of $4mm^2$, $16mm^2$ and $100mm^2$.

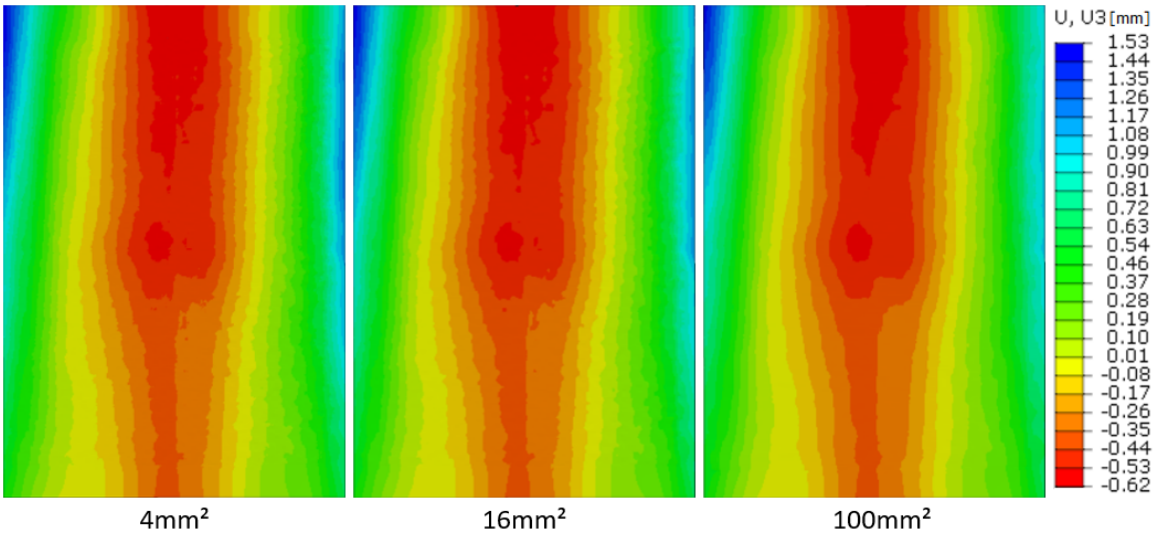

Figure D.1: DIC measured imperfection FE implementation accuracy as a function of the searched area

As it can be seen from this figure, as the searched area increases, so does the smoothness of the imperfect shape, which can be best seen by comparing either of the first two pictures from figure D.1 with the last one. This is comes as a direct consequence of a greater number of DIC measurement points found, therefore the average of more Z coordinates is applied on the FE model skin nodes. Out of these three imperfection tolerances, the one with a searched area of $4mm^2$ is considered to have the better accuracy, as it had a smaller number of averaged points. When comparing the scales of the DIC skin imperfection measurement from figure 4.40 with the one of the DIC skin imperfection measurement FE model implementation from figure D.1, once can see that the one from the FE model is larger. In order to check if indeed the imperfection is applied correctly, the csv file from the DIC skin measurement was visually inspected. This inspection had the purpose of finding the Z coordinate that gave a -0.62mmm deflection in the FE model, since this would be included in this csv file. The other $1.53mm$ one would not be included, since this is located at the side edge of the panel, area which is not included in the DIC measured points. Upon the visual inspection, the $0.62mm$ displacement was indeed found in the DIC measurement csv file. This means that indeed the skin imperfection had been applied correctly to the FE model panel's skin and that the scale from figure 4.40 is not entirely accurate.

```python
import numpy as np
import matplotlib.pyplot as plt
import scipy.linalg
import scipy.optimize as optimize
from matplotlib import rc
from mpl_toolkits.mplot3d import Axes3D
from matplotlib import cm
from matplotlib.ticker import LinearLocator, FormatStrFormatter
import pandas as pd
import os
import re
import glob
os.getcwd()

Panel_L = 495.3
Panel_W = 344.8


# Options
interp = 0 # 1 for interpolating missing imperfection nodes, else 0
ord = 3    # order of the interpolation 2: quadratic, 3: cubic
order = 2  # order of the interpolation 1: linear, 2: quadratic

write_output = 1 # 1 to write the output, 0 to skip

print_panel_points = 0  # Prints the panel FE model nodes

plot_interp = 0        # 1 to plot the interpolated coordinates
plot_indiv_surf = 0     # 1 to plot the individual IML/OML imperfect surface shapes
plot_indiv_points = 0   # 1 to plot the individual IML/OML  imperfect scatter points

# averaging range of imperfection points in [mm],
x_tol = 1
y_tol = 1

panel_1_IML = 'Panel_1_IML.csv' # in the csv file this panel is actually the second WI-19-0000 one
panel_1_OML = 'Panel_1_OML.csv'
panel_2_IML = 'Panel_2_IML.csv' # in the csv file this panel is actually the first WI-18-0076 one
panel_2_OML = 'Panel_2_OML.csv'

# reads the columns containing the [X,Y,Z] coordinates of the measured skin imperfection
P1_IML = pd.read_csv(panel_1_IML, delimiter=';', usecols=[' X', ' Y', ' Z'], dtype={" X": float, " Y"
   : float," Z": float})
P1_OML = pd.read_csv(panel_1_OML, delimiter=';', usecols=[' X', ' Y', ' Z'], dtype={" X": float, " Y"
   : float," Z": float})
P2_IML = pd.read_csv(panel_2_IML, delimiter=';', usecols=[' X', ' Y', ' Z'], dtype={" X": float, " Y"
   : float," Z": float})
P2_OML = pd.read_csv(panel_2_OML, delimiter=';', usecols=[' X', ' Y', ' Z'], dtype={" X": float, " Y"
   : float," Z": float})

# vectors used to plot the measured imperfection
X_panel_1_IML = P1_IML[' Y'] + Panel_L/2
Y_panel_1_IML = P1_IML[' X']
Z_panel_1_IML = P1_IML[' Z']
ZP1_IML_sort = Z_panel_1_IML.sort_values()

X_panel_1_OML = P1_OML[' Y'] + Panel_L/2
Y_panel_1_OML = P1_OML[' X']
Z_panel_1_OML = P1_OML[' Z']
ZP1_OML_sort = Z_panel_1_OML.sort_values()

X_panel_2_IML = P2_IML[' Y'] + Panel_L/2
Y_panel_2_IML = P2_IML[' X']
Z_panel_2_IML = P2_IML[' Z']
ZP2_IML_sort = Z_panel_2_IML.sort_values()

X_panel_2_OML = P2_OML[' Y'] + Panel_L/2
Y_panel_2_OML = P2_OML[' X']
Z_panel_2_OML = P2_OML[' Z']
ZP2_OML_sort = Z_panel_2_OML.sort_values()

# vectors used to modify the FE panel model nodes, with the alignment done to match the FE model
   coordinate system
```

```
X_imp_OML1 = np.zeros((94552, 1), dtype=float)
Y_imp_OML1 = np.zeros((94552, 1), dtype=float)
Z_imp_OML1 = np.zeros((94552, 1), dtype=float)

X_imp_OML1 = X_panel_1_OML.iloc[:].values + Panel_L/2
Y_imp_OML1 = Y_panel_1_OML.iloc[:].values
Z_imp_OML1 = -1*Z_panel_1_OML.iloc[:].values

X_imp_OML2 = np.zeros((94552, 1), dtype=float)
Y_imp_OML2 = np.zeros((94552, 1), dtype=float)
Z_imp_OML2 = np.zeros((94552, 1), dtype=float)

X_imp_OML2 = X_panel_2_OML.iloc[:].values + Panel_L/2
Y_imp_OML2 = Y_panel_2_OML.iloc[:].values
Z_imp_OML2 = -1*Z_panel_2_OML.iloc[:].values

# interpolation used to determine the imperfect coordinates of the FE model nodes without corresponding DIC measured coordinates
data = np.c_[X_imp_OML1, Y_imp_OML1, Z_imp_OML1]
X,Y = np.meshgrid(np.arange(0.0, 500.0, 1), np.arange(-175.0, 175.0, 1))
XX = X.flatten()
YY = Y.flatten()

if interp == 1:
    if ord == 2:
        def func(data, a, b, c, d, e, f, g):
            return a*data[:, 0]**2 + b*data[:, 1]**2 + c*data[:, 0]**2*data[:, 1] + d*data[:, 0]*data[:,1]**2 + e*data[:, 0] + f*data[:, 1] + g

        guess = (float(1), float(1), float(1), float(1), float(1), float(1), float(1))
        C, pcov = optimize.curve_fit(func, data[:, :2], data[:, 2], guess)

        zz = np.dot(np.c_[XX ** 2, YY ** 2, XX ** 2 * YY, XX * YY ** 2, XX, YY, np.ones(XX.shape)], C).reshape(X.shape)

        def interp_f(X, Y):
            return C[0]*X**2 + C[1]*Y**2 + C[2]*X**2*Y + C[3]*X*Y**2 + C[4]*X + C[5]*Y + C[6]

    elif ord == 3:
        def func(data, a, b, c, d, e, f, g, h, i, j):
            return a*data[:, 0]**3 + b*data[:, 1]**3 + c*data[:, 0]**2*data[:, 1] + d*data[:, 0]*data[:,1]**2 + e*data[:, 0]**2 + f*data[:, 1]**2 + g*data[:, 0]*data[:, 1] + h*data[:, 0] + i*data[:, 1] + j

        guess = (float(1), float(1), float(1), float(1), float(1), float(1), float(1), float(1), float(1), float(1))
        C, pcov = optimize.curve_fit(func, data[:, :2], data[:, 2], guess)
        #print(C)

        zz = np.dot(np.c_[XX**3, YY**3, XX**2*YY, XX*YY**2, XX**2, YY**2, XX*YY, XX, YY, np.ones(XX.shape)], C).reshape(X.shape)

        def interp_f(X, Y):
            return C[0]*X**3 + C[1]*Y**3 + C[2]*X**2*Y + C[3]*X*Y**2 + C[4]*X**2 + C[5]*Y**2 + C[6]*X*Y + C[7]*X + C[8]*Y + C[9]
        #zz = params[0]*X_panel_1_OML**2 + params[1]*Y_panel_1_OML**2 + params[2]*X_panel_1_OML**2*Y_panel_1_OML + params[3]*X_panel_1_OML*Y_panel_1_OML**2 + params[4]*X_panel_1_OML + params[5]*Y_panel_1_OML

    if ord != 3:
        if order == 1:
            # best-fit linear plane
            A = np.c_[data[:, 0], data[:, 1], np.ones(data.shape[0])]
            C, _, _, _ = scipy.linalg.lstsq(A, data[:, 2])  # coefficients

            # evaluate it on grid
            Z = C[0] * X + C[1] * Y + C[2]

            def interp_f(X, Y):
                return C[0]*X + C[1]*Y + C[2]

            # or expressed using matrix/vector product
            # Z = np.dot(np.c_[XX, YY, np.ones(XX.shape)], C).reshape(X.shape)
```

```
132
133         elif order == 2:
134             # best-fit quadratic curve
135             A = np.c_[data[:, :2]**2, np.prod(data[:, :2], axis=1), data[:, :2], np.ones(data.shape[
    0])]
136             C, _, _, _ = scipy.linalg.lstsq(A, data[:, 2])
137 
138             # evaluate it on a grid
139             Z = np.dot(np.c_[XX ** 2, YY ** 2, XX * YY, XX, YY, np.ones(XX.shape)], C).reshape(X.
    shape)
140 
141             def interp_f(X, Y):
142                 return C[0]*X**2 + C[1]*Y**2 + C[2]*X**2*Y + C[3]*X*Y**2 + C[4]*X + C[5]*Y
143 
144 # imperfection plotting
145 if plot_interp == 1:
146     # plot points and fitted surface
147     fig = plt.figure()
148     ax = fig.gca(projection='3d')
149     ax.plot_surface(X, Y, zz, rstride=1, cstride=1, alpha=0.2)
150     #ax.plot_surface(X, Y, zz, rstride=1, cstride=1, alpha=0.2)
151     plt.xlabel('X')
152     plt.ylabel('Y')
153     ax.set_zlabel('Z')
154     ax.axis('equal')
155     ax.axis('tight')
156     plt.show()
157 
158 # Tri-surface plots
159 
160 if plot_indiv_surf == 1:
161     #----------Tri-surface panel 1 IML----------------------
162     fig = plt.figure(1)
163     ax = fig.gca(projection='3d')
164     ax.plot_trisurf(X_panel_1_IML, Y_panel_1_IML, Z_panel_1_IML, cmap='rainbow', linewidth=0.2,
    antialiased=True)
165     ax.set_xlabel('X [mm]')
166     ax.set_ylabel('Y [mm]')
167     ax.set_zlabel('Z [mm]')
168     plt.title('Panel WI-18-0076 (1) IML imperfection')
169     plt.show()
170 
171     #----------Tri-surface panel 1 OML----------------------
172     fig = plt.figure(2)
173     ax = fig.gca(projection='3d')
174     ax.plot_trisurf(X_imp_OML1, Y_imp_OML1, Z_imp_OML1, cmap='rainbow', linewidth=0.2, antialiased=
    True)
175     ax.set_xlabel('X [mm]')
176     ax.set_ylabel('Y [mm]')
177     ax.set_zlabel('Z [mm]')
178     plt.title('Panel WI-18-0076 (1) OML imperfection')
179     plt.show()
180 
181     #----------Tri-surface panel 2 IML----------------------
182     fig = plt.figure(3)
183     ax = fig.gca(projection='3d')
184     ax.plot_trisurf(X_panel_2_IML, Y_panel_2_IML, Z_panel_2_IML, cmap='rainbow', linewidth=0.2,
    antialiased=True)
185     ax.set_xlabel('X [mm]')
186     ax.set_ylabel('Y [mm]')
187     ax.set_zlabel('Z [mm]')
188     plt.title('Panel WI-19-0001 (2) IML imperfection')
189     plt.show()
190 
191     #----------Tri-surface panel 2 OML----------------------
192     fig = plt.figure(4)
193     ax = fig.gca(projection='3d')
194     ax.plot_trisurf(X_imp_OML2, Y_imp_OML2, Z_imp_OML2, cmap='rainbow', linewidth=0.2, antialiased=
    True)
195     ax.set_xlabel('X [mm]')
196     ax.set_ylabel('Y [mm]')
197     ax.set_zlabel('Z [mm]')
198     plt.title('Panel WI-19-0001 (2) OML imperfection')
```

```
    plt.show()

# Scatter plots

if plot_indiv_points == 1:
    #-----------------Scatter panel 1 IML--------------------
    fig = plt.figure()
    ax = fig.add_subplot(111, projection='3d')
    ax.scatter(X_panel_1_IML, Y_panel_1_IML, Z_panel_1_IML, c=ZP1_IML_sort, cmap='rainbow')
    ax.set_xlabel('X [mm]')
    ax.set_ylabel('Y [mm]')
    ax.set_zlabel('Z [mm]')
    plt.title('Panel WI-18-0076 (1) IML imperfection')
    plt.show()

    #-----------------Scatter panel 1 OML--------------------
    fig = plt.figure()
    ax = fig.add_subplot(111, projection='3d')
    ax.scatter(X_imp_OML1, Y_imp_OML1, Z_imp_OML1, c=ZP1_OML_sort, cmap='rainbow')
    ax.set_xlabel('X [mm]')
    ax.set_ylabel('Y [mm]')
    ax.set_zlabel('Z [mm]')
    plt.title('Panel WI-18-0076 (1) OML imperfection')
    plt.show()

    #-----------------Scatter panel 2 IML--------------------
    fig = plt.figure()
    ax = fig.add_subplot(111, projection='3d')
    ax.scatter(X_panel_2_IML, Y_panel_2_IML, Z_panel_2_IML, c=ZP2_IML_sort, cmap='rainbow')
    ax.set_xlabel('X [mm]')
    ax.set_ylabel('Y [mm]')
    ax.set_zlabel('Z [mm]')
    plt.title('Panel WI-19-0001 (2) IML imperfection')
    plt.show()

    #-----------------Scatter panel 2 OML--------------------
    fig = plt.figure()
    ax = fig.add_subplot(111, projection='3d')
    ax.scatter(X_imp_OML2, Y_imp_OML2, Z_imp_OML2, c=ZP2_OML_sort, cmap='rainbow')
    ax.set_xlabel('X [mm]')
    ax.set_ylabel('Y [mm]')
    ax.set_zlabel('Z [mm]')
    plt.title('Panel WI-19-0001 (2) OML imperfection')
    plt.show()


#------------------Wireframe---------------
# fig = plt.figure()
# ax = fig.add_subplot(111, projection='3d')
#
# # Plot a basic wireframe.
# ax.plot_wireframe(X, Y, Z, rstride=10, cstride=10)
# plt.show()


#----------------------Surface3d--------------------

# fig = plt.figure()
# ax = fig.gca(projection='3d')
#
# # Make data.
# X_S = np.arange(X_min, X_max, 0.3)
# Y_S = np.arange(Y_min, Y_max, 0.3)
# Z_S = np.arange(Z_min, Z_max, 0.3)

# X_P, Y_P, Z_P = np.meshgrid(X_S, Y_S, Z_S)
#
# # Plot the surface.
# surf = ax.plot_surface(X_P, Y_P, Z_P, cmap=cm.coolwarm,
#                        linewidth=0, antialiased=False)

# # Add a color bar which maps values to colors.
# fig.colorbar(surf, shrink=0.5, aspect=5)
```

```
#
# plt.show()

# reads the original input file
abq_inp = 'Model_II_tabBC_DIC.inp'

n_rows = 129978
skip_rows = 9           # in the abaqus input file one line of fake nodes was added ' 0,0,0,0 ', for the pandas module to see the file as a CSV file

                        # Verify if the first and last coordinate match the abaqus input file!!!
# reads the FE model node cooridates form the abaqus input file
abq_inp1 = pd.read_csv(abq_inp, delimiter=',', skiprows=skip_rows, nrows=n_rows, usecols=[0, 1, 2, 3], dtype={0: int, 1: float, 2: float, 3: float})

# Assigns a vector for each of the X, Y, and Z FE model coordinates, together with the node ID which will be used to prescribe a displacement along the Z axis
Node_ID_abq = pd.read_csv(abq_inp, delimiter=',', skiprows=skip_rows, nrows=n_rows, usecols=[0], dtype={0: int})
X_panel_1_abq = pd.read_csv(abq_inp, delimiter=',', skiprows=skip_rows, nrows=n_rows, usecols=[1], dtype={1: float})
Y_panel_1_abq = pd.read_csv(abq_inp, delimiter=',', skiprows=skip_rows, nrows=n_rows, usecols=[2], dtype={2: float})
Z_panel_1_abq_old = pd.read_csv(abq_inp, delimiter=',', skiprows=skip_rows, nrows=n_rows, usecols=[3], dtype={3: float})


# initialises the X, Y, Z coord of the old and new input file
Node_ID = np.zeros((n_rows, 1), dtype=float)
X_abq = np.zeros((n_rows, 1), dtype=float)
Y_abq = np.zeros((n_rows, 1), dtype=float)
Z_abq_old = np.zeros((n_rows, 1), dtype=float)
X_abq_OML = np.zeros((n_rows, 1), dtype=float)
Y_abq_OML = np.zeros((n_rows, 1), dtype=float)
Z_abq_OML = np.zeros((n_rows, 1), dtype=float)
Z_abq_new_OML = np.zeros((n_rows, 1), dtype=float)
Z_abq_new = np.zeros((n_rows, 1), dtype=float)
Z_abq_new_interp = np.zeros((n_rows, 1), dtype=float)
# reads the relevant columns from the input file


#print(Y_panel_1_abq)

# transforms the coordinate columns into array type date
Node_ID = Node_ID_abq.iloc[:].values
X_abq = X_panel_1_abq.iloc[:].values
Y_abq = Y_panel_1_abq.iloc[:].values
Z_abq_old = Z_panel_1_abq_old.iloc[:].values

print(' zabq last', Z_abq_old)
#print(Z_panel_1_abq_old)

# generates the vectors to print the panel OML skin points
o=0
for q in range(len(X_abq)):
    if (Z_abq_old[q] == 0) and (-172.4 <= Y_abq[q] <= 172.4):
        X_abq_OML[o] = X_abq[q]
        Y_abq_OML[o] = Y_abq[q]
        Z_abq_OML[o] = Z_abq_old[q]
        o=o+1

# prints the panel's OML skin points
if print_panel_points == 1:
    fig = plt.figure()
    ax = fig.add_subplot(111, projection='3d')
    #ax.scatter(X_panel_1_abq, Y_panel_1_abq, Z_panel_1_abq_old, c='r', cmap='rainbow')
    #ax.scatter(X_imp_OML2, Y_imp_OML2, Z_imp_OML2, c=ZP2_OML_sort, cmap='rainbow')
    #ax.scatter(X_imp_OML1, Y_imp_OML1, Z_imp_OML1, c=ZP1_OML_sort, cmap='rainbow')
    ax.scatter(X_abq_OML, Y_abq_OML, interp_f(X_abq_OML, Y_abq_OML))
    #ax.scatter(X_abq_OML, Y_abq_OML, Z_abq_OML)
    ax.set_xlabel('X [mm]')
    plt.xlim(0, 500)
    plt.ylim(-250, 250)
```

```
    #plt.zlim(0, 500)
    ax.set_ylabel('Y [mm]')
    ax.set_zlabel('Z [mm]')
    plt.show()


#------------------------------input file----------------------------------

# the script output part
if write_output == 1:

    # creates the file names containing the tolerance used to generate the results
    namef1 = 'Imp1_NewCoord_Xtol_' + str(x_tol) + '_Ytol_' + str(y_tol) + '_InterpOrd_' + str(ord
) + '.csv'
    namef2 = 'Imp1_BC_Sets_Xtol_' + str(x_tol) + '_Ytol_' + str(y_tol) + '_InterpOrd_' + str(ord) +
'.csv'
    namef3 = 'Imp1_BC_Disp_Xtol_' + str(x_tol) + '_Ytol_' + str(y_tol) + '_InterpOrd_' + str(ord) +
'.csv'
    namef4 = 'Imp1_BC_Sets_Xtol_' + str(x_tol) + '_Ytol_' + str(y_tol) + '.csv'
    namef5 = 'Imp1_BC_Disp_Xtol_' + str(x_tol) + '_Ytol_' + str(y_tol) + '.csv'


    # opens the files with new coordinates, node sets and BC applied
    f1 = open(namef1, 'w')
    f2 = open(namef2, 'w')
    f3 = open(namef3, 'w')

    f4 = open(namef4, 'w')
    f5 = open(namef5, 'w')

    Z_abq_new[:] = Z_abq_old[:]
    Z_abq_new_interp[:] = Z_abq_old[:]

    i=0
    j=0
    #print(i)
    # generates new Z displacement for the FE model nodes in the abaqus model
    for i in range(len(X_abq)):
        #print('i=', i)

        #print(Z_abq_old[i])
        # checks if the points belong to the OML side of the panel (OML has Z coord, panel width =(-
172.4;172.4)
        if (Z_abq_old[i] == 0.0) and (-172.4 <= Y_abq[i] <= 172.4):
            index_avg = 0   # averaging index
            Z_new_sum = 0   # averaging sum

            # generates the node set and the coordinate modified or displacement applied to the node
 along the Z direction
            # by averaging the imperfection z coordinate over an area/tolerance specified in x_tol
and y_tol
            for j in range(len(X_imp_OML1)):        # index is now j since the no of nodes from the
abq and imperfection file differ
                if (X_imp_OML1[j] - x_tol) <= X_abq[i] <= (X_imp_OML1[j] + x_tol):
                    if (Y_imp_OML1[j] - y_tol) <= Y_abq[i] <= (Y_imp_OML1[j] + y_tol):
                        index_avg = index_avg + 1
                        Z_new_sum = Z_new_sum + Z_imp_OML1[j]

            # checks if the abq Z coordinate had an equivalent imp z coordinate and if not, the new
abq z coordinate/displacement can be interpolation based
            if index_avg == 0:
                if interp == 1:
                    Z_abq_new_interp[i] = interp_f(X_abq[i], Y_abq[i])
                Z_abq_new[i] = Z_abq_old[i]
            else:
                Z_abq_new[i] = Z_new_sum/index_avg
                Z_abq_new_interp[i] = Z_new_sum/index_avg

            # writes output is the panel FE model node has a DIC measurement point in its proximity
            if index_avg != 0:
                # writes the file containing the FE model node sets for which displacement BC will
be applied
                f4.write('*Nset, nset=Imp1_BC_' + str(int(j)) + '_NodeID_' + str(int(Node_ID[i])) +
```

```
'\n')
                f4.write(str(int(Node_ID[i])) + ',' + '\n')

                # writes the file containing disp BC syntax for the FE nodes with a DIC measurement point in its proximity
                f5.write('** Name: Imp1_BC_' + str(int(j)) + '_NodeID_' + str(
                    int(Node_ID[i])) + ' Type: Displacement/Rotation' + '\n')
                f5.write('*Boundary' + '\n')
                f5.write('Panel-1.Imp1_BC_' + str(int(j)) + '_NodeID_' + str(int(Node_ID[i])) + ', 1, 1' + '\n')
                f5.write('Panel-1.Imp1_BC_' + str(int(j)) + '_NodeID_' + str(int(Node_ID[i])) + ', 2, 2' + '\n')
                f5.write('Panel-1.Imp1_BC_' + str(int(j)) + '_NodeID_' + str(int(Node_ID[i])) + ', 3, 3, ' + format(float(Z_abq_new[i]), '.5f') + '\n')


            Z_abq_new_OML[i] = Z_abq_new_interp[i]

            # print(i)
            # writes the node sets syntax for the interpolation case
            f2.write('*Nset, nset=Imp1_interp_BC_' + str(int(i)) + '_NodeID_' + str(int(Node_ID[i])) + '\n')
            f2.write(str(int(Node_ID[i])) + ',' + '\n')

            # writes the disp BC syntax for the interpolation case
            f3.write('** Name: Imp1_interp_BC_' + str(int(i)) + '_NodeID_' + str(
                int(Node_ID[i])) + ' Type: Displacement/Rotation' + '\n')
            f3.write('*Boundary' + '\n')
            f3.write('Panel-1.Imp1_interp_BC_' + str(int(i)) + '_NodeID_' + str(int(Node_ID[i])) + ', 1, 1' + '\n')
            f3.write('Panel-1.Imp1_interp_BC_' + str(int(i)) + '_NodeID_' + str(int(Node_ID[i])) + ', 2, 2' + '\n')
            f3.write('Panel-1.Imp1_interp_BC_' + str(int(i)) + '_NodeID_' + str(int(Node_ID[i])) + ', 3, 3, ' + format(
                float(Z_abq_new_interp[i]), '.5f') + '\n')
            # print('i = ', float(i), ' X = ', float(X_abq[i]), ' Y = ', float(Y_abq[i]), 'Z_old = ', float(Z_abq_old[i]),
            #       ', Z new = ',
            #       float(Z_abq_new[i]), ', Z interp = ', float(Z_abq_new_interp[i]), ' interp abq xy = ',
            #       float(interp_f(X_abq[i], Y_abq[i])))

        #g1 = ('*Nset, nset=Imp1_interp_BC_' + str(i) + '_NodeID_' + str(Node_ID_abq[i]))

        # formats the
        ff = format(float(Z_abq_new_interp[i]), '.5f')
        #print(ff)
        #print('i = ', float(i), ' X = ', float(X_abq[i]), ' Y = ', float(Y_abq[i]), 'Z_old = ', float(Z_abq_old[i]), ', Z new = ',
             #float(Z_abq_new[i]), ', Z interp = ', (float(Z_abq_new_interp[i])), ' interp abq xy = ',
             #float(interp_f(X_abq[i], Y_abq[i])))
        #print('i = ', i, ' X = ', X_abq[i], ' Y = ', Y_abq[i], 'Z_old = ', Z_abq_OML[i], ', Z new = ', Z_abq_new_OML[i], ', Z interp = ', Z_abq_new_interp[i], ' interp abq xy = ', interp_f(X_abq[i], Y_abq[i]))


        # writes the new coordinates syntax
        #f1.write(str(float(Node_ID)) + '  ,' + str(float(X_abq)) + '  ,' + str(float(Y_abq)) + '  ,' + str(float(Z_abq_new_interp)))

        # writes the new coordinates syntax
        f1.write(str(int(Node_ID[i])) + '  ,' + str(float(X_abq[i])) + '  ,' + str(float(Y_abq[i])) + '  ,' + str(
            float(Z_abq_new_interp[i])) + '\n')

    f1.close()
    f2.close()
    f3.close()
    f4.close()
    f5.close()

    print('Z_old, Z_new')
```

```
458     for i in range(len(X_abq)):
459         print(Z_abq_old[i], Z_abq_new[i])
460 
461     print('max delta: ', max((Z_abq_new - Z_abq_old)), 'min delta: ', min((Z_abq_new - Z_abq_old)))
462 
463     # figures plot if output is requested
464     fig = plt.figure()
465     ax = fig.add_subplot(111, projection='3d')
466     #ax.scatter(X_panel_1_abq, Y_panel_1_abq, Z_panel_1_abq_old, c='r', cmap='rainbow')
467     #ax.scatter(X_imp_OML2, Y_imp_OML2, Z_imp_OML2, c=ZP2_OML_sort, cmap='rainbow')
468     #ax.scatter(X_imp_OML1, Y_imp_OML1, Z_imp_OML1, c=ZP1_OML_sort, cmap='rainbow')
469     ax.scatter(X_abq_OML, Y_abq_OML, Z_abq_new)
470     ax.set_xlabel('X [mm]')
471     plt.xlim(0, 500)
472     plt.ylim(-250, 250)
473     #plt.zlim(0, 500)
474     ax.set_ylabel('Y [mm]')
475     ax.set_zlabel('Z [mm]')
476     plt.show()
477 
478     fig = plt.figure()
479     ax = fig.add_subplot(111, projection='3d')
480     #ax.scatter(X_panel_1_abq, Y_panel_1_abq, Z_panel_1_abq_old, c='r', cmap='rainbow')
481     #ax.scatter(X_imp_OML2, Y_imp_OML2, Z_imp_OML2, c=ZP2_OML_sort, cmap='rainbow')
482     #ax.scatter(X_imp_OML1, Y_imp_OML1, Z_imp_OML1, c=ZP1_OML_sort, cmap='rainbow')
483     ax.scatter(X_abq_OML, Y_abq_OML, Z_abq_new_interp)
484     ax.set_xlabel('X [mm]')
485     plt.xlim(0, 500)
486     plt.ylim(-250, 250)
487     #plt.zlim(0, 500)
488     ax.set_ylabel('Y [mm]')
489     ax.set_zlabel('Z [mm]')
490     plt.show()
491 
492     fig = plt.figure()
493     ax = fig.add_subplot(111, projection='3d')
494     # ax.scatter(X_panel_1_abq, Y_panel_1_abq, Z_panel_1_abq_old, c='r', cmap='rainbow')
495     # ax.scatter(X_imp_OML2, Y_imp_OML2, Z_imp_OML2, c=ZP2_OML_sort, cmap='rainbow')
496     # ax.scatter(X_imp_OML1, Y_imp_OML1, Z_imp_OML1, c=ZP1_OML_sort, cmap='rainbow')
497     ax.scatter(X_abq_OML, Y_abq_OML, Z_abq_new_OML)
498     ax.set_xlabel('X [mm]')
499     plt.xlim(0, 500)
500     plt.ylim(-250, 250)
501     # plt.zlim(0, 500)
502     ax.set_ylabel('Y [mm]')
503     ax.set_zlabel('Z [mm]')
504     plt.show()
505 
506     # file written to verify if the interpolation works
507     f0 = open('interp_verif.csv', 'w')
508     for i in range(len(X_abq)):
509         f0.write('Z abq new' + str(float(Z_abq_new[i])) + 'Z abq new interp' + str(float(
    Z_abq_new_interp[i])) + '\n')
```